FLOWS IN A MODEL FURNACE

AND HEAT EXCHANGER

MARIA FOUNTI
B.Sc.(Eng.), M.Sc., D.I.C.

Thesis submitted for the degree of
Doctor of Philosophy
in the University of London

Imperial College of Science and Technology
(Department of Mechanical Engineering)

September, 1983

To my mother Elizabeth
and in memory
of my father Aristides

ABSTRACT

Velocity measurements are reported for a model heat exchanger flow with strong pressure drop and extended regions of recirculation and in a model furnace with a three-dimensional burner geometry and are intended to assist the appraisal of turbulence and combustion models for the prediction of complex geometry turbulent flows, the development and testing of three-dimensional calculation methods and the design of relevant engineering equipment. Measured values of the three-orthogonal mean velocity components and their corresponding fluctuations are provided and special attention was given to the measurement of boundary and inlet conditions. In addition, temperature and heat flux measurements are reported for a kerosene spray flame in the model furnace. The significance of the results for such purposes is discussed and appraised.

Use of laser-Doppler anemometry was essential and appropriate instrumentation was critically developed and used. For the high turbulence intensity measurements in the heat exchanger a frequency counter was interfaced to, and controlled by a microprocessor. The performance of the system was ascertained and experiments were performed in a free jet to quantify the effects of velocity and amplitude bias. They were found to affect the mean and rms velocities by up to 5% and 15% respectively. A filterbank signal processor was used for the velocity measurements in the model furnace and the kerosene spray flame and its perfomance was evaluated with simulated and real Doppler bursts. The established accuracy for the mean and rms velocities was 3% and 6% respectively and this was achieved away from the spray.

A perspex model simulating the shell-side flow in a shell and tube heat exchanger with disc and doughnut

baffles and in the absence of thermal effects was used to obtain velocity and wall pressure measurements. The effect of baffle spacing was examined for various Reynolds numbers in the fully turbulent regime. In general, this baffle arrangement promoted turbulent mixing and lengthened the flow path inside the test section. Pressure gradients dominated the flow field and the wall pressure losses were clearly related to wall friction effects.

In the model furnace, four different flow and geometrical configurations were examined: two confined isothermal flows with swirl numbers of zero and 0.70, a spray flame, and its corresponding isothermal flow in the absence of the liquid fuel. The spray was generated by a twin-fluid, air-blast atomiser with a spray angle of around 20 degrees and droplets with a mean Sauter diameter greater than 100 μm. The flame was stabilised by a disc encircling the atomiser and by the quarl geometry of the furnace. High values of axial and swirl velocity were measured close to the burner and corresponded to the secondary atomising air. Reynolds stresses in the spray flame were approximately 50% higher than for the corresponding isothermal case with maxima for the axial and swirl velocities in the vicinity of the edge of the spray. Maximum temperatures of 1380 degrees Celsius were achieved on the centre line between 0.39 and 0.430 furnace diameters from the burner exit.

Calculation methods were evaluated with the help of sample predictions of the isothermal flow in the furnace geometry. The combination of a finite-difference approach, with the k-ε-model of turbulence, revealed the sensitivity of the downstream flow to the initial conditions and that particular features of the flow, for example, the central and corner regions of recirculation could not be determined with great accuracy. The numerical and turbulence assumptions are discussed in relation to the results.

ACKNOWLEDGEMENTS

Prof. J.H. Whitelaw, my supervisor, guided me through the research program with advice and genuine criticism and for this I am deeply indebted to him.

In the early stages of the experimental work, Prof. D.F.G. Durao introduced me to laser Doppler anemometry and since then has influenced my views on signal processing techniques. Prof. P. Hutchinson, Dr. G. Wigley and Dr. J. Truelove showed active interest and helped me practically during my stay at the Atomic Energy Research Establishment, Harwell. I am obliged to Prof. F. Durst for his assistance during the writing-up period at the University of Erlangen-Nürnberg.

I am obliged to Dr. Y. El Banhawy and Dr. E. Ioannïdes for their assistance with the work in liquid spray flames and Mr. C. Vafidis for his help with the measurements in the heat exchanger model. I have also benefited from valuable discussions with Dr. A. Taylor, Prof. N. Vlachos, Mr. C. Verriopoulos and Dr. M. Yianneskis and with Dr. G. Scheuerer at the University of Erlangen-Nürnberg.

Last, but not least, I want to thank all my colleagues and friends at the Fluids Section for their moral support and encouragement, particularly Ms. G. Carvalho and Mr. P. Stolakis, Dr. Y. Levy and Dr. Z. Khan, Mr. B.A. Younis, Dr. A. Bicen and Mr. C. Arcoumanis.

I am grateful to Mr. J. Laker for the construction of the electronic parts and to Messrs. W. Crew, O. Vis, R. Church and M. Roper for the execution and help with the experimental apparatus.

I thank Ms A. Messner for the excellent typing of this thesis and Mr. R. Potter for the accurate execution of the diagrams Miss E. Archer, our librarian, and Mr. G. Tindall of the Reprographics Department have also been most helpful.

I am obliged to the medical staff of the Imperial College Health Centre, and particularly Dr. T. Addenbrooke, for their attention.

Financial support was provided by the Atomic Energy Research Establishment and at the last stages by my mother, and I gratefully acknowledge it.

TABLE OF CONTENTS

		Page(s)
ABSTRACT		3
ACKNOWLEDGEMENTS		5
TABLE OF CONTENTS		7
LIST OF TABLES		10
LIST OF FIGURES		12
LIST OF EQUATIONS		19
GLOSSARY OF SYMBOLS		21
CHAPTER I	INTRODUCTION TO THE THESIS	26
1.1	Flows considered and the present contribution	26
1.2	Outline of the thesis	31
CHAPTER II	LASER DOPPLER VELOCIMETRY INSTRUMENTATION	33
2.1	Introduction	33
2.2	Optical configurations	36
	2.2.1 Description of a laser Doppler anemometer with forward-scattered light	36
	2.2.2 Errors related to the optical arrangements	41
2.3	A microprocessor controlled frequency counting system	44
	2.3.1 Data acquisition system	45
	2.3.2 Performance characteristics	50
	Effect of sample size on confidence level	53
	Variation of frequency with tolerance level for 8/16 cycle comparison mode	56
	Effect of threshold level	58

	Further tests in real flow conditions	59
2.4	Performance evaluation of a filterbank system	62
	2.4.1 Operational characteristics	62
	2.4.2 Performance tests	67
	Preliminary tests with artificial bursts	68
	Amplifier Response	70
	Effect of particle concentration	72
2.5	Some consequences of bias effects	75
2.6	Concluding remarks	84
	Figures for Chapter II	87
CHAPTER III	HEAT EXCHANGER FLOWS	116
3.1	Introduction	116
	3.1.1 Purpose of investigation and modelling requirements	116
	3.1.2 Literature review	120
3.2	Experimental arrangement	134
	3.2.1 Flow configuration	135
	3.2.2 Optical arrangement and signal processing	136
	3.2.3 Measuring technique and error estimates	140
3.3	Results	145
	3.3.1 Entrance flow characteristics	146
	3.3.2 Wall-pressure distributions	148
	3.3.3 Velocity characteristics	151
3.4	Discussion	158
	3.4.1 Effect of baffle-spacing and Reynolds number	158
	3.4.2 Tendency to similarity of the flow	160
	3.4.3 Implications for heat exchanger design	161
3.5	Concluding remarks	166
	Figures for chapter III	168

CHAPTER IV	FURNACE-TYPE FLOWS	187
4.1	Introduction	187
	4.1.1 Purpose of investigation and outline of chapter	187
	4.1.2 Previous related work	189
4.2	Experimental and computational program	194
	4.2.1 Flow configurations and burner arrangement	194
	4.2.2 Velocity measurements and assessment of their accuracy	199
	4.2.3 Temperature and heat flux measurements and error estimates	206
	4.2.4 Experimental program	212
	4.2.5 Finite difference equations and the TEACH computer code	218
	4.2.6 Computational Program: boundary and initial conditions	219
4.3	Results	225
	4.3.1 Isothermal annular jet flows in a plexiglass enclosure	225
	4.3.2 Isothermal swirling flow with quarl in a model furnace: Experimental/Computational results	227
	4.3.3 Kerosene-fuelled spray flame in a model furnace	233
4.4	Discussion and concluding remarks	239
	4.4.1 Summary	239
	4.4.2 Implications of the results for calculation procedures	242
	Figures for chapter IV	244
CHAPTER V	CLOSURE TO THE THESIS	292
5.1	Summary of findings	292
	5.1 1 Signal Processing Systems	292
	5.1.2 Heat Exchanger Flows	293
	5.1.3 Furnace-type Flows	294
5.2	Recommendations for future work	296
REFERENCES		299

LIST OF TABLES

Table No.		Page(s)
2.2.1	Specifications of the rotating diffraction grating	43
2.3.1	Error sources and estimates for the frequency counter	52
2.3.2	Optical parameters for water flow	53
2.3.3	Characteristics of optical system for a single shot configuration	61
2.4.1	Filterbank frequencies	63
2.4.2	Electronic response of the filterbank	73
2.5.1	Summary of contributions related to velocity bias	76
3.1.1	Some geometric and flow parameters affecting heat exchanger design	118
3.1.2	Recent experimental findings for wall-reattaching flows	121-123
3.1.3	Recent experimental findings for flows past bluff-bodies	124
3.2.1	Operating conditions for heat-exchanger model	137
3.2.2	Optical parameters for heat exchanger flows	138
3.2.3	Doppler-broadening effects	142
3.2.4	Effects due to signal processing	143
3.2.5	Error estimates and corrections for heat exchanger flows	144
3.3.1	Summary of quantitative findings for heat exchanger flows	156
4.2.1	Furnace operating conditions	196
4.2.2	Optical parameters for furnace-type flows	200
4.2.3	Error estimates for isothermal and	

Table No.		Page(s)
	combusting flows in furnace	202
4.2.4	Fuel-spray characteristics	215
4.2.5	Effect of combustion air and atomising air on the size of unconfined spray flames	216
4.2.6	Characteristics of confined spray flames	217

LIST OF FIGURES

Fig. No.		Page(s)
2.2.1	Optical configuration of a forward-scattered light, fringe mode LDA	87
2.3.1	Frequency counter block-diagram	88
2.3.2	Typical waveforms in present counter	89
2.3.3	Digital Interface for frequency counter	90
2.3.4	Software flowchart	91
2.3.5	Variation of measured mean and rms frequencies with sample size	92
2.3.6	Signal validation criteria	93
2.3.7	Water flow. Effect of threshold level:frequency counter	94
2.3.8	Effect of threshold level: Cambridge tracker	95
2.3.9	Effect of threshold level: Disa tracker	96
2.3.10	Free jet. Centreline axial velocity distribution: Frequency counter	97
2.3.11	Schematic of optical and signal processing arrangements for a single shot configuration, Arcoumanis et al (1981)	98
2.3.12	Traces of instantaneous axial velocities over two successive cycles in a single-shot configuration	99
2.4.1	Block diagram of a filterbank processor	100
2.4.2	Radial profiles of mean and rms axial velocities of a free jet: Filterbank	101
2.4.3	Effect of threshold level on the variation of turbulence intensity	102

Fig. No.		Page(s)
	on the centreline of a free-jet	
2.4.4	Effect of frequency shift reversal on measured turbulence intensity	102
2.4.5	Methods used for generating simulated Doppler bursts	103
2.4.6	Variation of mean and rms frequencies against signal gain for different signal amplitudes	104
2.4.7	Frequency response of the filterbank amplifier	105
2.4.8	Variation of measured frequency with gain	106
2.4.9	Variation of maximum signal amplitude with amplifier gain	107
2.4.10	Centreline mean velocity profiles in a turbulent jet: Effect of particle concentration	108
2.4.11	Centreline axial normal stress profiles in a turbulent jet: Effect of particle concentration	109
2.4.12	Effect of gain on SDC along the centreline of a jet	110
2.4.13	Effect of gain on SDC and on the amplitude of a Doppler signal	111
2.5.1	Water-flow: Effect of discrimination level (slow sampling)	112
2.5.2	Water-flow: Effect of discrimination level (fast sampling)	112
2.5.3	Air-flow: Effect of discrimination level	113
2.5.4	Air-flow: Effect of discrimination level (particle dense flow)	114
2.5.5	Air-flow: Effect of discrimination level (particle rare flow)	115

Fig. No.		Page(s)
2.5.6	Water-flow: Comparison between different sampling methods	115
3.1.1	Diagram of fluid streams on the shell-side of a segmentally baffled heat exchanger	168
3.1.2	Typical arrangement of disc and doughnut baffles in a shell and tube heat exchanger	168
3.2.1	Water flow rig and optical arrangement	169
3.2.2	Heat exchanger model	170
3.3.1	Symmetry tests upstream of first baffle	171
3.3.2	Symmetry tests upstream of first baffle	172
3.3.3	Symmetry tests upstream of first baffle	173
3.3.4	Variation of wall static pressure coefficient	174
3.3.5	Velocity vectors for Set A and Set B in heat exchanger model	175
3.3.6	SET A: Radial profiles of mean axial and radial velocities	176
3.3.7	SET B: Radial profiles of mean axial and radial velocities	177
3.3.8	SET A: Radial profiles of normal stresses	178
3.3.9	SET B: Radial profiles of normal stresses	179
3.3.10	SET B: Similarity profiles behind doughnuts	180
3.3.11	SET B: Similarity profiles behind discs	181
3.3.12	SET A: Similarity profiles behind doughnuts	182

Fig. No.		Page(s)
3.3.13	SET A: Similarity profiles behind doughnuts	183
3.3.14	SET A: Similarity profiles for a low Reynolds number	184
3.3.15	SET A: Centreline profiles of axial velocities	185
3.3.16	SET B: Centreline profiles of axial velocities	186
4.2.1	General layout of furnace arrangement	244
4.2.2	Cylindrical enclosure and coordinate system	244
4.2.3	Basic-geometrical configuration of burner	245
4.2.4	Burner and atomiser arrangements for spray-flame experiments	245
4.2.5	Details of the air-blast atomiser	246
4.2.6	The suction pyrometer	247
4.2.7	Calibration curve for uncooled micro-suction pyrometer	248
4.2.8	Effect of suction rate	248
4.2.9	Thermocouple locations on furnace walls	249
4.2.10	Location of thermocouples on the furnace walls	249
4.2.11	Velocity p.d.f.'s in the spray flame	250
4.2.12	Particle concentration around spray region	251
4.2.13a	Effect of fuel nozzle diameter and combustion air on flame characteristics	252
4.2.13b		253
4.2.14	Finite difference grid	254
4.2.15	Initial profiles used in the calculation procedure	255

Fig. No.		Page(s)
4.2.16	Graphical reconstruction of the fuel spray and atomising air for calculation purposes	255
4.2.17	Predicted axial velocities for two atomising-air velocities	256
4.2.18	Predicted axial velocities for different grid distributions	256
4.2.19		257
4.2.20	Effect of under-relaxation factors	257
4.2.21	on the solution convergence	257
4.2.22		257
	Isothermal annular flow without swirl:	
4.3.1	Reproducibility of axial velocities	258
4.3.2	Symmetry of axial velocities(z=100mm)	259
4.3.3	Symmetry of axial velocities(z=400mm)	260
4.3.4	Axial velocity profiles	261
4.3.5	Inlet axial velocities	262
4.3.6	Inlet radial velocities	263
	Isothermal annular flow with $S_w = 0.70$:	
4.3.8	Inlet axial velocities	264
4.3.9	Inlet radial velocities	265
4.3.10a	Inlet mean circumferential velocities	266
4.3.10b	Inlet fluctuating circumferential velocities	267
4.3.11	Axial velocity profiles	268
4.3.12	Radial velocity profiles	269
4.3.13	Circumferential velocity profiles	270

Fig. No.		Page(s)
	Isothermal swirling flow with quarl:	
4.3.14a	Inlet axial mean velocities	271
4.3.14b	Inlet axial normal stresses	272
4.3.15	Inlet mean tangential velocities	273
4.3.16a	Axial mean velocities	274
4.3.16b	Axial normal stresses	275
4.3.17a	Radial profiles of mean tangential velocities	276
4.3.17b	Radial profiles of tangential normal stresses	277
4.3.18	Contours of constant axial mean velocity	278
4.3.19	Isotachs of tangential mean velocity	278
4.3.20	Effect of atomising air on the length of recirculation: Comparison between experiments and calculations	279
4.3.21	Axial velocities. Comparison between experiments and calculations	280
4.3.22	Circumferential velocities. Effect of atomising air: Comparison between experiments and calculations	282
4.3.23	Effect of combustion air on the shape of the recirculation zones: Comparison between experiments and calculations	282
4.3.24	Effect of combustion air swirl number on axial velocities: Comparison between experiments and calculations	283
4.3.25	Effect of combustion air swirl number on tangential velocities: Comparison between experiments and calculations	284

Fig. No.		Page(s)
	Combusting flow:	
4.3.26	Radial profiles of mean axial and circumferential velocities	285
4.3.27	Radial profiles of axial and circumferential normal stresses	286
4.3.28	Liquid-spray flame	287
4.3.29	Radial profiles of mean temperature	288
4.3.30	Wall and centreline temperature distributions	289
4.3.31	Wall heat flux distribution	289
4.3.32	Isotachs of axial velocities	290
4.3.33	Isotachs of tangential mean velocities	291
4.3.34	Isotherms.	290

LIST OF EQUATIONS

Eqn. No.		Page(s)
2.1	Relation between Doppler frequency and velocity	37
2.2	Control volume dimensions	38
2.3	Equation for the diameter of a focused laser beam	38
2.4	Formula for fringe spacing in control volume	38
2.5	Equation for number of fringes in control volume	38
2.6	Broadening error in the rms of velocity fluctuations due to transit time broadening	42
2.7	Error due to velocity gradient broadening	42
2.8	Ensemble-averaged mean and rms velocities	53
2.9	Yanta's formula for the number of data points required for the calculation of ensemble-averaged mean velocities	54
2.10	Yanta's formula for ensemble-averaged rms velocities	55
2.9a	Error in mean velocity due to sample size	55
2.10a	Error in rms of velocity fluctuations due to sample size	55
2.11	Output amplitude of a filterbank	64
2.12	integrator and its relation to the probability density distribution	64
2.13	Equation for signal processing time required by the filterbank	65

Eqn. No.		Page(s)
3.1	Borda-Carnot pressure-rise coefficient	150
3.2	Maximum pressure drop behind the discs in heat-exchanger model	150
3.3	Maximum pressure drop behind doughnuts in the heat-exchanger model	150
4.1	Lorenz-Lorentz law	203
4.2	Relation of refractive index to temperarture	204
4.3	Equation for suction velocity of pyrometer	208
4.4	Pyrometer efficiency equation	210
4.5	Equation for the calculation of heat transfer to furnace walls	211
4.6	Heat transfer equation for furnace	212
4.7	Mass conservation equation	218
4.8	Momentum conservation equation	218
4.9	The equations for "k" and "ε"	218
4.10	The general form of finite-difference equations	219
4.11	Logarithmic wall functions	219
4.12	Swirl number formula	225

GLOSSARY OF SYMBOLS

Roman characteristics

A_f	: Amplitude Output of Filterbank Integrators
a, b, c	: Half-axes in Control Volume (corresponding to x, y, z in cartesian coorinates)
B	: Ratio of Area of Disc to area of Doughnut-hole in Heat Exchanger Model
B.R.	: Linear Blockage Ratio in Heat-Exchanger Model (w.r. to D_S)
c_p	: Wall Static-Pressure Coefficient $(p-P_{ref})/ 1/2\rho U_b^2$
$c_{p_{B.C.}}$	: Borda-Carnot Pressure Rise Coefficient
D	: Internal Diameter of Upstream and Downstram pipes to the Heat-Exchanger Model
d_c	: (=H_n) Doughnut-Hole Diameter in Heat Exchanger Model (mm)
d_d	: Disc Diameter in Heat-Exchanger Model
d_e	: Beam Waist Diameter of Laser Beam before Focussing Lens
D_e	: Separation of the two Parallel Laser Beams as they leave the Focussing Optics
d_f	: Diameter of Focused Laser Beam at $1/e^2$ Beam Intensity
$d_n/2$	: (=S) Doughnut Step in Heat Exchanger Model (mm)
D_s	: Heat Exchanger Model Internal Diameter (mm)
$\overline{F}$, $\tilde{f}$	: Mean and Instantaneous Values of Doppler Signal Frequency
f	: Focal Length of Focussing Lens (mm)
f_D	: Doppler Frequency (Chapter 2)
f_{sh}	: Imposed Doppler Frequency Shift
H	: Baffle Window in Heat Exchanger (% Cut of baffle Diameter), (Chapter 3)

H_d : Disc Window , Heat Exchanger Model $(D_s - d_d)$

h.e. : Heat Exchanger

H_n : Doughnut Window Height, Heat Exchanger Model $(D_s - d_n)$

k : Turbulent Kinetic Energy $1/2\ (\overline{u^2} + \overline{v^2} + \overline{w^2})$

l : Baffle Pitch in Heat Exchanger Model (Spacing between Successive Baffles) (mm)

L : Total Length of the Heat Exchanger Model (mm)

l_i : Entrance Length in the Heat Exchanger Model before First Baffle (mm)

l_o : Exit Length in the Heat Exchanger Model after Last Baffle (mm)

$\dot{m}$: Mass Flow Rate (kg/s)

$\dot{m}_{a,a}$: Mass Flow Rate to Atomising Air in Furnace

$\dot{m}_b$: Mass Flow Rate through Heat Exchanger Model based on Bulk Velocity $(=\rho U_b/(\pi D_s^2/4)$

$\dot{m}_{c,a}$: Mass Flow Rate of Combusting Air in Furnace Geometry

$\dot{m}_f$: Kerosene Mass Flow Rate in Furnace

$\dot{m}_r$: Recirculation Mass Flow Rate

N : Total Number of Baffles in Heat Exchanger Model

N : Number of samples used for Ensemble-Averaged Velocities

n : Number of Cycles in a Doppler Burst

n : Refractive Index of Medium (Chapters 3 and 4)

N_f : Number of Fringes within the Control Volume

p : Local Wall-Static Pressure (mm H_2O)

p(f) : Probability Density Function (Chapter 2)

P_n : Normalised Frequency Probability Function (chapter 4)

P_d : Photomultiplier Pinhole Diameter

P_{ref} : Reference Pressure at Entrance of Heat Exchanger Model (0.8 D_s upstream first

Baffle) (mm H_2O)

$\dot{R}$: Volumetric Flux Rate of Fluid through the Control Volume

R : Radius of Furnace

R_1, R_a : Radius of Annulus in Furnace and Perspex Enclosure

r : Distance along Radial Coordinate in Furnace

r_d : Disc Radius in Heat Exchanger Model (mm)

r_n : Doughnut Radius in Heat Exchanger Model (mm)

S : $d_n/2$

S_w : Swirl Number (Chapter 4)

S.D.C. : Signal Duty Cycle for Filterbank Signal Processor. Percentage of the total time for which signals are present = 1 - Dropout rate = 1 - (Time during which no signal is present/ Total time of signal duration)

S.P.T. : Signal Processing Time of Filterbank

$\langle\tau_i\rangle$: Particle Arrival Time in Control Volume

$\langle\tau_m\rangle$: Minimum Recycle Time of Microprocessor

$\langle\tau_p\rangle$: Residence Time of a Particle in the Control Volume

$\langle\tau_s\rangle$: Sampling Time (average time between two consecutive samples-chapter 2)

$\langle\tau_t\rangle$: Turbulent Time-scale of the Energy Containing Fluctuations

T : Mean Temperature in Spray Flames (Chapter 4)

T_{wall} : Furnace Wall Temperature (°C)

$\bar{U}$, $\bar{V}$, $\bar{W}$, : Mean Velocity Components along x, y, z coordinates

$\sqrt{\overline{u^2}}, \sqrt{\overline{v^2}}, \sqrt{\overline{w^2}}$: Rms of Velocity Fluctuations along x, y, z coordinates respectively (Chapter 3)

$\bar{U}$: Ensemble-Averaged Mean Velocity (Chapters 2 and 3)

U_b : Bulk-Velocity (Chapter 3)($4\dot{m}/\rho\pi D_s^2$)(m/s)

U_i : Instantaneous Velocity for ith Sample (Chapter 2)

U	: Velocity of a Particle through the Measuring Volume in the Plane of the Minor Axes (Chapter 2)
$\bar{U}_{max}$	: Maximum Centreline axial Velocity (m/s)
$\bar{v}$, $\tilde{v}$	: Radial Velocity (Chapter 4)
V_{p-p}	: Peak-to-Peak Amplitude of Doppler Burst (mV)
V_{cut}	: Amplitude Cut in the Doppler Burst (mV)
$\bar{W}$, $\tilde{w}$	: Swirl Velocity (Chapter 4)
x, y, z	: Cartesian Coordinates in Heat Exchanger Model
z	: Axial Coordinate Distance Along Furnace Centreline

Greek characters

$\Delta\tau i$	: Time between the (i-1)th and ith Sample (Chapter 2)
δx	: Axial Spacing of Finite Difference Grid (Chapter 4)
Δx	: Control Volume Length
Δy	: Control Volume Width
δr	: Radial Spacing of Finite Difference Grid
δ_f	: Fringe Spacing in Control Volume
ε	: Isotropic Rate of Dissipation of Turbulent Kinetic Energy.
$\theta/2$	: Half-angle of Beam Intersection (Chapter 2)
λ	: Wavelength of Laser light
μ	: Instantaneous Scattering Particle Density (m^{-3})
μ_t	: Scalar Turbulent Viscosity
μ	: Viscocity of Fluid
ν	: Kinematic Viscocity
ρ	: Density of Water, 1.006 kg/m³ at 17°C, (Chapter 3)

ρ_a	: Density of air (kg/m³) (Chapter 4)
σ_F	: Transient Time Broadening Error in the rms of Velocity Fluctuations
σ_g	: Velocity Gradient Broadening Error
σ_i	: Broadening Error due to Diffraction Grating
$\phi_{k=n}$	: nth order-pair angle of Diffraction Grating

Operators

$<\cdots>$	: Time-Averaged Value
$\sim$	: Instantaneous Value

Subscripts

a,a	: Atomising-Air (Chapter 4)
b	: Bulk Velocity (Chapter 3)
a	: Annulus (Chapter 4)
c,a	: Combustion-Air (Chapter 4)
f	: Fuel (Chapter 4)

CHAPTER I
INTRODUCTION TO THE THESIS

1.1 Flows considered and the present contribution

The majority of engineering applications of heat transfer in turbulent flows aim to achieve high rates of heat transfer at low cost through the design of new and improved engineering devices. Different approaches are adopted to promote heat transfer and may involve a variety of complicated fluid flow mechanisms. On the shell-side flow of a shell-and-tube heat exchanger, for example, it is desirable to create flow separation to raise the level of effective thermal conductivity of the fluid near the wall. Alternatively, swirl motion may be imparted to the flow inside a furnace with the twofold aim of raising the overall level of heat-transfer coefficient and of producing a more uniform distribution of heat transfer.

The provision and control of complex flows, such as those described above, requires detailed understanding of the mechanisms which control the flow and, if possible, a calculation method which can predict the geometrical configurations and flow boundary conditions required to achieve them. Adequate mathematical descriptions exist for some simple situations (for example heat conduction, laminar convection, simple turbulent flows), but many practical fluid phenomena remain (such as complex turbulent flows, turbulent combustion, two-phase flows, unsteady flows) for which there is less certainty about the reliability and applicability of calculation methods. Experimental results are thus required to improve understanding and to evaluate and widen the applicability of calculation methods. With these in mind,experimental data are reported in this thesis for two model geometries, a

shell-and-tube heat exchanger and a furnace, and aim to describe in detail the velocity flowfield and in the latter case also the temperature field.

Shell-and-tube heat exchangers generally involve round tubes mounted in cylindrical shells with their axes parallel to that of the shell. They can be employed as "heaters" or "coolers" for a variety of applications that include oil coolers in power plants and process heat exchangers in the petroleum-refining and chemical industries. Many variations of the basic type exist. The differences lie mainly in the detailed features of construction that determine the fluid flow path through the heat exchanger and particularly in the choice of baffles used to support and space the tubes in the heat-transfer matrix. The relationship between heat transfer and pressure drop is less well understood in regions of recirculating flow where local flow instabilities may exist as a result of fluidelastic interactions or vortex shedding and can lead to periodic excitation of the tube bundle. The flexibility in geometry, such as shell, bundle and baffle styles and configuration, is one of the major reasons for the wider use of shell-and-tube heat exchangers. Arrangements of disc- and doughnut-shaped baffles, with the disc larger than the doughnut-hole, are thermally more effective than arrangements of segmental baffles but mechanical disadvantages have limited their industrial application. They are, however, convenient for the present purpose and the model arrangements examined here are of this type.

Relatively few problems of heat-exchanger performance can be reliably solved from knowledge of heat transport in simple flows. On the other hand, computer codes are being developed to obtain numerical solutions of coupled partial differential equations for elliptic and three-dimensional flows and offer exciting possibili-

ties. For example, Patankar et al (1974) have described a procedure which appears to provide a useful foundation and introduces the effects of baffles and tubes by a resistance to fluid motion in the governing equations. Also, Sparrow et al (1977) have formulated a method to represent the flow and heat transfer characteristics in ducts of periodically varying cross-section by assuming periodic variation of velocity and pressure components. Such procedures can and have been adapted to the shell-side flow of steam-generators used in nuclear reactor circuits, such as the CANDU (work by Carver et al (1981) cited by Martin et al (1982)). Acceptance of these numerical schemes depends to a large extent upon verification of calculated results by comparison with experimental data. However, in most practical situations, the flow-field is governed by more geometrical parameters than can be conveniently examined experimentally. Generalisation, separation and isolation of the involved physical processes, coupled in most cases with scaling-down in model sections, are thus required although this may involve the risk of losing some of the characteristics of the flow phenomenon present in the full-scale heat exchanger.

In this sense, secondary flow streams, thermal effects and the tube-bundle were eliminated from the heat exchanger model. Laser Doppler anemometry was used for the velocity measurements because of its non-intrusive nature. Mean and rms values of the three velocity components and the variation of pressure along the model wall are reported for different baffle spacings and Reynolds numbers based on the shell-diameter and bulk velocity. The results allow the assessment of the effect of geometrical confinement and initial conditions on the flow pattern and are of importance for the improvement of the heat transfer coefficient and the damping of flow-induced vibrations which vary directly with the local velocity and are influenced by confinement and turbulence level.

The second part of this thesis deals with the measurement of velocities, temperature and heat flux characteristics of the flows in furnace geometries with different degrees of swirl and employing liquid fuels. The effects of swirl in combustion systems have been known, in general terms, and utilised for many years. The need for fuel economy in the operation of practical combustion systems has initiated extensive studies aimed at understanding the detailed aerodynamics of combusting swirling flows and developing efficient and economical procedures to predict them. Thus, accurate and extensive experimental data are necessary, especially to quantify the effects of initial and boundary conditions. The isothermal results presented in this thesis help to fulfill this purpose and allow the quantification of the effects of swirl on the size and shape of recirculation zones.

In liquid fuelled flames, spray characteristics such as evaporation rate, droplet size and velocity are determined by the conditions at the fuel nozzle and the interaction between the spray and the surrounding air and can act as additional combustion-rate controlling parameters. The basic idea involved in all applications of spray flames, such as diesel engines, jet engines, gas-turbine combustors, furnaces etc, is the atomisation of the liquid fuel into individual small droplets that have a large aggregate surface area, thus increasing the rates of vaporisation, heat transfer and combustion. Quantification of the extent to which the spray influences the overall combustion process and aerodynamic characteristics of the flow represents another target of the thesis.

Prediction procedures, turbulence and combustion models intended for industrial furnaces and oil flames are of steadily increasing realism and refinement, see for example Bradshaw et al (1981) and Faeth (1981). Numerical

solutions of the two-dimensional time-averaged Navier-Stokes equations have been successfully used for the prediction of the flow and heat transfer characteristics in small-scale axisymmetric furnaces with gas-fuels, see for example Hutchinson et al (1977), and liquid-fuels, see El Banhawy et al (1981a). Recent developments in digital computers and in numerical solution procedures have made it possible to solve the three-dimensional equations and simultaneously to increase the number and details of physical and chemical processes which can be simulated by them, Jones and Whitelaw (1982).

Liquid fuel combustion is a complex two-phase phenomenon involving the fuel droplets in the liquid phase and the oxidising gas and combustion products in the gaseous phase. The complexity of the combustion process is further increased by factors like the non-uniform distribution of droplet sizes, their different injection velocities in conjunction with their interaction with the turbulent flowfield and the complexity of flow geometry. The current status of droplet and liquid combustion has been reviewed among others by Faeth (1977,1981) and the availability of combustion models to treat the liquid-phase, for example, by Ioannides et al (1978). These models allow the calculation of droplet size range, trajectories and velocity or, in simpler form, the size range with the assumption that the droplet velocities are identical to those of the gas.

The application of existing predictive procedures to the present flows was beyond the scope of this thesis. However, the limitations of existing two-dimensional computer codes and their turbulence models are considered in relation to previous work and, to support the discussion, sample calculations have been performed and the results are reported for the isothermal flow corresponding to the spray flame geometry. The two-dimensional mean flow equa-

tions were solved with a finite difference technique and the turbulent nature of the flow was represented by the k-ε-model, where the turbulent transport is represented by an eddy viscosity defined in terms of the kinetic energy of turbulence (k) and its rate of dissipation (ε). This approach was employed in order to demonstrate the dependence of predicted flow patterns on geometry and initial flow conditions.

The geometrical and aerodynamic complexities of the flows necessitated the development and validation of appropriate signal processing systems to be used in conjunction with laser Doppler anemometry. For the high turbulence intensities encountered in the model heat exchanger, a home-built frequency counter was interfaced and controlled by a microprocessor. Appropriate software was developed to allow versatile collection and storage of sampled data. The performance of the system was ascertained and experiments were performed in a free jet to quantify the effects of statistical bias. The poor signal-to-noise ratios in the model furnace and, in particular the spray flame suggested the use of a filterbank signal processor for the velocity measurements. Its performance was extensively evaluated with simulated Doppler bursts and real signals from a free-jet.

1.2 Outline of the thesis

The remainder of this thesis is organised into four chapters. Chapter II provides the background for the experimental methods with emphasis on the description of the frequency counter and interface and on the performance tests conducted both with the frequency counter and the filterbank signal processor. The results of these tests accompany the description of the corresponding instrument whereas an account on the consequences of bias

effects and the results obtained in a free-jet to demonstrate their significance for turbulent flows, are presented in a separate subsection.

Chapters III and IV are devoted to the experiments performed in the heat-exchanger model and the furnace respectively. Both chapters are organised in a similar manner, providing reviews of the related literature, descriptions of the test models and instrumentation together with estimates of the errors incurred. The results are presented and discussed in the context of better understanding of the flows and the implication for calculation procedures. A description of the finite difference equations to be solved for the calculation procedure and of the turbulence model are included in chapter IV. Computed results are presented and compared to the corresponding experimental results and modelling needs for future predictive work are assessed.

Finally, the achievements of this thesis are summarised in chapter V and suggestions are made for further work.

CHAPTER II
LASER DOPPLER VELOCIMETRY INSTRUMENTATION

2.1 Introduction

Laser Doppler velocimetry was used for the measurement of the velocity characteristics of the flows reported in this thesis. The technique makes use of the light scattered by particles suspended in and following the flow, to allow local time-resolved measurements of fluid velocity without disturbing the fluid phenomenon under investigation. Hence, and provided optical access to the fluid is available, there is no theoretical limitation to the measurement of turbulence intensities and/or flow direction.

Although the foundations of laser Doppler velocimetry have been set more than fifteen years ago, and by now the principles of the technique have been well documented, see for example Durst, Melling and Whitelaw (1976, 1981), Durrani and Greated (1976), Watrasiewicz and Rudd (1976), Drain (1980), both optical and signal processing methods continue to develop to meet the requirements for accurate and reliable measurements of turbulent velocities in complex flows. There are several factors that can affect the choice of type of signal processing system including the nature of the flow under investigation, the density and uniformity of scattered particles in the flow the signal to noise ratio of input signal as well as the required accuracy of the measurement and the type of information required (i.e. power spectrum, average frequency, "instantaneous" value of frequency etc.).

Signal processing methods in the frequency-domain, like spectral analysis, and in the time-domain frequency tracking are, by now, well understood and established.

The burst-type or individual realization signal processor has received particular attention because of the flexibility and versatility of digital signal processing. This, in conjunction with the recent advent of microcomputers, offers the possibility of fast, highly accurate and stable measurements together with easy and multiple access to storable information. Nevertheless, there has been some controversy regarding the correct methods of signal processing and sampled-data handling with burst-type processors which may result in possible bias of the computed statistical flow parameters.

It is the aim of this chapter to assess the capability of two different systems, a burst-type frequency counter and a filterbank signal processor, to measure in highly turbulent flows. The frequency counter measures the time for an integer number of zero crossings of a high-pass filtered Doppler burst and the filterbank collects signals whose frequencies correspond to the frequency bandwidth of several parallel filters and allocates them to a specific filter. Both processors can be operated either in the digital mode or,through a digital-to-analog converter, in the continuous, tracking mode. For the velocity measurements in the heat exchanger and furnace flows the digital mode was primarily used because of its advantages in storing, retrieving and subsequently manipulating data, and the absence of limitations in the handling of turbulence intensity levels.

Tests were performed to establish the extent to which the method of signal and data processing can influence the accuracy of the measurements. In the first instance, the suitability and accuracy of each processing system was substantiated by mean and fluctuating velocity measurements in an air free-jet and by comparison with simultaneous measurements with a frequency tracker. The free-jet was chosen because it represents a well-docu-

mented, stable, reproducible and self-similar flow.In the case of the counter processor, assessment of its suitability required the investigation of the effect of sample size, threshold and tolerance level settings as well as the investigation of data processing methods in order to obtain a bias-free result. The latter required the development of appropriate software and for this reason the counter was interfaced to an APPLE-II microprocessor. Subsequently, results were obtained in the water flow of chapter three which simulates the shell-side flow of a heat-exchanger.

Tests were performed with the filterbank to demonstrate the influence of input signal amplitude by altering the signal amplification and the threshold level setting. Further tests examined the effect of particle concentration on the measured frequency. The data were processed both with analog and digital methods and the differences are quantified and explained. The filterbank has been designed to operate with low quality signals and variable particle concentration, such as those encountered in a spray flame and it has been used for the furnace measurements for this reason.

With the use of digital processors, where statistical flow quantities are calculated from individual realisations, the accuracy depends on the precision of the individual measurement (usually identifiable) and on the deviation of the sampled velocity distribution from the true one. It is well-known that there are problems in interpreting the signals from the randomly arriving particles since the statistics of the particle arrival are correlated with the velocity. With laboratory scale flows we need to know how important these bias effects are, that is in which way they can influence the accuracy of measurements and how they can be minimised. Filter and amplifier response can also act in a consistent manner

to bias the measured velocity positively or negatively. Consideration of each bias error individually can be erroneous and there is a need for a practical approach to allow quantification of bias-errors to an extent adequate for engineering purposes.

The contents of this chapter are organised as follows: in subsection 2.2.1 the principles and common characteristics of the various optical systems employed for test purposes and for the measurements of chapters three and four are described. Although the optical parameters were different for each flow, the optical arrangements were selected as the simplest appropriate for the task in question. Subsection 2.2.2 briefly reviews the errors related to optical arrangements: a topic directly relevant to the appreciation of the results. Errors arising from improper operation or inherent in the burst-counter and filterbank, and the principles of their operation are discussed in sections 2.3 and 2.4 respectively. Section 2.5 deals with the quantification of errors associated with the method of data processing and analysis. The chapter closes in section 2.6 with a summary of the expected accuracy from the two processors.

2.2 Optical Configurations

2.2.1 Description of a laser Doppler anemometer with forward-scattered light

The optical arrangements employed the so-called dual beam mode (or otherwise called differential or fringe mode) that has been found to be the most suitable for measurements in small-scale air and water flows, Durst and Whitelaw (1971). This type of optical arrangement is shown in figure 2.2.1 and has the advantages of ease of alignment and comparative accuracy. The intersection of

two equally intense and coherent laser beams forms the control volume which is a region of interference between the two electromagnetic waves producing areas of high and low energy within the region. In the intersection region a system of interference fringe planes is formed, and because of the Gaussian light intensity of the beams, it achieves a near-ellipsoidal shape with boundaries which can be defined as a fraction ($1/e^2$) of the maximum intensity. A particle passing through the control volume with velocity U, in the plane of the minor axes produces a periodic variation in the scattered light intensity due to the interference of the light beams. Obviously, the angle between the incident beams enters the expression for the relation between Doppler frequency and velocity, which for the coordinate system defined in Figure 2.2.1 can be written as:

$$U = \frac{\lambda}{2 \cdot \sin(\theta/2)} f_D \qquad (2.1)$$

where λ is the wavelength of the laser beam. It is seen that the velocity of the particle is linearly related to the frequency of the scattered light intensity, f_D, and the constant of proportionality is uniquely defined by parameters that are independent of the flow. Eqn. (2.1) applies to any light transmitting fluid that contains particles which are assumed to travel at a velocity equal to that of the fluid.

The control volume, defined by the $1/e^2$ contour of the fringe modulation region, is near-ellipsoid with half axes a, b and c along the coordinate axes of figure 2.2.1 given by:

$$2a = \frac{d_f}{\cos(\theta/2)}$$

$$2b = d_f \tag{2.2}$$

$$2c = \frac{d_f}{\sin(\theta/2)}$$

where d_f is the $1/e^2$-diameter of the focused laser beam:

$$d_f = \frac{4}{\pi} \frac{\lambda \cdot f}{d_e} \tag{2.3}$$

and d_e is the beam waist diameter of the laser beams before the focussing lens. The interference fringes are parallel planes normal to the x-axis in figure 2.2.1 with a constant mutual distance δ_f given by

$$\delta_f = \frac{\lambda}{2\sin(\theta/2)} \tag{2.4}$$

The number of fringes within the control volume, N_f, is given by:

$$N_f = \frac{8}{\pi} \frac{f}{d_e} \tan(\theta/2) = \frac{4}{\pi} \frac{D_e}{d_e} \tag{2.5}$$

where D_e is the separation of the two parallel beams as they leave the focussing optics and f is the focal length.

The control volume is not necessarily equal to the measuring volume. If we define the measuring volume as the region in space from which Doppler signals are detected, its size is determined by the position and focal length of the collection lens and the dimensions of the

photomultiplier pinhole. The amplitude of the signal relative to the trigger level of the signal processing electronics also affects the dimensions of the measuring volume. Increasing signal amplitude allows particles farther away from the measuring volume centre, where the illumination is less intense, to be detected thereby increasing the effective measuring volume.

The provision of directional sensitivity in the velocimeter is essential in flows with regions of recirculation. It is allowed for by a frequency difference, or shift, between the two beams that form the control volume and obviously before the focussing lens. A comprehensive review of frequency shifting techniques is available in the literature (Durst and Zaré, 1974) and for the Doppler frequencies encountered in the present experiments the frequency shift was derived from the frequency difference between the first order maxima of a rotating radial diffraction grating. The grating acts both to provide the frequency shift and as a beam splitter (see figure 2.2.1). Frequency shifting confers two further advantages concerning the demodulation of the Doppler signal. It increases the separation, in frequency space, between the Doppler-shift frequency and the "pedestal" frequency associated with the time of flight of a scattering centre across the light beams: this is important in regions where the flow lies at large angles to the sensitivity vector of the velocimeter (Durst and Zaré, 1974). The second advantage has to do with the ability to select a range of the Doppler frequency demodulator which can accommodate the spread (due to turbulence) of the velocity probability density distribution at every point in the flow. The selection of a suitable range is made possible by varying the magnitude of the applied frequency shift.

The photomultiplier converts the light frequency information into electronic signals. The conversion

involves low noise amplification of the electronic signal, caused by the reception of photons on the surface of the photocathode, to a level suitable for signal processing.

The function of the signal processing system is to obtain information relevant to the velocity characteristics of the flow from the Doppler signal reproduced by the photomultiplier. A typical signal has the following characteristics:

(I) The signal is discontinuous with envelopes which contain Doppler signals, i.e. it has a "drop out rate" which is defined as the ratio of time without signal to total time.

(II) The signal frequency within each envelope, as already explained in subsection 2.2.1, is linearly proportional to the instantaneous velocity of the particle passing through the measuring volume perpendicularly to the major axis.

(III) The envelope size is a function of the size, position and velocity of the particle.

(IV) The signal carries noise contributions from both the optical system and photomultiplier. The optical noise is due to random noise fluctuations of the laser beams and random vibrations of the optical system. Electronic noise, on the other hand, is produced inside the photomultiplier and may be either thermal or shot noise. The quality of the signal strongly influences the accuracy with which the frequency can be measured and depends on the laser power, the transmitting and receiving optics, the scattering properties of the particles and the performance characteristics of the photomultiplier.

After the photomultiplier, signals from different types of optical arrangements are not fundamentally distinguishable and the same signal processing considerations apply. Important considerations in the design and choice of signal processing systems are the signal quality, dropout rate and turbulence level.

2.2.2 Errors related to the optical arrangements

Errors can arise as a consequence of the incompatibility between the dimensions of the measuring volume and the instantaneous length scales the fluid undergoes within it, from the stability of the frequency shift or from the photomultiplier response. The first are generally termed as "broadening" errors and the most common ones are:

Optical noise broadening which is associated with the optical components of the anemometer. It may be the result of fluctuations of the optical properties of the laser beam, vibrations of the optical benches, refractive index fluctuations, scattered light from walls, etc. Thus, even when a constant velocity is measured and the velocity spectrum can be expected to be a Dirac-delta function, optical noise may cause a broadening of the spectrum.

Transit time broadening is the result of the finite time the scattering particle travels through the control volume. The random arrivals and departures of individual particles into and out of the scattering volume cause phase and frequency fluctuations which give a finite width to the measured Doppler spectrum. Transit time broadening is associated with measurements using analogue signal processing methods, such as frequency analysis and frequency tracking. When more than one particles travel

through the control volume, the resulting Doppler signals may be in or out of phase. When they are in phase, the resulting signal is stronger than the individual signals. However, when the individual Doppler signals are out of phase, the resulting signal is weaker. Melling (1975) has shown that the broadening error in the rms of the velocity fluctuations, σ_F, is proportional to the Doppler frequency f_D and may be evaluated as follows:

$$\frac{\sigma_F}{f_D} = \frac{1}{2\sqrt{2\pi N_f}} \tag{2.6}$$

which is in accordance with other workers e.g. George and Lumley (1973) and Edwards et al (1971), (1973). For the frequencies encountered in the present experiments, around 2 MHz, and for the optical arrangements used this error was never greater than 0.15%.

Velocity gradient broadening of the Doppler spectrum may result when measurements are conducted in flows with spatial velocity variations, a finite size control volume and when there is a mean velocity gradient. In addition, when spatial variations of particle concentration exist in flows with spatial velocity gradients, an additional broadening of the spectrum may result. Velocity gradient broadening is usually significant only near walls. Particles moving through the scattering volume at different lateral locations scatter light at varying frequencies independently of the turbulent velocity fluctuations. A simple method of evaluating the broadening error has been proposed by Melling (1973). The error due to velocity gradient broadening σ_g is evaluated as follows:

$$\frac{\sigma_g^2}{f_D^2} = \frac{dy^2}{U_o^2} \left(\frac{dU}{dy}\right)_o^2 \tag{2.7}$$

Research into the sources of broadening and their effects have been reported, for example, by Edwards et al (1971), Goldstein and Kreid (1967), Greated and Durrani (1971), George and Lumley (1973), McLaughlin and Tiederman (1973).

Electronic noise of the photomultiplier and the signal processing system, such as shot and thermal noise, may broaden the Doppler spectrum further.

Instrument Noise Broadening: the main contribution towards instrument noise broadening comes from the rotating diffraction grating. The specifications of the diffraction grating used for the measurements of chapters three and four are shown in table 2.2.1.

Table 2.2.1: Specifications of the rotating diffraction grating

No. of lines	18,000
Diameter	152 mm
Concentricity	± 25 μm
Surface flatness	6 μm
1st order beam attenuation	43%
Rotational speed range	5-5,000 rpm ± 1%

Deterioration in the quality of signals obtained with a rotating diffraction grating as compared to, for example, a beam splitter, stem mainly from imperfection in the manufacturing process (usually bleaching). Although the present gratings were mounted on a heavy brass

flywheel and located with precision needle bearings, the inherent vibrations caused errors which increase with rotational speed. An overall estimate of the broadening error σ_i caused by the random fluctuations in the speed of the grating corresponds to approximately 0.3% of the measured mean values.

2.3 A microprocessor controlled frequency counting system

The need to obtain velocity information in highly turbulent flows with high or low densities of scattering particles necessitated the design and construction of a counter processor capable of accepting low amplitude Doppler bursts at fast arrival rates. The instrument was designed and constructed at Imperial College by Durao, Laker and Whitelaw and, it times a scattering particle over a known number of interference fringes within the measuring volume and thus enables evaluation of instantaneous velocity. Use of simple high-speed logic and a high-frequency clock (100 MHz) allowed measurements in a continuous frequency range up to 30 MHz with an instrument re-cycle time of 40 μs. An additional analog-to-digital converter could provide an analog output of the counter.

In flows with high particle concentration, where Doppler bursts are separated by brief periods of dropout and random phase changes, the semi-continuous nature of the signal favours the use of the analog-mode with on-line real-time integration to provide time-averages of mean and rms velocities. Alternatively, with low particle concentrations or when flexible sampling and ensemble-averaging of data is required (unsteady, periodic or highly turbulent flows) the digital mode of the counter

is to be favoured. The counter was interfaced with an ITT 2020 microcomputer (identical to an APPLE-II) controlled by a 6502 machine language code. Additional software features, such as the measurement of time between two consecutive bursts, the storage of a large sample size and random selection from it, the calculation of probability density distributions, skewness and flatness factor etc. have also been accounted for.

2.3.1 Data acquisition system

The logic and principle of operation of the counter are described here with specific attention to the digital operation mode.

The signal from the photodetector, see figure 2.3.1, requires external bandpass filtering to remove the D.C. component (the pedestal frequency) and the high-frequency noise. The filtered signal is then fed to either of the counter inputs. It is firstly amplified by a fixed gain preamplifier, with a flat response between 0.05 to 24MHz, and then supplied to:

a) a limiter circuit (a Schmitt trigger) that removes any amplitude variations of the signal and produces a waveform that represents the zero crossings of the bandpass filtered signal. (Typical waveforms are shown in figure 2.3.2).

b) a preamplifier whose variable gain is externally adjusted to provide a burst with an amplitude above an internally set threshold level, (high level detector in figures 2.3.1 and 2.3.2) thus reducing the possibility of triggering on the noise signal in the absence of the Doppler frequency component.

The outputs from a and b are compared, validated and subsequently fed to a "counter" which produces an output pulse of duration covering exactly 8 (or 16) and 16 (or 32) cycles of the Schmitt trigger output. These pulses represent the time taken by a particle to cross 8, 16 or 32 fringes in the measuring volume. The pulse corresponding to the first 8 (or 16) cycles is fed to a 100 MHz - clock comparator and then to a (x2) multiplier and stored temporarily while the pulse corresponding to the first 16 (or 32) cycles is compared to a 100 MHz clock and stored. Inversion to the time information (provided in binary form) gives the required frequency which due to the necessary binary operation, is stored temporarily as a two 8-bit word (a mantissa and an exponent), and is available for further digital processing. A digital to analog converter transforms the readings to a voltage representing the instantaneous velocity variation suitable for analog processing.

The zero-crossing detection, threshold level validation, comparison to 100 MHz clock and storage of information are performed simultaneously with the burst detection by the counter (i.e., there is no time lag between detection of burst and storage of time information). The time required for the frequency calculation and satisfaction of the validation criterion

and until the instrument is ready to accept a new burst is 40 μs. The counter accepts only one measurement from each burst, which is temporarily stored until new data from another burst is validated.

If a change in signal frequency or amplitude occurs during a signal burst due, for example, to a sudden phase change caused by noise fluctuations (e.g. frequency shift), or two particles crossing simultaneously the measuring volume, it is necessary to detect and delete the corresponding frequency measurement. To achieve this, the

pulse output from the 8-cycle store is doubled and compared to the pulse output from the 16-cycle store and the result, a short length timing window is accepted or not depending upon the satisfaction of an externally controllable tolerance level (0.2 - 50% difference between 8 x 2 first and 16 first cycles), named validation criterion. If this criterion is not satisfied the reset logic is activated and the frequency reading in the counter is discarded as the signal is no longer considered periodic. Pulse-duration comparison can be performed either between the first 8-16 cycles or the first 16-32 cycles of the burst. The latter obviously requires more than 32 fringes above the preset threshold level and it becomes necessary with frequencies higher than 12 MHz, because they produce a short duration pulse.

The gating facilities of the counter as indicated on figure 2.3.1, are

- Trigger level Monitor pulse which when added to the input bandpass burst, provides a display on an oscilloscope of the amplitude validated part of the burst.
- Blanking Output signal, which when used with an HP-1740 oscilloscope provides display of frequency validated signals.
- Gate Input. It cancels the threshold detector operation and provides facility for measurements in continuous signals.
- Pulse-train gate input allows for external control of sampling time by means of an applied pulse-train. (Suitable for periodic/unsteady flows).

A serial interface card is used to transfer data from the counter to one of the eight input/output ports of the microcomputer. The frequency information is stored as two eight-bit binary words, a mantissa and an expo-

nent. The four most significant bits of the exponent word are used as a flag to check the signal arrival. When new data arrives at the store, a pulse is sent to a Flip/Flop gate which is activated and the result is stored to the "flag" part of the "exponent", see figure 2.3.3. Simultaneously, a second gate is activated and stops new data from being accepted for storage. After the data has been accepted for further manipulation the flag is reset (Value Ø) and new data is allowed to enter the store.

Figure 2.3.3 also shows the logic for the pulse-train gate. It is basically the same as for the general case with an extra gate applied to satisfy both the arrival of new data and the presence of a pulse, before the Flip/Flop flag is activated.

The "Mantissa-Exponent" information is stored in two memory locations of the microcomputer and the instantaneous frequency is provided as

$$f_D = \left(\frac{\text{MANTISSA}}{2^{\text{EXPONENT}}} \right)/10$$

The ITT 2Ø2Ø microcomputer comprises a 65Ø2 microprocessor with a 48 K, 8-bit word memory, an ASCII Keyboard, a floppy disc and a video monitor. Data collection is achieved in 65Ø2 machine language code, and the processing of data, via supporting programs, in BASIC.

In the first place a program has been developed to calculate ensemble-averaged mean velocities, standard deviations, skewness and flatness factors and ensures long times between the sampling of Doppler signals. The flow-chart for this "SLOW-sampling" program is shown in figure 2.3.4. The machine language subroutine is called by the BASIC program, a value of exponent and the corresponding Mantissa are selected and the instantaneous frequency

calculated in BASIC. The data is checked for validity and stored temporarily. The "data-collection" loop is repeated every 94 ms, and this sampling time can be varied between 40 ms and 5 secs. Once a prespecified number of data points has been collected the "ensemble-averaged" velocities are calculated. Graphics can display the variation of frequency with number of data points, which can also take the form of frequency against time (when sampling is performed at fixed rates). Velocity probability distributions are also calculated. The LDA conversion factor, frequency shift and normalising velocities can also be input so that a direct reading of velocity is provided.

A second program allows the collection of all validated signals from the counter. The BASIC software is essentially similar to the "SLOW-sampling" program but the machine language code differs in that up to 11,000 data points can be collected and stored in binary-form at any time, and subsequently processed by the BASIC program. The minimum re-cycle time of the microprocessor limited the minimum sampling time to 70 μs. Two versions of this FAST program were developed. The first collected a data point and waited until a new value appeared at the counter (assuming that the particle arrival time to the counter was longer than 70 μs; which was mostly the case with the water flow of chapter III, where the counter was primarily used). The second collected one data point every 70 μs, independently of the particle arrival rate. As a result, the same value could be read twice or more until a new particle arrived. This second method of fast sampling simulates the analog operation in that each data point was weighted with its residence time. FAST collection of data points is, in principle, more appropriate for LDA-measurements since it accumulates information from every single validated Doppler burst and there is no loss of time resolved information. The sampling process

(i.e. at uniformly or non-uniformly spaced intervals in time) must, however, be statistically independent of the process being sampled.

A machine language program was developed to collect up to 5,000 data points and simultaneously record the time between every two consecutive bursts. Time-weighted velocities could then be calculated. This program, in conjunction to the pulse-train input, can be used, e.g. in unsteady or periodic flows, with appropriate software to allow "ensemble-averaging" over several "periods" of the flow. The software was developed to evaluate the performance of the counter and its interface and then to allow the quantification and reduction of forms of bias. It should be noted that software development is an open-ended task and that the present programs can be modified and extended to provide the required information in different forms and detail.

2.3.2 Performance characteristics

The compatibility of the microprocessor to the counter, the operation of the flags, linearity and noise characteristics of the system were checked with continuous sinusoidal signals of known frequency, with simulated Doppler bursts of constant frequency and with the single-shot facility of the counter. The counter and the interfaced APPLE were found to be able to trace frequencies between 0.05-10 MHz satifactorily with a maximum deviation from the correct value of $\pm$ 0.25% of the input frequency. The minimum data collection time of the system was found to be 77 μs, slightly higher than the APPLE's minimum cycle-time (70 μs).

Errors in the frequency measurements result from:

a) binary operation of the counter and the use of 8-bit words. This error is independent

of the local frequency and is equal to 0.196% of the instantaneous value. Van Atta (1975) reported that the ambiguity equal to the last significant bit in the quantitizing process can be serious if the ratio of the rms level of the signal to the quantitizing increment is not sufficiently large, as can happen with samples of large values or skewness or flatness.

The nature of this error signifies that the frequency resolution is worse for the higher frequencies and becomes better as the lower limit of acceptable frequencies is reached.

b) As shown in table 2.3.1 the error due to the 8-bit accuracy of the APPLE was of the order of 0.5% in the standard deviation for - 7500 - data points and increased with increasing sample size. It was negligible for mean values.

In order to quantify the performance characteristics of the counter and its related software, a water flow was chosen. Measurements were taken in a 74 mm diameter perspex pipe with a 54 mm disc centrally located to it. The flow had a Reynolds number of 4.9×10^4 and bulk velocity of 0.495 m/s. The measurements were taken either at 0.5 diameters before the disc or at 0.28 diameters after the disc, well within the recirculation region. The optical parameters relating to the above system are indicated in table 2.3.2. Frequency shift of 1.3 m/s was provided by a radial diffraction grating and the flow was seeded with the naturally occuring particles in water. Measurement accuracy was subject to correct threshold level and validation criteria settings.

Error Source	Implication / Sampling	% Error in Measured Frequency			Comments
		No. of Samples	Mean	Rms	
8-DIGIT ACCURACY OF COUNTER	(*) FAST SAMPLE COLLECTION	2	0	0	A fixed-known frequency was fed to the counter, and ensemble averages were calculated for various sample sizes. (*) The method of sample collection does not contribute to the error. It is used here to indicate the different structure of the two programs.
		10	0	1.61×10^{-2}	
		50	1.3×10^{-6}	4.955×10^{-2}	
		100	2.6×10^{-6}	7.609×10^{-2}	
		200	7.8×10^{-6}	1.89×10^{-1}	
	SLOW SAMPLE COLLECTION	20	0	1.89×10^{-1}	
		200	7.8×10^{-6}	1.215×10^{-1}	
		2500	9.2×10^{-6}	3.43×10^{-1}	
		5000	6.5×10^{-6}	3.94×10^{-1}	
		7500	26.1×10^{-6}	4.54×10^{-1}	
SAMPLE SIZE	SLOW COLLECTION	200	2.5	8.0	For the calculation of % errors see Yanta (1973). Values quoted here are for a 99% confidence level and a turbulence intensity of 22%.
		2500	0.7	3.5	
		5000	0.5	2.4	
		7500	0.4	1.99	
		10000	0.35	1.68	
		12500	0.33	1.58	
DIGITAL MODE	Limits accuracy of frequency resolution due to binary transport of information	N/A	0.196	0.196	

Table 2.3.1: Error sources and estimates for the frequency counter

Table 2.3.2: Optical parameters for water flow

Laser:	5 mW He-Ne. $\lambda = 6.32 \times 10^{-7}$m
Focal Length of Focussing Lens:	f = 100 mm
Radial Diffraction Grating:	$0 \leq f_{sh} \leq \pm 2.5$ MHz
Long Term Stability:	0.3%
Short Term Stability (rms):	0.5%
Fringe Volume Dimensions (in Water)	
Width:	y = 0.316 mm
Length:	x = 1.410 mm
Measured beam-intersection half-angle:	$\theta/2 = 8.027°$
Number of Fringes (stationary Disc):	140
Frequency Response Constant:	441.36 KHz/ms^{-1}

Effect of sample size on confidence level

It is assumed that the distribution function obtained from a set of N measurements (i.e. the sample size) is representative of the turbulence process. Neglecting velocity bias, if U_i is the measured velocity and N the number of data taken, then the average velocity and standard deviation are:

$$\bar{U} = \sum_{i=1}^{N} U_i/N \quad \text{and} \quad \sqrt{\overline{u^2}} = \left[\sum_{i=1}^{N} (U_i - \bar{U})^2 /N\right]^{1/2} \qquad (2.8)$$

It is obvious that a satisfactory mean and/or rms value depends on the number of data points used.

Yanta (1973) provides the following formulae, used here to estimate the number of data points needed to achieve a certain confidence level that the experimental mean value differs from the true population mean value by a known (or specified) relative error:

$$N = \frac{z_c^2 \quad (\sigma/\mu)^2}{(\frac{\mu-\bar{x}}{\mu})^2} \tag{2.9}$$

where z_c^2 equals 1.645, 1.96 and 2.58 for 90-, 95- and 99- per cent confidence limits,

$$(\sigma/\mu)^2 = \frac{\text{population standard deviation}}{\text{population mean}} = \frac{(\sqrt{\overline{u^2}})^2}{\overline{U}}$$

and

$$(\frac{\mu-\bar{x}}{\mu})^2 = \text{required confidence level} = \frac{(\text{population mean-sample mean})}{\text{population mean}}$$

For example:

for a 99% confidence level

$$z_c = 2.58$$

$$\frac{\mu-\bar{x}}{\mu} = 1.00 - 0.99 = 0.01$$

Hence $$N = \frac{2.58^2 \ (\sqrt{\overline{u^2}}/\overline{U})^2}{(0.01)^2} = 66564 \ \frac{(\sqrt{\overline{u^2}})^2}{\overline{U}}$$

Thus for a 20% turbulence intensity 2663 data points are required for a 99% confidence limit. It is interesting to note that the number of data points is dependent on the local flow conditions. Similarly for the standard devia-

tion, see Yanta (1973), the required number of data points is given by:

$$N = \frac{z_c}{2\left(\frac{\sigma - \sigma_s}{\sigma_s}\right)^2} \qquad (2.10)$$

where $\frac{\sigma - \sigma_s}{\sigma_s} = \frac{\text{population rms - sample's rms}}{\text{sample's rms}} =$ required confidence level.

Rearrangement of (2.9) and (2.10) gives that for a given number of data points, N, the errors involved are

$$(\text{error in mean velocity})^2 = \frac{z_c^2 \, (\sqrt{\overline{u^2}} \, / \overline{U})^2}{N} \qquad (2.9a)$$

$$(\text{error in standard deviation})^2 = \frac{z_c^2}{2N} \qquad (2.10a)$$

The above analysis suggested that for a reasonably high number of data points, N, and for a given turbulence intensity the measured mean and rms frequencies should become independent, at least for practical purposes, of the number of sampled data points. The deviation of measured frequency from the expected one, when plotted against the number of collected data points should indicate the degree of uncertainty introduced to the system due to the counter and its interface.

Figure 2.3.5 shows the variation in the measured mean and rms frequencies when different methods of sample collection and data averaging are used. In table 2.3.1 the percentage error incurred, calculated from equations (2.9a) and (2.10a), is tabulated. This is the percentage error purely due to sample size and, that would have been expected if no other sources of uncertainty were present. In figure 2.3.5 the results are non-dimensionalised with

the measured values of $\bar{U}$ and $\tilde{u}$ when 5000 data points were collected. It can been seen that both SLOW (curve a) and FAST (curve b) sample collection give ensemble-averaged mean velocities which depend on the number of samples. As the number of samples decreases, the error bands increase and tend to infinity. As expected, all curves intersect at an ordinate value of unity and 5000 samples. The spread of all results for numbers of samples greater than, for example, 300 is less than 4% but distinct trends exist and can be explained. With the fast sampling arrangement, 15000 samples required around 20 seconds which is hardly long enough to stasistically average this water flow. It is to be expected that the correct mean and rms values are around 0.97 and 1.01 respectively. The slow sampling arrangement, in contrast, required around 15 minutes and small differences from asymptotes to 1.01 and 0.97 can easily be explained by non-turbulent broadening over periods of this length. In general, it is evident that around 10000 samples are required to obtain uncertainties of less than 0.5% and 1.5% in the mean and rms values respectively at 22% turbulence intensity.

Variation of frequency with 8/16 cycle-comparison mode for various tolerance levels

In the operation of the counter errors can arise if signals are obtained from particles that cross the measuring volume at large angles, if there are not sufficient cycles left in the burst after a discrimination level is set, if a second particle enters the measuring volume during the timing interval or if high-frequency noise is present and results in multiple-crossings. If the measurements of the Doppler period obtained between the first 8 and the first 16 cycles agree to a prespecified precision (tolerance level) they are accepted for further processing.

The correct measurement depends on the correct setting of threshold level and tolerance level. This implies a compromise between accepting data of lesser accuracy and insufficient measurements to obtain a reliable value of mean and rms velocities. Figure 2.3.6 shows the measurement of frequency for tolerance levels between 0.2 and 50%. A very low trigger level was used to indicate that an erroneously high velocity will be measured as a result of noise when the precision is reduced. With a prespecified precision of 0.2% between the first 8 and 16 cycles and with a low trigger level, it is assumed that a correct measurement is obtained. The figure indicates that errors up to 3% and 10% in the mean and rms values can occur when the tolerance is reduced by 50%. For most purposes, a tolerance level up to 10% will be adequate even with a very low threshold level. If the threshold level is increased, the tolerance level can be increased as well, but this can result in amplitude bias of the measured values. Evaluation of the chosen tolerance level can be made by observing the percentage of validated signals (on the LED frequency display of the counter) when compared to the particle arrival rate (which can be observed on an oscilloscope). A very high percentage of validated signals can indicate that noise is being counted.

Further checks can be made by comparing the measured frequency with a 0.2% tolerance level to that obtained with a 10% tolerance level. Correct choice of trigger level results in a mean frequency value independent of tolerance level settings up to 12%. Beyond this value, i.e. for 24% or 50% tolerance level settings the data arrival rate is reduced and obviously this results to a biased measurement.

Effect of threshold level on measured mean and rms

The importance of threshold level has already been mentioned in relation to the tolerance level. An additional effect stems from the relationship between signal amplitude and particle velocity, see Durao et al (1980b). This causes a biasing of the measured velocity towards lower values and can be introduced particularly when a high discrimination level is used which inevitably prevents recognition of the low amplitude-high velocity bursts. The subject will be dealt with in more detail in section 2.5.

Figures 2.3.7, 2.3.8 and 2.3.9 show the variation of measured mean and rms frequency with increasing threshold level for three different instruments: the present-counter, a Cambridge-Consultants tracker and a DISA-55N20 tracker. The two tracking systems (figures 2.3.8 and 2.3.9) exhibit an initial drop in measured mean and rms values associated with the cut-off of base-noise from the signal. As the discrimination level is further increased a "working-range" is reached where the measured frequency does not depend on the selection of trigger level. Beyond that range, the drop-out period of the signal is very long and the instruments do not respond satisfactorily. For both analog-systems the working range corresponds to 20-40% of the maximum peak-to-peak voltage of the amplified signal.

A similar pattern is observed in figure 2.3.7 for the present counter. After the initial drop in mean and rms values due to the removal of noise, a constant frequency is reached independent of discrimination, corresponding again to 20-40% of the maximum peak-to-peak amplitude of the signal. The rms values are not exactly uniform and it is suspected that this is due to the influence of amplitude-bias. Beyond this region the mea-

sured values drop. An incorrect setting of the threshold level can result in large errors, say for example 5% of the mean value, but experience and care can ensure that the magnitude of the amplitude bias can be kept below.

Further tests in real flow conditions

The measurements shown in figure 2.3.10 were obtained on the centre-line of a 10 mm nozzle diameter-jet emerging into stagnant surroundings. This particular flow is well documented, see for example Durao et al (1974), and for this reason it was also used for testing the filterbank, and to obtain the results reported in section 2.5. The Reynolds number was equal to 0.5×10^4 and the optical system comprised a 5 mW helium-neon laser, a beam-splitter without frequency shift and a 100 mm focusing lens resulting in a 9.09° half-angle between the incident beams and a transfer function of 2.00 ms^{-1}/MHz. Seeding was provided by a silicon-oil atomiser, with average arrival rate between particles of 3 ms, measured on the centreline of the jet and at 0.50 mm from the nozzle. SLOW collection of Doppler signals was used: one burst was collected every 94 ms, as arranged by the software. The chosen time scales, guaranteed that the particle collection rate was always slower than both the integral time scales and particle arrival rates encountered on the centre-line of the jet, and velocity bias effects were expected to be small. The threshold level was set at 25% of the maximum burst amplitude at one nozzle diameter downstram the jet exit. At this location the maximum mean velocities are expected which correspond to the smallest burst amplitudes, due to the correlation of velocity and burst amplitude.

This choice of threshold level was expected to minimise amplitude bias. Figure 2.3.10 compares measurements

obtained with the present-counter, the Cambridge-Consultants Tracker and those obtained by other investigators. The results from the counter are in good agreement with those obtained with the tracker with maximum differences of less than 2% in the local measured velocity as expected from the preceding error analysis.

Using the "TIME-INFORMATION" program outlined in section 2.3.1 measurements have been obtained in the first half of the expansion stroke of an axisymmetric piston-cylinder assembly as described by Arcoumanis et al (1981). The system consisted of a cylinder of constant radius which was closed at one end by the cylinder head and at the other by the piston. The clearance volume at Θ = 360° represented the chamber at time equal to zero, before the initialization of the cycle and was filled with air at elevated pressure and temperature.

The optical system is shown in figure 2.3.11 and the optical parameters are shown in table 2.3.3. The counter was used at its maximum sampling rate of 25 KHz which was an order of magnitude higher than the expected frequencies of turbulent fluctuations. The frequency of Doppler signals was counted against clock pulses from the 100 MHz clock and the period of the first 8 and 16 zero crossings was compared to be within a preset tolerance level of 0.2%. The two traces of figure 2.3.12 were obtained over successive cycles during the first 90° of the expansion stroke (with a corresponding time of 75 ms). The digital frequency output was gated with the pulse-train facility of the counter which corresponded to the movement of the assembly half-speed shaft. The gate of this circuit was opened and closed after a preset number of pulses was received from an optical shaft encoder coupled to the assembly. To ensure that Doppler signals were present at a sufficient rate to allow a near-continuous trace of results, silicone oil droplets were added in large concen-

Table 2.3.3: Characteristics of optical system for a single-shot configuration

Half angle of intersecting beams	6 4°
Fringe spacing	2.8 μm
Diameter of intersecting region at $1/e^2$ intensity location	58 μm
Length of intersection region at $1/e^2$ intensity location	520 μm
Number of stationary fringes	21
Frequency shift	1.83 MHz

trations. Pairs of frequency and time between particles were stored and subsequently plotted as velocity versus crank angle and time The measurement point was on the axis and at a distance of 30 mm from the cylinder head and was chosen to reflect the trend of the instantaneous piston speed.

It can be seen that the developed software was able to capture the frequency variations from one cycle to the next, which are due to the statistical nature of turbulence. It should be mentioned that as the piston moves away from the cylinder head, the concentration of the silicone oil seeding particles is reduced and this is reflected in the last 40 degrees of the measuring cycle as gaps in the traces of figure 2.3.12. In order to account for the variation of burst amplitudes and particle rates

over a measuring cycle the threshold level was set at a low level and the tolerance level was kept at 0.2%.

The results shown are consistent with those previously obtained by ensemle-averaging over many movements of the piston, or in an internal combustion engine. In particular, the variation of velocity is shown to be significant, due to turbulence, as well as to the near simple harmonic motion of the piston, Arcoumanis et al (1981).

2.4 Performance evaluation of a filterbank system

2.4.1 Operational characteristics

Baker (1974) and Baker and Wigley (1975) have described and tested the performance of the filterbank signal processing system. The instrument was developed by the Electronics and Applied Physics Division of AERE, Harwell as a special purpose instrument intended to work with signals of low signal duty cycle (of order 1%), of poor quality (i.e. low signal to noise ratio) and occuring over a relatively wide frequency bandwidth. Signals of this nature typically occur in highly turbulent unseeded gas flows. The instrument consists of a series of sixty filters within the frequency range from 0.631 to 9.55 MHz. Each of these filters has a constant ratio of 5% between the bandwidth and the centre frequency. Consequently there is an uncertainty of 2.5% on each measurement. The values of the centre frequencies, as shown in table 2.4.1, increase logarithmically in a ratio of 1.047129/1, thus producing overlap of adjacent filters at approximately the 3db points. The centre-frequencies are preset with a $\pm$ 0.5% accuracy and the bandwidth with a $\pm$ 0.1% accuracy of the true value.

The filterbank block-diagram is shown in figure 2.4.1. From the photomultiplier, the signals are supplied to the 60 bandpass filters. The signals are then amplified and the gain adjusted to limit the output signals to one Volt peak-to-peak. An interrogating system identifies the most resonant filter channel and, subject to the signal amplitude in this channel exceeding a preset threshold value, a D.C. level proportional to the centre frequency of this channel is presented to an "on-line" frequency output. Logic circuits prevent two outputs from being generated simultaneously and hold the last value of frequency if the signal amplitude falls below the threshold level. The frequency output in this mode is similar to that obtained from a tracker processor. A long time average of this output is metered as a mean frequency value. The rms value of the fluctuations at this output can be measured directly with a suitable external RMS-meter. The maximum signal is continuously monitored as it determines the preamplification level of the input Doppler signal. A threshold level is set as a percentage of the peak value of the maximum signal to reduce the system's response to noise. The proportion of time for which the maximum signal of each filter exceeds the threshold level is used as a measure of duty cycle and can be metered down to levels less than 0.5%.

Table 2.4.1: Filterbank frequencies

Plug-in	FILTER NUMBER									
	Centre Frequency (MHz)									
Unit no	0	1	2	3	4	5	6	7	8	9
1	0.631	0.661	0.692	0 724	0.759	0.794	0.832	0.871	0.912	0.955
2	1.000	1.047	1.096	1.148	1.202	1.259	1.318	1.380	1.445	1 514
3	1.585	1.660	1.738	1 820	1.905	1.995	2.089	2.188	2.291	2.399
4	2.512	2.630	2.754	2.884	3.020	3.162	3.311	3.467	3.630	3.802
5	3.981	4 169	4.365	4.571	4.786	5.012	5.248	5.495	5.754	6.026
6	6.31	6.61	6.92	7.24	7.59	7.94	8.32	8.71	9.12	9.55

Additionally, the frequency spectrum can be displayed in one of two ways. An analogue store at the output of each filter, accumulates a voltage when that filter is selected as the most resonant and its signal is above the threshold. By scanning repetitively the outputs of all 60 stores and applying to an external oscilloscope, a dynamic histogram display is obtained which builds up continuously until the input to the instrument is removed. At this stage the voltage on each of the 60 stores can be inspected and stored on a paper tape.Alternatively the voltage being accumulated on each store can be allowed to leak away with a selected time constant. The oscilloscope display will then stabilise itself and show a frequency spectrum which has been averaged over a time comparable to the time constant used.

Since the bandwidths of the filters increase linearly with the filter centre-frequencies, the amplitude output A_f of the integrator corresponding to any particular filter, f, is related to the probability density function P(f), as follows:

$$A_f = C.\ P(f).f \qquad (2.11)$$

where C is an arbitrary constant such that:

$$P(f)\ df = 1 \qquad (2.12)$$

i.e.
$$C = \frac{A_f}{f}\ df$$

The main restriction in the operation of the filterbank comes from the fixed distribution of filters. At high turbulence intensities 40 filters may contribute to the formation of the spectrum, whereas at low frequencies less than 10 filters may contribute (Baker, 1974). Unavoidably, the resolution decreases as the number of fil-

ters is reduced. Since all the filters are continuously and simultaneously compared, the frequency response of the filterbank is restricted only by the response time of the individual filters, which is given approximately by the reciprocal of the filter bandwidth. For the present frequency range (0.6 - 10 MHz) because of the logarithmic increase in the filter bandwidth, the frequency response varied between 30 and 250 KHz.

For all measurements with the filterbank it is necessary to determine the signal processing time, or integration time, required to ensure that a sufficient number of samples (i.e. Doppler bursts) have occured to provide a statistically valid result. For relatively low turbulence levels ($<30\%$) the signal processing time (SPT) can be given according to Baker (1974) by :

$$SPT = \frac{Nn}{(SDC)} \quad \frac{1}{\overline{f}_D} \qquad (2.13)$$

where $\overline{f}_D$ = the mean Doppler frequency
n = Number of cycles in a burst
N = no. of samples

For N greater than 10^4, the SPT becomes meaningless because the errors in mean and rms velocities, according to the preceding analysis in section 2.3.2, become less than the resolution of the filterbank.

The probability distribution P(f), see eqn. 2.12, can be subjected to velocity bias error when the particle concentrations are low, since the influence of the weighting factor incorporated in A_f can be such as not to correct the correlation between the velocity and the particle arrival rate. This can be true for particle arrival times larger than the local turbulent time scales (for explanation see section 2.5). With high particle concentrations and when the spectrum is built in

such a way so as to permit the weighting of the individual frequencies, or correspondingly of the capacitor output with the signal duration, the resulting probability distribution should not be biased.

Since the filter bandwidths are proportional to their frequency, the spectrum obtained with a filterbank is $f_D \cdot P(f)$ rather than the normal probability of velocity $P(f)$. Also, because of their different bandwidths the filters are not subject to the same "white" noise level. To avoid the possibility of introducing a biasing error due to the different range of particle sizes being selected at different frequencies, the thresholds should be set for the same signal strengths rather than for the same signal to noise ratio.

According to Drain (1980) logarithmic spacing of the channels is not well suited for use with frequency shift as the frequency spacing and resolution are not then simple functions of velocity. The frequency shift should be chosen to prevent too great a drop in resolution at the high frequency end of the range.

It is for these reasons that Baker and Wigley (1975) have suggested that:

1. At least 8 cycles per Doppler burst should be used (Otherwise a skewed spectrum would be obtained)

2. To obtain a smooth spectrum, maximum signal amplitudes from 20 db down to 3 db above the threshold level (and intermittencies from 1% to 100%) can be used.

3. Frequency shift restrictions should be imposed as follows:
   For up-shifted spectra the minimum frequency of the

spectrum must be greater than half the frequency shift and for down-shifted spectra the maximum frequency of the spectrum must be less than half the shift value.

4. For proper operation the filterbank requires an input signal of 5 — 20 mV prior to amplification. The amplified voltage should not exceed 1 Volt p/p but normally should be greater than 200 mVolts. The "maximum signal" output should not exceed 20 Volts.

2.4.2 Performance tests

As discussed above, filter amplitudes are subject to systematic errors of varying magnitude. Baker (1974), who primarily investigated the performace of the filterbank using the built-up spectrum to obtain mean and rms values externally, suggested that the response of the filter outputs can be corrected by comparison with a known input frequency. The accuracy of the analog output of the filterbank had not been extensively investigated, although its use is easier and faster. Errors inherent in the design of the filterbank should become more obvious when the analog facility is employed, because of the method of operation of the instrument.

Using the analog output of the filterbank, tests were performed to quantify the effects of input signal amplitude, threshold level, signal amplification and particle concentration on the measured mean and rms velocities. Subsequently by comparison to a known frequency input the response of the instrument was adjusted and used to perform the velocity measurements reported in chapter 4. To evaluate the filterbank's performance simulated Doppler bursts and real signals from the free jet described in the last part of section 2.3.2 were used.

Radial scans at two and five nozzle diameters from the free-jet exit, shown in figure 2.4.2, confirmed that although mean velocities could be measured with the expected accuracy of 2.5%, turbulence intensities were progressively underestimated as the level of the fluctuations increased. This can be a result of the logarithmic arrangement of the filter bandwidths. If a particle passes with a frequency close to the edge of the frequency range covered by a certain filter, it is sensed by the filter as having the centre-frequency of the specific filter. Thus, the logarithmic progression of the centre frequencies of the 60 band-pass filters essentially means that more weight is given to low velocity particles, rather than the high velocity particles. Variation of the threshold level, i.e. discarding noise and bursts at a prespecified level of the peak amplitude level of the signal as in figure 2.4.3, showing the turbulence intensity variation along the centreline of the free-jet, affected the measured values by up to 4%, which nevertheless remained underestimated by about 10% when compared to the data of Durao et al (1974). Similarly, reversing the frequency shift, see figure 2.4.4, did not improve the situation, although it influenced the measurements again by about 4%.

Preliminary tests with artificial bursts

To investigate the influence of signal amplification and threshold level independently, artificial signals were generated, using two different methods, with the instrumentation shown in figure 2.4.5. Method A produced "Doppler" signals of constant frequency by superimposing the output of a sine-wave signal generator to a square wave. The bursts were adjusted to contain "Doppler" cycles at a frequency equal to the centre frequency of any particular filter under test. The amplitude, width and

"burst" spacing could be varied. The latter was arranged to produce signal intermittencies between 0.1% to 20%. Method B, similar to the one used by Baker and Wigley (1975) produced bursts of sinusoidal form varying at a linear rate through a prespecified frequence-range and burst spacing. This was accomplished by using a Voltage Controlled Oscillator (Wavetek model 144), with a sweep facility for linearly ramping the oscillator frequency output through a given frequency range . The Wavetek sweep rate was linear to $\pm$ 0.2% and the output signal frequency accurate to 0.25%.

Initially, "Doppler" bursts were generated by method B and with a time delay of 25 μs between them. The mean frequency measured with a frequency tracker was 5.02 MHz and the rms frequency was 2.44 MHz. The respective frequencies measured with the filterbank were 4.99 MHz and 2.45 MHz. The spectrum was built starting from the 13/14th filter (f_D = 0.75 MHz) and stopped at the 59th filter (f_D = 9.00 MHz). The sweep time for the ramp (τ_{sweep}) was kept constant at 0.4 ms for 10 MHz (f_{max}), i.e. the delay time was 40 μs per MHz The intermittency for the present case defined as $\frac{\tau_w}{\tau_s}$ x 100% was equal to 1.6%. The response of each filter is approximately equal to the inverse of the filter centre frequency. The presently measured mean frequency 4.99 MHz corresponds to the case where all 60 filters are being activated and to an average time delay of 20 μs. Namely, the filterbank on average will not recognise particles arriving faster than 20 μs. At the upper end of the spectrum at the 60th filter, the mean frequency is 9.55 MHz and the corresponding delay time 10 μs. Correspondingly, at the lower spectrum end, the mean frequency is 0.75 MHz and the delay time is 133 μs. This necessarily means that low velocity particles, which arrive less frequently, will be weighted with a longer residence-time than the faster moving particles. It is implied that this uneven weighting of particles

will introduce a form of bias similar in trend to the velocity bias, and possibly this is the reason for the biasing of turbulence intensities towards the lower values.

Amplifier response

The frequency response of the input amplifier to the filterbank was found to be non-linear. At the high frequency end of the filters (filters 55 to 59) the probability density distributions obtained using artificial bursts generated with method B were positively skewed and definitely non-Gaussian in shape. To demonstrate this a variable known frequency shift was added to bursts of known frequency generated by method A. The mean frequency measured with a mean-meter was checked if it increased by the same amount as the applied frequency shift. For mean frequencies below 4 MHz the error was within 3.0% but, for higher frequencies it could be as high as 15% of the local frequency. Tests with artificial bursts (method B), shown in figure 2.4.6, with various input signal amplitudes, ranging from 5 mV to 20 mV indicated that the "flat" response range of the amplifier narrowed as the input signal amplitude was increased for a constant threshold level 10% of the maximum signal amplitude. Mean frequencies could be measured, as expected, with a 3% accuracy, and rms values were within 6% of the correct reading. Variation of the threshold level did not alter the trends appreciably. Similar tests with constant frequency bursts (method A) indicated, through inspection of the amplified signal amplitude, that the gain for small signals (below 10 mV) was greater at low frequencies whereas the gain for large signals (above 20 mV) was greater at high frequencies. Since a signal amplitude threshold level has to be chosen to reduce the system response to noise, this non-linear response could bias

the frequency measurements. Figure 2.4.7 shows the case for a 15 mV input signal. There is clearly an operational flat range in the amplifier response, between 4 to 18 db which although alters the signal amplitude, does not affect the accuracy of measurements, for input frequencies between 1 to about 6.5 MHz. Hence, it is possible to choose a certain level of amplification for a pre-set threshold level to counteract the non-linearity of the input amplifier. At this threshold level the frequency response is flat over a limited frequency range, depending on the input signal amplitude and frequency, to better than $\pm$ 1 db. If the threshold level is decreased it should not have any effect on the maximum signal amplitude or the measured frequency. If it is increased, it might result to a non-linear response of the input amplifier, if the amplitude of the input signal is below 10mV.

The influence of gain on measured mean and rms values was verified for a range of threshold levels from 3% to 22% of the maximum signal, with real Doppler bursts, obtained on the centre line of the free-jet, see figure 2.4.8. The input signal amplitude was 20 mV and the bursts, without frequency shift, contained about 32 cycles. It is clear from the mean-frequecy results that a plateau exists in a range of gain from approximately 8 db to 24 db and that, if threshold levels between 5 and 15% are considered, the mean frequency can be evaluated as 2.0 $\pm$ 0.05 MHz. This represents an uncertainty slightly better than $\pm$ 3% and is more or less what was expected. The rms frequency results are considerably less reassuring. As the figure shows, there is a vague tendency towards a plateau but the use of the same limits of gain and threshold would result in uncertainties of around $\pm$0.04 in 0.2 MHz, i.e. around $\pm$10%. To these numbers, the results of the several other sources of possible errors should be added and, in the end, the uncertainty in the rms frequency will not be less than $\pm$ 15% of the local

value. Repetition of the same test with different input signal amplitudes showed that when the amplified signal amplitude was higher than 1.4 V, with the amplifier response being non-linear and when higher order filters started resonating the probability density distributions where skewed towards higher frequencies. The results of figure 2.4.8, were obtained with the "CLIP" protection facility incorporated into the filterbank and aimed to cut off all signal amplitudes above 1.4 V, and were repeated at different axial locations along the centre-line of the air-jet, with different turbulence intensities and the trends were confirmed. Mean velocities were in agreement with pitot-tube measurements and values obtained with a frequency tracker.

To demonstrate the effects of amplitude "clip" a few measurements were taken with artificial bursts of constant frequency (method A) and are shown in figure 2.4.9. For higher frequencies the clipping of the maximum signal amplitude starts at lower gains, in accordance with the non-linear response of the amplifier and the same is true for the higher input signal amplitudes.

Effect of particle concentration

In examining the effect of particle concentration, expressed in the instrument as the Signal Duty Cycle (SDC), the laser power and photomuliplier sensitivity had to be carefully adjusted. For the case of low seeding rate,the maximum laser power was used in conjunction with the optimum sensitivity of the photomultiplier. For the highly seeded case, the photomultiplier power was reduced so that only bursts from the seeding particles were sensed, and not the naturally occuring ones. In this latter case the SDC was necessarily considerably increased.

Figure 2.4.10 shows the variation of frequency on the centreline of the jet with two different particle concentrations. As expected, the mean frequency was reproducible within 3%. For the lower seeding rate, and for tubulence intensities higher than 10%, the rms values were overestimated by 8% as shown in figure 2.4.11. This can be the indication of a velocity biased result and the relative magnitudes of the local particle arrival time, the resonant circuit time constant and the particle lifetime through the control volume should be considered. The Signal Duty Cycle was measured at the jet exit and without any amplification or frequency shift. The threshold level was at 7% of the maximum signal amplitude.

Figure 2.4.12 presents the variation of the SDC on the centreline of the turbulent jet for various gains.It can be seen that for the higher seeding rate and with gains above 8 dbs the SDC achieves values which are higher than about 1% and correspond to particle arrival times of about 24ms. It can be anticipated that with the higher particle concentration some filter outputs remain below the threshold level for a longer time than others. The period for which the processed signal exceeds the threshold level is proportional to the transit time of the particle through the control volume.Hence, lifetimes that correspond to higher frequencies can lead to overestimation of the turbulence intensity. Table 2.4.2 shows how the resonant circuit time constant is related to the lowest signal frequency that can be processed.

Table 2.4.2: Electronic response of filterbank

Seeding	Control Volume diameter (μm)	Filterbank time-constant (μs)	Particle Velocity (m/s)	Transit Time (μs)	No of cycles
LOW	200	50	1.78	119	95
HIGH	200	50	0.89	238	190

It can be seen that the filterbank time constant corresponds to 40 cycles, i.e. it is comparable to the delay time of the resonant filter. Therefore, the measured lifetime of the processed signals will always exceed the actual transit time. However, in practice, it is expected that the action of the threshold level on any processed signal amplitude will reduce this overestimation. Figure 2.4.13 confirms the above statement and demonstrates the effect of increasing the gain versus the signal duty cycle with the corresponding signal duration and number of cycles. The results were obtained using artificial Doppler bursts of constant frequency (method A).

The performance tests reported in this section indicated that the amplifier response of the filterbank was not linear for the whole range between 1 MHz to 10 MHz, but the non-linearity could be minimised by careful selection of input signal amplitude and threshold level setting. Nevertheless, the error was more obvious in the measurement of the turbulence intensities which could not be estimated with an accuracy better than 6%. The accuracy on the mean velocities was always within 3% of the local value, in agreement with the prescribed error bandwidth by Baker (1974).

Variations in particle concentration in the flow were found to have the same effect on the mean and rms values, due to the logarithmic spacing of the filterbank channels and the difference between the measured lifetime of the processed signals and their actual transit time through the measuring volume.

For the measurements in the spray flame where high particle concentration variations were expected the spectrum facility of the filterbank was employed.

2.5 Some consequences of bias effects

The existence of a correlation between the particle arrival time, $< \tau_i >$, and consequently of sampling time $< \tau_s >$ to the local time instantaneous speed of the fluid in the measuring volume, known as "sampling" or "velocity" bias has been recognised, see for example McLaughlin and Tiedermann (1973). In practice, it may be possible to arrange experimental conditions and signal processing methods such as to minimise the effects of this correlation. This approach requires apriori knowledge of the flow conditions under which velocity bias becomes significant. Alternatively, if appropriate experimental conditions cannot be arranged, a method for the aposteriori elimination of velocity bias should be used.Several theoretical approaches have been proposed for its aposteriori correction, for example Edwards (1981), Erdmann and Tropea (1981), McLaughlin and Tiedermann (1973), Dimotakis (1976) and Buchhave (1975), as shown on table 2.5.1. Whatever the case may be, there is still much controversy whether a correction is really necessary, under which conditions would the magnitude of velocity bias become significant and whether it is the only factor that acts consistently to affect the sampled data. This uncertainty has remained because of lack of conclusive and extensive experimental data to support or disprove the effects of bias.

The sampling time $<\tau_s>$ between individual realisations is controlled by the signal-processing instrumentation and becomes correlated with the instantaneous velocity when $<\tau_s>$ is smaller than $<\tau_i>$ with consequent bias of measured probability distribution of velocity towards higher values. Dimotakis (1976) and Durao and Whitelaw (1980a, 1980b), for example, related the magnitude of velocity bias to the time-scale of the energy containing turbulent fluctuations $<\tau_t>$ to the particle residence

Table 2.5.1: Review of contributions related to velocity bias

	AUTHOR	STUDY / MATHEMATICAL FORMULATION	ASSUMPTIONS-CONDITIONS	FINDINGS-COMMENTS
THEORETICAL CONTRIBUTION	McLaughlin and Tiedermann (1973)	Bias due to the dependence of burst generation rate on velocity $\langle U\rangle=(\Sigma\frac{U_i}{N\lvert U_i\rvert})(\Sigma\frac{1}{N\lvert U_i\rvert})^{-1}$	-Spherical Control Volume -Uniform Seeding -Predominant velocity direction	-Velocity bias exists: Removal by 1-D analysis is adequate for practical purposes -Errors up to 10% in $\bar{U}$, 15% in $\sqrt{u^2}$ for 30% turbulence intensity
	Buchhave (1975)	Response of LDA-system to large $\bar{u}/\bar{U}$, 3-D Gaussian turbulence	-No frequency shift -Spherical Control Volume -Monodispersed particles -No velocity gradients in cv	-Velocity bias exists: Removal by 3-D analysis considering anisotropic cross-section - 1-D analysis by $1/\lvert U_i\rvert$ overcompensates results.
	Dimotakis (1976)	Data reduction techniques for low and high particle arrival rates $\langle U\rangle=(\Sigma U_i\tau_i)(\Sigma\tau_i)^{-1}$	-Monodisperse particles -Velocity vector enclosed by an elliptic cone -No frequency shift	-At low particle concentrations use time integrals -At high particle concentration use ensemble average weighted by the probability of particle occurence. -Velocity bias depends on relationship of $\langle\tau_t\rangle$ and $\langle\tau_i\rangle$
	Edwards (1981)	Sampling of velocity at regular-fixed time intervals: Weighting with $\langle\tau_s\rangle$ and particle density	-Measurement intervals should be less than $1/2f_{max.}$ and longer than $\langle\tau_p\rangle$	-Statistical bias is a function of particle density and sampling interval -Minimum when detector obtains one measurement every sample period.
EXPERIMENTAL CONTRIBUTION	Hoesel and Rodi (1976)	Removal of velocity bias / Air-jet	Uniform Seeding	Weighted-average with $\langle\tau_p\rangle$: $\bar{U}=(\Sigma U_i\Delta\tau_{pi})(\Sigma\Delta\tau_{pi})^{-1}$ $[\overline{u'^2}]$ = $((\Sigma(U_i-\bar{U})^2\Delta\tau_{pi})(\Sigma\Delta\tau_p)^{-1})$
			Non-uniform seeding	Weighted-average with $\langle\tau_i\rangle$: $\bar{U}$, $[\overline{u'^2}]$ as above, but substitute τ_{pi} & τ_{ii}
	Dürao et al (1980a)	Combined effect of velocity and amplitude bias	$\tau_t > \tau_i > \tau_s$	-Velocity bias present - Not obvious for low rms values. Can be removed by weighting with $\langle\tau_i\rangle$
			$\tau_i > \tau_t > \tau_s$	As above / Magnitude underestimated due to amplitude bias. Removable by weighting with $\langle\tau_i\rangle$
			$\tau_s > \tau_t > \tau_i$	Removed by slow sampling
	Johnson et al (1981)	Velocity bias at low particle concentrations.	Weighting with τ_i $\bar{U}=\frac{\Sigma U_i\tau_i}{\Sigma\tau_i}$	-Velocity bias increases with turbulence levels and is independent of particle occurence rate for low seeding.
	Erdmann and Tropea (1981)	Velocity bias at high particle concentration, controlled by sampling times	$\tau_s \sim \tau_t$	Velocity bias strong at low particle concentrations increases with turbulence intensity and decreases with particle rate
			$\tau_s \gg \tau_t$	Reduces to zero at very large and very small particles rates
			$\tau_s \ll \tau_t$	Velocity bias depends on turbulence intensity and reduced controlled period. Assumes maximum value

time in the control volume $<\tau_p>$ (i.e. the duration of the burst), to the particle arrival time $<\tau_i>$ and the sampling time $<\tau_s>$. Bias will be greatest when $<\tau_s>$ is less than $<\tau_t>$ and decreases as $<\tau_s>$ becomes larger than $<\tau_t>$ provided $<\tau_i>$ is less than $<\tau_t>$.

In practice, $<\tau_i>$ or $<\tau_p>$ have to be determined for each realisation since they differ from flow to flow, from one point in the flow to another, and from instant to instant. For complete elimination of the error, knowledge of either the joint probability density function for the three components of velocity, Dimotakis (1976), Buchhave (1975), or of the residence time of the particle, Buchhave (1978), Höesel and Rodi (1977), is required. The appropriate formulae are given in Table 2.5.1. Both approaches render correction tedious since they require extended computer storage. Durao and Whitelaw (1975, 1979), proposed to store all samples contributing to a measurement and then select randomly from them. George (1978) indicated that random selection does not always apply since the randomly arriving particles do randomly sample the flow velocity. Johnson et al (1981) studied the effects of velocity bias experimentally and with low particle concentrations. Their experiments showed that the removal of velocity bias becomes necessary only at high turbulence intensities and that the magnitude is independent of particle occurrence rate for low seeding. Erdmann and Tropea (1981) took into account in their theoretical study the probability distribution of the particle arrival rate and assumed that samples were collected at intervals uncorrelated with $<\tau_t>$. Their analysis, supported by a few experiments, indicated that under these conditions velocity bias depends on $<\tau_t>$, $<\tau_i>$ and $<\tau_s>$. The results reported in this section support their theorectical findings. Finally, Edwards (1981) has also calculated the magnitude of velocity bias for conditions similar to those reported by Erdmann and

Tropea, and indicated that the measurement accuracy depends on the flow characteristics and method of data handling and suggested methods for minimising the bias magnitude under certain conditions.

Amplitude bias can also complicate the task of correct measurement from individual realisations as the signal amplitude of high velocity particles may be smaller than that of low velocity particles, Durao and Whitelaw (1979). With systems where the signal validation criterion depends on amplitude, as already has been indicated in sections 2.3 and 2.4 for the frequency counter and filterbank respectively, a reverse bias can be introduced via the discrimination level and leads into the rejection of high velocity-low amplitude signals. Additionally, variation of the discrimination level results in an apparent change of the particle arrival rate which is itself biased due to the nature of discrimination. These two opposing effects, velocity and amplitude bias, are considered here According to Durao and Whitelaw (1979, 1980a, 1980b), amplitude bias depends on the laser power, the speed of response of the photomultiplier tube, turbulence intensity of the flow and the presence or absence of frequency shift. Also, the signal amplitude can be affected by the location within the measuring volume where a particle crosses it.

The results presented here were obtained either in the water flow or in the round-jet used also for the counter and filterbank performance tests. The geometrical configurations and laser Doppler anemometers are described in section 2.3.2. For the investigation of the bias effects the jet was seeded with either silicon-oil droplets of average diameter 2 μm and particle arrival times less then 3 ms from an aspiration atomiser, of the type described by Melling and Whitelaw (1973), or corn-oil droplets atomised via an atomiser (Norgren Pneumatic

Products L11-200-MLR) with a variable particle diameter between 1 - 10 μm and particle arrival rates ranging from 1 - 80 ms. Two photomultipliers of very different rise time (EMI 9558B and EMI 9817) were used and the signals were amplified (Harwell amplifier 95/2151) and high pass filtered (Krohn-Hite) to remove the pedestal and finally fed to a Hewlett-Packard (model 5360A) counter interfaced to an Apple-II microprocessor. The filter and amplifier characteristics were known and the frequency band did not influence the Doppler bursts. The counter had a minimum cycle time of 3 ms and the measurement time between consecutive bursts was externally adjusted via the Apple; using the Apple minimum cycle time all measured frequencies were processed. The characteristics of the counter were arranged to allow one measurement from each Doppler burst and over a preset time which was always about 50% shorter than that corresponding to the shortest Doppler burst. External triggering of the signal on an oscilloscope prior to the counter was used to vary the Doppler burst arrival rate and discrimination level in a range which did not lead to significant noise errors or to the measurement of signal period from one burst to another. The Apple software used logic to discard frequencies more than three-standard deviations from the mean. The measured values of mean and rms frequencies were based on 4000 individual samples which were ensemble averaged with the error of 0.6% in the mean and 2% in the rms. for a 95% confidence level, Yanta (1973). Bias corrections were not applied to the calculated values of mean and rms and the figures show the mean velocity calculated as:

$$\overline{U} = \frac{1}{N} \sum_{i=1}^{N} U_i$$

and the rms as:

$$\sqrt{\overline{u^2}} = \sqrt{\frac{1}{N} \Sigma (U_i - \overline{U})^2} = \sqrt{\frac{\Sigma U_i^2}{N} - (\frac{\Sigma U_i}{N})^2}$$

Skewness and flatness factors were also obtained.

The integral turbulent time-scales were calculated from power spectral distributions or from the ratio of the characteristic length to the mean velocity. These estimates can result in errors up to 30% in the calculation of the local turbulent time-scales, $<\tau_t>$, which were not important for present purposes. The signal to noise ratio of Doppler bursts exceeded 20 db for all experiments.

The percentage error introduced to the mean and rms velocities when the discrimination level is altered is shown in figures 2.5.1 and 2.5.2 for the water-flow and 2.5.3 to 2.5.5 for the air-flow. The two flows differed essentially in the uniformity of seeding particles. Correlations of $<\tau_s>$, $<\tau_i>$ and $<\tau_t>$ for each case are shown on the respective graph. For the air-flow the results have been normalised with the mean values obtained from pitot-tube measurements and for the water flow as reference velocity (presumably correct) was chosen the one that corresponded to 25% cut of maximum signal amplitude. The choice was made after several measurements at different signal amplitudes and cuts were compared to values obtained from a Cambridge-Consultant frequency tracker, where the amplitude discrimination criterion was known. The abscissae of those four figures show the discrimination level non-dimensionalised with the maximum signal peak voltage. In all cases, independently of the relative magnitudes of $<\tau_s>$, $<\tau_i>$ and $<\tau_t>$, measured mean and rms values decreased as the discrimination level was increased.

The results of figure 2.5 3, obtained on the centre-

line of the free-jet at a 15% turbulence intensity, introduce the effect of varying the discrimination level to give apparent particle arrival times from 2 ms to 200 ms, indicated in brackets on the figure with sampling times of 3 ms and 300 ms. As the discrimination level was increased and with the fastest collection time, the particle arrival times decreased and for values of $< \tau_i >$ smaller than the integral time scale, the measured mean was higher as would be expected from velocity bias. The increase of V_{cut} rapidly reduced the effect of this bias and as the value of $< \tau_i >$ begins to exceed $< \tau_t >$ and for the higher values of V_{cut}, amplitude bias lowers the measured mean and rms values. With $< \tau_i >$ close to $< \tau_t >$ and the larger value of $< \tau_s >$ the mean velocity is lower as would be expected from the reduction in velocity bias, and for larger values of V_{cut}/V_{p-p} the amplitude bias increases in importance and lower velocities are measured; under these conditions, and with larger $< \tau_s >$, the mean tends to be lower than with the faster $< \tau_s >$ because of the reduced percentage of lower velocity bursts in conjuction with the removal of velocity bias.

The effect was more evident in the water-flow (figure 2.5.1) where the relative error due to the amplitude bias was about $\pm$ 5% and 15% in mean and rms respectively for a 20% turbulence intensity. In this case velocity bias was removed by the slow sampling, $< \tau_s >$ = 94 ms, and the effective particle arrival rate associated with the increase of the discrimination level was always less than 60 ms. In the same flow, repetition of the procedure with fast sampling (figure 2.5.2) indicated an initial region of steep monotonic frequency drop, associated again with amplitude bias, since velocity bias was present ($< \tau_s > \sim < \tau_i >$ and $< \tau_t > > < \tau_i >$). Further increase of the discrimination level resulted into an apparent reduction of $< \tau_i >$, so that $< \tau_i >$ was always bigger than $< \tau_t >$ and $< \tau_s >$ was always the same as $< \tau_i >$ and correlated to

the velocity fluctuations. This resulted to an increase of measured frequencies and they would probably have reached their initial values if amplitude bias did not introduce an opposite effect again of about 15% as in the previous case. The correlation of $<\tau_s>$ to $<\tau_t>$ and $<\tau_i>$ is also shown by the fluctuations in rms values.

The same trends are indicated in figure 2.5.4 where the measurements were repeated with the sampling time controlled by the counter (not the microprocessor). With the shorter sampling rates and higher trigger levels the counter had to wait for a particle to arrive, which re-introduced a dependence to the particle arrival rate with consequent biasing towards higher velocities. Even with the longest sampling times, velocity bias is present as indicated by the 10% increase of the rms values at the highest discrimination levels.

Figure 2.5.5 shows results for a turbulence intensity of 22% and a particle concentration which resulted in $<\tau_i>$ larger than $<\tau_t>$ and the velocity bias which is noticeable for all sampling times. The numbers in brackets again refer to the resulting particle arrival time achieved through variation of the discrimination level. It can be seen that even with the same value of particle arrival time, obtained with different discrimination levels, the velocity values are different. The same trends were observed for the rms and the overall effect of amplitude bias was about 6%. The variation with $<\tau_s>$ is not monotonic and correlated to the local value of turbulence, and consequently to $<\tau_t>$.

Finally, three different sampling methods are compared in figure 2.5.6. Measurements were obtained at 0.28 disc diameters downstream of a disc centrally located in the water-flow. The discrimination level was set to a low value and the software allowed a measurement of time bet-

ween consecutive bursts which varied from 1.5 ms in the forward-flow region to 6.8 ms in the recirculation zone. In the figure, typical values of $\langle\tau_s\rangle$, $\langle\tau_i\rangle$, $\langle\tau_t\rangle$ and $\langle\tau_p\rangle$ for these two zones are provided. The figure shows that the particle concentration tends to vary from a near constant value in the recirculation region, to a second and higher value in the downstream region. Three sets of velocity values are presented and correspond to a slow sampling time of 94 ms to ensemble average 2500 samples, fast sampling to ensemble average 11000 signals, and finally the analogue output of the counter was used to time-average a signal with the same integration time as the total collection time for 11000 samples with fast collection. The turbulent integral time scale of the flow varried from 6 ms in the forward flow region to 80 ms in the recirculation zone and both were larger than the particle arrival times which were smaller or equal to $\langle\tau_s\rangle$. In its analogue mode the counter operated with an output which corresponded to a high particle arrival rate and with old values held until new values were observed.

The results show the same trends and for many purposes the accuracy of any of the three measurements is adequate. Outside the recirculation region and due to the low value of V_{cut}, the fast collection led to high values of mean velocity which is consistent with velocity bias; the same is true in the recirculating flow. The analogue results tend to be lower but by a smaller amount than that obtained with the slow sampling rate. The magnitude of the discrepancy between the fast and slow sampling methods in absolute terms, tends to be lower in the recirculation region partly because the average sampling time approaches more closely the turbulent time scale. In this region the analogue result is significantly different as a consequence of the very high turbulence intensity values and of the longer period of drop out.

2.6 Concluding remarks

In this chapter a description of the common characteristics of the laser Doppler anemometers used for the velocity measurements of chapter three, in a water model of a heat-exchanger, and of chapter four in a model furnace with a liquid-fuelled spray flame have been presented. The performance of the two signal processing systems used for the water-model measurements, a frequency counter, and for the liquid spray flame, a filterbank processor were evaluated. Both systems could operate either in the digital or analog mode and were evaluated in the former. Measurements were obtained with both artificially generated Doppler signals and with real bursts.

The counter has been found capable of measuring in high and low particle density flows and in a wide range of turbulence intensities. The digital output interface allowed measurements either at a fixed slow sampling rate, or at a fast sampling rate with simultaneous recording of the arrival time between consecutive particles. Mean and rms values of frequency, skewness and flatness factors, probability density distributions and histograms of frequency versus number of particles have been obtained. The effects of tolerance level setting and threshold level on the mean and rms levels were examined and quantified. The instrument was tested in turbulent and unsteady flows. Mean and rms values of ensemble-averaged frequencies could be obtained with an accuracy of 0.196% of the true frequency. The error originated from the 8-digit frequency recording accuracy of the counter and the binary transport of the information from the counter to its interface. Sample size affected the measurement accuracy. For example, with 2500 samples the error in mean and rms frequencies was 0.7% and 3.5%. The

same errors were 0.33% and 1.58% for 12500 samples. Incorrect setting of tolerance level and threshold level could influence mean velocities by up to 5%, depending on the turbulence level. These error bandwidths apply also for the results of chapter three.

The influence of velocity and amplitude bias was extensively investigated in air and water flows with the fast counter and a commercially available counter of slower re-cycle time, both interfaced to microprocessors. The trends from both processors were similar and the results provided an insight in evaluating the magnitude of velocity and amplitude bias generally in air and water flows The results confirmed that velocity bias is present except when the time scale of sampling is larger than both the time scale corresponding to the particle arrival rate and the integral turbulent time scale. Even under these conditions, velocity bias is removed only when sampling times are externally controlled and uncorrelated to the particle arrival rates and velocity fluctuations. With low particle arrival rates the method of sampling had, as expected, no discernible effects.

In the present flows amplitude bias was always a potential problem and the choice of discrimination level was crucial for its removal. In general, it has an opposing effect to that of velocity bias and can be used to compensate it. Both velocity and amplitude bias tend to increase with turbulence intensity but, depending upon the shape of the probability density distribution, will reach a maximum at an intensity of around 35%.

The magnitude of the resulting error in the present flows, with turbulence intensities in the range from 5% to 25%, did not exceed 5% of the mean velocity, even under conditions of careless choice of threshold level setting and fast sampling times. Under these conditions,

corresponding discrepancies in the rms values can be of the order of 10% of the local value. To ensure that errors are minimised, a careful consideration of the relative values of sampling time, turbulent time scale, particle arrival time and discrimination level is necessary for each specific application.

The filterbank was capable of dealing with poor quality intermittent signals. However, the resolution was generally rather coarse because of the limited number of filters and the logarithmic frequency spacing of the channels. The amplifier incorporated to the instrument was found to have a non-linear frequency response that resulted to a biased high gain for small amplitude signals at low frequencies and for large signals at high frequencies. After calibration of the amplifier with artificial signals it was possible to set an amplification level for a pre-set threshold level that produced a linear frequency response of the amplifier for a limited range of input signal amplitudes. The filter response was sensitive to temperature variations and band-pass filter settings. Tests were performed to evaluate the effect of signal amplification, threshold level and particle concentration on the measurement accuracy. In general, the mean frequency could be obtained from the analog voltage output of the filterbank with an accuracy of $\pm$ 3% of the local value. The uncertainity in the normalized rms values was found to be twice this figure. For the velocity measurements in the model furnace, the analog output of the filterbank was used for the isothermal flows and only wherever the turbulence intensities were below 25%. Above this level, and for the combustion measurements the sprectrum facility was employed. In this manner, the uncertainties in the rms values are expected to be less than the above recorded values.

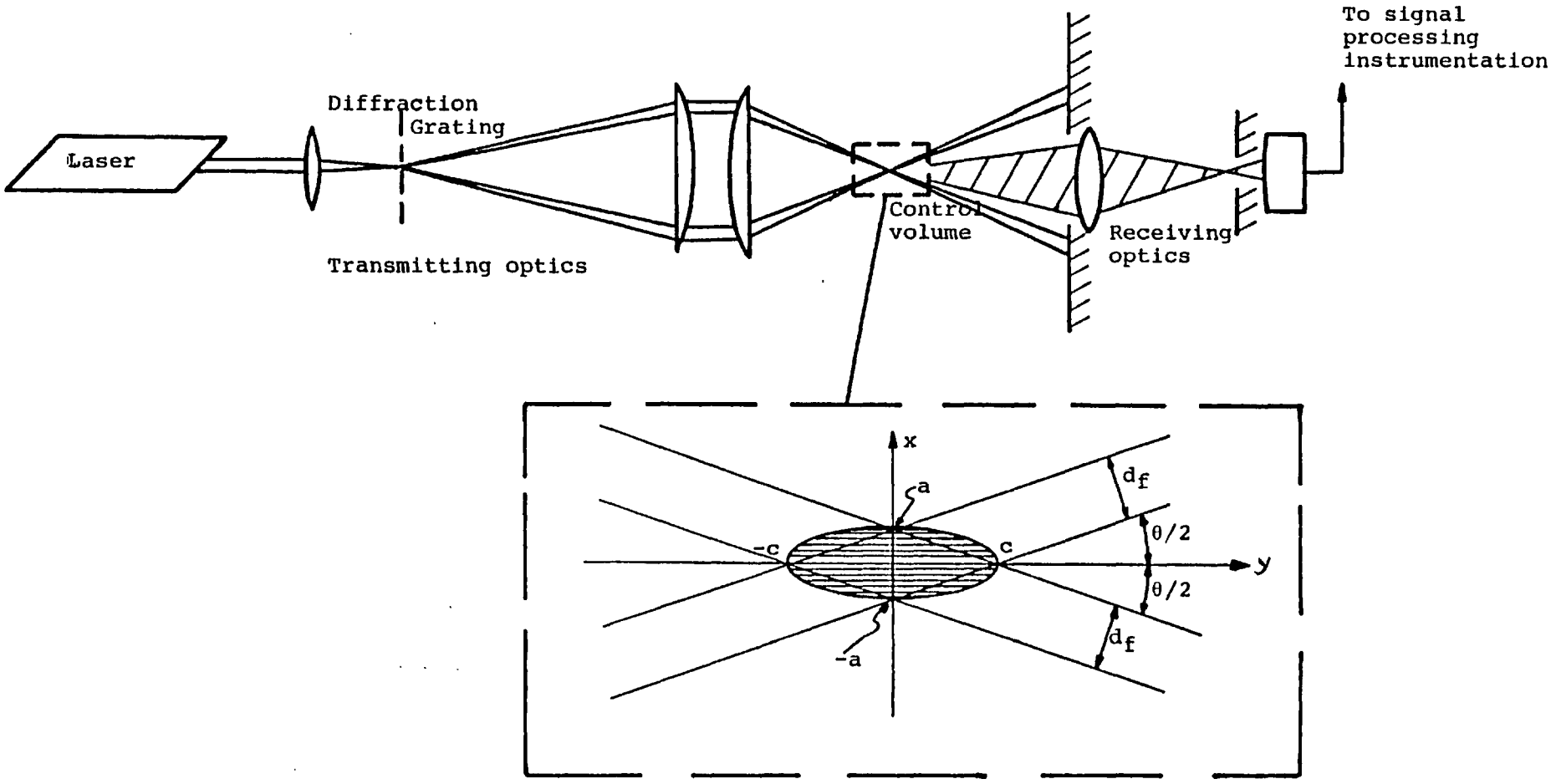


Figure 2.2.1 : Optical configuration of a forward-scattered light, fringe mode LDA.

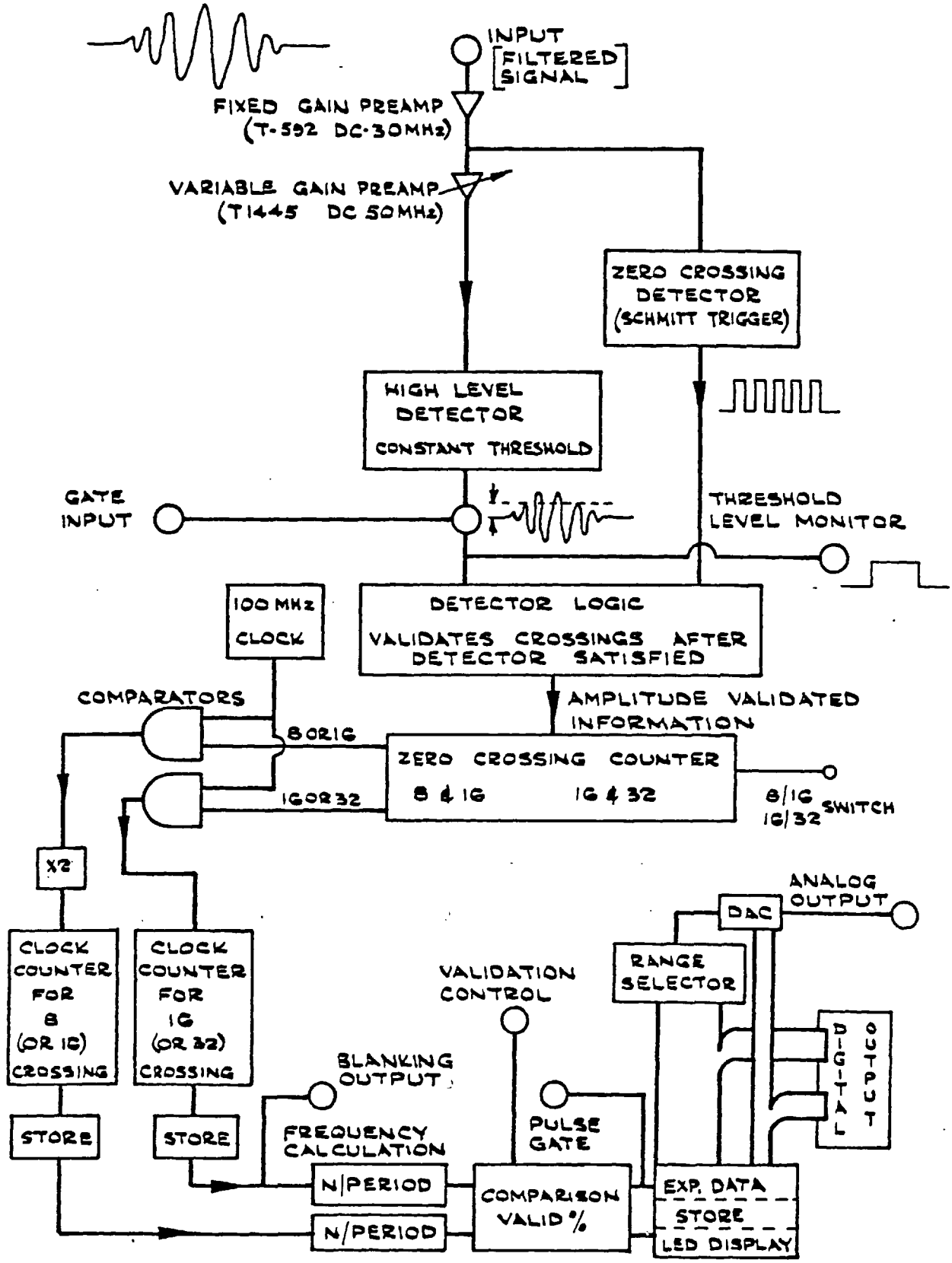


Figure 2.3.1 : Frequency counter block-diagram.

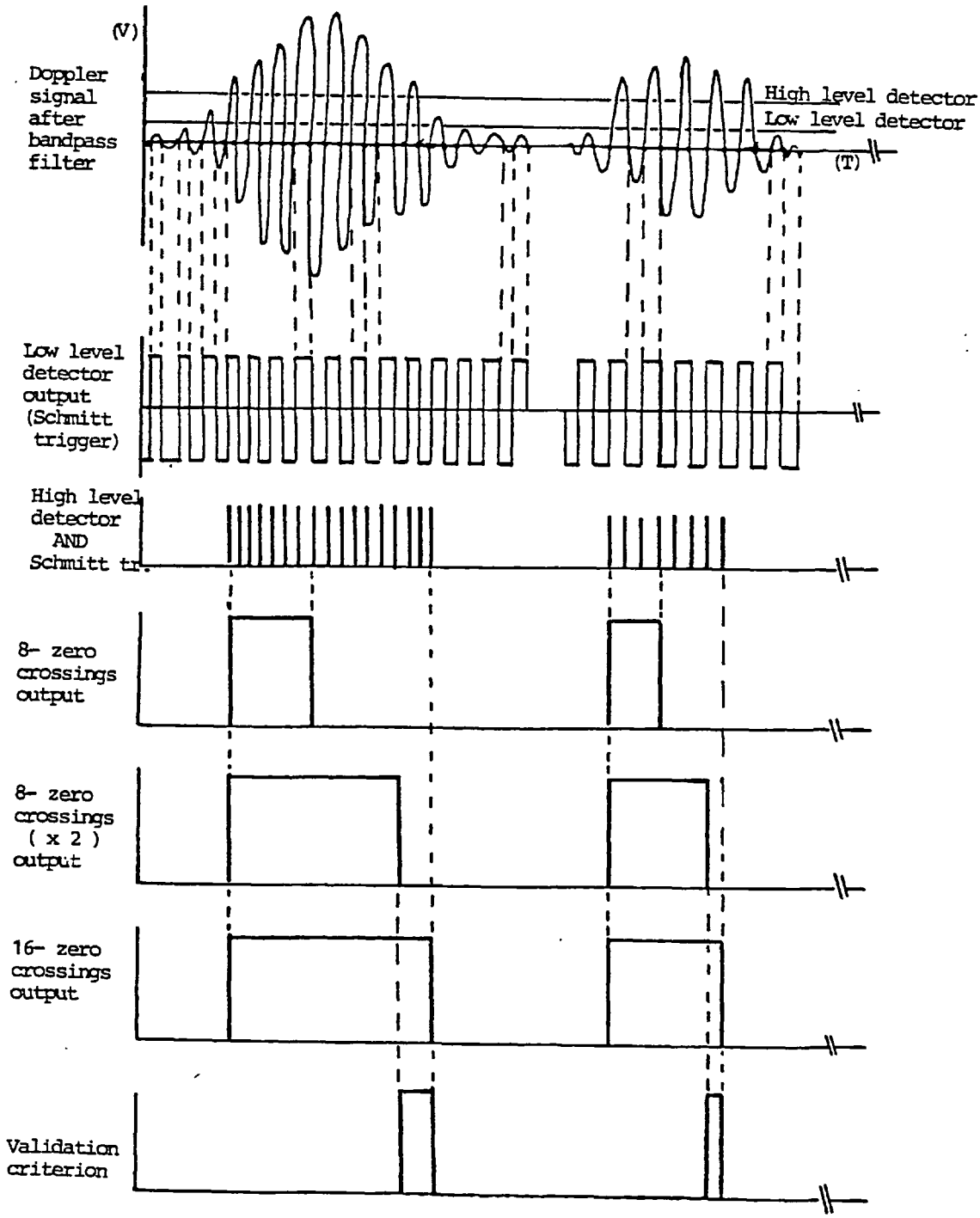


Figure 2.3.2 : typical waveforms in present counter

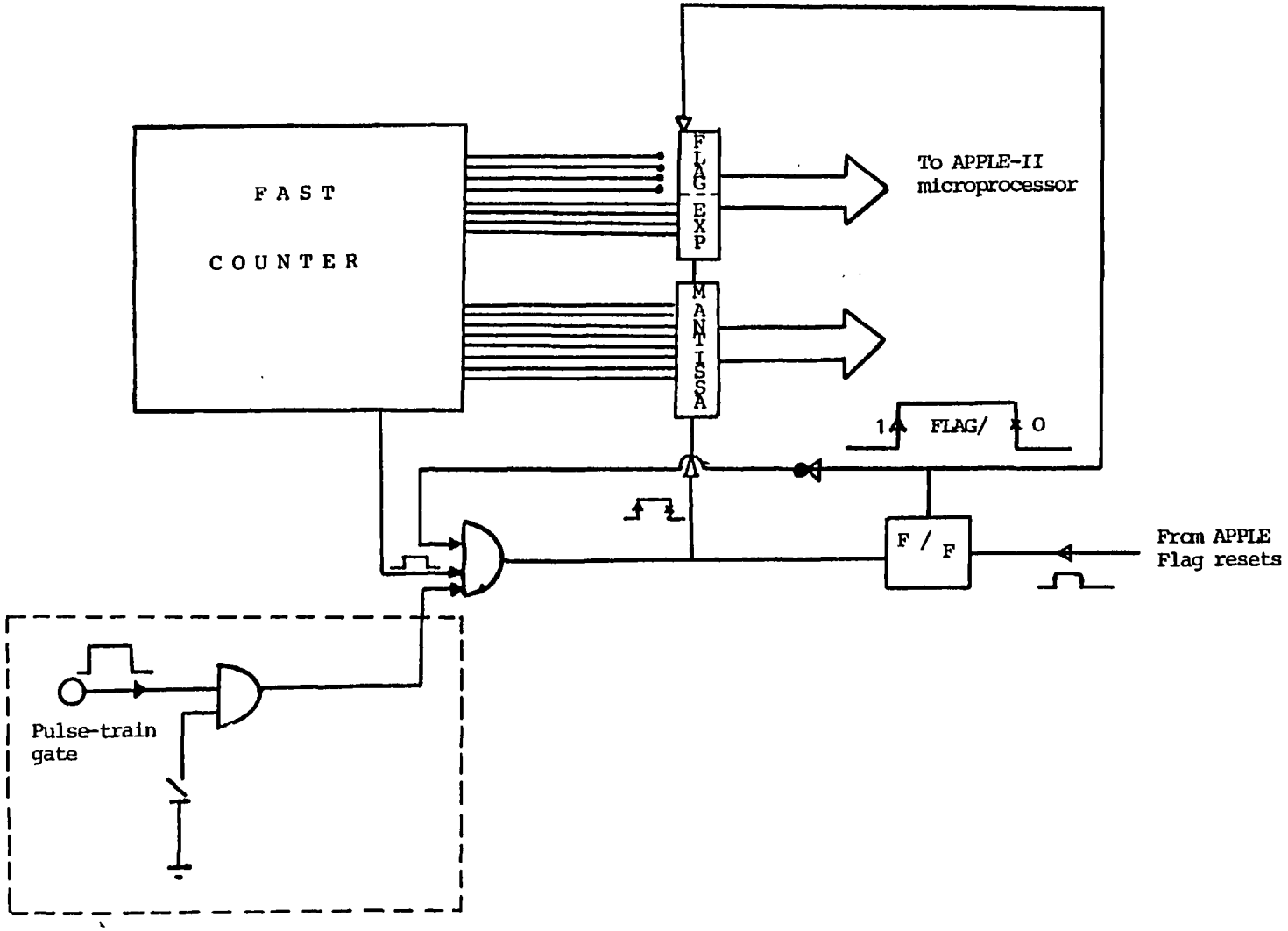


Figure 2.3.3 : Digital interface for frequency counter

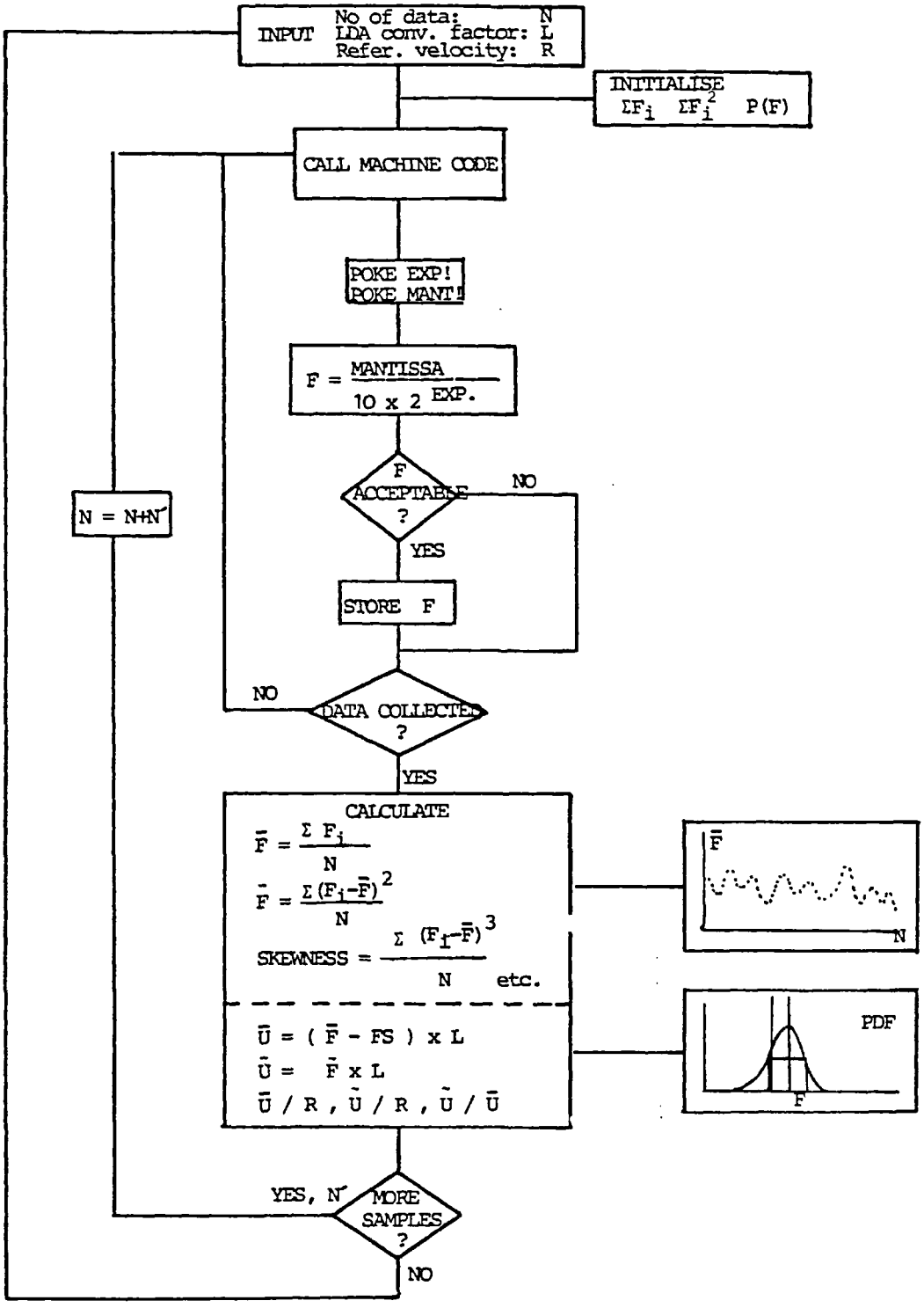


Figure 2.3.4 : Software flowchart.

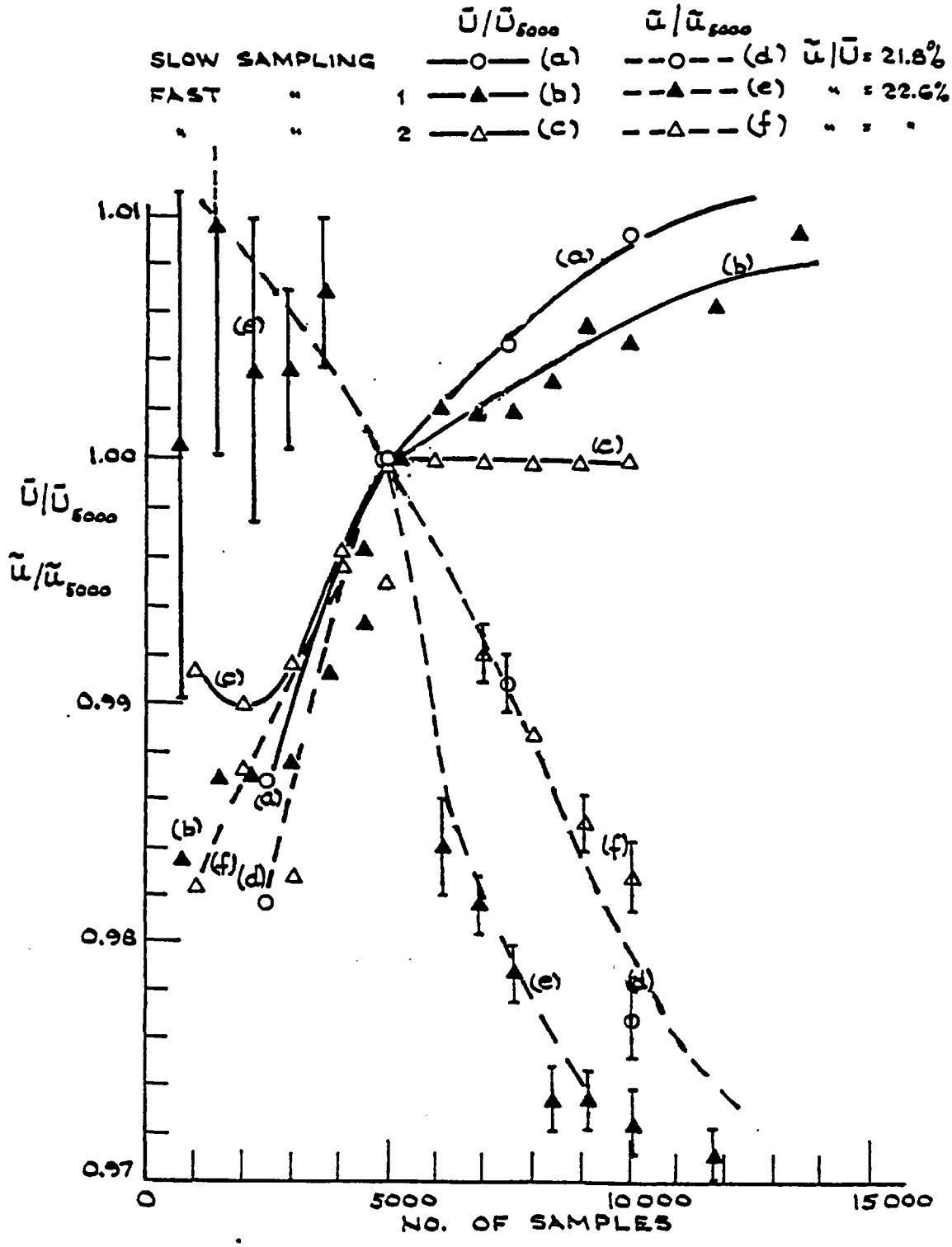


Figure 2.3.5 : Variation of measured mean and rms frèquencies with sample size

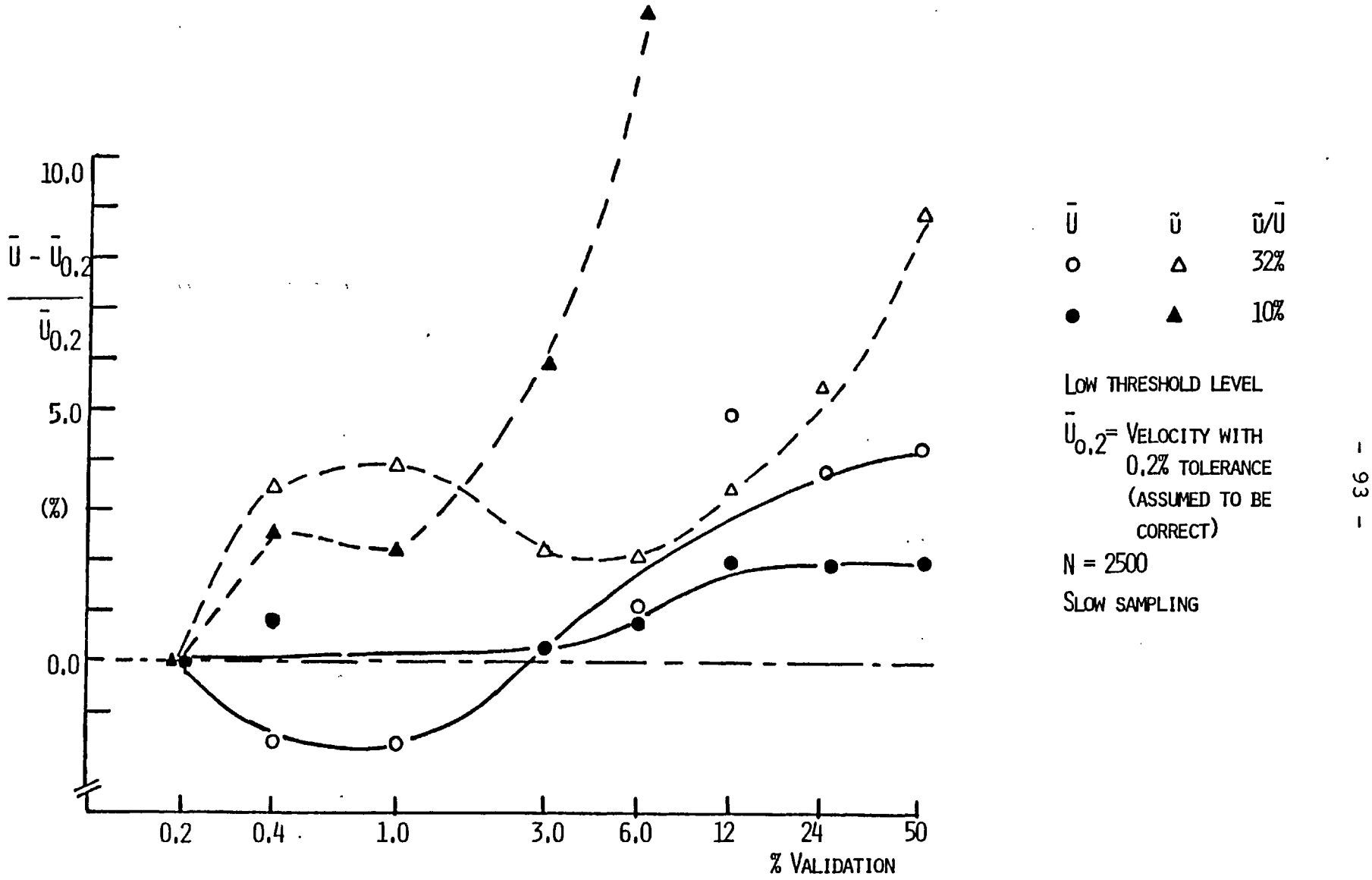


Figure 2.3.6 : Signal validation criteria

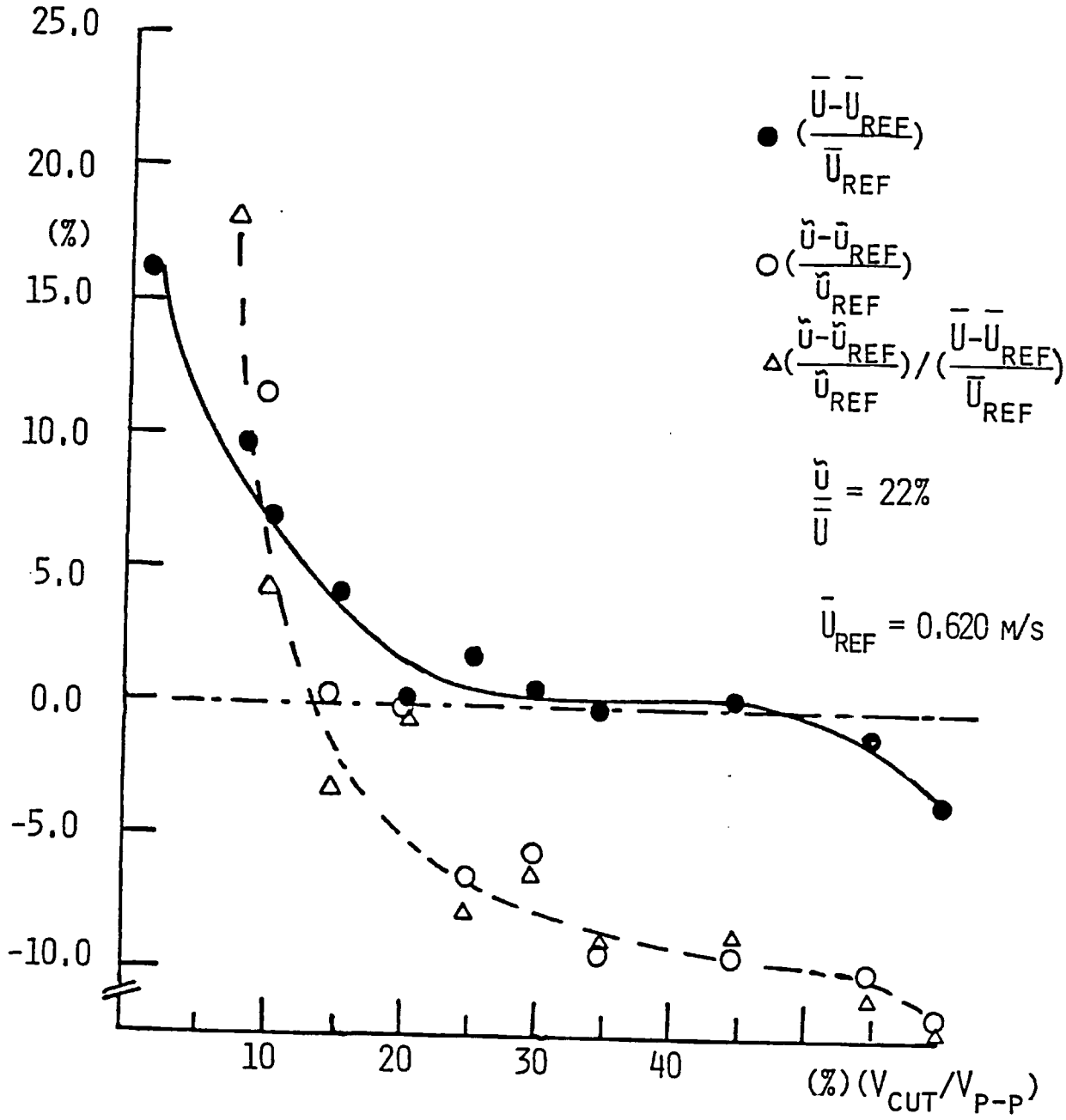


Figure 2.3.7 : Water flow. Effect of threshold level: frequency counter

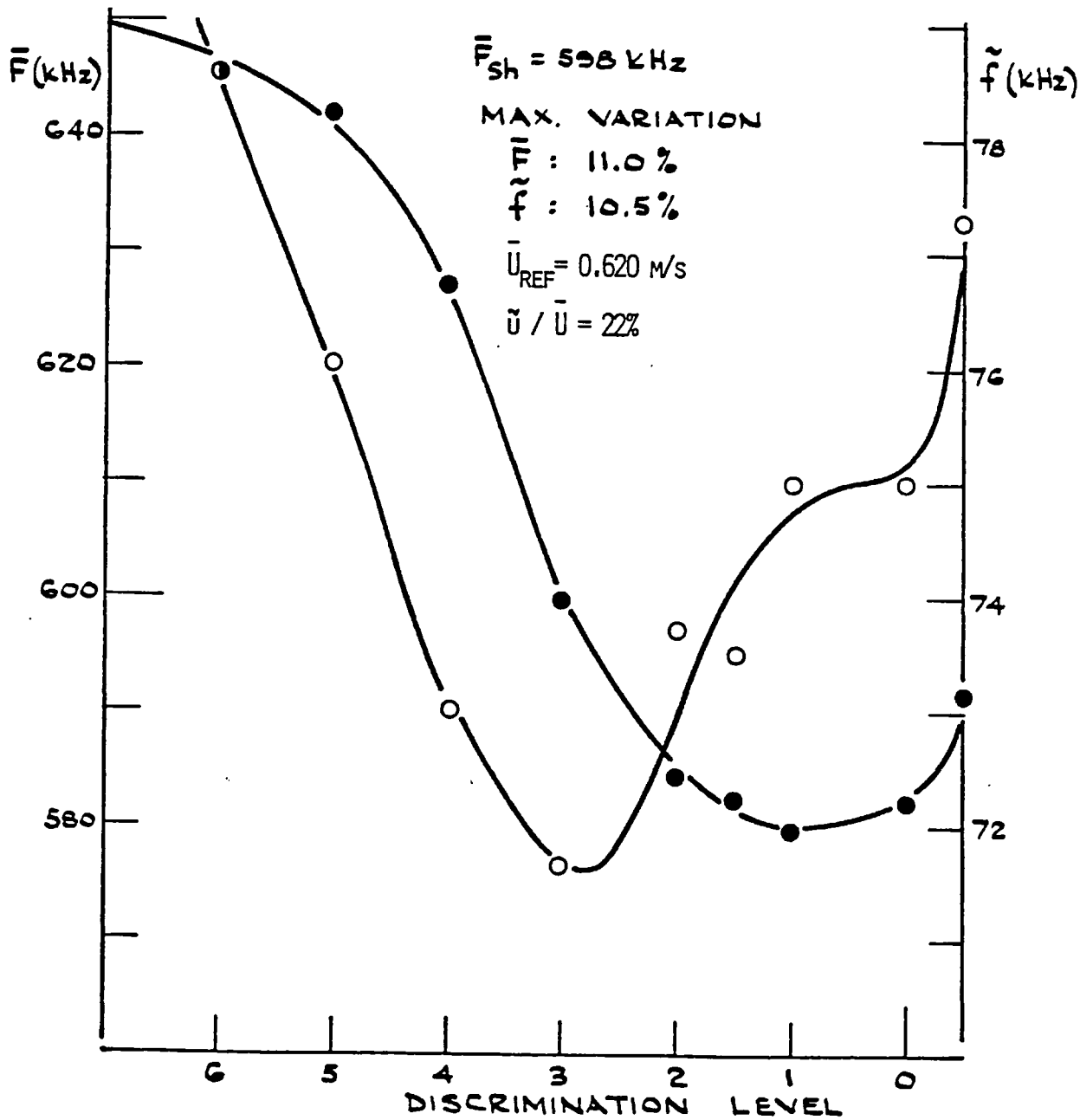


Figure 2.3.8 : Effect of threshold level:Cambridge tracker.

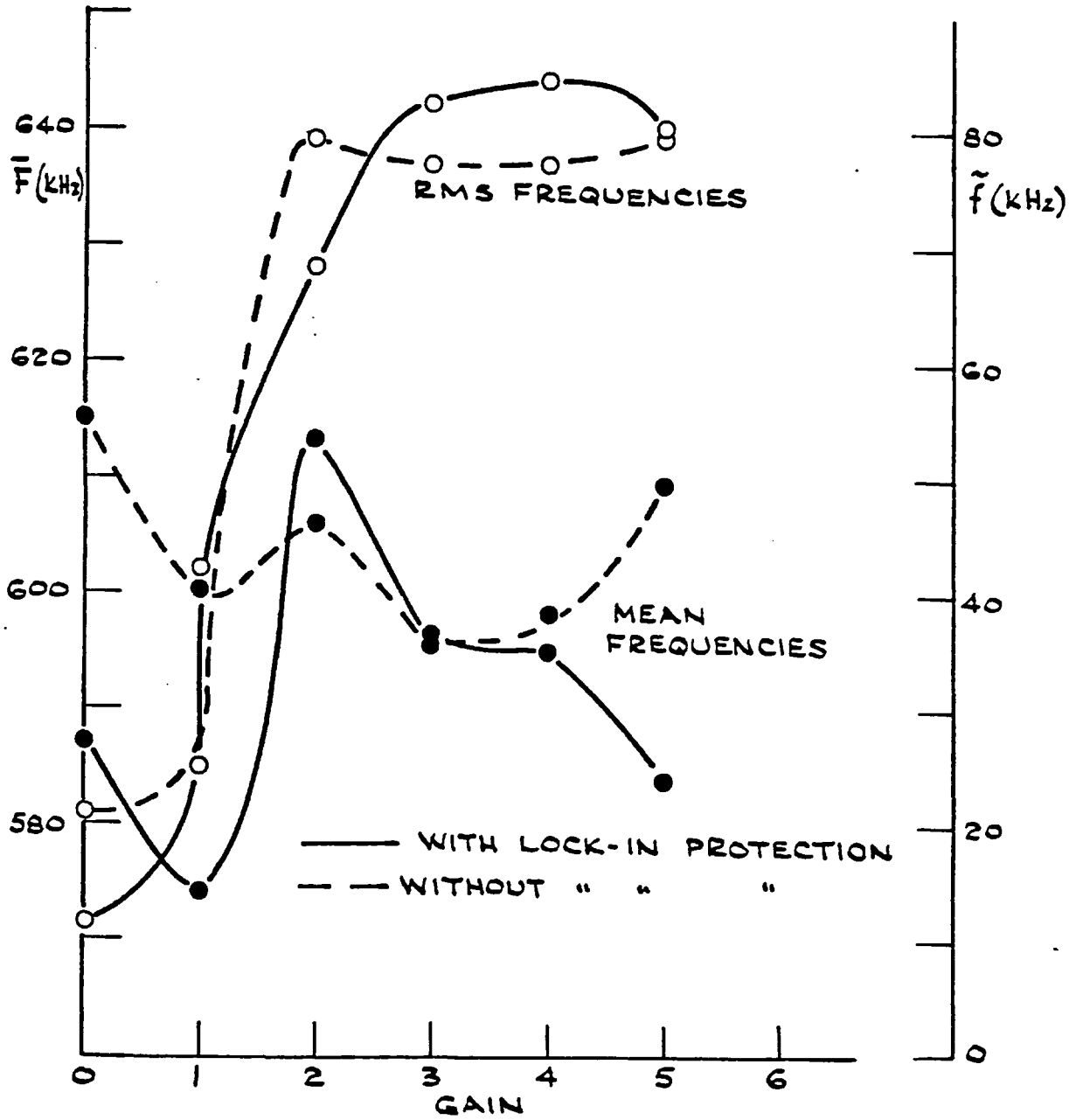
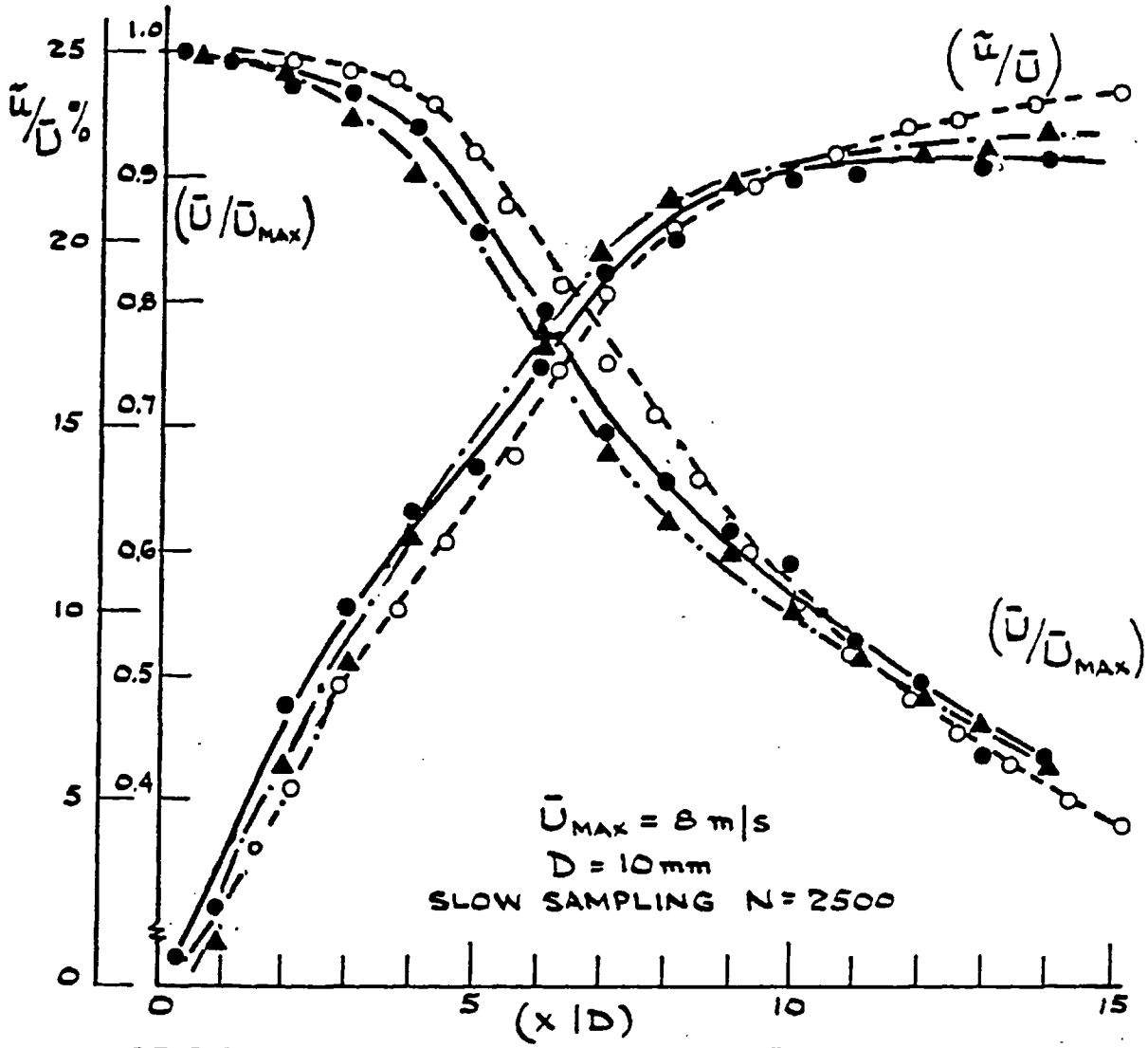


Figure 2.3.9 : Effect of threshold level; DISA tracker



AUTHOR		Re x 10⁻⁴
○	DURÃO } L.D.A. (1976) TRACKER	0.54
●	L.D.A. (1981) [FS φ 2 - COUNTER]	0.54
▲	L.D.A [CAMBRIDGE TRACKER]	"

Figure 2.3.10 : Free jet. Centreline axial velocity distribution : Frequency counter.

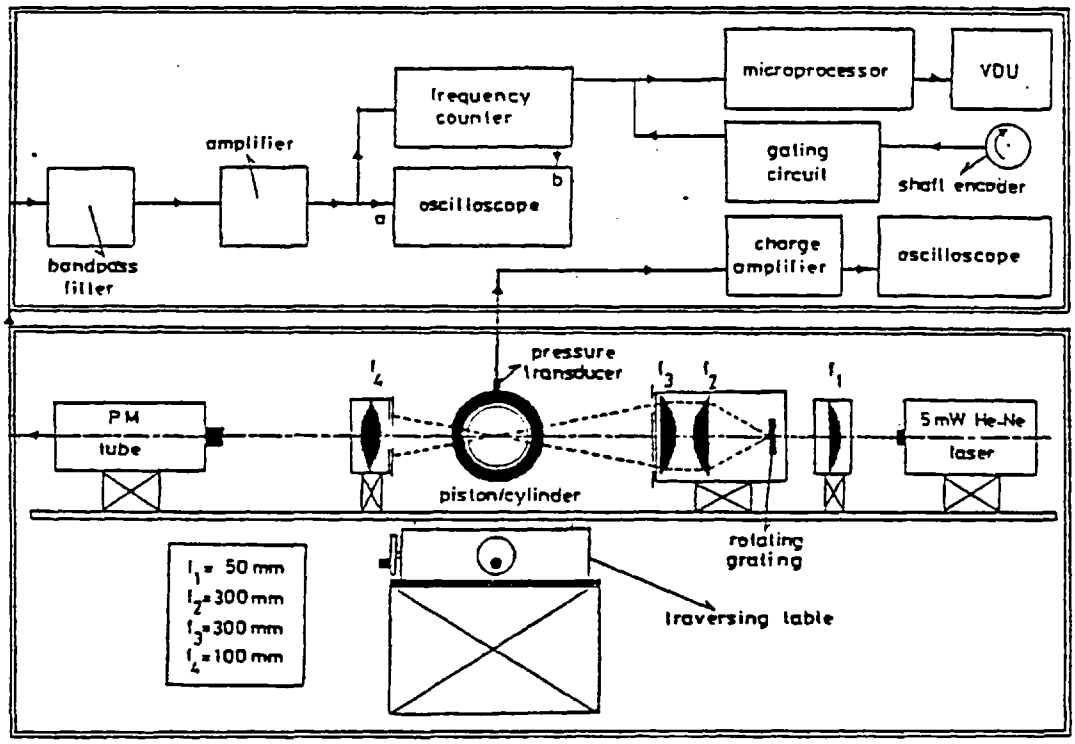


Figure 2.3.11 : Schematic of optical and signal processing arrangements for a single-shot configuration (Arcoumanis et al, 1981).

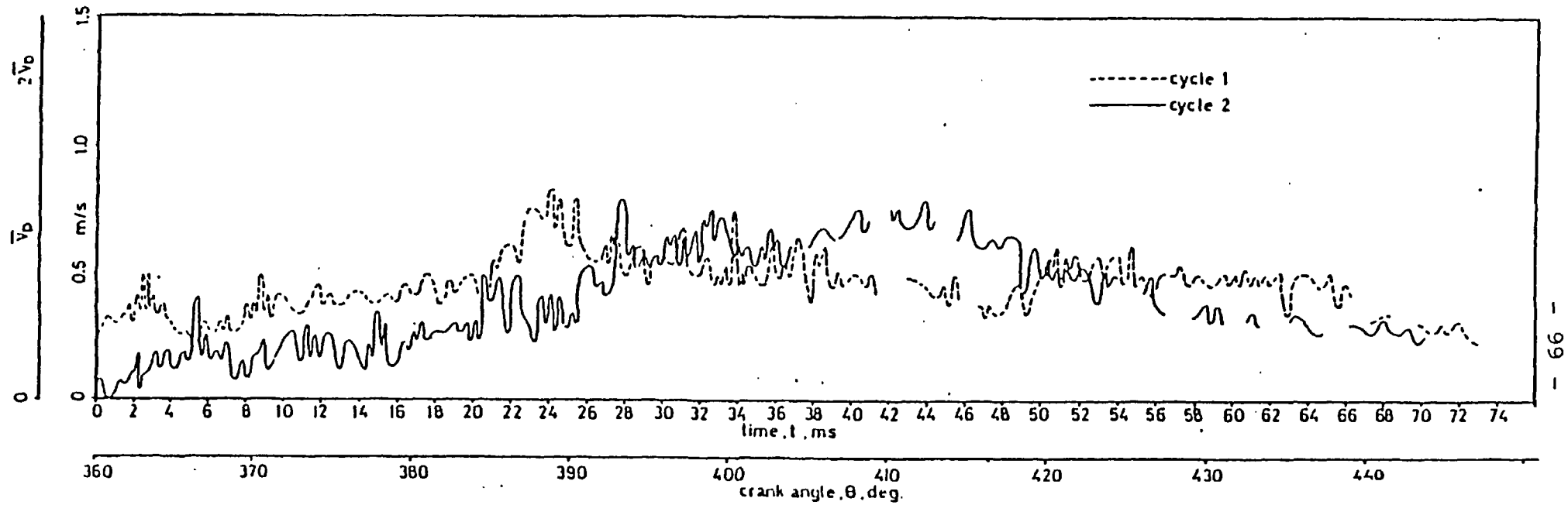


Figure 2.3.12 : Traces of instantaneous axial velocities over two successive cycles in a single shot configuration.

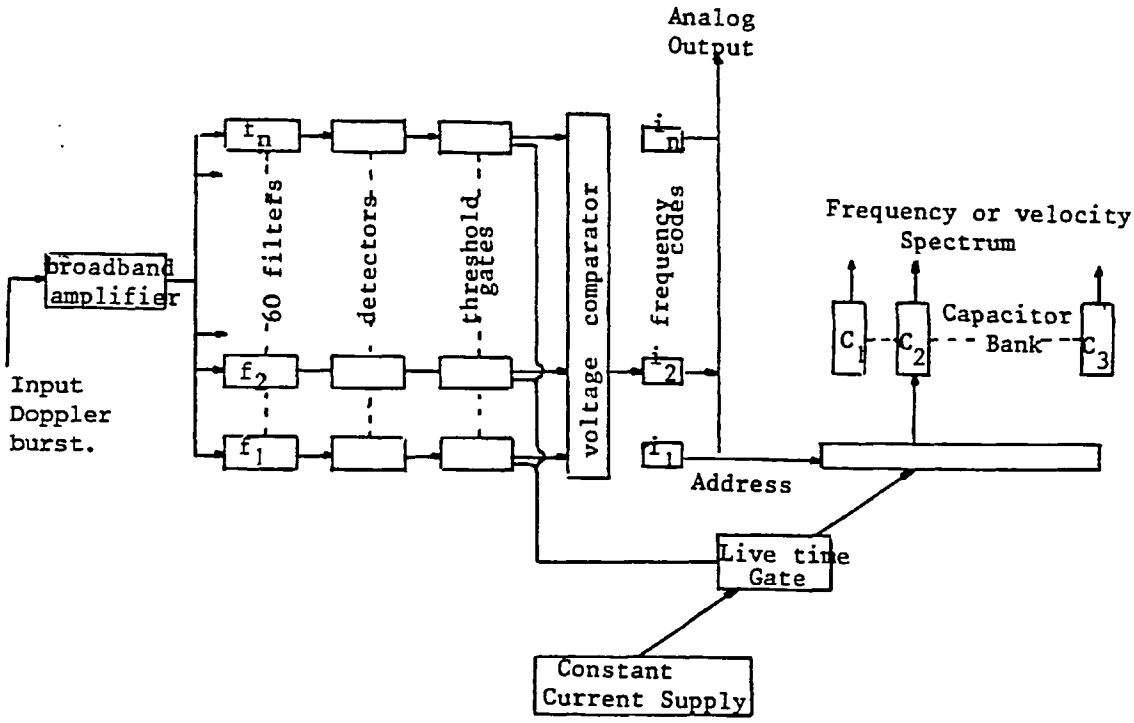


Figure 2.4.1 : Block diagram of a filterbank processor.

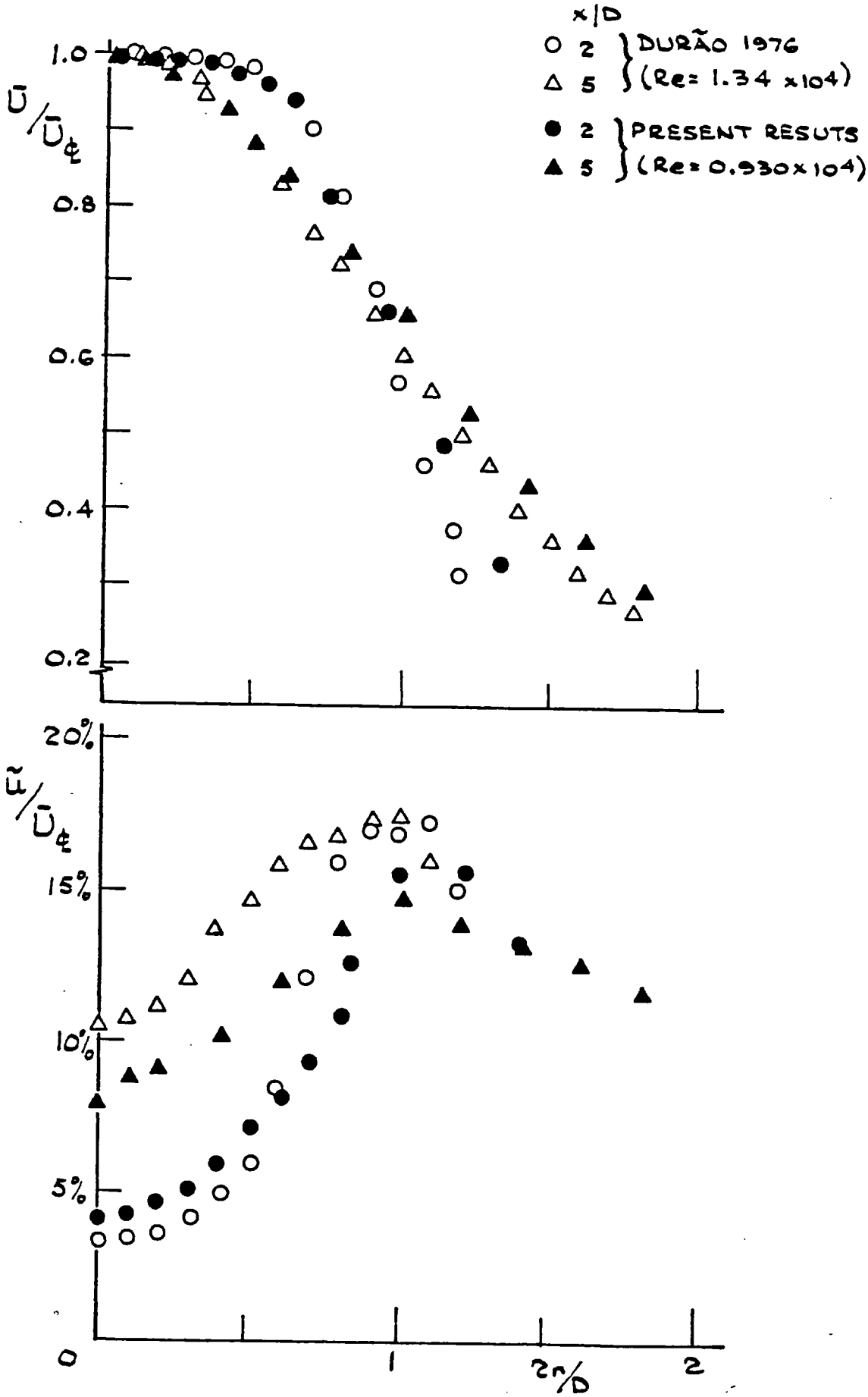


Figure 2.4.2 : Radial profiles of mean and rms velocity of a free jet: Filterbank signal processor.

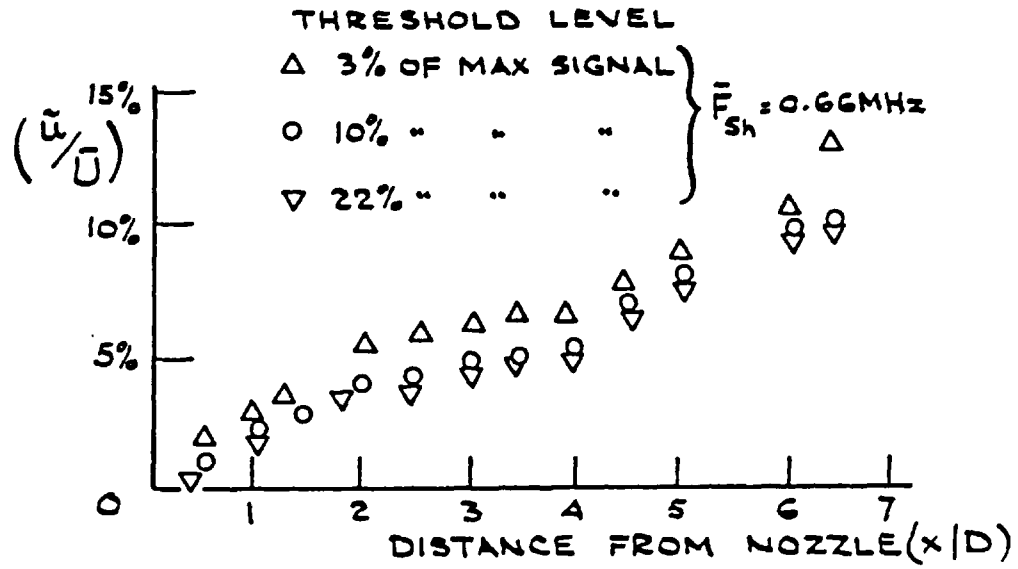
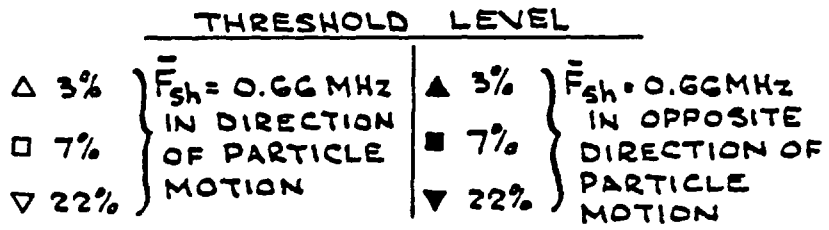


Figure 2.4.3 : Effect of threshold level on the variation of turbulence intensity on the centreline of a free jet.



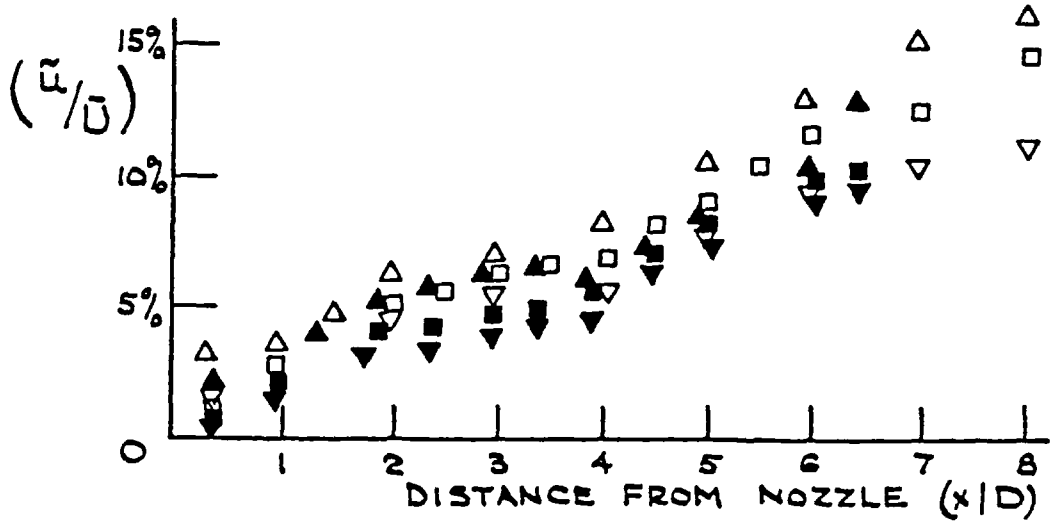


Figure 2.4.4 : Effect of frequency shift reversal on measured turbulence intensity.

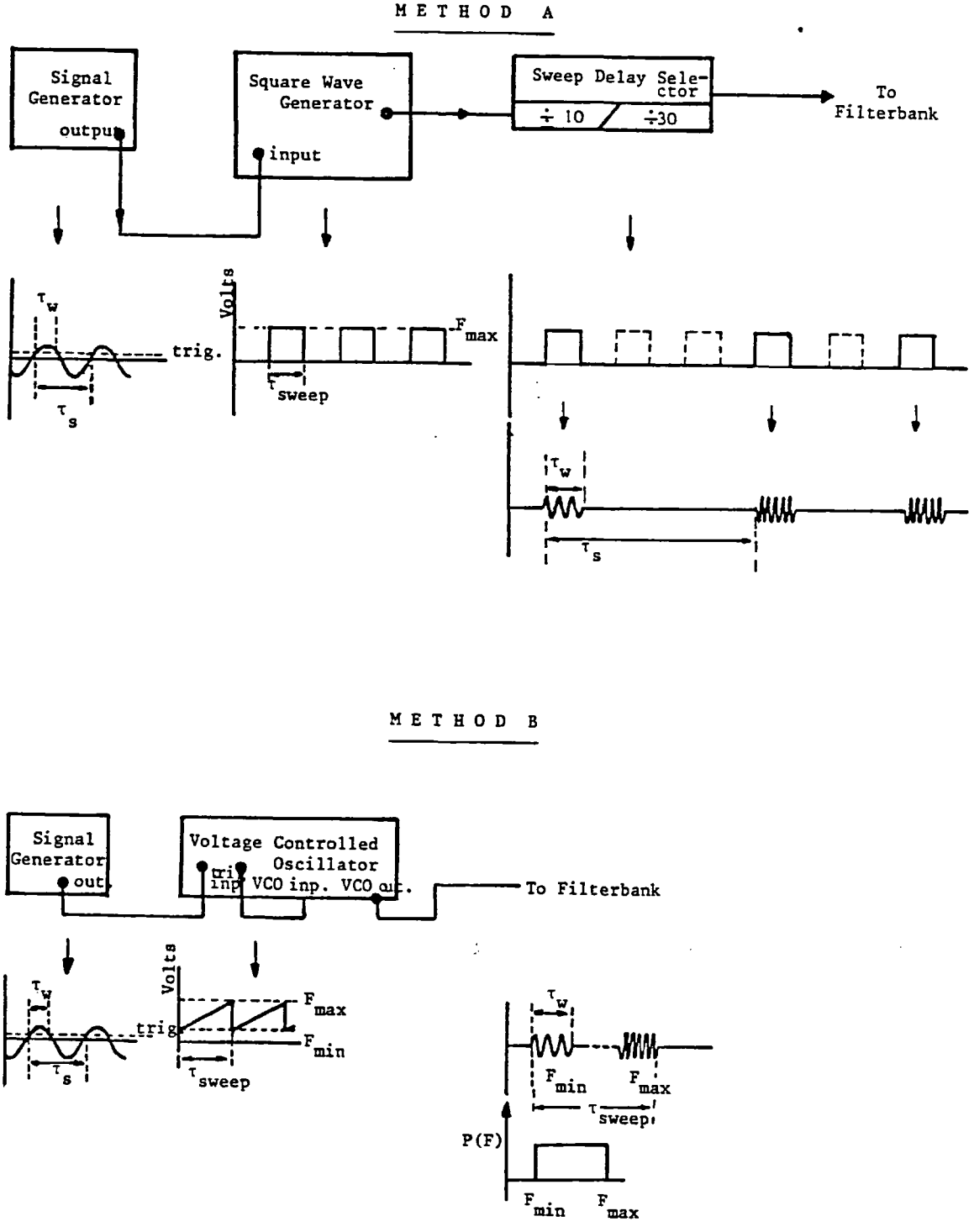


Figure 2.4.5 : Methods used for generating simulated Doppler bursts

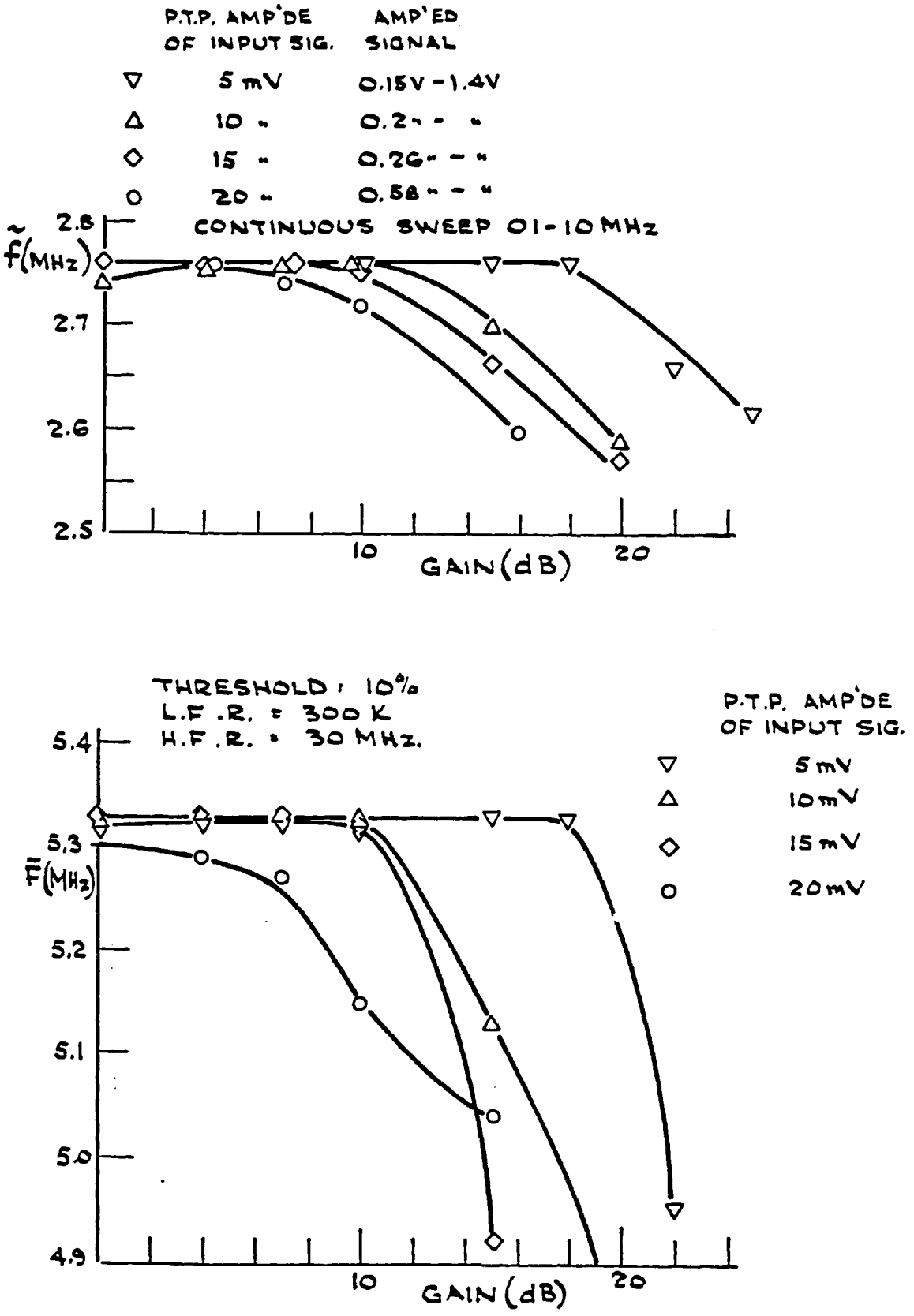


Figure 2.4.6 : Variation of mean and rms frequencies against signal gain for different signal amplitudes (Artificial signals- Method B).

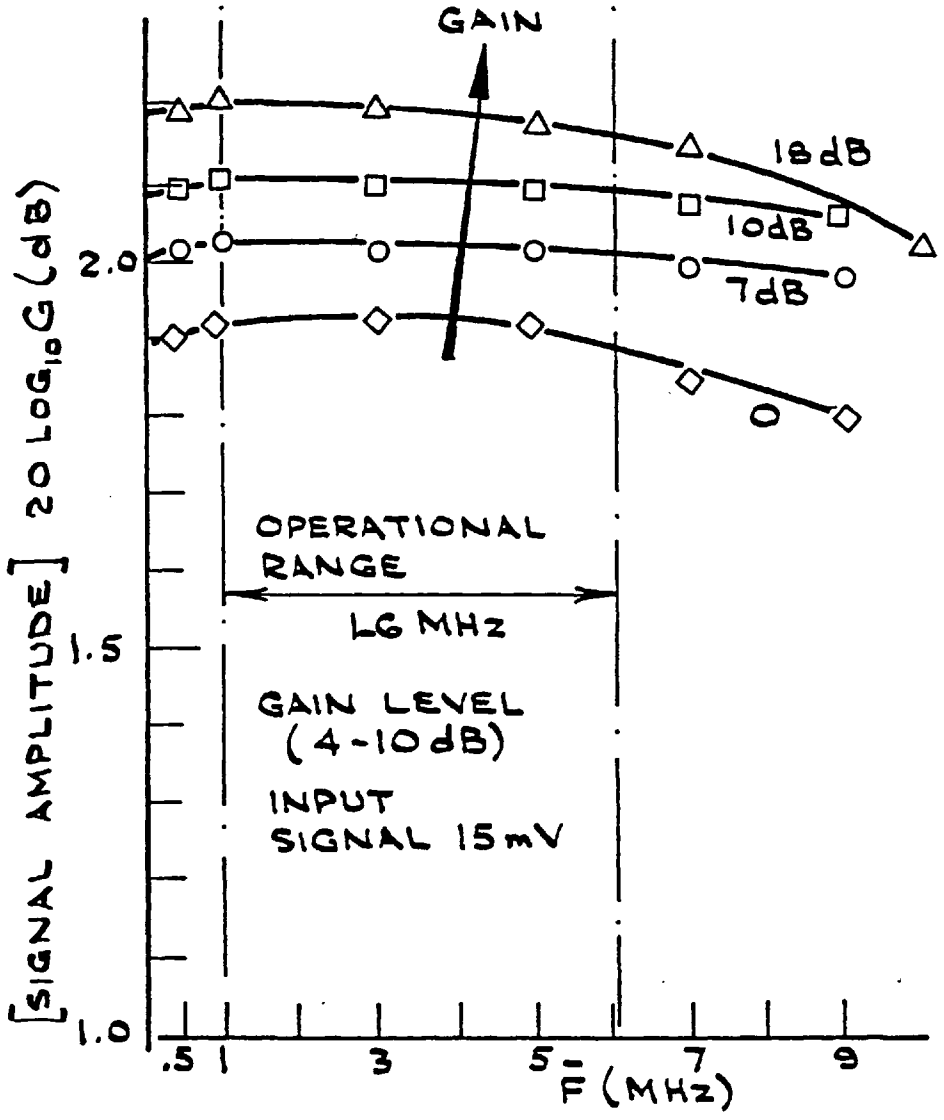


Figure 2.4.7 : Frequency response of the filterbank amplifier (Artificial signals of constant frequency Method A).

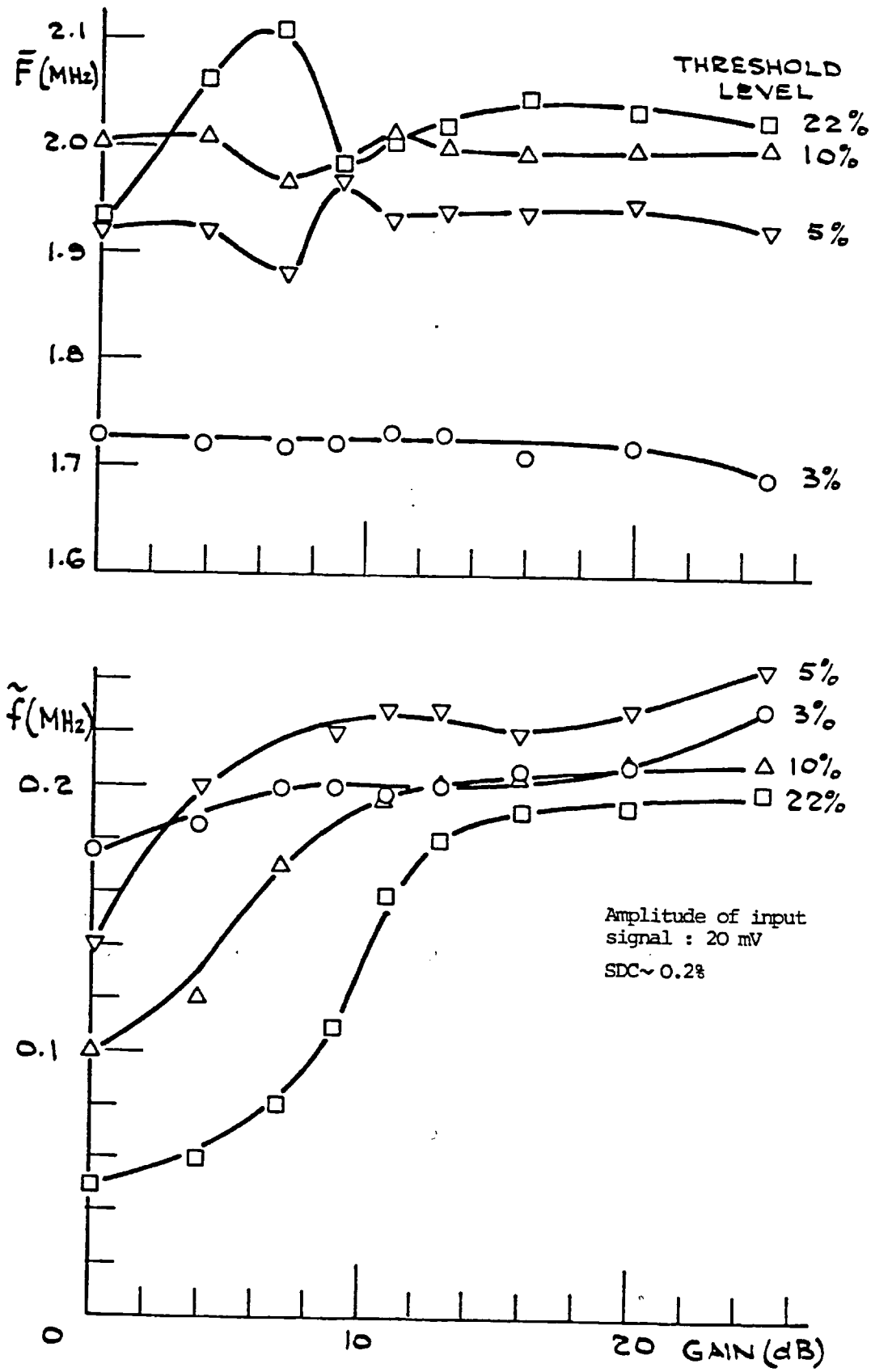


Figure 2.4.8 : Variation of measured frequency with gain. Centreline of turbulent jet.

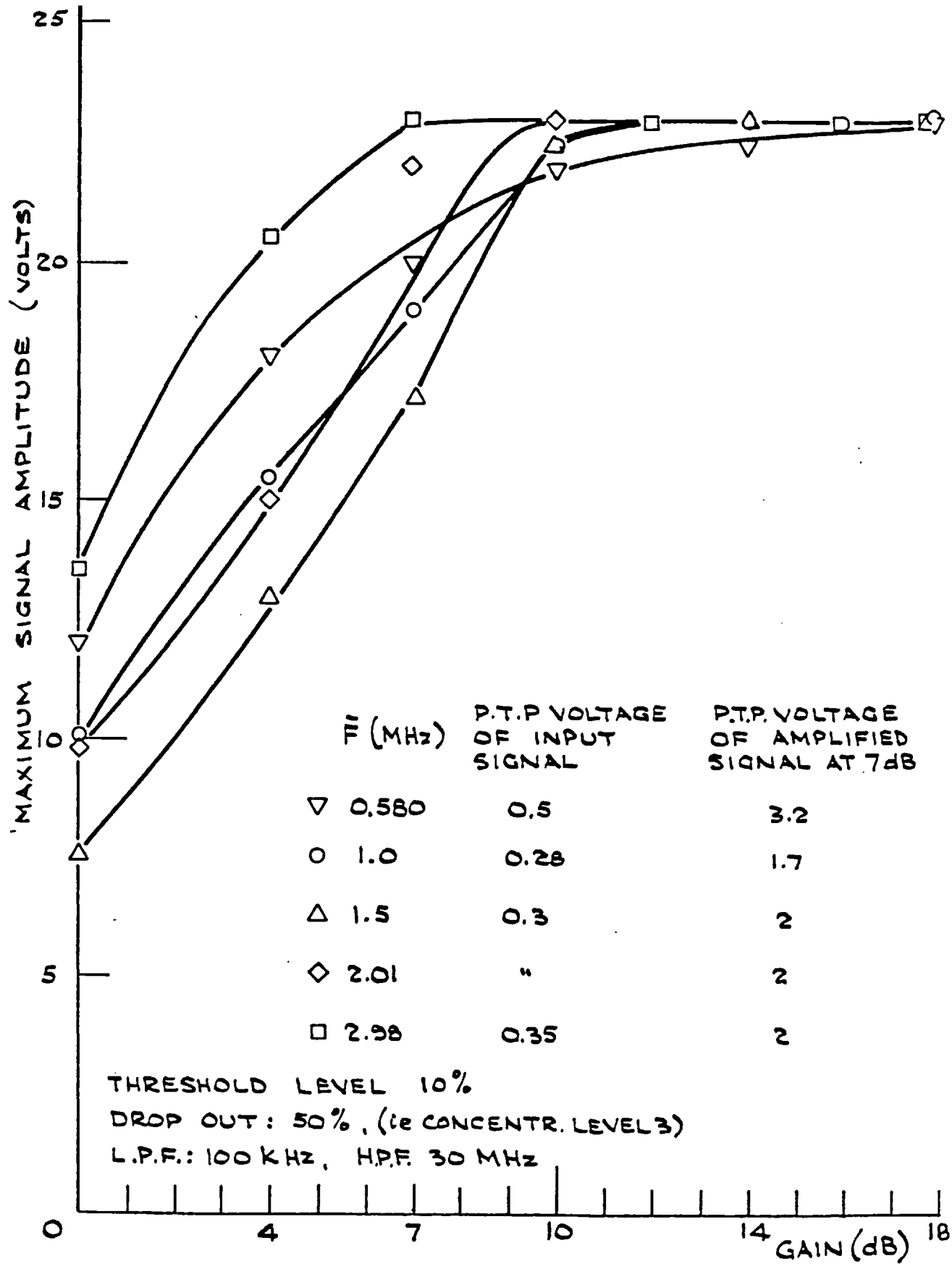


Figure 2.4.9 : Variation of maximum signal amplitude with amplifier gain (artificial bursts - Method A).

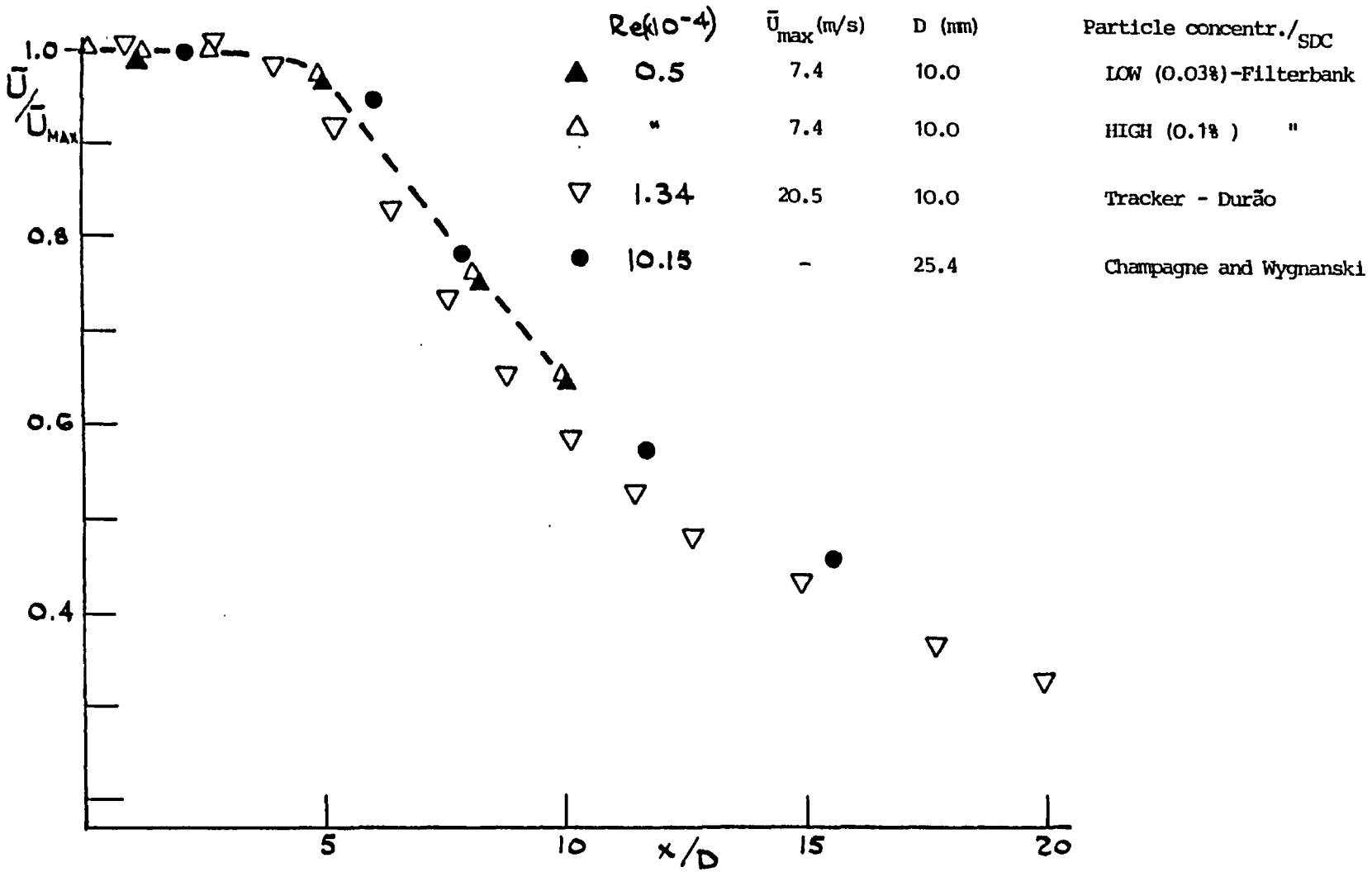


Figure 2.4.10 : Centreline mean velocity profiles in a turbulent jet: Effect of particle concentration.

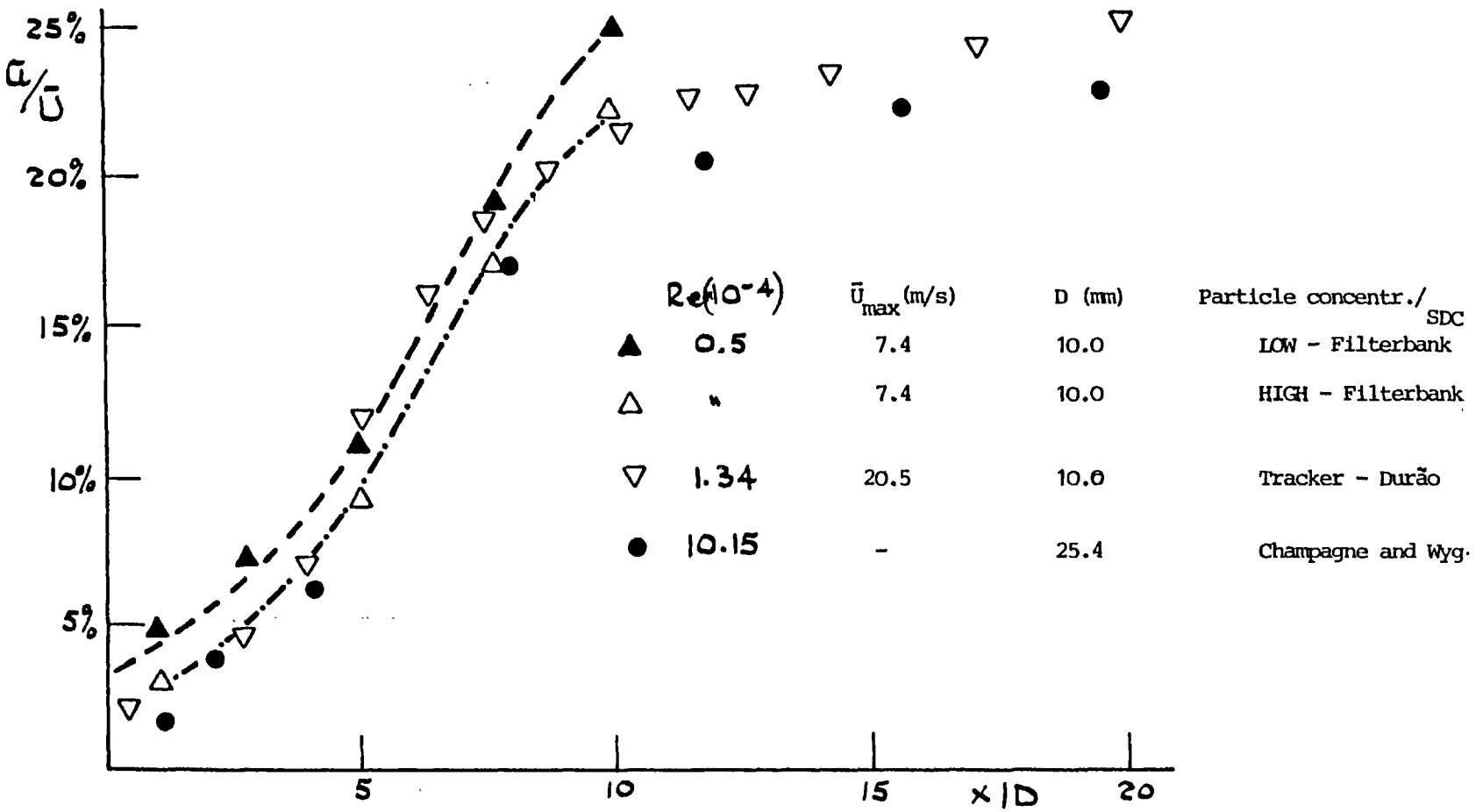


Figure 2.4.11 : Centreline axial normal stress profiles in a turbulent jet: effect of particle concentration.

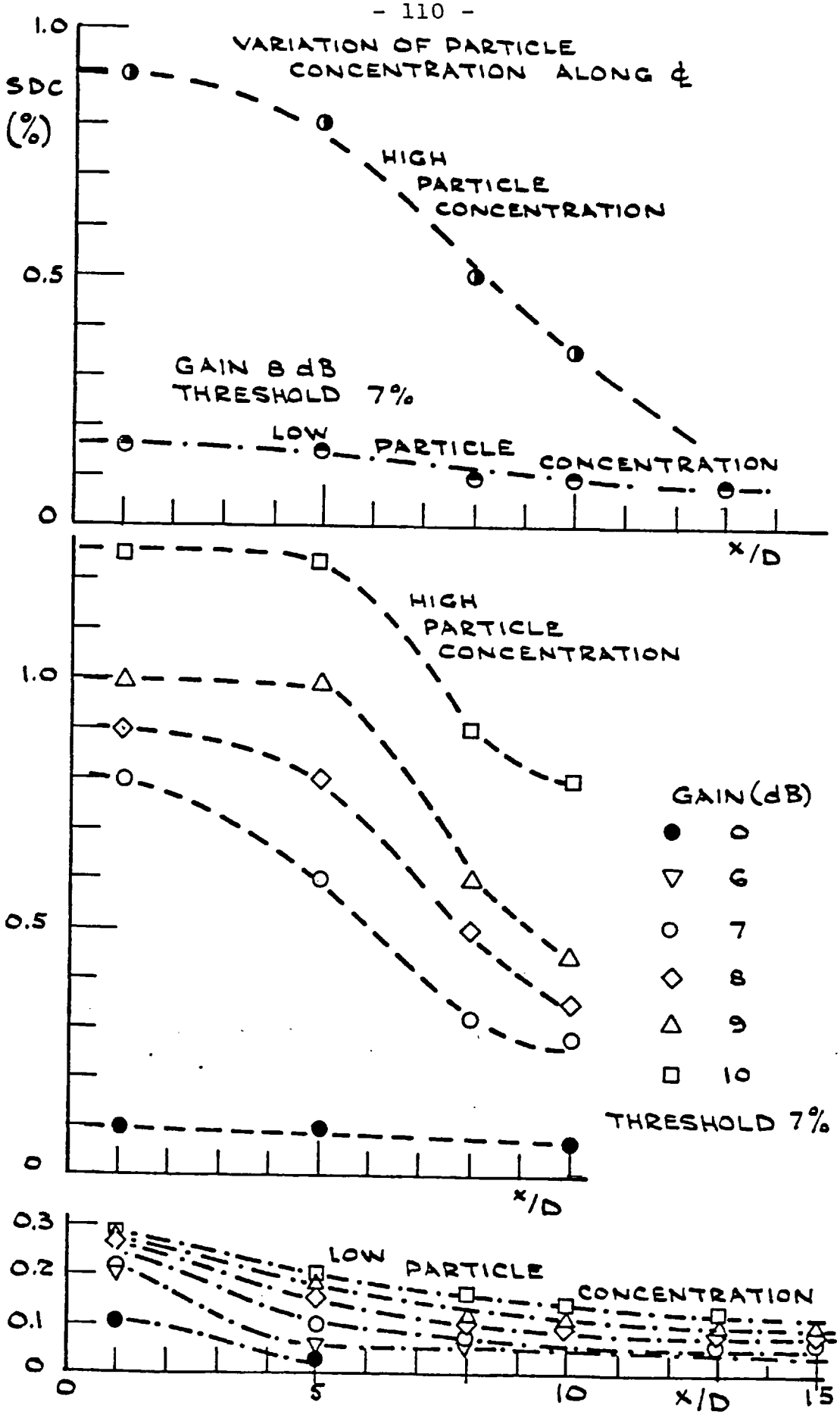


Figure 2.4.12 : Effect of gain on the SDC along the centreline of a jet.

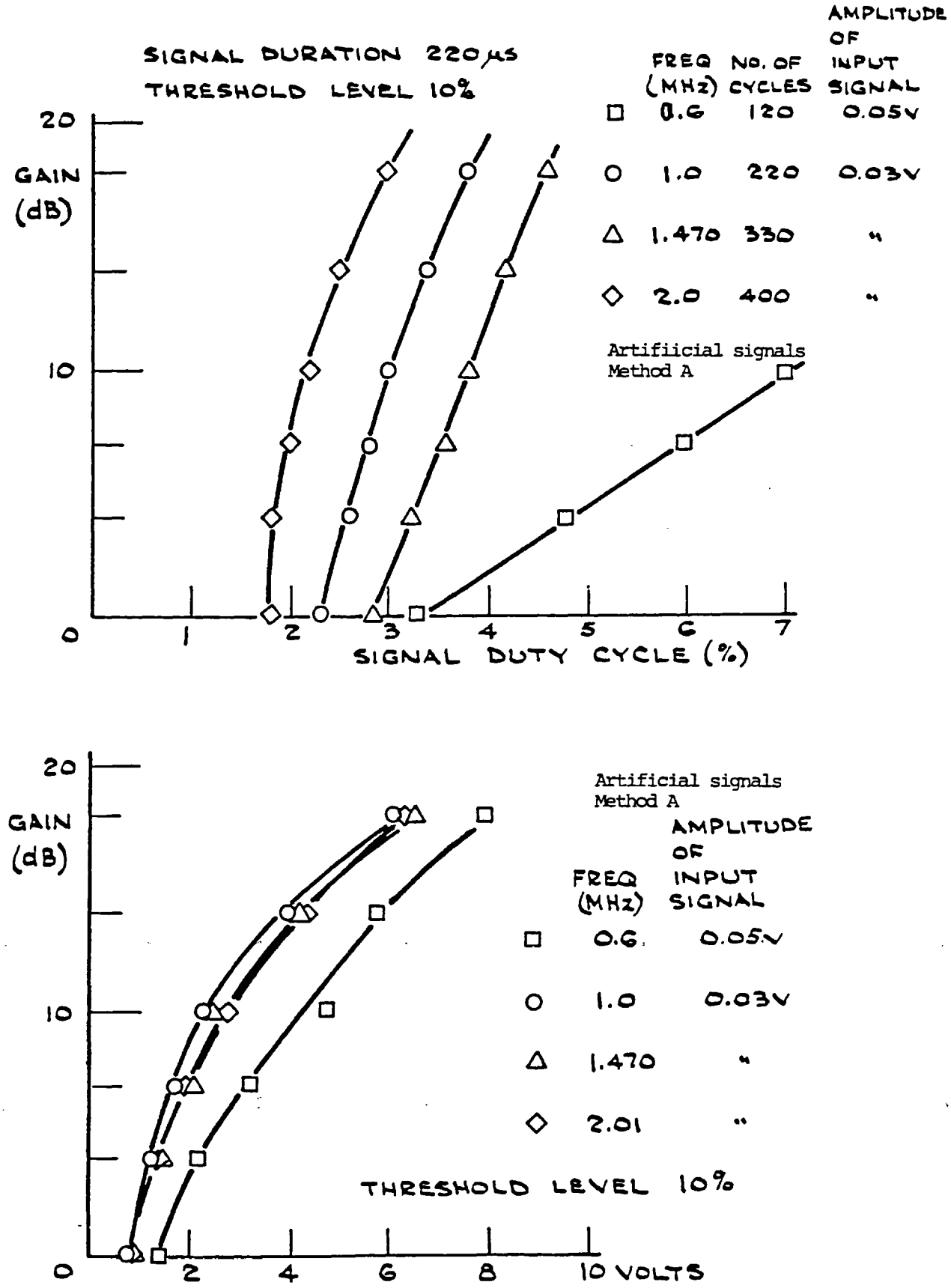


Figure 2.4.13 : Effect of gain on the SDC and on the amplitude of a Doppler signal.

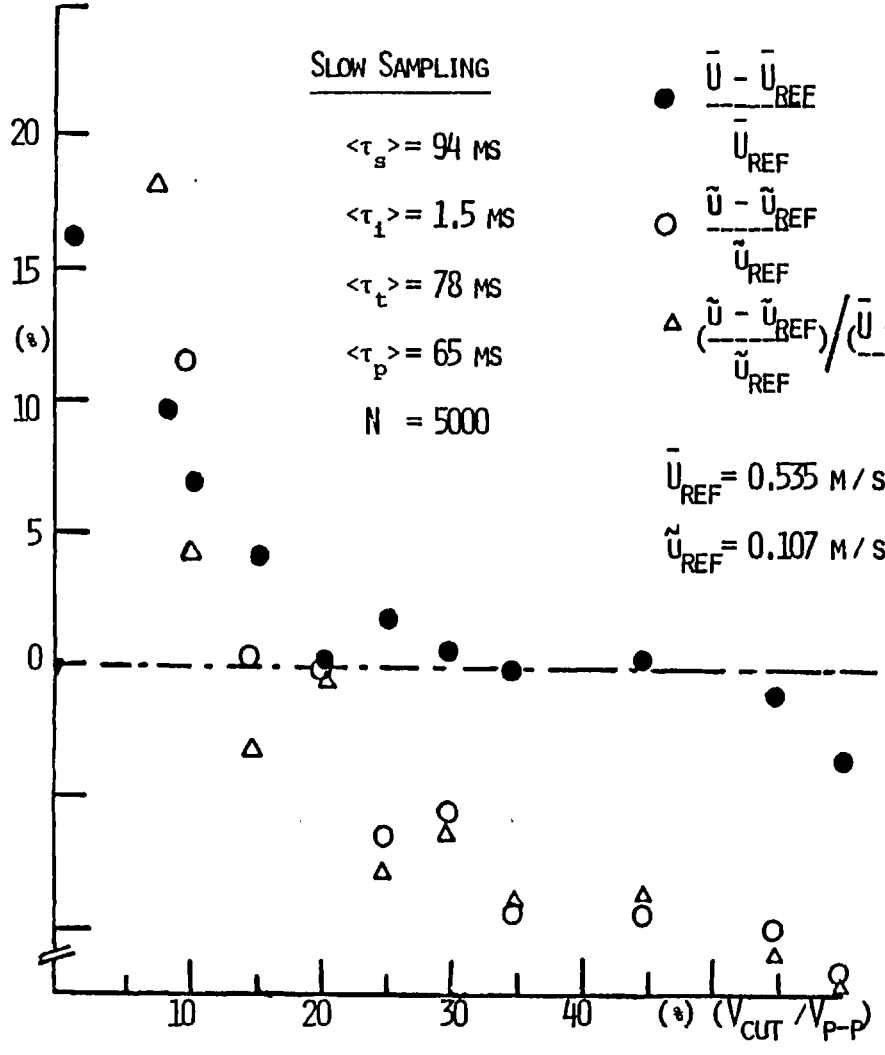


Figure 2.5.1 : Water flow: Effect of discrimination level (slow sampling)

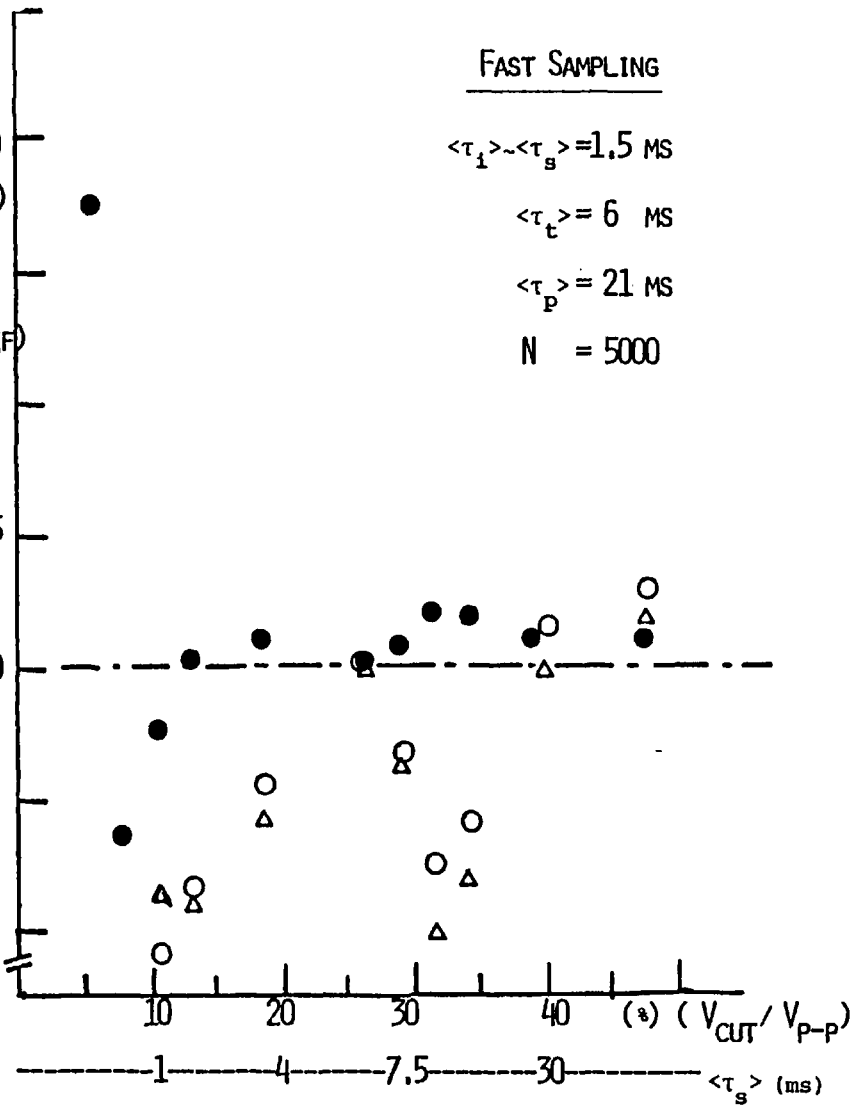


Figure 2.5.2: Water flow: Effect of discrimination level (fast sampling)

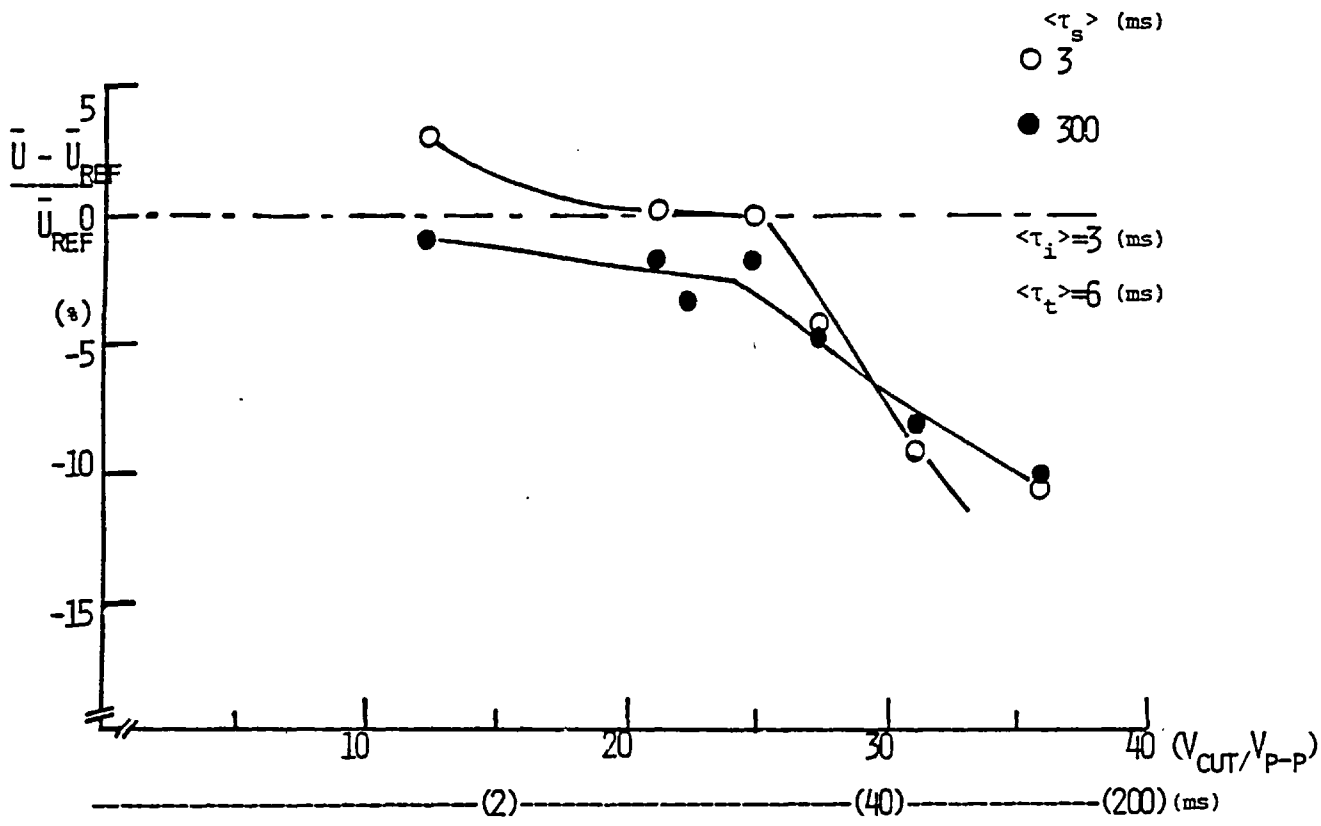


Figure 2.5.3 : Air- flow: Effect of discrimination level

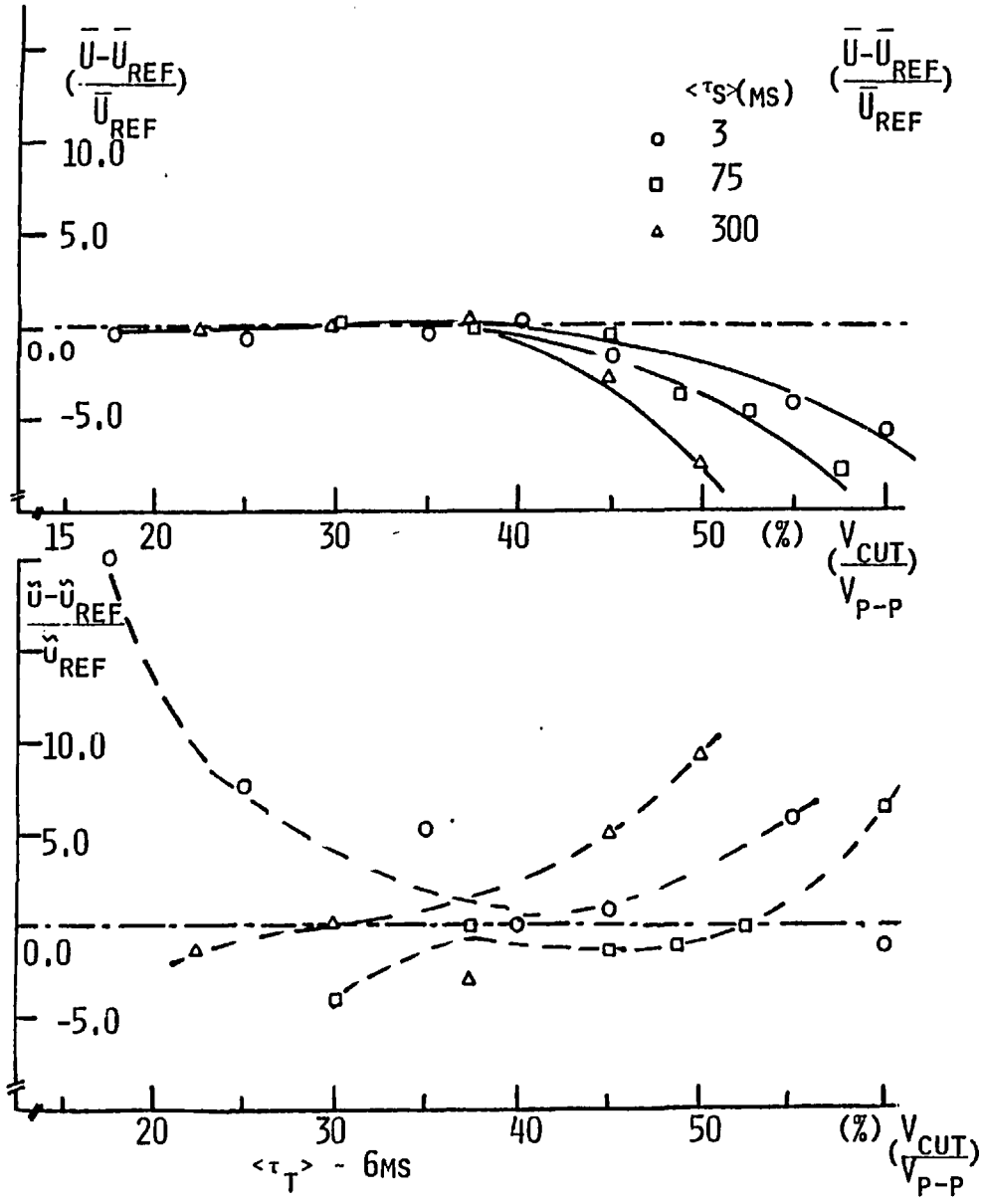


Figure 2.5.4 : Air-flow: Effect of discrimination level(particle dense flow)

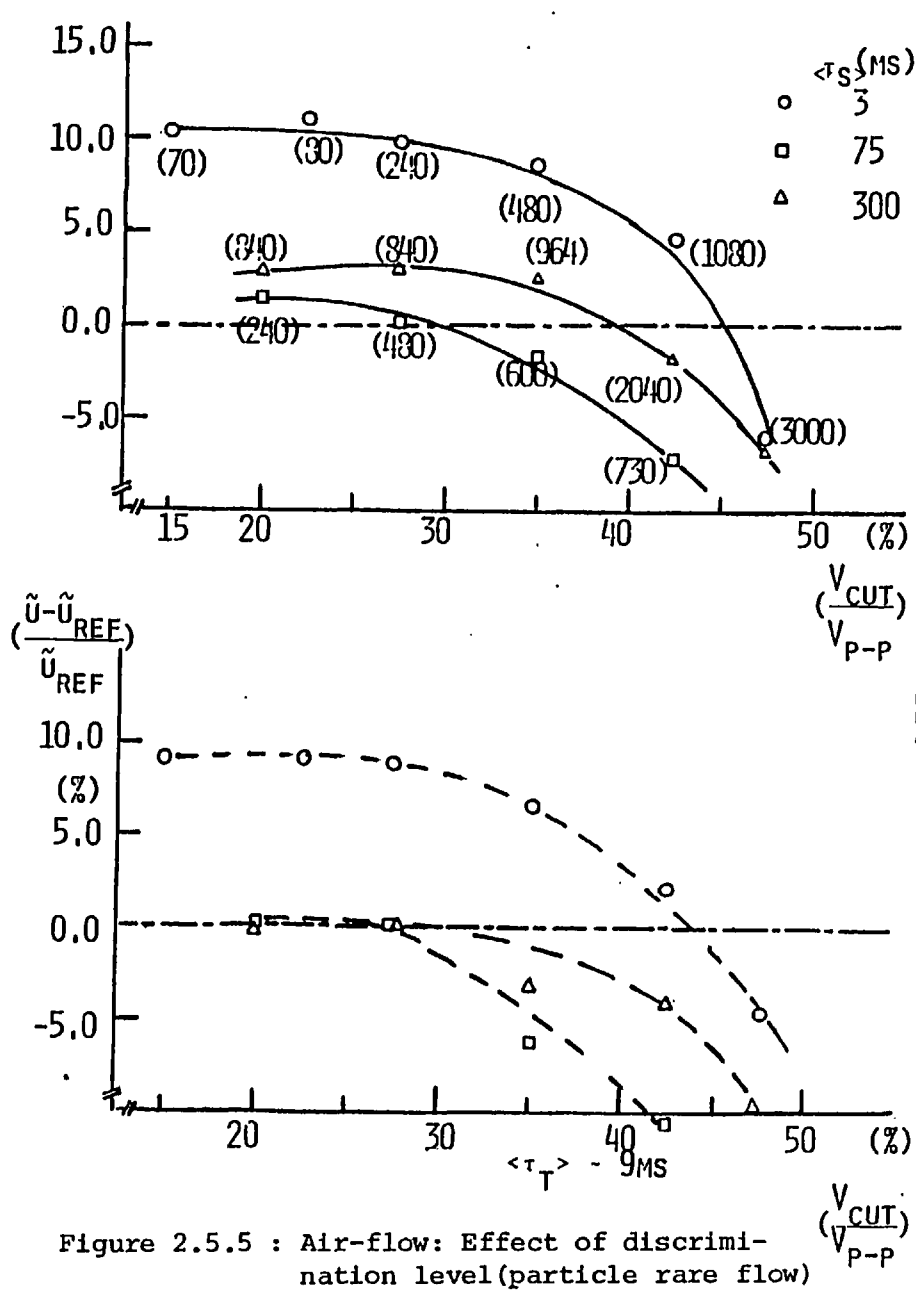


Figure 2.5.5 : Air-flow: Effect of discrimination level(particle rare flow)

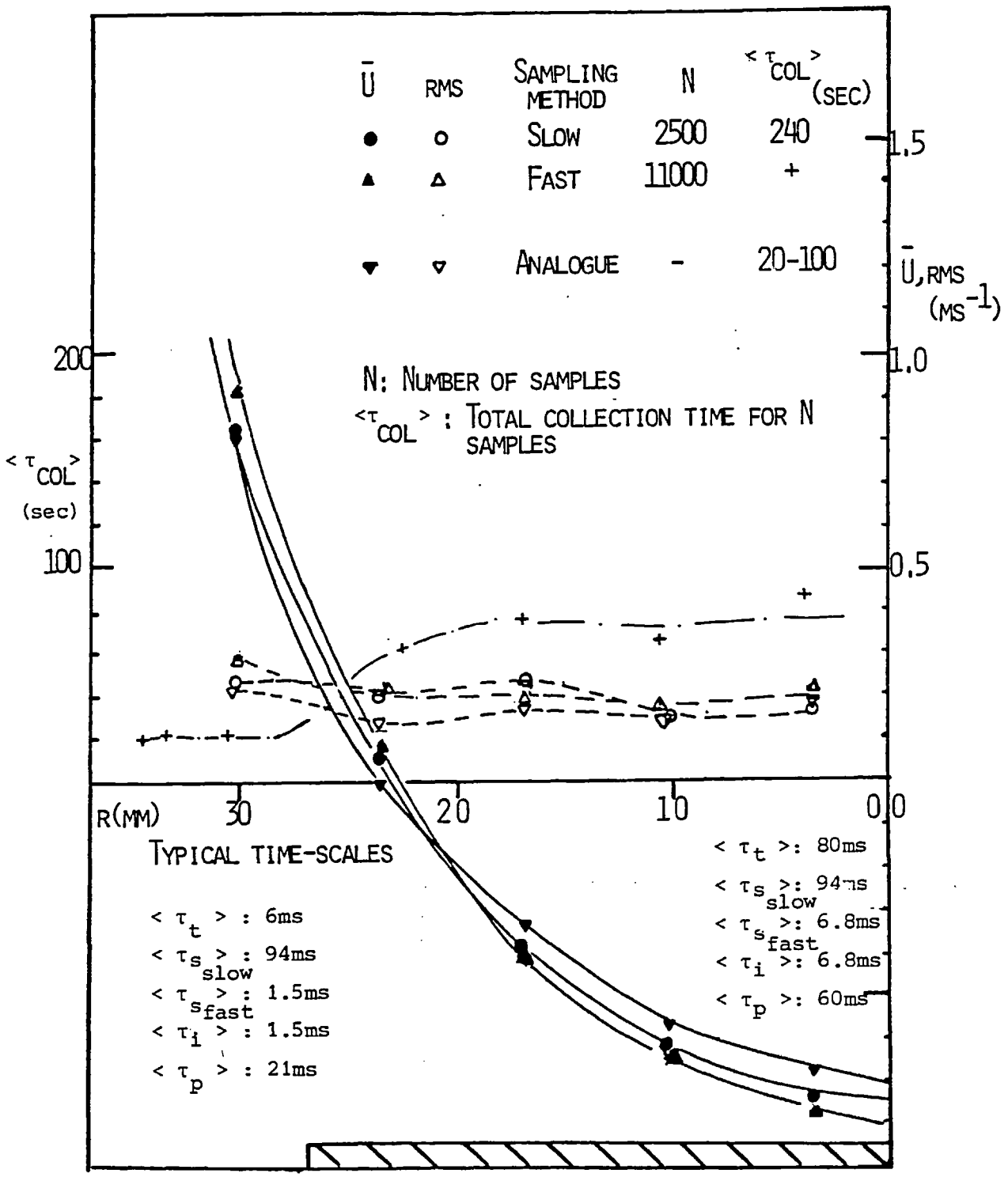


Figure 2.5.6: Water-flow: Comparison between different sampling methods.

CHAPTER III

HEAT EXCHANGER FLOWS

3.1 Introduction

3.1.1 Purpose of investigation and modelling requirements

The experimental investigation of the flow patterns in a model heat exchanger has been undertaken with the aim to assist the improvement of design of shell and tube heat exchangers. The pressure drop and heat transfer performance may be improved by better understanding of the local flow properties, especially within the recirculation regions, and the structural integrity by avoiding the perodic excitation of the tube bundle which can arise from vortex shedding or cavity excitation. The present investigation provides information of this type for simple heat exchanger flows which can also aid the formulation and appraisal of calculation methods.

Single and double segmental baffles are common practice in the various types of shell and tube exchangers and are used to improve the heat transfer coefficient by promoting turbulent mixing. They also lengthen the flow path inside the shell by redirecting the shell side flow at right angles to the tubes, and they support the tube bundle, see for example Fraas et al. (1965). Arrangements of alternating disc and doughnut-shaped baffles are thermally more effective than segmental baffles because the tube bundle is not bypassed, but, because of mechanical disadvantages, (the tie rods lie within the bundle and the central tubes are supported through the tubes lying in the overlap between the disc and the doughnut) they have found limited industrial

application. They are, however, convenient for the present purposes and the axisymmetric model arrangements examined here are of this type. The NESTS-concept, see Boyer et al (1980), where die-formed strips are assembled in layers to form a homogeneous pattern of diamond-shaped openings which support the tubes, thus reducing the problem of fluidoelastic instability, provides a possible compromise between heat transfer performance and mechanical complexity. The present results are likely to form the background for a future examination of this type of arrangement.

An axisymmetric water-model was constructed to simulate the shell-side flow in a disc and doughnut baffle shell and tube heat exchanger. Water was chosen as the working fluid because of its naturally occurring particles, which facilitate the use of laser Doppler anemometry, and the possibility of obtaining high Reynolds numbers at relatively low pressures and velocities. The flows were in the fully turbulent regime and measurments are reported of the mean and fluctuating velocities, and wall-pressure distributions for three different Reynolds numbers and two different baffle spacings. Information relating to heat-exchanger design and to the performance of segmental baffles has been reported in the British Standard 3274 (1960), and for example Tinker (1951), Taborek (1979) and the NEL (1975). There is an obvious lack of information regarding disc and doughnut baffle arrangements. Some of the most important parameters that influence the flow path inside a heat exchanger and their implications are tabulated in table 3.1.1, which contains symbols defined in the nomenclature section of this thesis. The flow streams A to E, referred to in table 3.1.1, are shown diagramatically in figure 3.1.1 and are named according to Tinker (1951). Figure 3.1.2 shows a typical arrangement of a disc-and-doughnut heat exchanger indicating the various geometrical parameters

	ITEM	OPTIMUM RECOMMENDED MAGNITUDE	RESULTING PERFORMANCE/LIMITATIONS
Geometrie parameters	Ratio of baffle spacing to shell Diameter ($1/D_s$)	- $1/D_s$: 1/5 ~ 1 - Minimum l should be 2in or 1/5 D_s whichever the larger - (*)	- Minimum specification is based on the ability to clean the rod bundle and on manufacturer's experience that no benefit is obtained with closer spacings. - Maximum specification is based on avoidance of tube vibrations.
	Baffle Cut (H)	- H : 20% ~ 35% of baffle diameter	- Larger (H)'s usually taken with larger ($1/D_s$) in order to avoid excessive pressure drop across the baffle windows as compared to the bundle
	Ratio of baffle cut to baffle spacing (H/l)	No recomended optimum due to lack of data	- Pressure drop through baffle window is determined by the imposed (H/l)
	Entrance lenth (l_i) Exit length (l_o)	Should both be larger than (l)	- Magnitude determined by possibility to accommodate nozzles.
Flow parameters (Streams as defined in fig. 3.3.1)	A-Stream	5 ~ 15% of total flow rate	- A-stream becomes significant with small ($1/D_s$) - A-stream is thermally effective
	B-Stream	60 ~ 80% of total flow rate	- Choice of small ($1/D_s$) forces the flow into A, C, E-streams and therefore decreases the heat transfer performance
	C-Stream	10% of total flow rate	- A high value of C-stream can be a source of temperature-profile degradation. - Should be kept to a reasonable value by sealing devices
	E-Stream	15% of total flow rate	- Thermally highly ineffective, because it causes disturbance of the temperature-profile - Should be kept as low as possible

(*) Generally good practice to make the net flow passage area past the baffle approximately equal to that for cross-flow through the bundle so that the dynamic head is about the same in both restricted regions.

Table 3.1.1: Some geometric and flow parameters affecting heat exchanger design

and flow streams. For the design of the model used in the experimental investigation typical values for the geometrical parameters were taken from table 3.1.1. The description of the B-stream flow pattern was of primary interest. For simplification, A, C and E-streams, entrance and exit effects and thermal effects were eliminated although the test-model could be easily modified to incorporate them for a future investigation of possible interactions. A detailed description of the test section and of the parameters investigated is given in section 3.2.1. Section 3.2.2 describes the experimental technique, and provides an account on the errors involved.

The presence of multiple baffles results in an increase in the local heat transfer coefficient because they delay the development of the thin thermal boundary layers, present in the upstream region, and increase the pressure drop due to the higher skin friction associated with the successive boundary layer restarts after each doughnut. The flows examined are characterised by separation initiated at surface discontinuities, such as the corner of an annular rib, the so-called "doughnut", or at the tip of a flat disc normal to the main flow direction As it will be confirmed, the flow pattern of this configuration cannot be readily anticipated from the known behaviour of the flow over individual baffles The relative position of each baffle to its neighbours perturbs and alters the flowfield upstream and downstream of the baffle. Understanding of the flow mechanism behind each constituent baffle is necessary in order to define their relative influence. Hence, and in order to provide the background for the analysis of the results, a brief survey of the experimental work in turbulent flows past steps, ribs, sudden expansious and flat discs is presented in subsection 3.1.2. Having established the basic characteristics of separated and recirculating flows, the results are presented and discussed in section 3.3. and

3.4 respectively. The chapter closes with concluding remarks in section 3.5.

3.1.2 Literature review

The flow about a baffle, whether this is surface mounted or suspended in the fluid, involves a separation region of recirculating flow in its near-wake which is characterised by a large total pressure loss, intense mixing and turbulence generation. The characteristics of such flows can be very different depending on whether the baffle is attached to a surface or not, its forebody shape, blockage and initial conditions. The findings of some recent experimental investigations for flows over backward facing steps, obstacles, fences, sudden expansions and for the separated wake flows past discs are tabulated in tables 3.1.2 and 3.1.3 respectively. They are relevant to the heat-exchanger geometry in that they establish the range of expected recirculation lengths and the distribution and magnitudes of Reynolds stresses. From table 3.1.2 it can be seen that the presence of the wall gives rise to generally longer recirculation lengths, smaller streamline curvature and hence smaller pressure drops than for flows with a free stagnation point (see table 3.1.3).

The flow over a sudden expansion, seen as the axisymmetric case of the flow over a backward facing step, bears similarities to the flow over the doughnut in the heat exchanger model. Qualitatively, the flow differences between the sudden expansion and doughnut flow should be similar to the differences of the flow over a step and a surface mounted obstacle or plate. Plane and axisymmetric geometries differ in that the characteristic dimension in the former is the channel diameter, whereas in the latter the pipe diameter is no longer characteristic, but the

AUTHOR	FLOW SURROUNDINGS / EXPERIMENTAL METHOD	Blockage Ratio	FLOW CONDITIONS				RESULTS	
				Max. rms fluctuation			Reattachment length	
			RE (*)	$\tilde{u}/U_o$	$\tilde{v}/U_o$	$\tilde{w}/U_o$		
Armaly, Durst Pereira Schönung (1980, 1983) Tropea (1982)	Backward facing step / LDA $\bar{U},\tilde{u}$	h/H = 0.5	<1200 laminar	—	—	—	19 steps. Increases with Re	-Reattachment length depends on obstacle height and Re in laminar regime
			1200-6600 transition	N/A	N/A	N/A	16-8 steps	
			>6600 turbulent	0.25	0.2	—	8-10 steps	-In transition zone flow becomes 3-D, with 3-recirculation zones -Independent of Re, blockage in fully turbulent regime.
Moss, Baker, Bradbury (1979)	Backward facing and forward facing steps in channel / $\bar{U}$(pulsed-wire) $\tilde{u}$(Hot-wire)	h/H = 0.909	5×10^4	0.04 before step	~0.021	—	0.6 steps	Max. reverse velocity: $0.5\ \bar{U}_o\ \dot{m}_r/\dot{m}_b = 0.01$
				0.10 above step	N/A	—		Max. reverse velocity: $0.3\ \bar{U}_o\ \dot{m}_r/\dot{m}_b = 0.07$
				0.4 after step	0.21	0.35	5.0 steps	Max. reverse velocity: $0.25\ \bar{U}_o\ \dot{m}_r/\dot{m}_b = 0.08$
Etheridge, Kemp (1978)	Backward facing step in free surface water tunnel / LDA $\bar{U},\tilde{u},\ \tilde{v},\ \overline{uv}$	h/H = 0.07	N/A	0.20	0.15	—	5.1 steps	-Free-stream turbulence 2% -Transition boundary layer at separation. -Boundary layer thickness to step height:2.0 -Length scale at reattachment increases at twice the rate of normal b/l

(*) Re: Reynolds Number based on channel or duct, or wind tunnel height
H: channel height; h: obstacle height or step height

Table 3.1.2: Recent experimental findings for wall-reattaching flows

AUTHOR	FLOW SURROUNDINGS / EXPERIMENTAL METHOD	Blockage Ratio	FLOW CONDITIONS				RESULTS	
			RE (*)	Max. rms fluctuation $\tilde{u}/\bar{U}_o$	$\tilde{v}/\bar{U}_o$	$\tilde{w}/\bar{U}_o$	Reattachment length	
Freeman (1975)	Sudden Expansion in pipe / LDA, $\bar{U}, \tilde{u}$	Expansion Ratio 2.1 : 1 (18D before expansion)	3×10^4	$\tilde{u}/\bar{U}_c$ = 0.18	N/A	—	2.3 large pipe diameter ~4.45 steps	-Eye of recirculation at 0.83D -Max. recirculation width: 0.74·r
Smyth R. (1979b)	Sudden Expansion in Duct / LDA, $\bar{U}, \tilde{u}, \tilde{v}, \tilde{w}, \overline{\tilde{u}\tilde{v}}$	Expansion Ratio 1.5	3.02×10^4	0.195	0.135	0.13	1.5 duct diameters ~4.5 steps	-Max. reverse velocity 0.083 m/s -Turbulent b/l
Crabb, Durao Whitelaw (1978)	Surface Mounted square rib, Wind Tunnel / LDA P, $\bar{U}, \tilde{u}$	h/H =0.08	2.7×10^4	0.4	—	—	~12.5 rib heights	-Thickness of rib affects reattachment. -Separation occurs before and extends above and beyond rib -Bi-modal frequency distribution (? Vortex shedding)
Okamoto S. (1981)	Flat plate in wind tunnel / P, HWA $\bar{U}, \tilde{u}, \tilde{v}, \tilde{w}$	h/H = 0.026	1.2×10^4	0.45	0.45	0.45	14.8 obstacle heights	-Model height to boundary layer thickness: 1.77 -No ceiling effects below h/H = 0.05 -Transitional phase of b/l.

Table 3.1.2: Recent experimental findings for wall-reattaching flows (continued)

AUTHOR	FLOW SURROUNDINGS / EXPERIMENTAL METHOD	Blockage Ratio	FLOW CONDITIONS	Max. rms fluctuation			Reattachment length	RESULTS
			RE (*)	$\tilde{u}/\bar{U}_o$	$\tilde{v}/\bar{U}_o$	$\tilde{w}/\bar{U}_o$		
Eaton, Johnston (1980)	Backward Facing step-air / $\bar{U}, \tilde{u}, \overline{uv}$ (Pulsed-wire, H.W.A) Thermal tuft, pulsed-wall probe for near wall measurements	h/H = 0.4 Area ratio: 1.6	$1.1 - 6.2 * 10^4$	0.22	N/A	N/A	8 steps	-Turbulence intensity decays rapidly in reattachment region: Decay begins one or two step heigths upstream of separation. -Large spanwise vortices which grew by pairing were present in the shear layer originating from a laminar boundary layer. -Not present in the turb. b/l upstream of x/h = 6 -"Flapping" of ± 1h of the reattachment point
Durst, Rastogi (1980)	Flow over a thin fence-air / Few LDA experiments, $\bar{U}$, $\tilde{u}$, Also Predictions	h/H = 0.25 - 0.5	$\sim 10^4$	—	—	—	13.3 h	

Table 3.1.2: Recent experimental findings for wall-reattaching flows (continued)

Author	Experimental Method / Flow Surroundings	Blockage Ratio	Re	Max. rms. fluctuations $\tilde{u}/\bar{U}_b$	$\tilde{v}/\bar{U}_b$	$\tilde{w}/\bar{U}_b$	Recirculation Length	Recirculation Width	Comments
Taylor (1981)	LDA $U,V,\tilde{u},\tilde{v},\tilde{w}$, P / Water flows discs and cones	25%	8×10^4	0.35	0.42	0.42	1.75d	0.62d	$\dot{m}_r/\dot{m}_b = 0.08$
		50%		0.36	0.26	0.36	2.20d	0.55d	$\dot{m}_r/\dot{m}_b = 0.12$
		25%		0.30	0.28	0.33	1.55d	0.55d	$\dot{m}_r/\dot{m}_b = 0.05$
Smyth (1979a)	LDA / Air flow past Disc	48%	13×10^5	0.30	0.27	-	1.40d	1.10d	- Max. Turbulence occurs around separation streamline
Bradbury (1976)	Comparison between HWA and pulsed-wir / Confined Plate $\bar{U},\tilde{u},\tilde{v},\tilde{w}$,	10%	3.8×10^5	0.35	0.65	0.35	1.98d	0.80d	$\dot{m}_r/\dot{m}_b = 0.24$ - Vortex shedding responsible for high values of u, v, w on c_t - Qualitatively incorrect results may be obtained by the h.w.a.
Durao and Whitelaw (1978)	LDA $\bar{U},\tilde{u},\bar{v},\tilde{v},\tilde{w}$ / Annular jet past disc	50%	$8.6 - 36.2 \times 10^3$	0.30	0.30	0.25	1.00d	-	- Increasing blockage decreases recirculation length - Anisotropy of centre line Normal stresses
Davies and Beer (1971)	HWA and pressure probes / Annular jet past disc	54%	$\sim \times 10^4$	-	-	-	1.16d	0.56d	$\dot{m}_r/\dot{m}_b = 0.12$ - Increasing bluffness increases recirculating mass flow rate
Winterfield (1965)	Passive Tracer / Confined disc	25%	$2 \times 10^3 \sim 2.2 \times 10^5$	-	-	-	2.00d	0.74d	- Increasing bluffness increases bubble length and decreases residence time

$\dot{m}_r$ = recirculating mass flow rate, $\dot{m}_b$ = mass flow rate based on bulk velocity, d = baffle-diameter

Table 3.1.3: Recent experimental findings for flows past bluff-bodies

area ratio is. It appears, and it can be confirmed from table 3.1.2, that the differences between the plane backward-facing step and sudden expansion are more quantitative than qualitative. The same does not apply to the flow over a backward-facing step when it is compared to that over a plane expansion. Obviously the constriction ratio is the important parameter. Also, in plane flows increases in the maximum pressure drop are associated with decreasing turbulent length scales. The opposite is true for axisymmetric geometries, Sullerey et al (1975).

Most of the recent work has concentrated on the backward facing step, since this is the simplest two-dimensional reattaching flow. It differs that over an obstacle in that in the first case separation at the sharp corner occurs with the streamlines approaching nearly parallel to the step surface, whereas in the case of a thin obstacle there is a significant upstream influence, due to streamline curvature before the obstacle, which is carried also downstream of separation. In both cases the boundary layer from upstream separates at the downstream corner forming a free shear layer. For the backward facing step flow the dividing streamline is fixed at the edge of the step and slightly curved through the first half of the separated flow region. In the case of an obstacle, for example Castro et al (1977), or a rib with a finite thickness, Crabb et al (1978), Schofield et al (1981), the upstream boundary layer separates at the flowfacing corner of the obstacle and can generate a second recirculation region on the top surface of the obstacle depending on the obstacle dimensions and initial conditions. The boundary layer may reattach or not on the top surface depending on the obstacle height and width. For all reattaching flows the shear layer immediately after the sharp corner is thin enough not to be influenced by the wall in this region, but it curves sharp-

ly downwards in the reattachment region, which, for instance, for a backward facing step occurs at about 6 to 8 step heights and impinges on the wall. Due to strong adverse pressure gradients and effects of stabilising curvature and interaction with the wall some of the fluid is deflected upstream in the recirculation zone with maximum negative velocities around 20% of the upstream the step or obstacle velocity. Normal and shear stresses decay rapidly in the recirculation zone.

The reattachment length, among other parameters, depends on the state of the initial boundary layer and its thickness. The experiments of Cheun et al(1981) indicated that a thicker initial boundary layer gives rise to an initially thicker shear layer and higher spreading rate. Moss et al (1979), suggested that at a ratio of boundary layer thickness to step height of about 0.5 its influence becomes small. Generally, the influence of the upstream boundary layer is more obvious on the local turbulence intensity which is higher with a thinner boundary layer.

Comparison of the works of Armaly et al (1980), De Brederode et at (1972), Moss et al (1979) indicates that for decreasing channel aspect ratios, for example between two to one, the ratio of reattachment length to step height decreases from nine to five. For aspect ratios greater than ten, (De Brederode et al), the effect on the reattachment length becomes negligible. The reattachment length, for a given aspect ratio, becomes independent of the Reynolds number when the separation boundary layer is fully turbulent, Eaton et al (1980), Armaly et at (1980), Tropea (1982). The effect of free-stream turbulence on the reattachment length has not been studied extensively. For the experiments of Cheun et at (1981), variation of the free-stream turbulence did not affect the reattachment lenght. They suggested that this was because the maximum turbulence in the boundary layer was higher than

the free-stream turbulence. In contrast, comparison with the works of Etheridge et al (1978) and of Tropea (1982), which had about 1% free-stream turbulence suggests that the reattachment length decreases with increasing free-stream turbulence.

For roughness elements and ribs, Crabb et al (1978) and Schofield et al (1981), found that the reattachment length is a function of height to width ratio of the element and of the ratio of boundary layer thickness to bluff-body height (at least for values close to one). Sami and Liu (1977) suggested that the reattachment length depends on the value of Reynolds number when the element height is of the same order as the boundary layer thickness. Reattachment lengths ranging from 12 to 17 element heights have been measured by the various experimentors, depending on the initial conditions. Schofield et al (1981), in their investigation of the flow through the gap, created when a wall mounted roughness element is split into two, deduced that decreasing the gap increases the turbulence intensity near the wall and decreases the local mean velocity. Vortices are shed from each side of the gap and depend on the gap size. They may influence the centreline flow development in the region immediately downstream of the gap.

Vortex shedding, similar to the above, or to that occurring in flows past three-dimensional obstacles, see Castro et al (1977), has mainly been observed for plane baffles, see Crabb et al (1978). Neither vortex shedding nor bimodal velocity probability density distributions have been observed for axisymmetric flows, confined, Taylor (1981), or unconfined, Durao et al (1978).

In the investigation of the wake past axisymmetric bluff bodies, pressure measurements and also estimation of the recirculation bubble length behind a wide variety

of cross-sectional and forebody shapes (for example Carmody (1964), Davies and Béer (1971), Calvert (1967), Winterfield (1965), Sullerey et al (1975)), have shown that bluffer bodies, which give rise to large streamline deflections at their trailing edge, result in larger pressure drops, longer and wider recirculation zones. Winterfield (1965) suggested that the length of recirculation is influenced more by bluffness than by blockage, at least for isothermal flows of less than 25% blockage.

Bradbury (1976), for a flow over a normal flat plate, Durao and Whitelaw (1978), Durao, Founti and Whitelaw (1979), for axisymmetric and three-dimensional annular jets past discs and Taylor (1981), for confined flows behind axisymmetric baffles have provided detailed descriptions of the mean and turbulent flowfield behind bluff-bodies, and their results are summarised in table 3.1.3. The results of Taylor (1981) confirmed that confinement reduces the length of recirculation, the forebody shape having a stronger influence than blockage. Increasing blockage for the same forebody, decreases the bubble length for unconfined flows, Durao and Whitelaw (1978), whereas the opposite is true for confined flows, Taylor (1981). Bluffness increases turbulent transport, Taylor (1981), and at high blockage ratios the maximum value of turbulent kinetic energy is no longer found at the rear stagnation point, as for unconfined flows (Durao et al (1978)), but rather within the free shear layer surrounding the recirculation zone. For unconfined flows, equally high values of turbulence quantities occur on the centreline at the free stagnation point. For the case of a flow over a normal flat plate, Bradbury (1976) has suggested an explanation for the high centreline values based on the existence of vortex shedding.

There have been few experimental investigations of interacting separated flows due to neighbouring bodies,

and the ones that existed until very recently, such as the work of Günter et al (1947) in a baffled heat exchanger, of Morel et al (1980) in two discs in tandem do not report the detailed flowfield. Very recent contributions, published after the completion of this work, include those of Martin et al (1982) and Berner et al (1983): both investigations deal with the flowfield in heat exchangers employing multiple segmental baffles, modelled as normal flat plates in two dimensional channel flow. Martin introduced the rod bundle and investigated the flow disturbance by its presence. Both investigations report measurements of axial mean and fluctuating velocities obtained with laser Doppler anemometry. Berner also reports pressure distributions. Although the geometrical configurations of these investigations are not directly relevant to the present one, useful knowledge can be obtained from their conclusions. Martin et al used refractive index matching to demonstrate the level of measurement detail that can be achieved in the wake of individual rods. They suggested that the geometry of the rod array influences the behaviour of individual wakes. The effect of the rods was to encourage a uniform velocity distribution and reduce recirculation. Berner et al examined the similarity of the flow pattern for different baffle cuts (defined as the percentage of the baffle diameter that ha been removed) and concluded that for a baffle spacing/channel depth equal to 0.4 and baffle cut of 30%, a minimum of four baffles is required to achieve similarity. For this geometrical configuration, the laminar and turbulent flow characteristics were similar.

Calculations of reattaching flows and of the flow about baffles can be achieved by numerical solution of the partial differential equations for the conservation of mass and momentum, together with the necessary boundary conditions. A brief description of such a calculation procedure is presented in chapter 4. Here it is

noted that, for turbulent flows, the components of the stress tensor in the time-averaged Navier-Stokes equations can be obtained from the solution of equations with the Reynolds stress components as dependent variables. In these equations higher order correlations appear for which modelling assumptions are necessary. In turbulence modelling it is common to characterise turbulence by one characteristic velocity and one length-scale (involving a Boussinesq-type approximation) or some related quantity (for example the dissipation rate, ε) and solve model transport equations for those parameters. The more general approach of solving the transport equations for the individual Reynolds stresses coupled with some lenth-scale is essentially more complex and can also be prohibitive in certain cases due to storage and cost requirements. The numerical techniques used to solve the finite-difference equations necessarily involve assumptions to connect the discrete nodes at which the dependent variables are evaluated, and these, together with the solution algorithm, can give rise to errors even when there are no assumptions in the differential equations and boundary conditions, see for example Leonard (1979). Numerical diffusion is particularly undesirable in calculations which are made to evaluate the performance of turbulence models. In parallel, inaccuracies in the discretization scheme in some recirculating flows can be as important as deficiencies in turbulence models.

The importance of the turbulence model and discretization scheme can be traced in the prediction of the flow past baffles and annular jets. Pope and Whitelaw (1976) calculated the unconfined flow about a disc, measured by Carmody (1964), with two turbulence models: the "k-ε"-model (Launder and Spalding, 1974) and the "Reynolds stress" model of Launder, Reece and Rodi (1975). Both models underpredicted the length of the recirculation bubble (by about one third) and the spread-

ing rate of the downstream wake. Their calculations, as suggested by Taylor (1981), may have suffered from numerical diffusion and the inclusion of the Reynolds stress model conferred no improvement in the agreement between calculation and experiment.

Leschziner and Rodi (1981) examined the performance of three discretization schemes and three turbulence-model variations in annular jet flows. Apart from the standard "k-ε" model, two variants of this were tested: one accounting for effects of streamline curvature on turbulence and the other for the preferential influence of normal stresses on the dissipation of turbulence energy. It was concluded that it is necessary to have more exact discretization schemes than the hybrid central upwind scheme, to bring out changes in the turbulence model. The results were appreciably improved by using the quadratic, upstream-weighted differencing scheme (Leonard, 1979) and accounting for effects of streamline curvature, but discrepancies still existed between measurements and calculations.

Taylor (1981) predicted the flow past confined baffles and the annular jet of Durao et al (1978), using the "k-ε" model. He compared his results with those of Pope et al and Leschziner et al and concluded that numerical diffusion errors can be reduced by effective grid refinement which must be accompanied by a method for assessing the magnitude and location of such errors. Even so, the length of recirculation was underpredicted due to overestimation of the radial diffusion of axial momentum in the recirculation region, and the two-equation model was held responsible.

The prediction of turbulent reattaching flows has been considered by a wide variety of investigators and the conclusions reached were similar to those for the flow past bluff bodies. The flow over a plane rib and a

fence in a channel have been examined by Durst and Rastogi (1980), and Castro, Cliffe and Norgett (1981) respectively. In both cases the solution domain extended far enough upstream and downstream of the obstacle in order to remove uncertanties due to the boundary conditions. Durst and Rastogi obtained their solution using the "k-ε" model and two upwind finite difference schemes (upwind-central and the skewed-hybrid scheme proposed by Raithby, 1976). Two types of curvature correction, proposed by Millizer et al (1977) and Launder et al (1977), were also incorporated. Agreement was good only for profiles upstream of the rib, where flow is dominated by pressure gradients. The flow over and behind the rib was poorly represented, with an underprediction in the axial velocity of 20 - 30% at ten rib heights downstream. Numerical experiments suggested that the discrepancies in the far-wake were due to the poor calculation of the recirculation bubble, and that the inclusion of curvature correction, at least for two-dimensional approaches did not offer substantial improvements in the calculation.

Castro et al calculated the laminar flow over a normal plate in order to exclude the effects of the turbulence model. The performance of the hybrid-difference (Spalding, 1972) and vector-differencing scheme, originally suggested by Raithby (1976) and further developed by Lillington (1981),was compared to the performance of a finite element method, introduced by Taylor and Hood (1973, 1974). They concluded that the nature and magnitude of errors depend first on the particular numerical method, but also on the region of the flow where each method is employed. The two finite-difference schemes were inaccurate in the region upstream of the boundary layer on the front of the plate and the resulting errors in the predicted flow might have subsequently been convected downstream of the barrier. Grid refinement near

the plate, so as to resolve the flow in the regions of large gradients just outside of the boundary layer rather than further upstream, where mesh Reynolds numbers are actually higher, can yield predictions with acceptable accuracy. In the downstream region the hybrid scheme was inadequate in comparison with the others, due to numerical diffusion. Castro et al concluded that the differences in the basic character of the flow upstream and downstream of the plate preclude the choice of a single numerical method that is ideal both in front and behind the barrier. The vector-differencing scheme and the finite-element method were generally more promising than the hybrid scheme, but also more expensive.

The last flow to be considered here is the flow past a backward-facing step. It formed one of the major test cases in the 1980-1981 Stanford Conference and the predictive results have been reviewed by Eaton (1982). The flow was computed by a total of 15 different computor groups. Nine of the methods used a Boussinesq (eddy-viscocity) model and of these seven were variations of the "k-ε" model of turbulence. Another two used a mixing-length model. Three of the methods used algebraic stress models, and one, used a full Reynolds-stress transport model. The most important parameter to predict in a backward-facing step flow is the reattachment length. The Boussinesq methods with the " k- ε " model underpredicted the reattachment length by about 20%. This is also true of one of the algebraic stress models and the full Reynolds-stress closure. However, the algebraic stress model used by Launder, Leschziner and Sindir (1982) employing a modified ε-equation in which curvature is taken into account, predicted the reattachment length and shear-stress levels satisfactorily. The reattachment region and downstream recovery were also computed adequately by Pletcher and Kwon (1982) who used an algebraically described length scale in the recovery region,

that was especially adapted to the backward-facing step. Almost all of the methods had difficulty in predicting the flow in the reattachment region and its downstream recovery, whereas the static pressure distribution was generally well predicted.

It is clear that field methods of the type used in the above calculations are the only promising ones for the prediction of recirculating flows. There are, however, difficulties to be overcome in relation to the turbulence model and discretization scheme and for the present case of heat exchanger flows the choice of discretization scheme and turbulence model require special consideration because of the geometrical and fluid-dynamic complexity of the flow. For example, it can be anticipated that the use of the hybrid central/upwind differencing scheme would require exceedingly fine grids for the simulation of the flow field and that a modification to the turbulence model may be required to account for the effects of streamline curvature.

3.2 Experimental arrangement

The first part of this section describes the experimental arrangement by considering the general flow configuration and the heat exchanger model, in subsection 3.2.1, and the laser Doppler anemometer and signal processing system in subsection 3.2.2. The measurement technique and the errors incurred in the measurements due to the geometric and optical set-ups are examined subsequently in subsection 3.2.3.

A more general description of the optical arrangement of the laser Doppler anemometer and the operational characteristics and performance evaluation of the fre-

quency counter used for the velocity measurements has already been presented in sections 2.2. and 2.3.

3.2.1 Flow configuration

The heat exchanger model was assembled in a closed-circuit water flow rig comprising three tanks, a pump and the necessary connecting piping as shown by figure 3.2.1. Water was pumped from the sump tank to the constant head tank and valves allowed the variation of the inlet head to the test section. The sump tank capacity was of the order of 10 m^3 and ensured negligible temperature rise over long operating periods without any consequent property changes. Aeration problems were removed by the incorporation of a flat gully to guide the water from the discharge tank to the sump tank.

The test-section, see figure 3.2.2, comprised a 74 mm $\pm$ 1.0 mm internal diameter (D_s) perspex pipe of 3 mm wall thickness and 475 mm length (about 6.5 D_s). A system of alternating and equi-spaced disc and doughnut baffles was connected and kept on axis by six 3 mm diameter brass rods. The connecting inlet and outlet pipes were of 54 mm diameter. Between the upstream diffuser-type expansion (45° transition angle) and downstream contraction (67° transition angle) two brass rings with three radial pylons were fixed and located the supporting rods, which were arranged in three sets of two, at 120 degrees separation, and at 4 mm and 15 mm radial positions from the pipe-wall. Each disc was screw-locked at the three inner rods and each doughnut at the outer three, hence minimising tube vibration effects. This arrangement allowed the variation of baffle spacing and diameter with respect to the pipe diameter and also permitted measurements of the three orthogonal velocity components.

Two different baffle-pitch geometries were examined corresponding to $1/D_s = 1$ (SET A) and $1/D_s = 0.5$ (SET B). The choice of disc and doughnut-hole diameter was the same for both sets of experiments and gave a disc-clearance to doughnut-hole area ratio of one: the blockage ratio for both was 53%. The distances before the first and after the last baffles were 1.5 D_s. The flow conditions, geometries and parameters investigated are tabulated in table 3.2.1. The chosen disc and doughnut cuts were 27% and 69% respectively, and they were in accordance with the information given in table 3.1.1.

3.2.2 Optical arrangement and signal processing

Velocity measurements were obtained with a laser Doppler anemometer in forward-scattered mode, mounted on a milling table which allowed movement of the optical components in three orthogonal directions. The heat exchanger model was immersed in a plane-walled, distilled water-filled trough to improve optical access and to minimise the effects of the different refractive indices between air, perspex and water. With this arrangement it was possible to obtain velocity measurements in the vertical plane, up to 0.8 D_s from the heat exchanger model wall.

The optical arrangement is shown in figure 3.2.1 and comprised a 5 mW He-Ne laser, a focussing lens (L_1), a rotating diffraction grating to provide beam-splitting and frequency shifting, a collimating lens (L_2) and an imaging lens (L_3) to focus the first order beams from the grating to form the measuring volume, a collection lens (L_4) and a photomultiplier (EMI 9558B) with a 0.3 mm pinhole diameter. The optical parameters are summarised in table 3.2.2.

RESULTS	GEOMETRICAL PARAMETERS				FLOW PARAMETERS				
	For all Measurements	D_s/l	N		Quantity Measured	$\bar{U}_{max}$ (ms^{-1})	U_b (ms^{-1})	Re_{bulk} x 10^{-4}	$\dot{m}$ (kg/s)
			Doughnut	Discs					
SET A	$(H_d/D_s)x100=27$	1	2	2	$P,\bar{U},\sqrt{\overline{u^2}}$ $\bar{V},\sqrt{\overline{v^2}},\sqrt{\overline{w^2}}$	1.026	0.619	4.55	3.57
	$(H_n/D_s)x100=69$				$P,\bar{U},\sqrt{\overline{u^2}}$	0.694	0.429	3.155	2.415
SET B	$d_d/2$ = 27 mm	2	4	4	$P,\bar{U},\sqrt{\overline{u^2}}$ $\bar{V},\sqrt{\overline{v^2}},\sqrt{\overline{w^2}}$	0.608	0.497	3.655	2.137
	$d_n/2$ = 11.6 mm				$P,\bar{U},\sqrt{\overline{u^2}}$	0.569	0.430	3.165	1.850
	l_i = 100 mm l_o^i = 118 mm (SET A) l_o^o = 65 mm (SET B)				$P,\bar{U},\sqrt{\overline{u^2}}$	0.476	0.341	2.54	1.465

Table 3.2.1: Operating conditions for heat exchanger model

Table 3.2.2: Optical parameters for heat exchanger flows

Specifications:	
Laser (Spectra-Physics Model 120):	5 mW He-Ne λ = 632.8 nm
Nominal Focal Length of Lenses:	L_1 = 150 mm (bi-convex) L_2 = 500 mm (plano-convex) L_3 = 100 mm (plano-convex) L_4 = 100 mm (bi-convex)
Radial Diffraction Grating (1st order beams, 57% light intensity conserved)	
Angle between 1st order beams:	1.52°
Frequency shift:	up to $\pm$ 2.5 MHz
No. of lines:	18,000
Long Term Stability:	0.3% of the local rms value
Short Term Stability	0.5%
Calculations (at $1/e^2$ intensity location)	
Beam Diameter at Focal Point:	0.313 mm
Measured Beam Intersection Half Angle:	8.027°
Fringe Volume Dimensions (in water): Width:	0.316 mm
Length:	1.410 mm
Fringe Spacing:	2.2657×10^{-3} mm
No. of Fringes (stationary disc):	140
Frequency Response Constant:	441.36 KHz/ms^{-1}

Two different signal processing systems were used. For SET A (with the baffle spacing of 1 D_s), the Doppler signal was high-pass filtered and demodulated by a Cambridge-Consultants frequency tracking demodulator. The tracking-range and slew-rate of the tracker limited measurement accuracy in regions of low-velocity and high turbulence intensity. The correct operating of the tracker was subject to the setting of the threshold level,the ability to accommodate both the magnitude (capture range) and rate of change (slew rate) in Doppler frequency from one burst to the next, and the drop-out rate. The amplitude of the signal at the input of the tracker was set so that it was larger than the noise level. In the absence of suitable signals the feedback loop was broken and the oscillator output held constant at the level of the last valid signal. A choice of high comparator level could result in cutting off the higher frequencies which correspond to lower amplitude signals, thus biasing the results. In zones of high turbulence intensity (above 40%) and large values of cross-flow velocity the capture range and slew rates of the tracker limited the accuracy of the measurements. The large range of frequency values encountered in such zones could not be accommodated within a preselected and fixed "tracking" range of the frequency tracker. High values of frequency shift could partially help to overcome the problem, by pushing the measured frequency to a higher frequency "tracking" range where a wider range of frequencies would be accommodated. The drop-out rate i.e. the ratio of processing time without signal to the total time was of the order of 2%, typical of water flows and well within the capabilities of the tracker.

The output of the tracker, a real time demodulation of the Doppler signal in voltage form, was further processed by a true-time integrator and an rms meter to pro-

vide values of mean and rms velocities respectively. The signal was integrated again to provide values of both quantities which were displayed in digital form.

The frequency counter used for SET B of the experimental program, where higher turbulence intensities were expected, was set to accept signals with a tolerance level of 0.2% between the first eight and sixteen cycles of each burst. The threshold level was set at about 15% of the maximum signal amplitude to ensure that no low amplitude signals were cut, thus avoiding the effects of amplitude bias, as explained in section 2.5. Graphical display of the variation of frequency with time, was used to check the suitability of the threshold level. The software allowed the calculation of ensemble-averaged values of mean and rms velocities, skewness and flatness factors, and probability density distributions. Sample collection was performed at a rate of one sample every 94 ms, which is a time scale longer than the particle arrival rate, which in turn was on average about 5 ms in the regions of positive velocity and about 70 ms in the recirculation zones. This minimised velocity bias effects.

3.2.3 Measuring technique and error estimates

Radial profiles of mean and rms values of axial, radial and azimuthal components of velocity were obtained at various axial stations behind each baffle and the system of coordinates is shown on figure 3.2.1, In the presentation of resuts, lengths are normalised with the test-section diameter and velocities with the inlet bulk velocity.

Constant mass flow rate through the test section was established by ensuring fixed pressure difference between the constant head tank and discharge tank. Values of mass

flow rate were obtained by integrating the velocity profiles upstream and downstream of the heat exchanger model and at 0.8 shell diameters upstream the first baffle. An average of the three values was accepted as the typical mass flow rate. The error incurred in the above calculation could be as high as 10%, whereas the stability of the outlet head was better than 0.3%. Reynolds numbers for each case examined are based on the bulk velocity, calculated by dividing the volumetric flow rate by the cross-sectional area of the heat-exchanger model.

The errors associated with Doppler broadening such as finite transit time broadening, mean velocity gradient broadening, turbulent velocity fluctuations broadening have been discussed in chapter 2. As explained in section 2.3.2, they stem from the incompatibility between the dimensions of the scattering volume and the length scale of the physical processes the fluid undergoes within it, and they result in a broader Doppler frequency probability distribution than that of the velocity, basically through an increase of the probability density function variance. Table 3.2.3 summarises these sources of broadening, the formulae used for estimating their magnitude and gives an estimate of their effect in the flows examined. In practice, no correction was applied to the measured results as the values reported in table 3.2.3 were sufficiently small to be neglected.

Table 3.2.4 summarises the effects that can arise from the processing of the Doppler bursts by analog (the frequency tracker) or digital (the counter) methods. Representative magnitudes of these effects are included in the table.

Maximum values of possible errors are given in table 3.2.5. With the frequency tracking demodulator and the comparatively low values of turbulence intensity, the

Table 3.2.3: Doppler-broadening effects

Error	Sensed in	Formula	Ref.	Magnitude
Velocity Gradient	Rms velocity	$\frac{\sigma_G^2}{\bar{f}_D^2} = \frac{dy^2}{U_o^2}\left(\frac{dU}{dy}\right)_o^2$	Melling (1975)	More significant near walls: $\sim 10^{-3} U_b^2$ and for V-velocities
Finite Transient Time Broadening	Rms velocity	$\sigma_F = f_D \cdot \frac{1}{2\sqrt{2\pi N_f}}$	Melling (1975)	0.15% U_b
(not applicable to counter)	"	$\sigma_F = \sqrt{\frac{U/2\pi}{2(b_x/4)}} \cdot \frac{\lambda}{2\sin\theta}$	George, Lumley (1973)	$\sqrt{2\times10^{-5}}\, U_b^2$
Velocity Fluctuation within measuring volume	Rms	Comparable to magnitude of mean velocity gradient or transit time broadening	Melling (1975)	$\sim 10^{-4} U_b$
Stability of Grating	Rms	Direct Measurement	-	0.3%

PROCESSING METHOD	ERROR SOURCE	IMPLICATION	MAGNITUDE
ANALOGUE: USE OF TRACKER	Tracker Output Transfer Function	In the conversion of voltage to Doppler Frequencies	Departure from linearity of tracker transfer function is negligible
		Accuracy of Voltage Output: 1% of full scale	Equal to $0.15U_b$ Removed by instrument calibration
	Voltage output of mean and rms meters/ Integration Time	In the averaging of voltages corresponding to Doppler frequencies	Random errors in mean-meter are ±1% of mean voltage measured Random errors in rms. meter have maximum values of 3% of smallest value in any one range of the unit
	Transfer Eqn.: $\bar{U} = \frac{\lambda}{2\sin\theta/2} \cdot \bar{f}_D$	In the conversion of Doppler Frequencies to velocities	Error in the measurement of half-angle: $\pm 0.3^o$
DIGITAL: USE COUNTER INTERFACED TO APPLE II	Counter Cycle Time (≃ 40μs) Microprocessor's Cycle Time (≃ 70μs)	In the discretization of a continuous random signal	26.1×10^{-6}% in local mean and 0.45% in local rms velocity
	Frequency Resolution	In the accuracy of Doppler frequency measurement due to the binary functioning of counter	0.196% of measured frequency (mean and rms)
	Signal validation	In the selection of Doppler bursts to be accepted for processing	0.2% difference in frequency between the first 8 and 16 Doppler cycles
	Sample size	In the confidence level for the construction of mean and rms values	For 10.000 samples and 95% confidence level Error in mean: < 1% of local value Error in rms: < 3% of local value
	Velocity Bias (Particle-rate arrival at control volume is proportional to the volumetric flux of fluid through the c.v.)	Biases measured velocites towards high mean values and lower variance. Can be removed (as in the present case) by slow sampling, i.e., when $\tau_s > \tau_i$, $\tau_s > \tau_t$, $\tau_t > \tau_i$ and $\tau_p << \tau_s$	τ_i (time scale of particle arrival rate) = 5 ms τ_t (time scale of energy containing turb. fluctuations) > 15ms τ_s (sampling time) ≃ 94 ms τ_p (residence time of particle in c.v.) > 11 μs

Table 3.2.4: Effects due to signal processing

maximum error in mean axial velocity, for example, did not exceed ± 1.5% of the maximum value. With the counter, the sampling was arranged to take place at a time scale longer than the particle arrival time scale and bias errors were negligible. As a consequence the maximum error in mean axial velocity was again less than 1.5% of the maximum value.

Table 3.2.5: Error estimates and corrections for heat exchanger flows

Quantity	Correction (due to curvature)	Maximum Systematic Error	Maximum Random Error
x	-No-	± 0.25 mm	± 0.02 mm
y	$y=y_{app}$ x1.3393 (U-comp)	± 0.25 mm	± 0.1 mm
	$y=y_{app}$ x1.2334 (w-comp)	± 0.25 mm	± 0.1 mm
z	no correction	± 0.5 mm	± 0.2 mm
$\overline{U}$	-No-	± 1.5%	± 0.8%
$\overline{V},\overline{W}$	-No-	± 2.5%	± 0.8%
$\overline{U}/U_b$	--	2.5%	± 1.5%
$\overline{u^2}$, $\overline{v^2}$, $\overline{w^2}$	--	3.5%	± 1.5%
m	--	10.0%	± 3.0%
C_p	--	3.0%	+ 1.5%

The passage of light through curved surfaces and media of different refractive index influenced the signal

strength and quality and necessitated corrections to the positioning of the control volume, as indicated in table 3.2.5. Errors due to finite transit time broadening (primarily relevant to analogue operation) mean velocity gradient broadening and velocity fluctuations within the measuring volume were estimated to be less than 10^{-3} U_b and no corrections were applied.

The pressure measurements were obtained with a U-tube water manometer connected to 0.5 mm pressure tappings at various axial locations on the top vertical wall - surface of the model. The wall pressure coefficient was calculated as $(p-p_{ref})/(1/2\rho U_b^2)$ where p_{ref} was the wall-static pressure at 0.8 D_s upstream the first baffle. The pressure tappings were blocked when pressure measurements were not in progress. They were also used for the removal of air-bubbles trapped in the re-circulation regions during the filling-up process of the heat exchanger model with water.

3.3 Results

In presenting the results the flow chracteristics at the entrance of the test section are first discussed. Pressure-coefficient distributions are presented for the three different Reynolds numbers and the two different baffle spacings investigated, according to the values tabulated in table 3.2.1. The mean and turbulence characteristics of the flow are then presented. A discussion of the implication of the results for heat exchangers follows in section 3.4.

3.3.1 Entrance flow characteristics

The length of pipe upstream of the test section ($16D_s$) gave rise to near fully-developed pipe-flow and the expansion upstream of the baffle arrangement caused the flow to separate from the upstream end. Symmetry tests were made with and without the baffles for values of Reynolds number equal to 4.5×10^4, 3.1×10^4 and 2×10^4 at different axial locations in the test-section. Comparison of the axial component measured at $0.54\ D_s$ after the expansion, figure 3.3.1, with and without baffles, revealed asymmetries which were always less than 2.5% of the local values. Near the wall, due to the presence of the first doughnut downstream, turbulence intensities increased by about 10% giving values around 35% (compared to 26% for the case without baffles and 16% for the fully-developed case, Schlichting, 1955). Asymmetries of about 5% of the local turbulence level are obvious in the region near the perspex wall and are associated with the deterioration of signal quality and, therefore measurement accuracy due to light refraction and dispersion as well as velocity gradient broadening.

The profiles of figure 3.3.2 obtained in the region before the baffles suggested that the length of the recirculation region downstream the expansion was less than $0.19\ D_s$. The development of the flow up to the first doughnut is affected by the Reynolds number as indicated in figure 3.3.2 and tends to become asymmetric for values less than $Re = 2 \times 10^4$. The convergence of the streamlines as the flow approaches the doughnut is faster for the lower Reynolds number due to the different reattachment lengths after the expansion for the two flows. Steep velocity gradients in the axial direction dominate the flow in the region close to the wall as the doughnut is approached. The increase of the centreline mean velo-

city with axial distance and the increase of local turbulence intensity near the wall indicate the developing nature of the flow and the local convergence of the streamlines in this region upstream of the baffles. Turbulence intensities, for $x/D_s = 0.946$, are highest in the axial direction, as shown in figure 3.3.3, with values around 35% and lowest in the radial direction, about 17%, with maximum differences occuring near the walls. At this location a radial mean velocity component with values around $0.05\ U_b$, was present with direction towards the centreline. Also, the absence of mean velocity variations in the azimuthal direction at $x/D_s = 0.946$ confirmed the axisymmetry of the flow and the absence of any circumferential periodicity and longitudinal vortices.

Attempts were made using flow visualization techniques to obtain an overall representation of the flowfield. Rapid turbulent mixing resulted to quick dispersion of the dyes (pottasium permaganate and fluorescein). The generation of hydrogen bubbles, via electrolysis and with the cathode fixed on the circumference of a disc or a doughnut, permitted a better flow-visualization. Nevertheless, and although no film or photographs were shot, the following were established via flow visualization:

- The supporting rods did not influence the flow or its symmetry locally. Only with baffle spacings less than $0.25\ D_s$ an influence could be observed in the region close to the wall.

- At the highest Reynolds number (4.55×10^4) and the longest baffle spacing examined, (i.e. $1\ D_s$), the baffle supporting rods could be seen to vibrate. The disturbance was successfully minimised by providing extra support upstream and downstream of the test-section without affecting the flow characteristics.

- The flows examined were axisymmetric. This was proved by turning the test-section upside down with the relative position of the supporting rods altered.

- At different Reynolds numbers, different flow patterns were observed between the first set of doughnut and disc and the subsequent ones. The recirculation zone features were similar beyond the second set of doughnut and disc. The mass of recirculating fluid behind the first doughnut decreased with increasing Reynolds number, whereas the shape of the recirculation bubbles behind the discs was not visually affected by an increase in Reynolds number. The same effect was observed when the size of the doughnuts was increased, resulting to an increased blockage. With this arrangement and at the highest Reynolds number, fluid could be seen to recirculate at the lee of both the discs and doughnuts.

- Decreasing the baffle spacing increased the observed length of recirculation zone behind the doughnuts whereas the recirculation behind the discs was again unaffected and extended upto the proceeding doughnut.

The above observations led to a decision of examining two flow situations of area blockage between doughnut/disc equal to one and with 4 and 8 baffles equispaced at one (SET A) and half (SET B) pipe diameters respectively.

3.3.2 Wall-pressure distributions

Variations of wall static pressure coefficient with axial distance are shown on figure 3.3.4. The dependence

of overall pressure drop between the first and last baffle on the geometry and Reynolds number is obvious and in agreement with the observations in the upstream flow. The presence of successive baffles results in abrupt changes in streamline curvature and boundary layer thickness due to the respective area changes with consequent effects on pressure gradients and wall friction. This action is indicated by strong pressure losses and little recovery behind each baffle. Hence, reducing the baffle spacing by 50% resulted to a 50% increase of the overall pressure drop between the first and last baffle. For SET A, increasing the Reynolds number decreased the overall pressure-drop, a direct result of frictional losses at the wall which is coincident with the different reattachment lengths of figure 3.3.5 and consequently pressure recoveries behind each baffle. For SET B the wall static pressure distribution is independent of the value of Reynolds number, indicating that the pressure distribution is strongly influenced by the geometrical configuration. For SET B, tubulence characteristics overcome the wall viscous effects and those of initial conditions.

The pattern of wall-static pressure distribution is similar for each doughnut-disc baffle set: after a slight increase in the static pressure coefficient before each doughnut, a result of the existing adverse pressure gradients near the wall due to the doughnut, a local minimum is reached at about half the reattachment length; this is also shown in figure 3.3.5. As local negative velocities decrease, the wall static pressure begins to recover and a local maximum occurs at the reattachment region, just before the following disc. The strong streamline curvature and high axial velocities in the gap near the wall due to the presence of the disc cause an abrupt drop in the local wall-static pressure which continues until the flow outside the disc-recirculation bubble ceases to accelerate after its maximum width. Re-

covery continues until the second doughnut is met by the flow, where the same pattern is repeated.

Attempts were made to calculate the pressure recovery behind each doughnut and disc using the "Borda-Carnot" pressure rise coefficient defined as:

$$C_{p_{B-C.}} \triangleq 2\ \alpha\ (1 - \alpha) \tag{3.1}$$

where α = area ratio between downstream and upstream sections of pipe, common to both doughnuts and discs. The maximum pressure drop behind any disc at the maximum recirculation bubble width could be estimated by:

$$\frac{p_{m,d} - p_o}{1/2\rho U_b^2} = \frac{1 - (1 - \alpha)^2}{(1 - (w^2/d_b^2))^2} \tag{3.2}$$

Similarly for a doughnut:

$$\frac{p_{m,D} - p_o}{1/2\rho U_b^2} = \frac{\alpha}{(1 - \alpha)^2} \tag{3.3}$$

where p_m = minimum wall pressure
p_o = wall pressure in the plane containing the trailing edge of the baffle
w = maximum width of recirculation bubble (for values see table 3.3.1)

The calculated maximum pressure drops behind the first and second doughnut and disc of SET B are shown in figure 3.3.4 together with the experimental results. The differences in magnitude between the calculated and measured values are the result of frictional losses and confinement, for which there is no allowance in the theoretical calculation of the Borda-Carnot pressure rise coefficient.

The results of Crabb et al (1978), indicated about 75% recovery of the pressure lost behind a two-dimensional rib with a thin-upstream boundary layer Kim et al (1978) showed that the pressure recovery behind a step is a function of downstream channel length. Evidence was given of the existence of streamline vortices in reattaching high speed flows, by Ginoux (1969), and Bradshaw (1976), which have an effect on the wall static pressure distribution. In his measurements behind a single disc, Taylor (1981) found that about one third of the possible recovery is lost due to friction and velocity and pressure fluctuations In this case of multiple baffles, the recovery was nearly complete behind each disc and can be due to the adverse pressure gradients on the flow-facing side of the following doughnut. Behind the first doughnut pressure recovery was about 50% and this value dropped by 25% for each subsequent doughnut, as a result of wall friction and velocity fluctuations.

3.3.3 Velocity characteristics

The magnitude and direction of the mean velocity is indicated on the vector plots of figure 3.3.5 for the baffle spacings of SET A and SET B and are based on the measured mean axial and radial velocity components. The influence of each baffle extends upstream and downstream of its boundaries. The parabolic-type profile, see figure 3.3.2, from upstream the first doughnut is distorted as fluid from the near wall region moves towards and into the gap created by the first doughnut. This action is indicated by an inclination of the velocity vectors in the centreline region around the doughnut, towards the centreline Immediately downstream of the first doughnut the separation region initiated at the gap edge bows towards the centreline, squeezes further the mainstream flow downstream of the gap and hence yields the increase

in the magnitude of the axial velocities measured in this region and shown in figures 3.3.6 and 3.3.7. The reverse flow region behind each doughnut is constrained by the shear layer flow which is directed towards the wall due to the presence of the following disc. Its influence is indicated by a deformation of the wall recirculation zone, which becomes thinner and elongated and in the case of SET B, with the smaller baffle spacing, extends practically upto the following disc. Maximum local axial and radial velocities lie close to the tip of the disc, as shown by the profiles at x/D_s = 0.88 and 0.81 behind each doughnut and upstream of each disc in figures 3.3.6 and 3.3.7, for SET A and SET B respectively, and are consistent with the domination of the upstream flow by pressure gradients. The reattachment length increased between the first and subsequent doughnuts and this is the direct consequence of the recirculation bubble at the trailing edge of the preceding disc extending into the gap of the following doughnut. The local maximum axial velocity is removed from the symmetry axis and, as indicated by the radial velocity profiles of figure 3.3.7, at x/D_s = 0.04 the corresponding mass is entrained by the preceding recirculation zone. The axial velocity profiles for SET A (figure 3.3.6) and SET B (figure 3.3.7) show a deceleration of the fluid closest to the centreline as the lee of each disc is approached accompanied by the corresponding acceleration towards the annulus created by the disc and the confining wall. Immediately downstream of the discs, the local maximum forward velocity is to be found very close to the confining wall, and this remains so upto the next doughnut.

The recirculation length and width and the corresponding mass flow rate in the recirculation zone behind each doughnut and disc is tabulated in table 3.3.1. On average, the reverse mass flow rate behind each doughnut is about 0.07 of the total mass flow rate, based on bulk

velocity and of the same order of magnitude as for the single step-expansions of Smyth (1979b), indicating that the strength of the reverse flow is not strongly influenced by the neighbouring baffles. The same is not true for the strength of reverse flow behind the discs. As indicated on table 3.3.1 and by the vector plots and also the centreline profiles of figures 3.3.15 and 3.3.16 for SET A and SET B respectively, the recirculation region behind each disc extends to 1.24 d_d and 0.7 d_d for SET A and SET B respectively, in both cases much shorter than the length of recirculation of 2.2 d_d measured behind a single disc by Taylor (1981). The wake, especially for SET B, shows no tendency towards a pipe flow because of the confinement imposed by the following doughnut. Correspondingly the width of the recirculation bubble (0.63 d_d at half the recirculation length) is more than that measured for a single disc (0.55 d_d Taylor). The magnitude of the recirculating mass flow is doubled between the first and second disc of SET B, and is about ten times more than that for a single disc again as a consequence of confinement and blockage (table 3 3.1).

Inspection of the radial velocity profiles, figures 3.3.6 and 3.3.7, shows that for both sets of measurements the initial magnitude of the radial velocity is only 15% of the local axial velocity, indicating the relatively small streamline curvature immediately downstream the first doughnut. Between the first doughnut and following disc the radial velocities increase by 100% and peak values of 1.5 $\overline{U}$ are reached at the tip of the following disc. For subsequent doughnut-disc sets this value is lower, as a result of flow adjustment to the geometry requirements. For the second doughnut radial velocities attain values of about 21% of the corresponding local axial velocity, a magnitude which is only 33% of the value the same component had just upstream of the dough-

nut. This is an effect of the preceding disc. High values of the radial velocities are retained immediately downstream each disc, with magnitudes of the order of 30% of the local maximum annular velocity. This is comparable with the magnitude of the radial velocity component at the trailing edge of a single disc, as measured by Taylor (28% of the local maximum annular velocity) taking into account the differences in blockage. The component decays as the next doughnut is approached and changes direction at $x/D_s = 0.27$, indicating that entrainment to the recirculation region is dominating.

Reducing the baffle spacing by half resulted to relatively longer recirculation lengths when normalised with the baffle-spacing. In abolute terms the amount of the reverse flow per unit width behind each disc was not affected, whereas it was doubled for each doughnut. As expected, and shown on figures 3.3.8 and 3.3.9 the adjustment of turbulence properties to the geometrical changes is more pronounced. Measurements of azimuthal velocity showed that for SET A no mean velocity component, obviously within the experimental error, was present in the azimuthal direction. For SET B, and after the second disc, a "swirling" component was generated, probably as a result of confinement coupled with small geometrical asymmetries that got amplified. As can be seen in figures 3.3.10 and 3.3.11, which compare the mean and rms velocity components at the same axial stations behind the four doughnuts and four discs of SET B, the magnitude of this component was not such as to influence the general flow characteristics. Similar profiles behind the doughnuts of SET A are shown in figures 3.3.12 and 3.3.13 for two axial locations. Between the first and second doughnut, turbulence quantities on the centreline are increased by about four times in the same manner as for SET B (figure 3.3.10) a consequence of geometrical configuration as will be discussed in section 3.4.2. Near

the wall the relative increase in normal stresses between the first and second doughnuts is between 30% to 50% of the previous local values, for both SET A and SET B. Figure 3.3.14 presents similarity profiles for the lower Reynolds number of SET A. The trends are essentially the same as before, as this is also confirmed by the centre-line axial velocity profiles of figure 3.3.15. Although the wall static pressure distribution for SET A was found to be dependent on the value of the Reynolds number and upstream flow conditions, the similarity profiles indicate that the friction effects, important near the wall, are not sensed in the mainstream region.

The normalised rms of velocity fluctuations behind the first and second doughnuts of SET A resemble that of a single backward facing step as described in section 3.1.2 with peak values in the axial direction, lying close to the dividing streamline increasing with downstream distance and approaching their maxima just before the reattachment region, thereafter the peak values decrease and move towards the centreline region. Between the first and second doughnut-disc sets rms values increase by about 25%. Table 3.3.1 summarizes the trends in the three normal stresses by tabulation of their values on the centreline, and also of the maximum velocity fluctuations, which occured near the walls. In general, for SET A, the $\sqrt{\overline{u^2}}$ component has the greatest magnitude and $\sqrt{\overline{v^2}}$ the least. After reattachment, where the longitudinal rate of strain is higher and because of the confinement imposed by the following disc, $\sqrt{\overline{v^2}}$ increases while $\sqrt{\overline{u^2}}$ and $\sqrt{\overline{w^2}}$ decrease.

Inspection of similar profiles for SET B (figure 3.3.11) shows that peak values are still to be found close to the dividing streamline but, because reattachment occurs just upstream of the following disc, they decrease with downstream distance and remain close to the

	Geometry	Baffle-spacing	Blockage ($\%D_s$)	Re_b $\times 10^{-4}$	$\bar{U}_{max}$	Max. rms. fluctuations $\sqrt{\overline{u^2}}/U_b$	Max. rms. fluctuations $\sqrt{\overline{v^2}}/U_b$	Max. rms. fluctuations $\sqrt{\overline{w^2}}/U_b$	Centre line $\sqrt{\overline{u^2}}/U_b$	Centre line Max. $\sqrt{\overline{w^2}}/U_b$	Recirculation Length	Recirculation Width*	$\frac{\dot{m}_r}{\dot{m}_b}$	$\frac{\dot{m}_r}{\dot{m}_{total}}$
SET B	1st doughnut	0.5 D_s	31	3.65	0.608	0.50	0.55	0.50	0.12	0.1	2.39S	0.605S	0.071	0.666
	2nd doughnut	"	"			0.75	0.80	0.60	0.47	0.45	3.13S	0.640S	0.113	0.101
	3rd doughnut	"	"			0.75	0.60	0.60	0.54	0.60	"	"		
	4th doughnut	"	"			0.75	0.60	0.60	0.54	0.60	"	"		
	1st disc	"	73	3.65	0.608	0.57	0.57	0.60	0.47	0.50	$0.678d_d$	$0.60d_d$	0.563	0.360
	2nd disc	"	"			0.78	0.72	0.75	0.54	0.80	$0.706d_d$	$0.65d_d$	1.08	0.519
	3rd disc	"	"			0.78	0.75	0.75	0.50	0.80	"	"	-	-
	4th disc	"	"			0.78	0.75	0.75	0.50	0.80	"	"	-	-
SET A	1st doughnut	1.0 D_s	31	4.55	1.026	0.60	0.39	0.45	0.14	0.10	4.13S	0.603S	0.047	0.0449
	2nd doughnut	"	"			0.78	0.55	0.55	0.40	0.55	-	-	-	-
	1st disc	"	73			0.72	0.60	0.85	0.40	0.60	$1.238d_d$	$0.60d_d$	1.0	0.516
	2nd disc	"	"			0.72	0.70	0.70	0.40	0.60	-	-	-	-
	Single disc Taylor (1980)	-	50%	6	1.62	0.36	0.26	0.36	0.15	0.06	2.20d	0.55d	0.12	-
	Smyth R. (1979) Sudden expansion	-	Expansion Ratio: 1.5	3	$\frac{0.78}{\bar{U}_b} = 0.67$ m/s	0.195	0.135	0.13	0.06	0.04	9S	0.75S	0.08	-

* Recirculation zone width measured at half recirculation length.

d_d = disc diameter

S = step or doughnut height

Table 3.3.1: Summary of quantitative findings for heat exchanger flows

wall. These peak values remain downstream the disc and a second peak in the profiles is associated with the recirculation bubble of the disc. For this second case, SET B, all three normal stresses have a similar magnitude and the near-wall rms values are increased by 50% between the first and second doughnuts. The history of the upstream flow is still evident after the second doughnut as indicated by the second peak in the rms profiles.

The above trends are consistent with the pattern of the measured wall pressure distribution and confirm that geometry effects predominate the flow pattern, particularly for SET B. In both cases, the centreline rms values of figures 3.3.15 and 3.3.16 are increased by about four times between the first and second doughnut and suggest that the disc-blockage imposes length-scales of the same magnitude as the annular gap and considerably smaller than the upstream length scales imposed by the doughnut. The development of normal stresses behind the discs for SET A resembles that of a single disc and there is not a significant increase in turbulence quantities between the first and second disc. The $\sqrt{\overline{v}^2}$ and $\sqrt{\overline{w}^2}$ values close to the centreline increase upto the rear stagnation point. As expected, $\sqrt{\overline{u}^2}$ and $\sqrt{\overline{w}^2}$ retain their highest values near the wall and $\sqrt{\overline{v}^2}$ the least.

For SET B, the maxima of the rms fluctuations do not move away from the wall, and the development of all three components is similar. The recirculation bubbles behind the discs are regions of intense turbulence generation and this is expressed through increase of the centreline $\sqrt{\overline{u}^2}$ values upto the next doughnut.

The values of normal stresses measured in the heat exchanger model are, in general, more than double the corresponding values for single discs or step-expansions as indicated in table 3.3.1.

The breaking up of larger eddy structures and the forced existence of small-scale and short-lived turbulence due to the imposition of length-scales, compatible with the size of the annular gap left by the discs, together with the axial velocity gradients, are responsible for the achievement of similarity in mean and turbulent flow quantitites, indicated by the drastic changes between the first and subsequent doughnuts (figure 3.3.10) and discs (figure 3.3.11). The passage of the flow through the second doughnut establishes similarity in turbulence quantities, whereas full similarity in mean quantities is only achieved after the second doughnut.

3.4 Discussion

3.4.1 Effect of baffle-spacing and Reynolds number

The initial conditions, such as the upstream velocity distribution, turbulence level, boundary layer thickness and Reynolds number are among the factors that could influence the size of the recirculation zone behind the doughnuts and discs. As has been shown, the dependence of the flow pattern in the heat exchanger model on the initial conditions disappeared after the second set of baffles and increasing the confinement removed the dependence of the flow on the initial turbulence intensity and Reynolds number. To study the effect of three-dimensional inlet conditions, Vafidis (1982) inserted a partial blockage upstream the first doughnut. The flow conditions and experimental set-up remained the same as for the present investigation. His results confirmed that symmetry recovered after the first disc and similarity in mean and turbulent quantities was achieved after the second disc.

Results over multiple two-dimensional ribs, see for

example Sami and Liu (1977), indicated that the reattachment length depends on the Reynolds number for turbulent flow with rib-height of the order of the boundary layer thickness. This explains the dependence of the reattachment length behind the first doughnut on Reynolds number measured for SET A, and the corresponding effect observed in the pressure distribution. The centreline profiles figure 3.3.15, show no obvious dependence on Reynolds number and thus support the argument that, this dependence is localized and is concentrated on the near wall region. Reducing the baffle spacing by half caused the reattachment lengths behind the doughnuts to extend upto the following discs and in conjunction with the increased turbulent mixing alleviated the dependence of the flow on the Reynolds number. With the Reynolds number defined as the ratio of largest to smallest length scales existing in the flow, and taking into account the breaking-up of larger length scales after the discs, the removal of this dependence can be possibly explained.

It has been shown that reducing the baffle spacing by half reduces in absolute terms, the recirculation length behind the doughnuts and discs to approximately half their initial value. Normalization of the recirculation lengths with the doughnut-step height and disc diameter respectively indicates that the respective lengths became longer with the increased confinement. Also, the reverse mass flow rate per unit width behind each doughnut was reduced whereas the opposite is true for the mass flow rate behind the discs. Comparison to the same quantity for single steps and discs shows that the amount of recirculating fluid per unit width behind a disc in this complex geometry is about ten times more than that for a single disc. For the doughnuts this quantity is the same as for single step-expansions. Reduction of the baffle spacing increased in overall the vector angles. The smaller disturbance of the radial profiles of axial velo-

city for SET A have their counterpart in the smaller values of radial velocity and the opposite is true for SET B.

From the above and as it has been suggested by flow-visualization, it can be anticipated that the blockage imposed by the doughnut is not the determining factor for the achievement of similarity in the flow properties, in contrast to the blockage imposed by the disc. It can be expected that increasing the diameter of the discs would also increase the turbulent transport behind them and could also affect the similarity in the flow.

Increasing confinement further by a reduction of the baffle spacing, would obviously affect the turbulence field, but would not have an apparent effect on the similarity of the flow profiles, as there must be a minimum number of baffle-sets required by the flow to readjust itself, as this was the case with the baffle spacing of SET B. A geometry modification that could speed up the achievement of similarity in the flow pattern is the interchange of the baffle order, i.e. first a disc and then a doughnut: this would have as a direct result the increase in turbulence quantities, similar to the pattern measured for SET B, and the faster rearrangement of the mean velocity flowfield.

3.4.2 Tendency to similarity of the flow

Turbulence quantities are important in that they are the primary agent for the readjustment and diffusion processes that occur in the flow. Small-scale and therefore short-lived turbulence exists near the wall and can make more rapid adjustments to changing conditions. Among the infinite number of characteristic turbulent length scales that can exist in the complex flow with multiple disc and

doughnut baffles three can be considered as characteristic length-scales, representative of the structural changes undergone by the flow. Large and energetic eddies of size comparable to the model diameter, D_s, are dominant in the part of the flow upstream of the first doughnut and near the centre-line region. They are carried downstreeam of the first doughnut into the reattachment region. As indicated by Bradshaw and Wong (1972) the large eddies in this region are broken up and that results in a significant decrease of the turbulent length scales downstream. The following disc restricts the size of the eddies to the diameter of the annular gap and imposes length-scales of this size. By definition, the existence of smaller length scales implies a higher dissipation rate which cannot be exclusively responsible for the increase in turbulence level measured downstream of the first disc (figures 3.3.8 and 3.3.9) unless, this is accompanied by an even higher production rate. This suggests the existence of an additional mechanism, possibly vortex stretching or production, indicated also by the axial velocity gradients and which could increase turbulence quantities. It becomes obvious that the processes involved are too complex to be fully understood. The passage of the flow through the second doughnut establishes similarity in the turbulence quantities (see figure 3.3.10) whereas similarity in the mean quantities is achieved after the second disc (figure 3.3.11). Thus, modification of the turbulence field preceded that of the mean flow, and had the same trends for all three velocity components.

3.4.3 Implications for heat exchanger design

The successful design of a heat exchanger requires knowledge of the relationships between pressure drop, heat transfer and fluid flow disrtibution. It is known

that interrupting the shell-side flow path with "doughnuts" results in an overall increase in the average heat-transfer coefficient because of the successive thermal boundary layer restartings after each doughnut. The turbulence induced by the blockage of the disc should further increase the heat transfer coefficient, but at the expense of a greater pressure drop as has been shown by the pressure measurements. The increased pressure drop and turbulent mixing measured here and also the dependence of pressure drop on Reynolds number, even for values as high as 3×10^4, suggest that disc-and-doughnut arrangements could be effectively used in types of heat exchangers where a good proportion of axial flow is desired on the shell-side, where the plant performance is sensitive to pressure drop and where the overall heat-transfer coefficient is insensitive to the tube-liquid heat transfer coefficient and depends primarily on the heat-transfer coefficient of the shell-side. This situation is common in liquid-to-liquid shell and tube heat exchangers. For instance, when an organic liquid having relatively poor heat transfer properties is heated or cooled by water which has much better heat transfer properties. In heat exchangers of this sort, the water usually flows through the tubes and the organic fluid on the shell-side. The temperature drop through the tube wall is ordinarily quite small.

The arguments of the previous two subsections were based on the velocity and pressure characteristics of the shell-side flow and, the inclusion of the tube bundle, and axial leakage through the clearance between the baffles and the shell will drastically affect the pressure drop and turbulent mixing along the model geometry. These geometrical modifications can form the basis for a future experimental investigation.

The many parameters involved in the design of shell

and tube heat exchangers make it extremely difficult to obtain an analytical solution that will give the desired combination of characteristics. Empirical relations are mostly used with a "cut-and-try" approach that depends on the designer's judgement and experience for convergence on a new design by extrapolation from tested units. Geometrical and fluid property similarity between the model - or tested unit - and the desired situation is essential in order to allow calculation of the pressure drop and heat transfer coefficient in a real exchanger from a given geometrical model configuration and given mass flow rates and inlet temperatures It is obvious that "computer" methods, such as the solution of the flowfield with two-dimensional or three-dimensional finite difference approaches, such as those developed by Patankar et al (1974, 1980), and referred to in the introduction of this thesis, allow accurate and fast solutions, parametric variations and easy geometrical modifications.

The field methods used for the prediction of the flowfield past single baffles can be extended for the prediction of the shell-side flow in heat exchangers. The mathematical model of turbulence must now account for both the turbulent stress and heat-flux fields, which necessarily will reduce the solution accuracy. As has been indicated in section 3.2.1, use of the "$k-\varepsilon$" model of turbulence, see Taylor (1981), even with allowance for the effect of streamline curvature, Leschziner and Rodi (1981) underpredict the recirculation length and flow recovery behind single baffles. Apart from the turbulence model, truncation errors due to the discretization scheme, and uncertainties in the boundary conditions are responsible for the discrepancies between experimental and computed data. For heat exchanger flows, where turbulent transport is responsible for the heat transfer performance of the unit, the defects in the prediction of the turbulent field become extremely important.

In the two equation turbulence model the eddy viscosity is used to characterise turbulence using two scalars, k and ε. It is obvious that assumptions involved in the modelling of transport equations for k and ε, and also the applicability of a scalar effective viscocity hypothesis in a flow where multiple length scales exist limit the performance of the turbulence model. The suggested imbalances between production and dissipation between a doughnut and the following disc, the rapid mean flow changes and the imposition of turbulent length scales compatible to the geometry requirements may restrict the performance of the two-equation model and should require changes in the turbulence model to account for the effects of streamline curvature. A higher order turbulence model, such as the Reynolds stress model where modelled transport equations for all Reynolds stresses as well as for ε are solved, is essentially free from the physical limitations of the two-equation model, and should theoretically behave better in a complex turbulent flow. Nevertheless, in view of the pressure domination of the flow in disc and doughnut arrangements it can be anticipated that a higher order turbulence model will offer no extra advantage to the two-equation model with the inclusion of the effects of streamline curvature and will involve extra storing and computational costs. Previously reported calculations in flows past two-dimensional obstacles and fences, Durst and Rastogi (1980), have shown that numerical meshes of the order of 28 (streamwise) x 34 (radial) nodes were required to resolve the flowfield adequately. Leschziner and Rodi (1981), performed their computations in an annular jet with a mesh consisting of 38 x 37 non-uniformly distributed grid lines with 21 x 16 uniformly distributed nodes located within the recirculation zone. Finer grids were not used because of computer storage and time-limitations. Taylor (1981) in his calculations required a 36 x 36 non-uniformly distributed grid to minimize truncation

errors in the numerical scheme. Castro, Cliffe and Norgett (1981) indicated the sensitivity of the predicted value of reattachment length past a thin fence on the grid refinement and distribution upstream of the fence. Since the upwind-differencing representation of convection involves a truncation error proportional to the grid spacing, the reduction of this error is related to the grid distribution and refinement.

The above examples illustrate that for the flow in a heat exchanger model, which involves multiple boundaries, a large number of grid nodes, probably twice as many as for a single baffle, will be required to resolve the flow field adequately and inevitably this will create storage and cost problems. Most probably this is the main limitation which can hinder accurate numerical solution. The inclusion of a higher order discretization scheme, such as the ones proposed by Leonard (1979) or Raithby (1976), reduces the number of grid nodes required, but simultaneously increases the computer storage and introduces the possibility of numerical overshoots in the boundaries.

Whatever the chosen computational approach, the results of this chapter describe, in careful detail, the inlet flow conditions and the flow close to the baffle tips, and can be used as boundary conditions for any calculation procedure. Even with the existing discrepancies between experimental and predicted results, the level of accuracy achieved with computational approaches of the kind described above is sufficient for most practical applications. For example, an error of 19% in the predicted recirculation length may be unacceptably large for many aerodynamic problems, but to predict the level of heat-transfer coefficient to that degree of accuracy would suffice for most real heat exchanger situations.

3.5 Concluding remarks

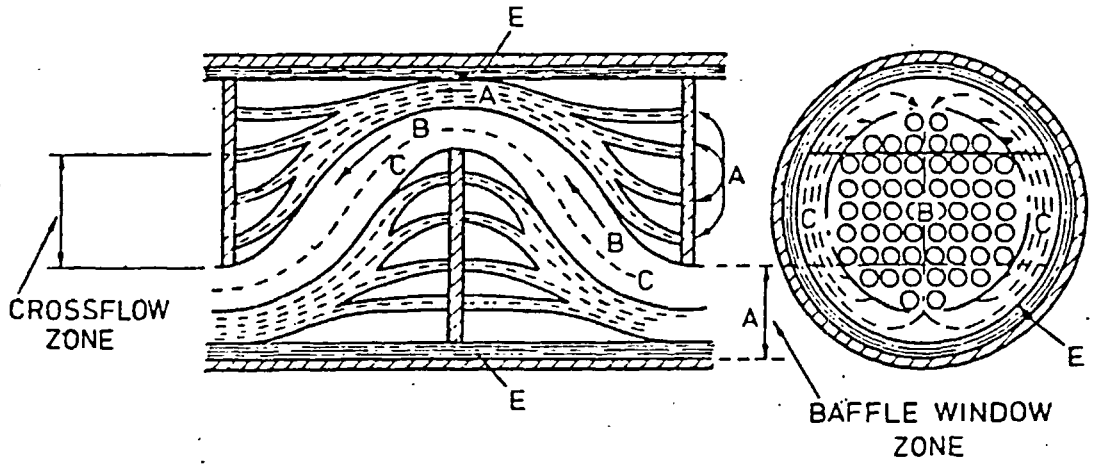
The experimental results revealed that the flow past multiple doughnut-and-disc shaped baffles is dominated by pressure gradients associated with the strong streamline curvature. Increasing the flow confinement, by reducing the baffle spacing, removes the dependence of the flow to the initial turbulence intensity level and Reynolds number and increases the overall pressure drop. The effects of flow confinement are more obvious in the turbulent field. The pressure drop and recovery behind each baffle follows the same general pattern as for similar shape single baffles, but with quantitative differences. Although similarity in both mean and turbulence quantities is achieved after the second set of baffles the wall pressure distribution does not follow the same trend and continues its overall monotonic drop indicating that wall-friction effects dominate the near-wall flow region.

The passage of the flow around the discs results in the imposition of turbulent length scales compatible with the annular gap. Production processes involved, result to an increase of turbulence quantities by about four times and similarity of the flow is achieved after the second set of doughnut-disc baffles. It can be anticipated that smaller blockage may delay the achievement of similarity of the flow. The recirculation zone behind each disc extended to the following doughnut. The separation regions behind the doughnuts were deformed and forced to exist within the shear layer flow pattern determined by the geometrical arrangement.

The results provide a basis to assist the development and appraisal of calculation methods for flows dominated by steep pressure gradients and where geometrical parameters characterise the flow development. The strong

streamline curvature can introduce problems associated with the numerical algorithm and, in view of the extent of pressure control, the characteristics of the turbulence model may not be relevant: namely a two-equation model may perform equally well as higher order approaches.

The extended recirculation regions behind the baffles emphasise the need for investigation of local heat-transfer characteristics, in order to help quantify and explain the heat transfer efficiency and its relationship to geometrical configuration.



A-stream: Tube-baffle leakage flow

B-stream: Cross-flow between baffles

C-stream: Bundle-shell bypass flow

E-stream: Baffle-shell leakage flow

Figure 3.1.1 : Diagram of fluid streams on the shell-side of a segmentally baffled heat exchanger (Tinker,1951)

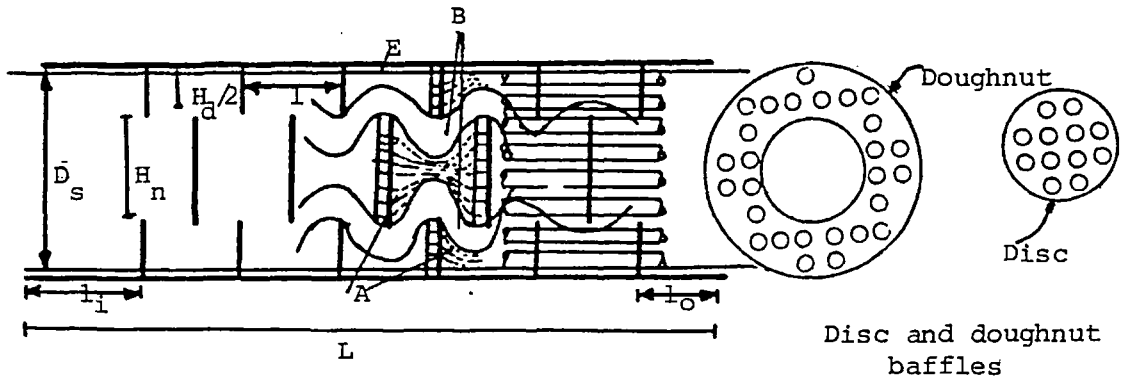


Figure 3.1.2 : Typical arrangement of disc and doughnut baffles in a shell and tube heat exchanger.

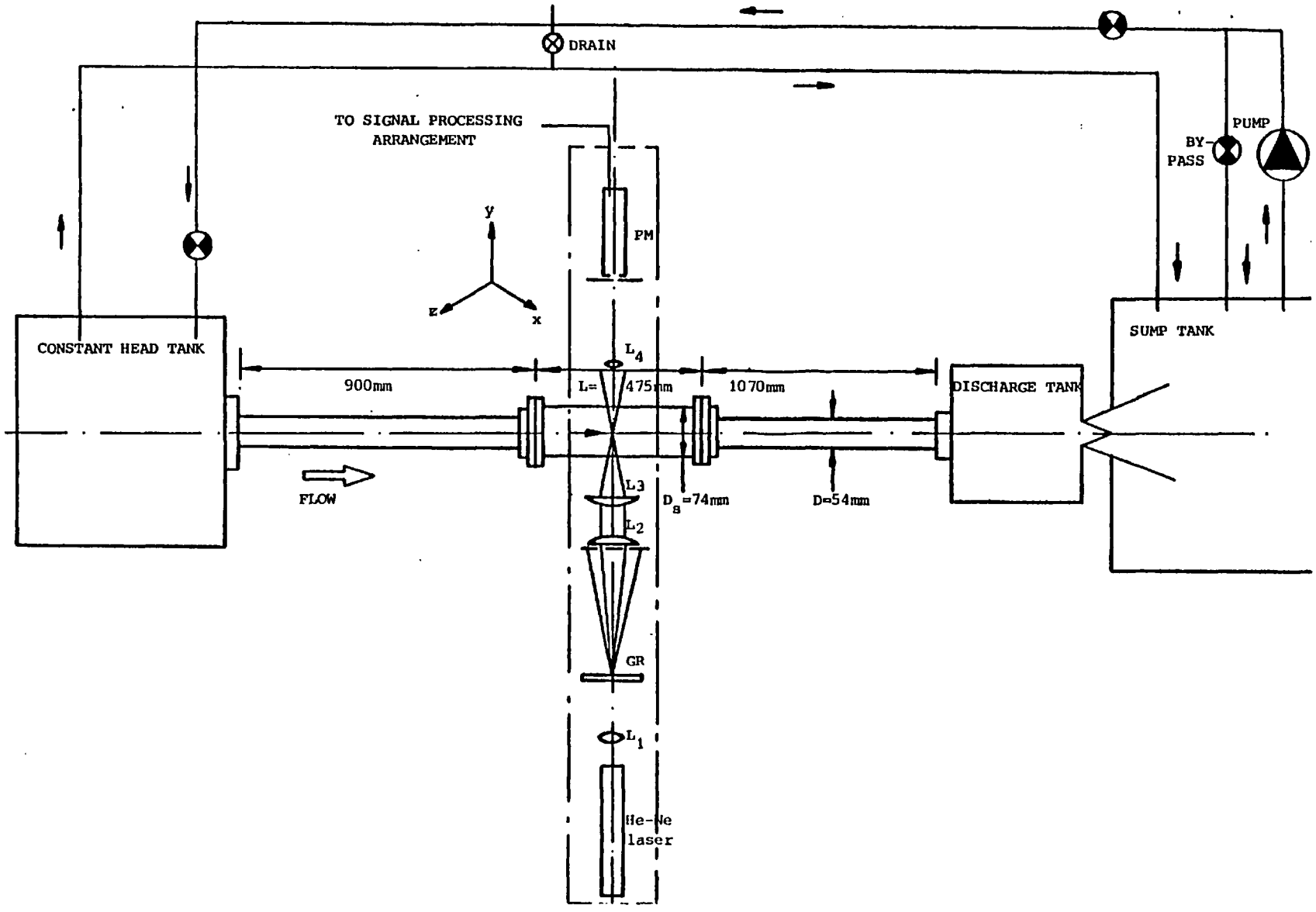


Figure 3.2.1 : Water flow rig and optical arrangement

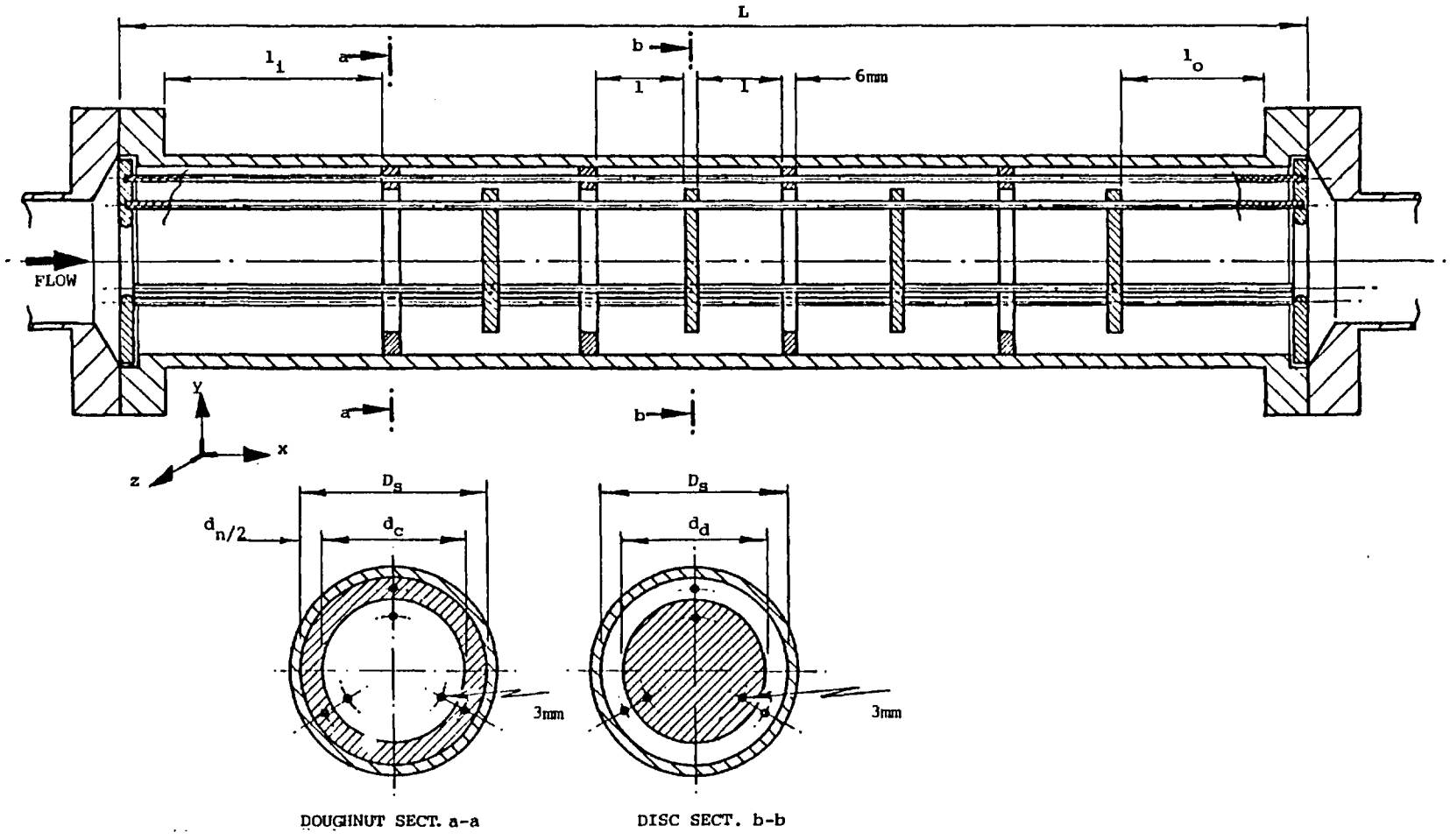


Figure 3.2.2 : Heat exchanger model.

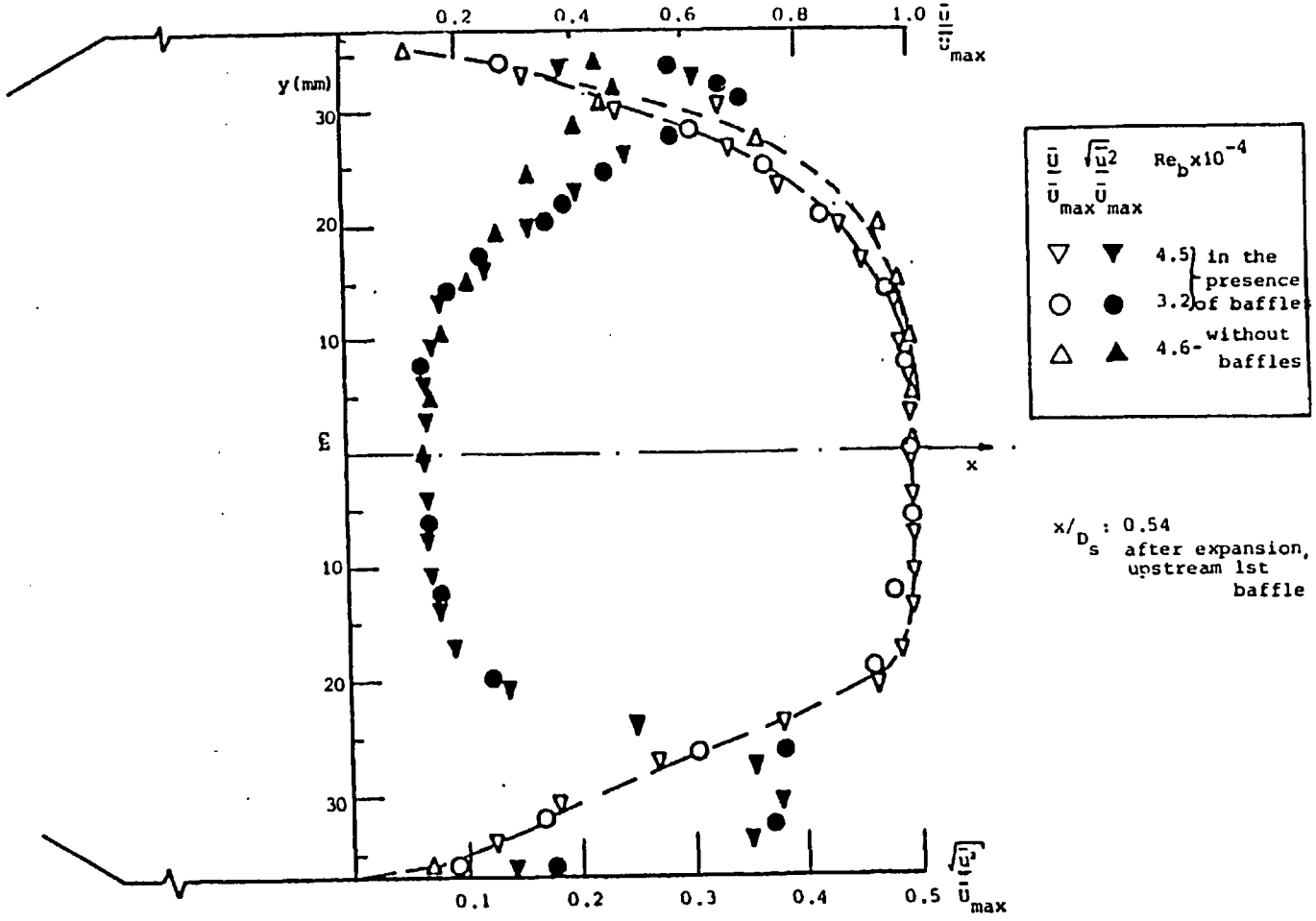


Figure 3.3.1. : Symmetry tests upstream of first baffle.

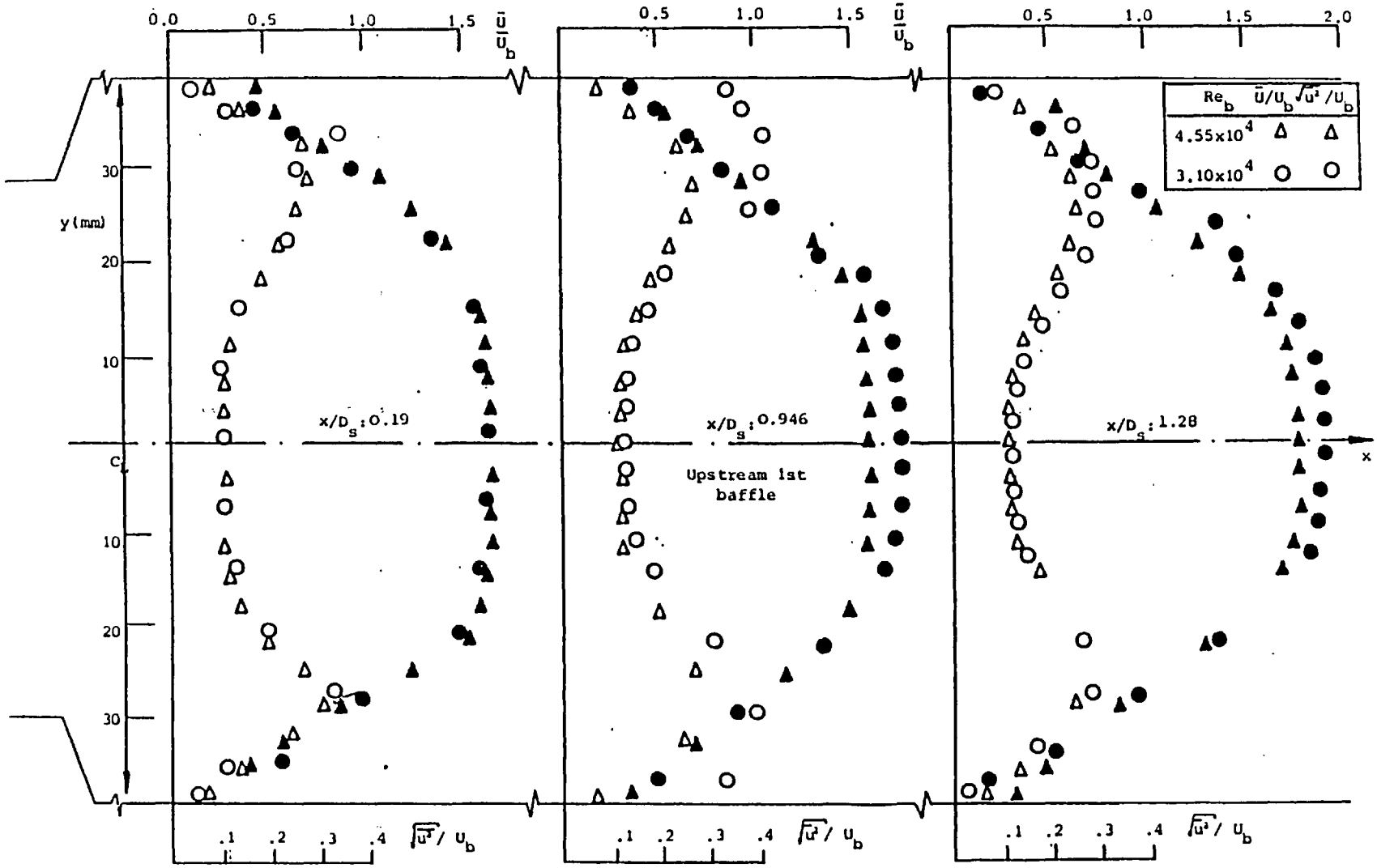


Figure 3.3.2. : Symmetry tests upstream of first baffle.

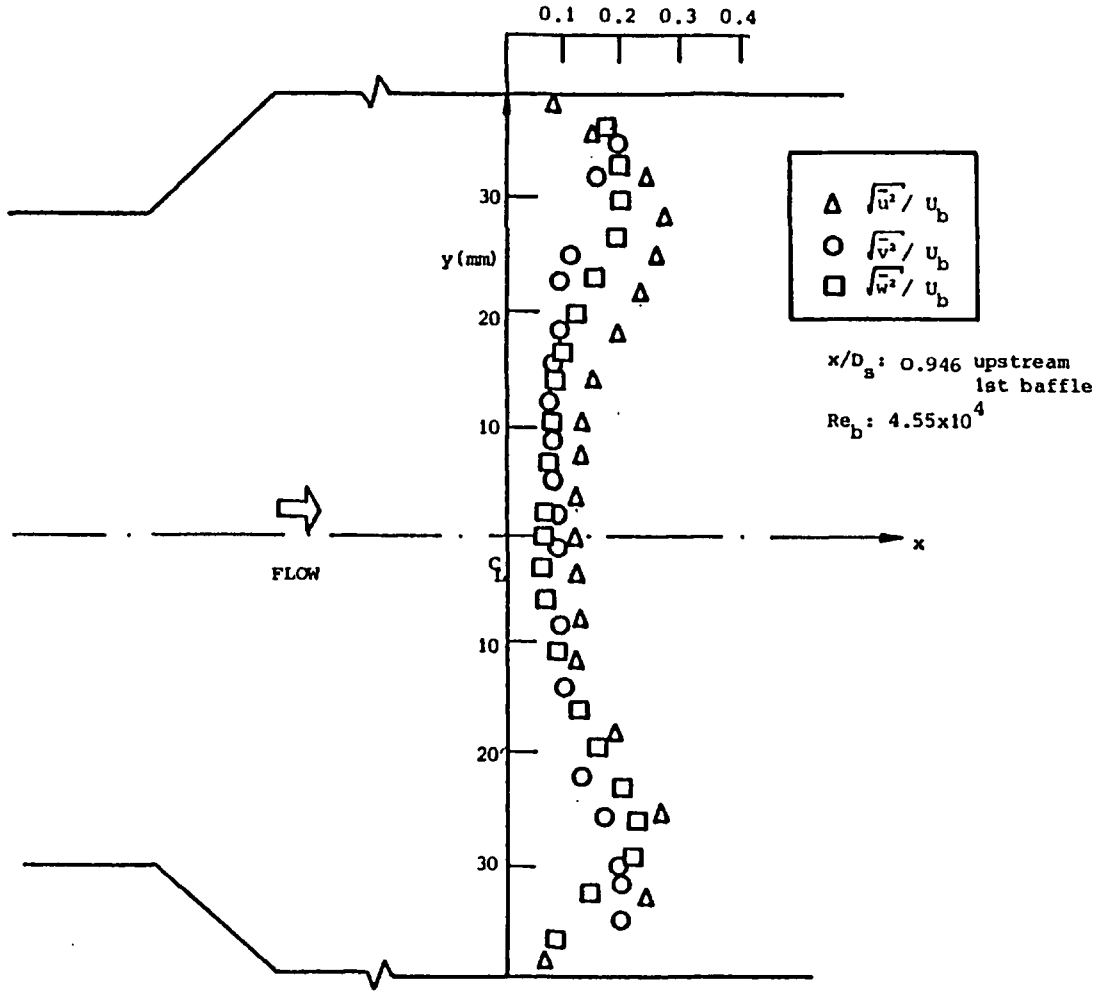


Figure 3.3.3. : Symmetry tests upstream of first baffle.

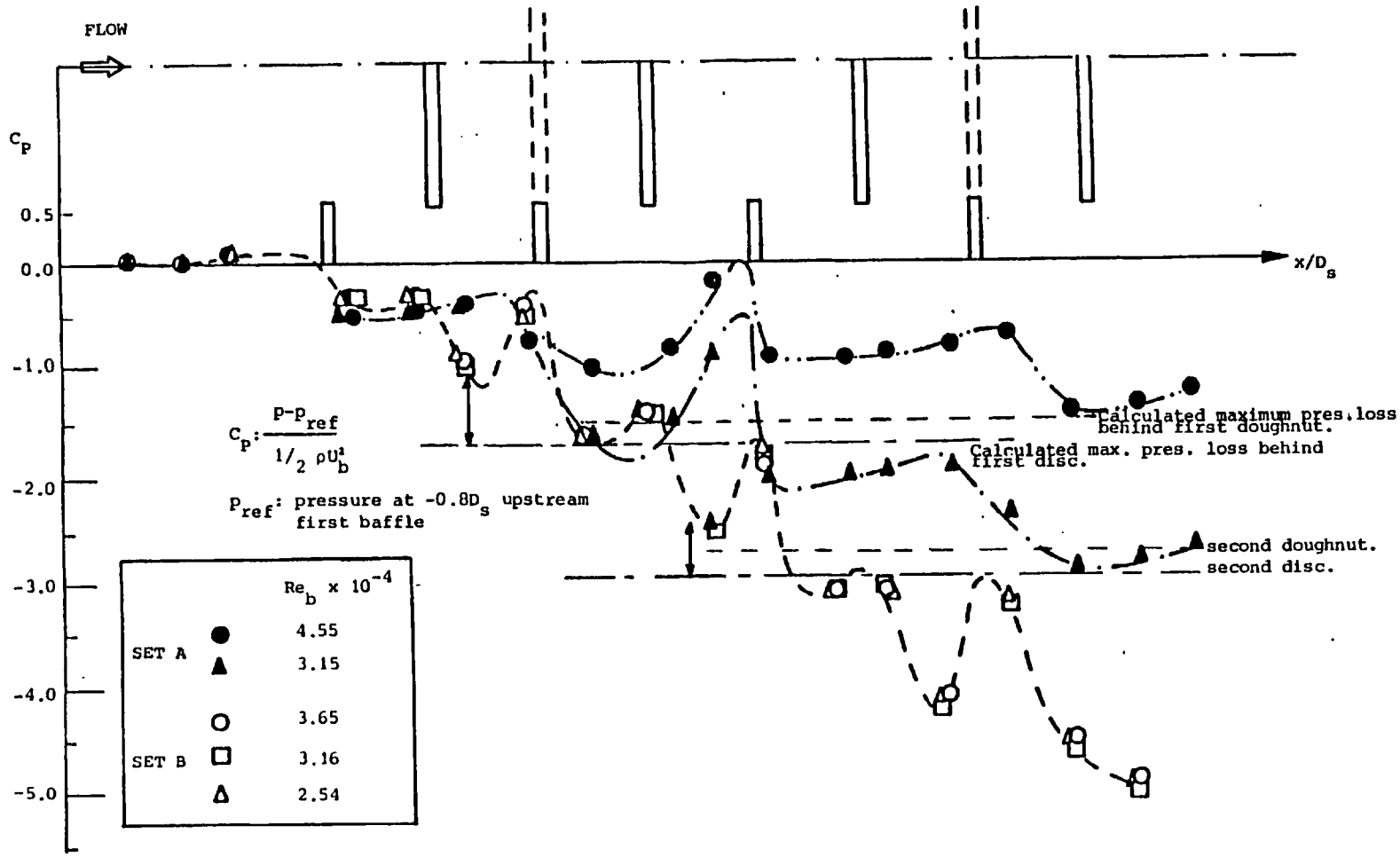


Figure 3.3.4. : Variation of wall static pressure coefficient.

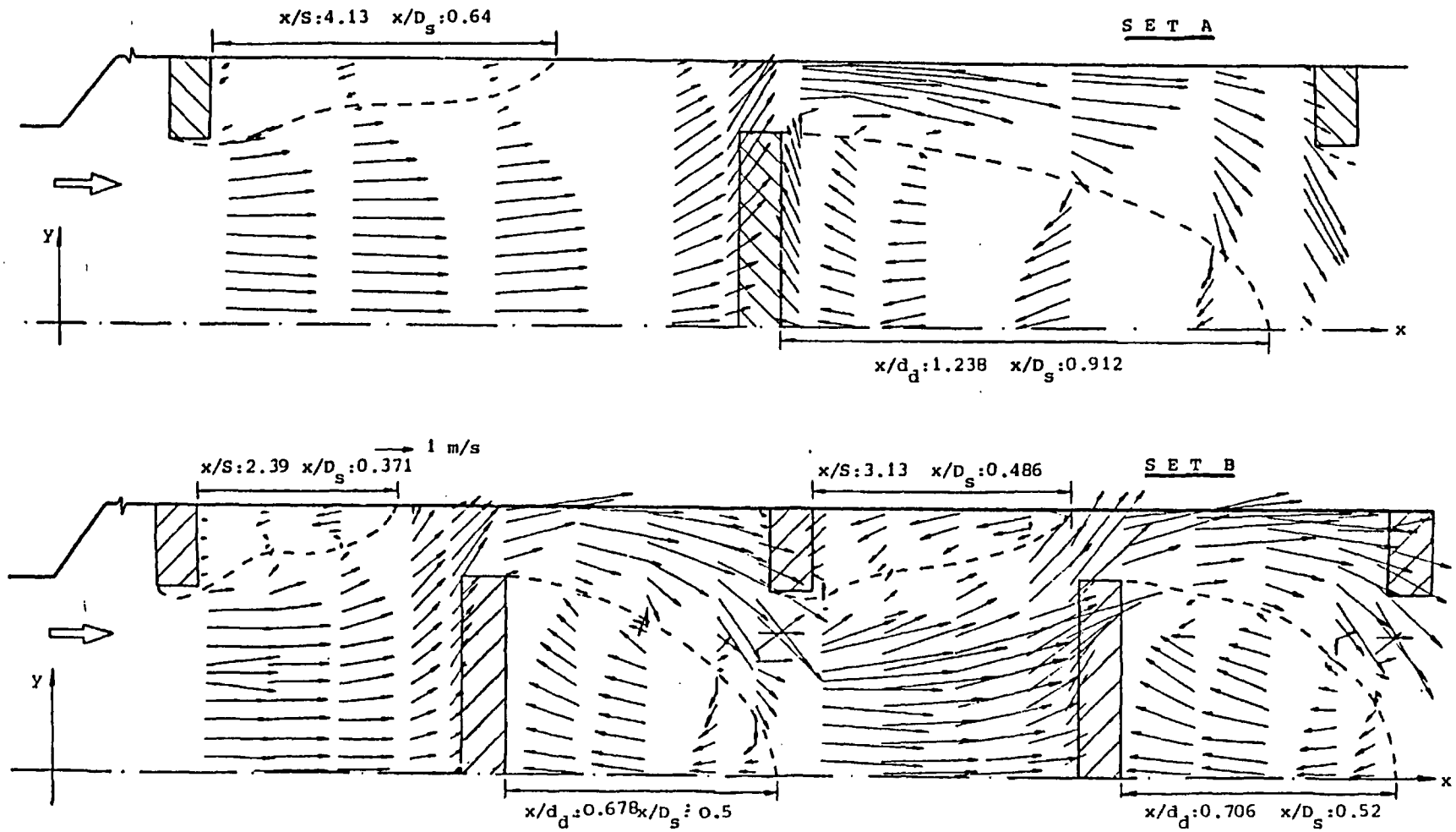


Figure 3.3.5. : Velocity vectors for set A and set B in heat exchanger model.

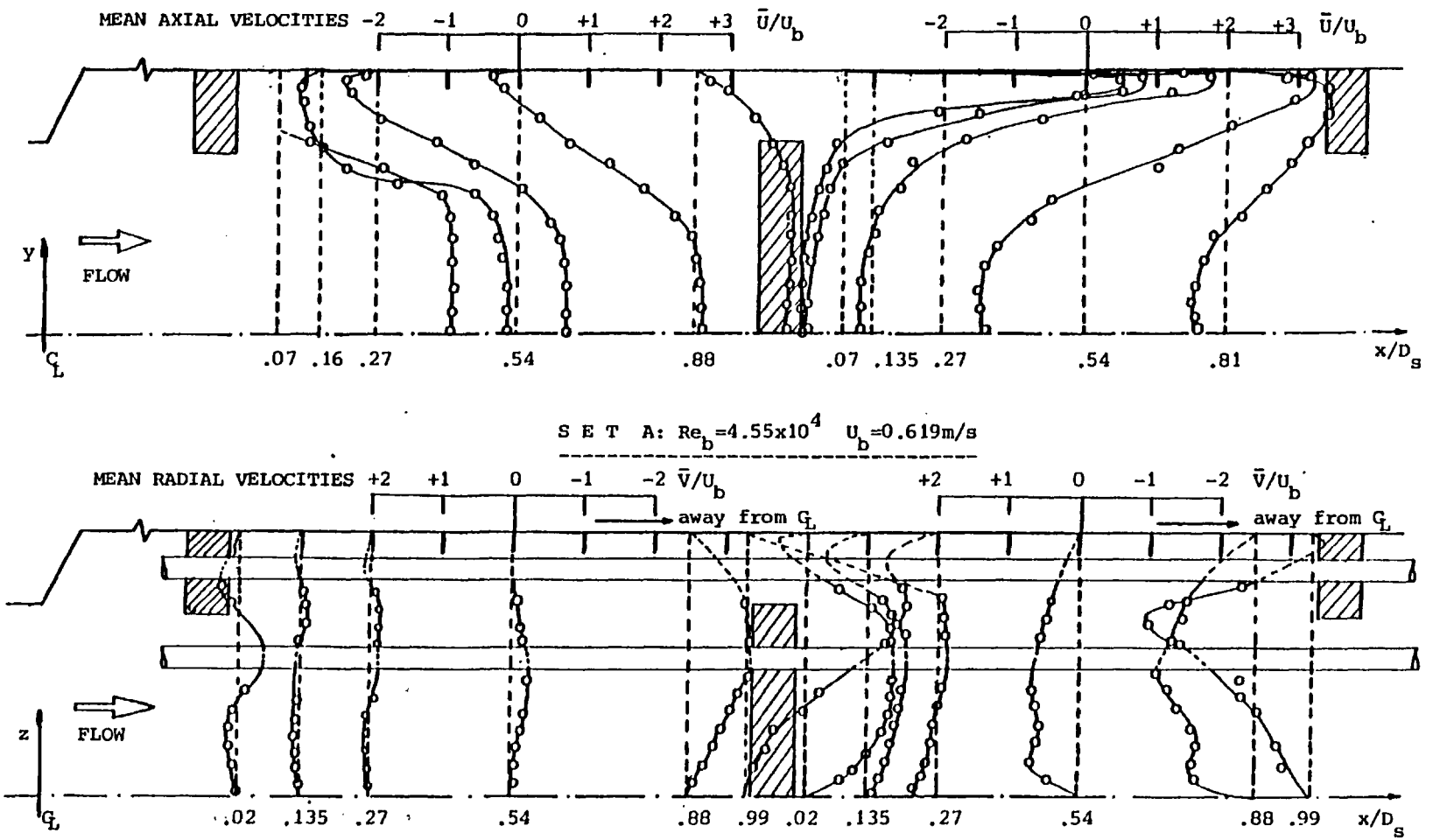


Figure 3.3.6. : SET A: Radial profiles of mean axial and radial velocities.

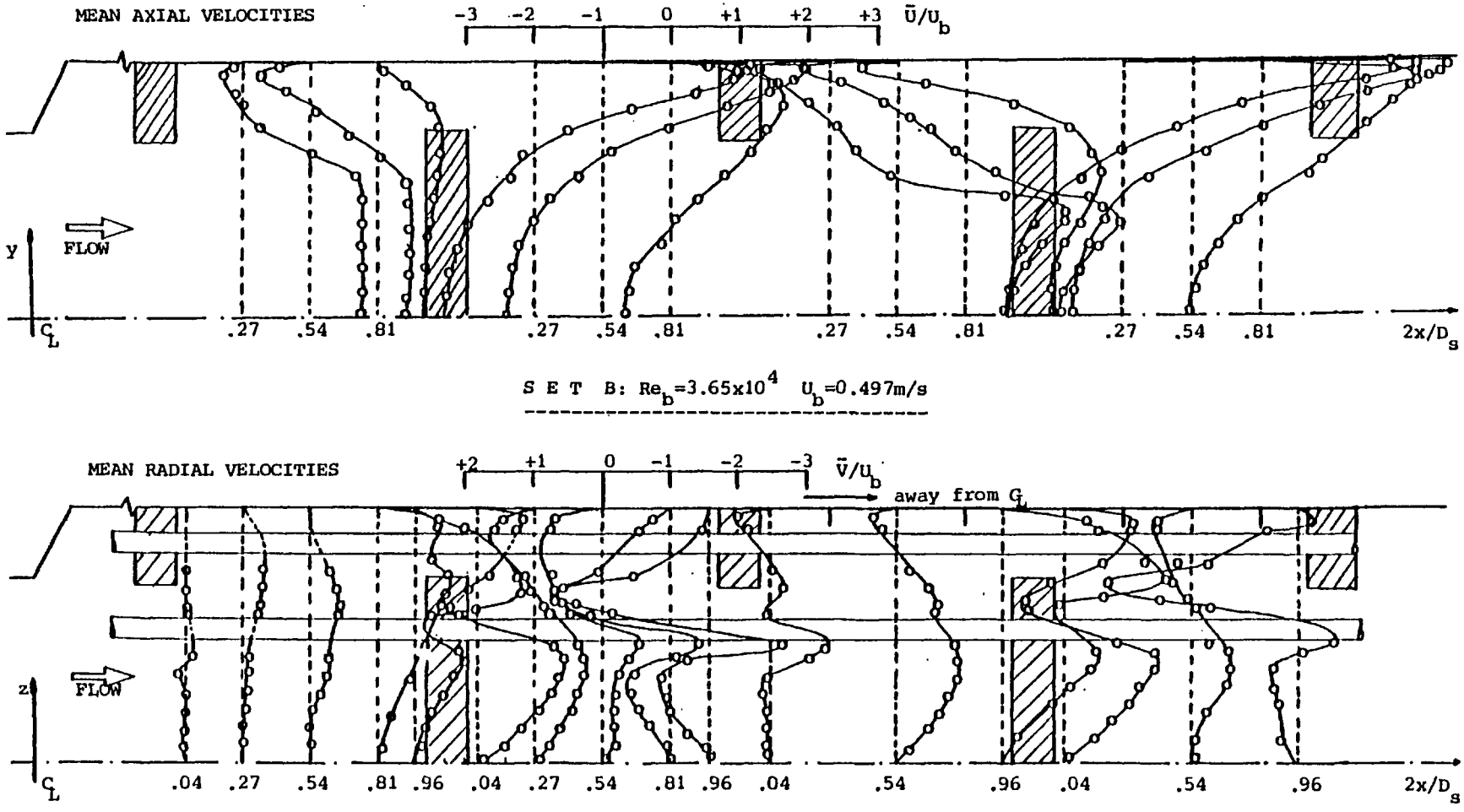


Figure 3.3.7. : SET B: Radial profiles of mean axial and radial velocities.

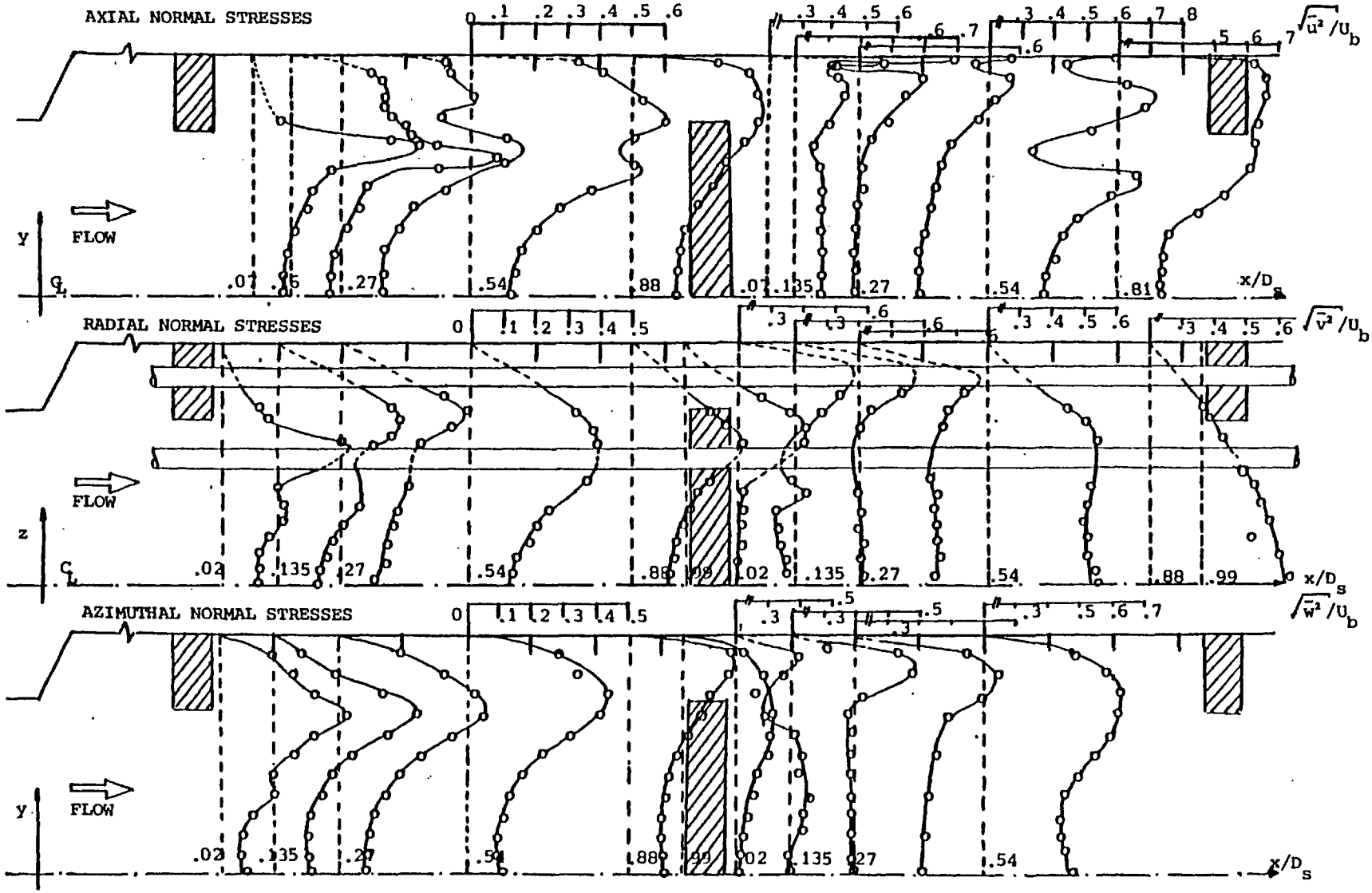


Figure 3.3.8. : SET A : Radial profiles of normal stresses.

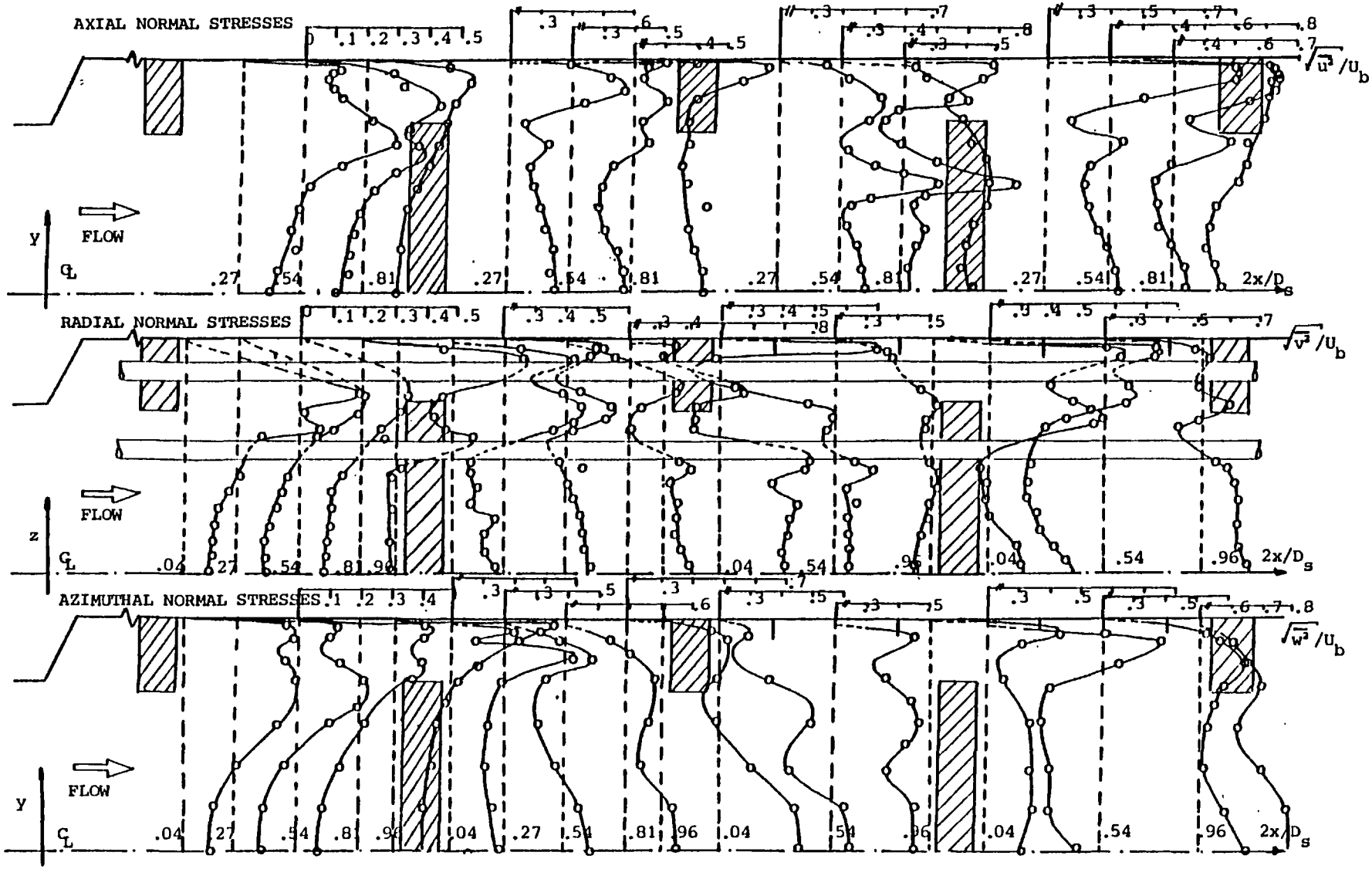


Figure 3.3.9 : SET B: Radial profiles of normal stresses.

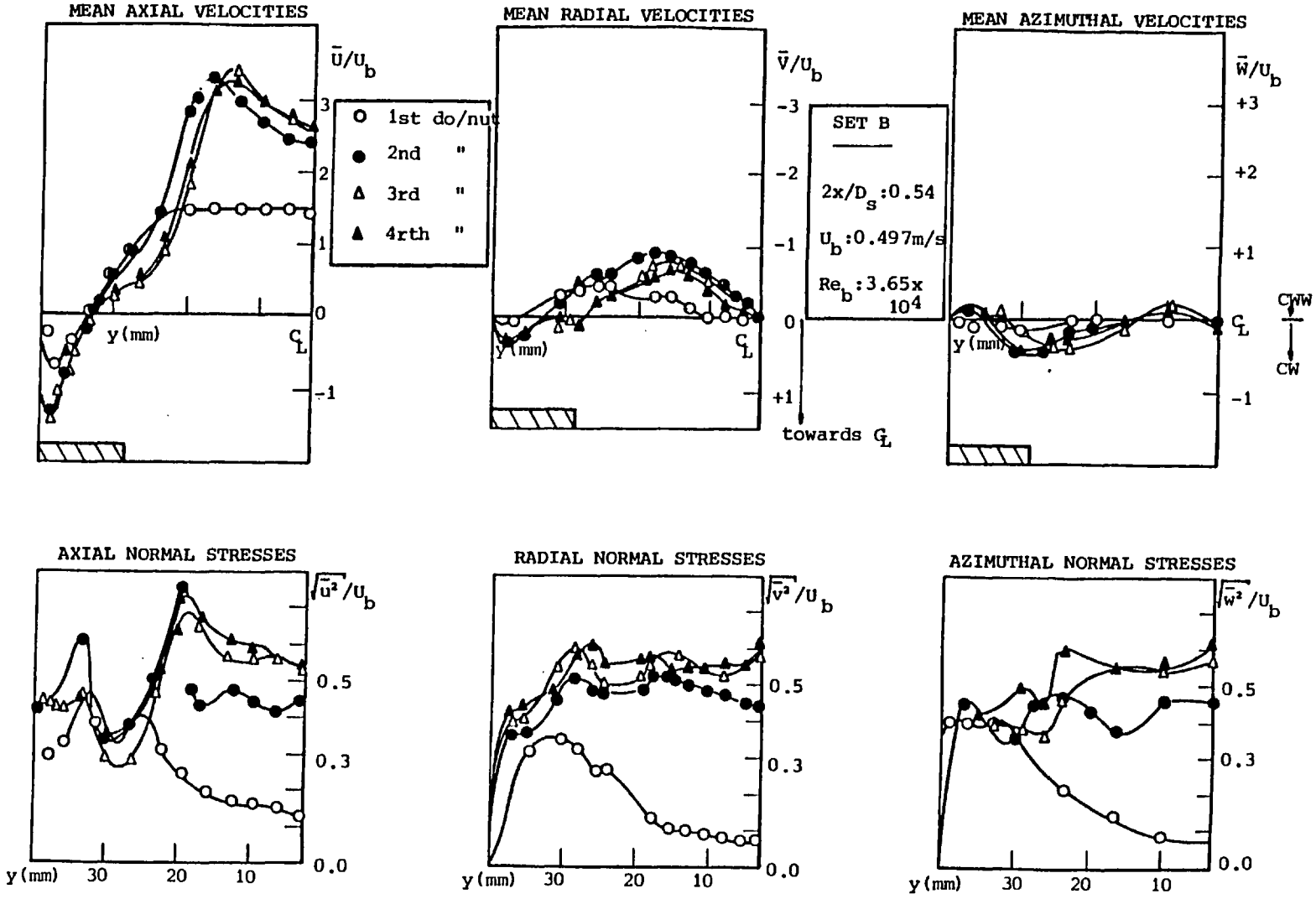


Figure 3.3.10. : SET B : Similarity profiles behind doughnuts.

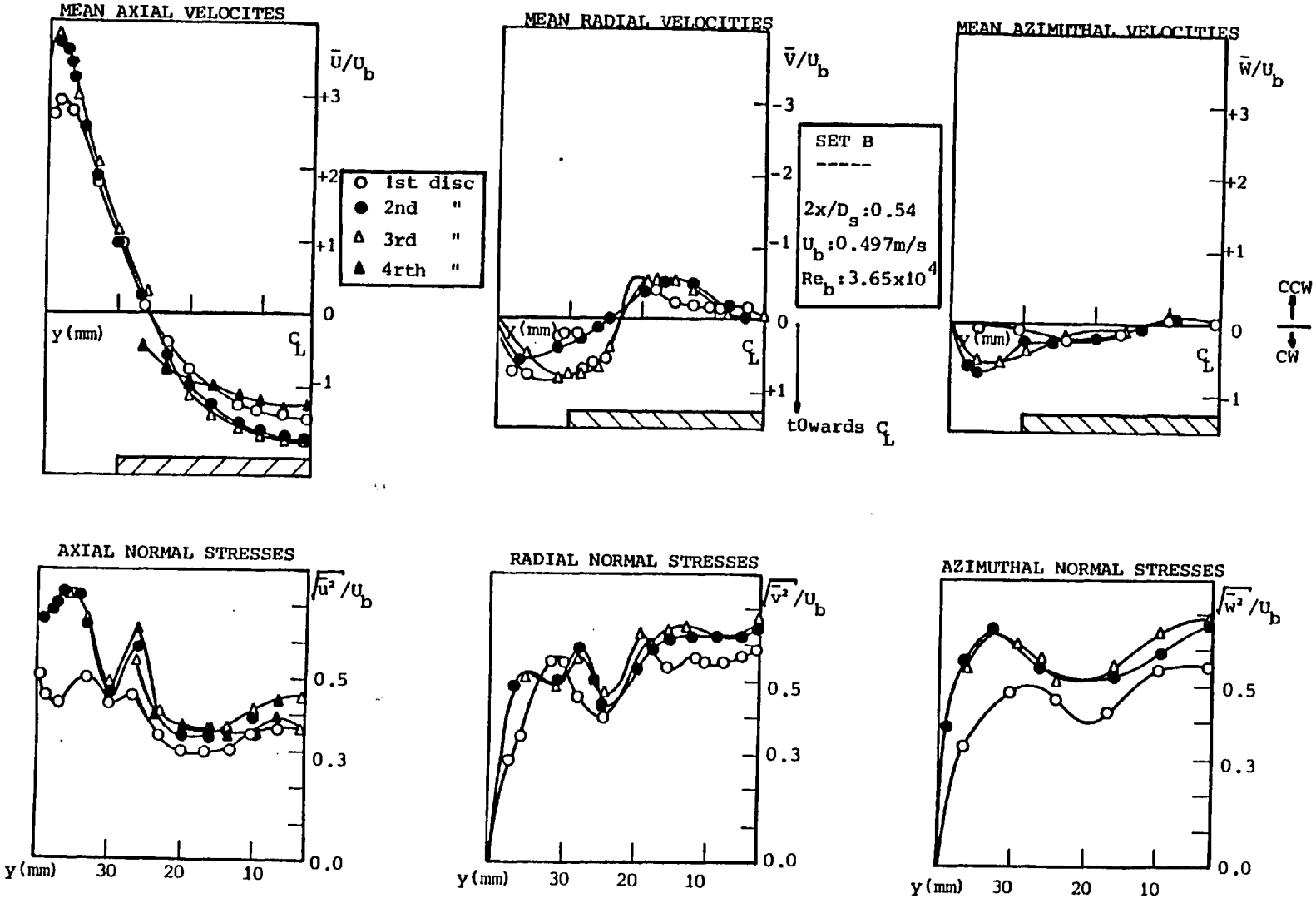


Figure 3.3.11. : SET B : Similarity profiles behind discs.

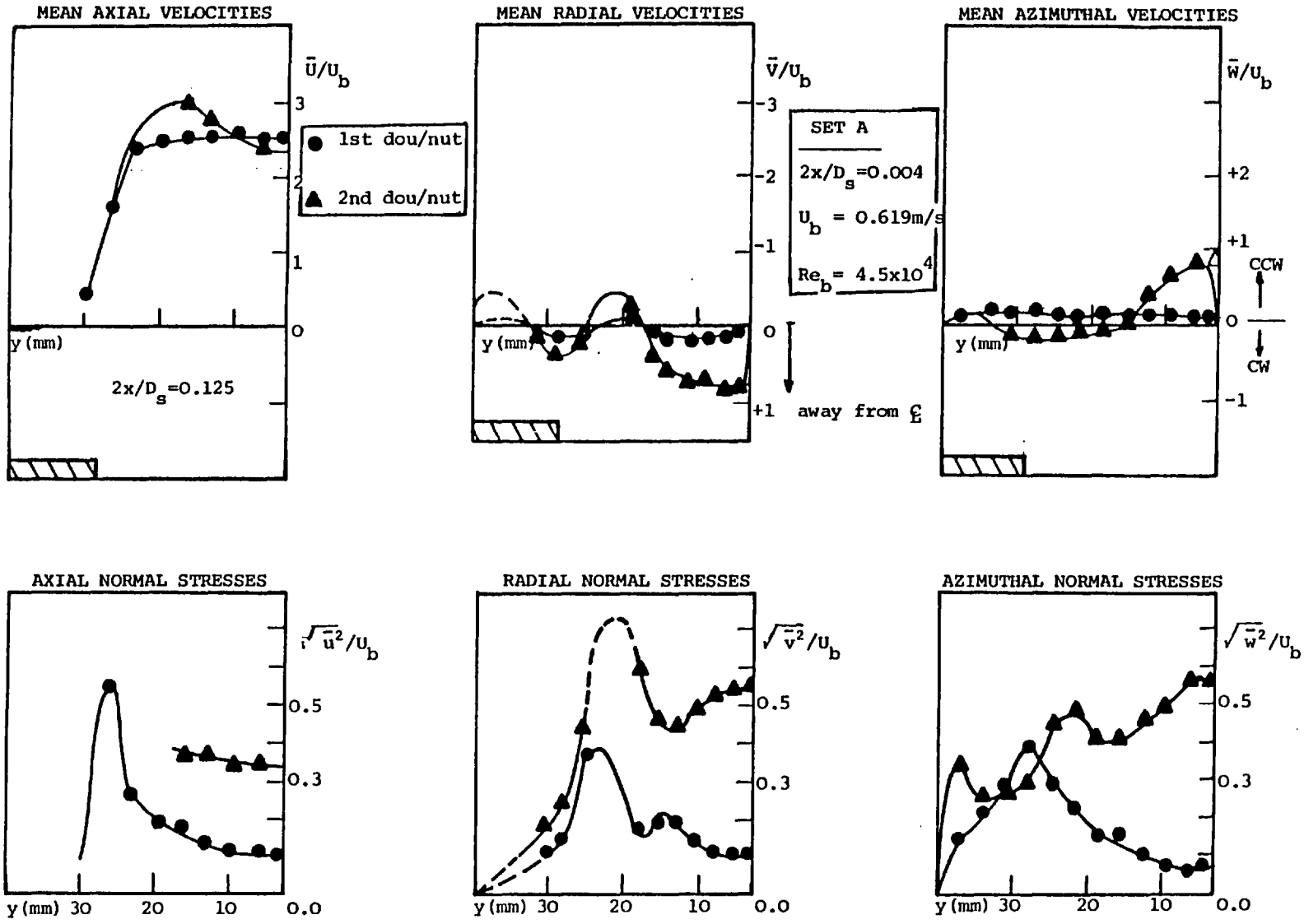


Figure 3.3.12. : SET A : Similarity profiles behind doughnuts.

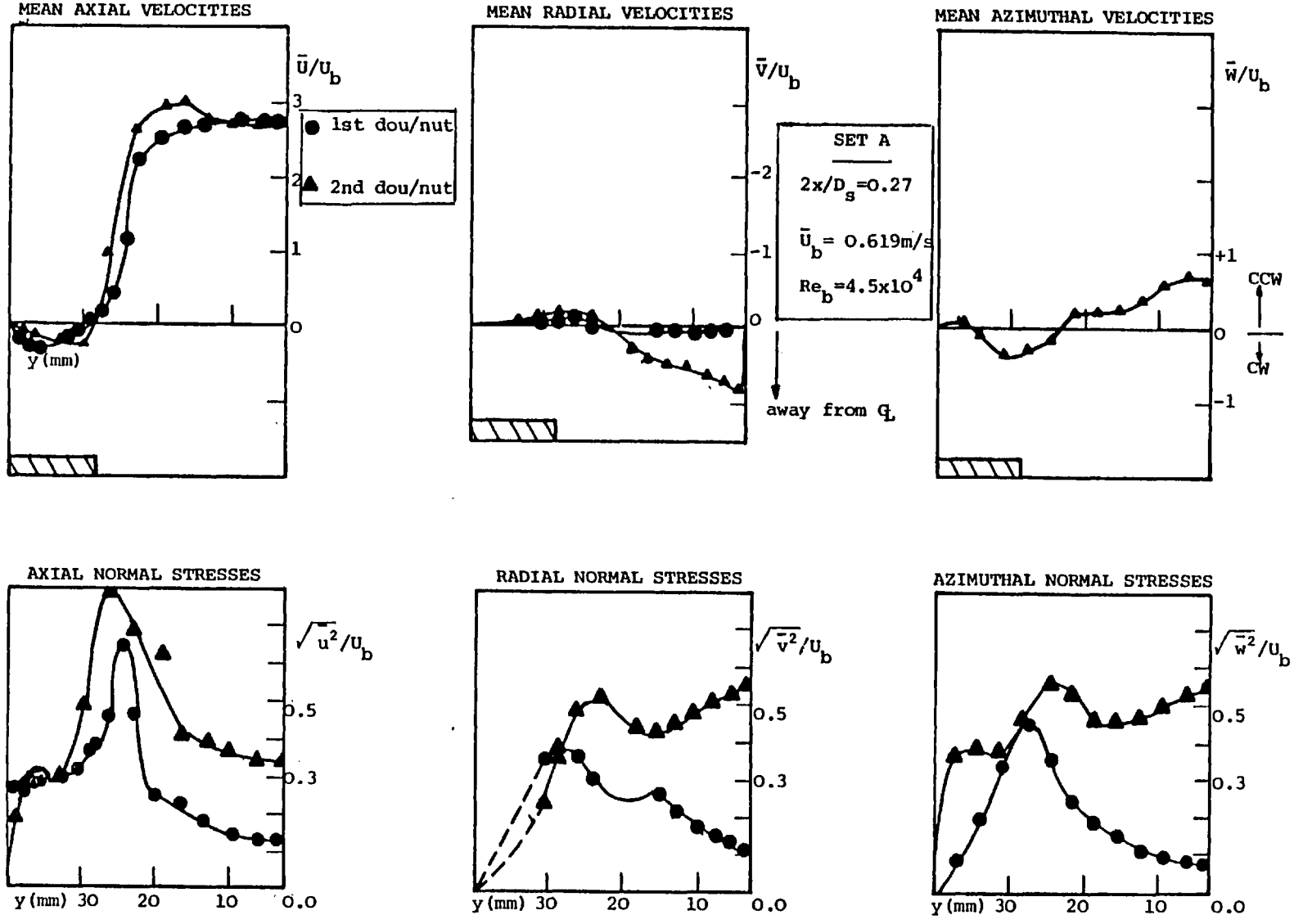


Figure 3.3.13.: SET A : Similarity profiles behind doughnuts.

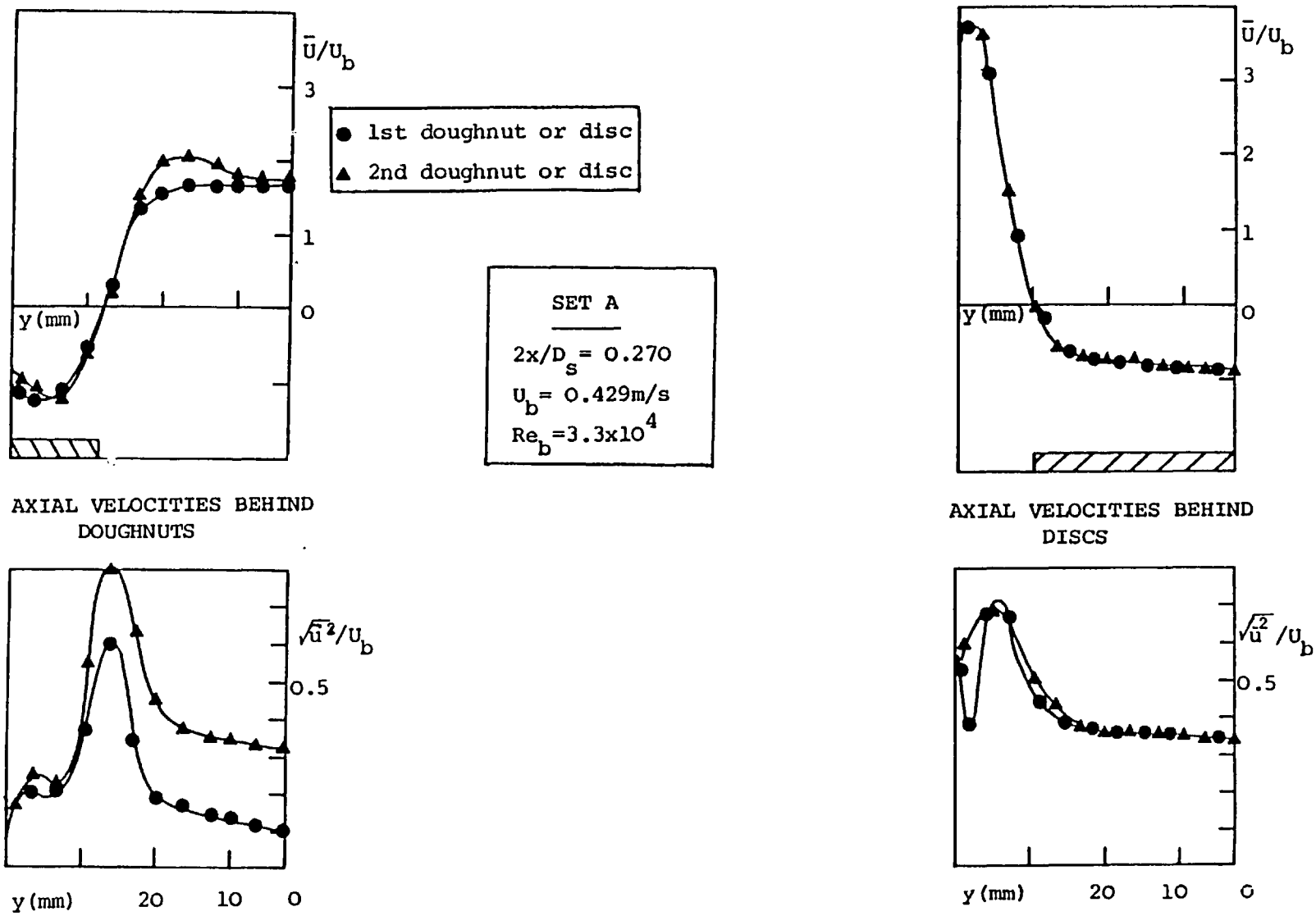


Figure 3.3.14. : SET A : Similarity profiles for a low Reynolds number.

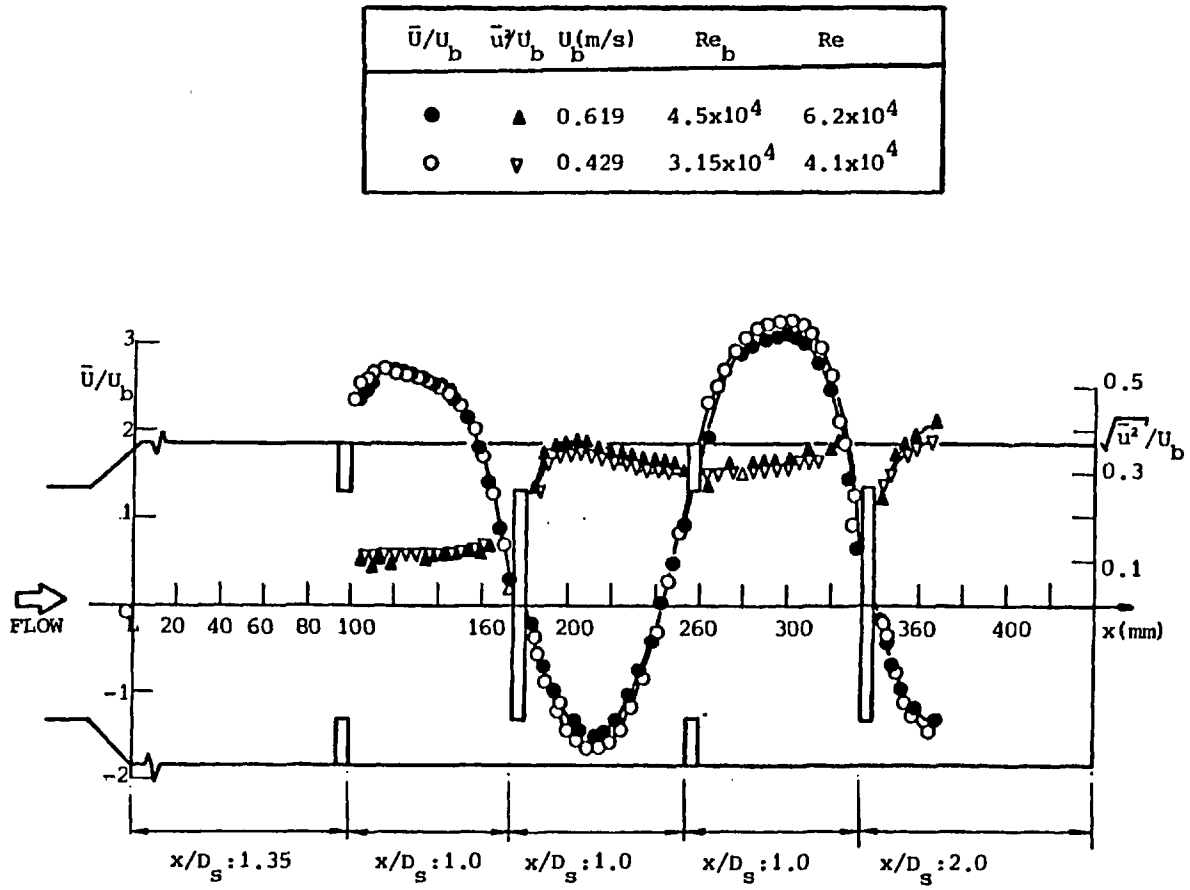


Figure 3.3.15. : SET A : Centreline profiles of axial velocities.

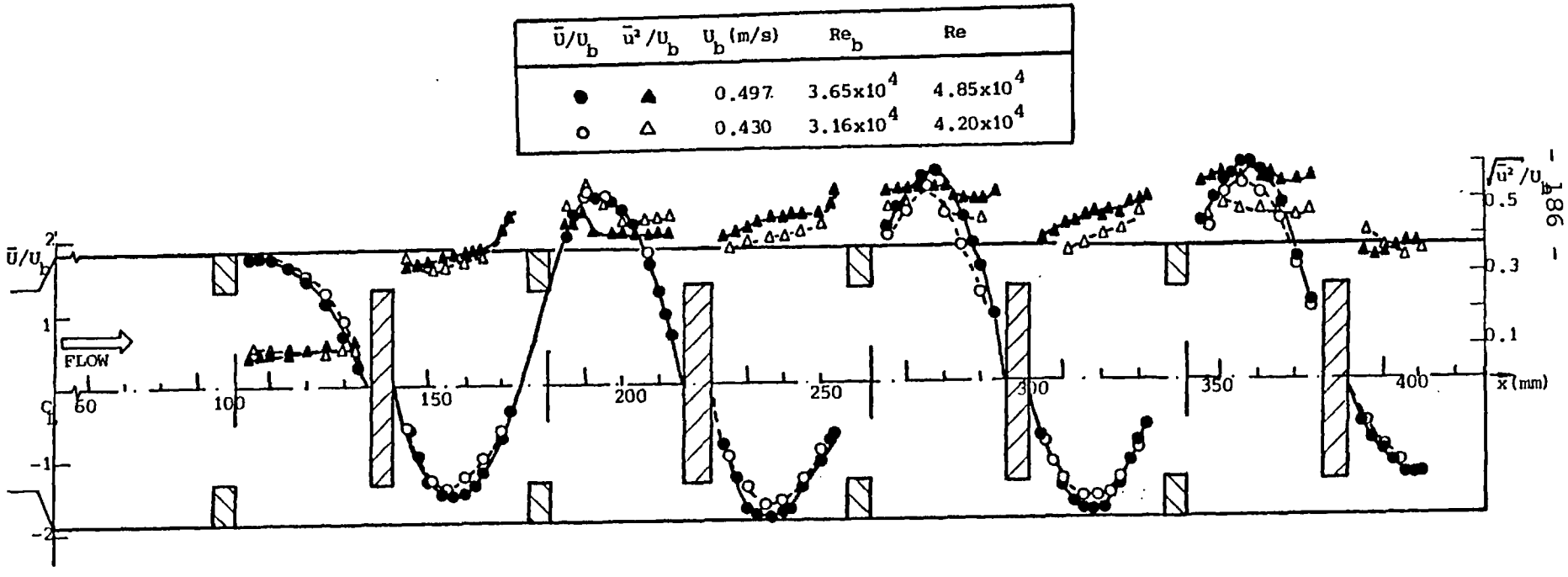


Figure 3.3.16. : SET B : Centreline profiles of axial velocities.

CHAPTER IV
FURNACE-TYPE FLOWS

4.1 Introduction

4.1.1 Purpose of investigation and outline of chapter

The experimental investigation reported in this chapter is concerned with the aerodynamic, temperature and heat transfer characteristics of flows in furnaces employing liquid fuels and emphasis is given to the effect of initial conditions and the interaction of the central jet to the surrounding combustion air.

In furnace geometries, the oil can be caused to enter the combustion chamber in the form of vapour or spray and the term "twin-fluid" atomisation signifies the use of a high velocity gas stream, air or steam, to atomise fuel in a relatively low velocity liquid fuel stream. With "twin-fluid", "air-blast" atomisers such as the one presently used, small fuel droplets are air-borne in the high velocity air-stream, so that their distribution throughout the combustion zone can be dictated by the atomising air flow pattern. The present burner was arranged to produce a hollow-cone polydisperse spray, with a cone angle of approximately 22° degrees. An additional parameter controlling the combustion rate and hence the spray evaporation rate, droplet size and velocity is the secondary (or combustion) air supply. Quantification of its influence on the overall flame characteristics and resulting heat transfer performance is necessary for the performance evaluation of small-scale oil fired furnaces. The turbulence characteristics of the combustion-air and its geometrical characteristics are among the factors that can influence the combustion process. In this context, three isothermal flows were

examined with different levels of swirl and increasingly complicated burner geometries. The most complicated incorporated a "quarl", a stabiliser disc and swirl vanes to enhance swirl and to stabilise the liquid-fuelled spray flame. For this geometry the velocity and temperature fields were measured. For the same geometry and under isothermal conditions, calculated results are presented and were obtained by numerical solution of the two-dimensional, time-averaged finite difference equations and incorporating the k-ε model of turbulence (TEACH-code).

This chapter is organised in three sections. In section 4.2 the characteristics of the laser Doppler anemometers used for the velocity measurements and of the suction pyrometer used for the temperature measurements and the method of performing heat flux measurements are described. In the same section a very brief introduction to the TEACH-computer code, the finite difference equations and the turbulence model are given; an assessment of the experimental and computational accuracy is included. Section 4.3 presents the measured and computed results, which include the quantification of the effects of secondary swirl and upstream boundary conditions. Results are presented for flows with zero swirl, swirl number of 0.70 and a third one with the same level of swirl and corresponding to the operating and geometrical conditions of the spray flame. The calculated results are then presented and they are followed by the combustion results.

The last section, 4.4, discusses the effect of swirl and spray-characteristics in furnace geometries and the implication of the experimental and computed results for calculation procedures.

4.1.2 Previous related work

Analytical and experimental studies into the evaporation and burning characteristics of single droplets and the structure of idealized arrangements of droplets, such as simple one-dimensional arrays or monodisperse droplets, have been made by Law (1976), Matarazan et al (1975), Rudinger (1975), Williams (1973, 1976), Twardus et al (1978), Chiu et al (1977) and Samson et al (1978a 1978b). They revealed the importance of droplet size, of the relative velocity of the droplets to the surrounding gas, of the concentration of both droplets and gases and of the interaction between the droplets themselves. It has also been shown that the spray burning is more of a "droplet cloud" process rather than burning of isolated "single droplets". The majority of droplets vaporize in groups and reaction occurs at the vapour/air interface surrounding the clouds, similar to a gas diffusion flame.

Chigier (1976), Chigier and Yule (1977), Styles and Chigier (1977), Yule et al (1982), reviewed the models of single droplets vaporization and used laser Doppler velocimetry to study the structure of unconfined spray flames emerging from burners incorporating pressure and twin-fluid atomisers. Using an air-blast atomiser, Khalil et al (1977) provided information on the velocity droplet number density and temperature of an unconfined kerosene spray-flame. These studies together with those of Tuttle et al (1976) and Mellor (1973) who studied confined flame environments, provide new knowledge on the efficiency of air-blast atomisation and of the influence on Sauter mean diameter and on the aerodynamic characteristics of flames. Tuttle and Mellor proposed physical models of spray combustion in simulated and actual gas turbine combustors, and confirmed that combustion characteristics of spray flames could not be explained satisfactorily solely

on the basis of homogeneous chemical kinetics effects and that combustion phenomena resembled those of gaseous diffusion flames in the sense that a liquid fuel spray feeds a diffusion type flame which surrounds the spray boundaries. All these flames were found to consist of a central core region with relatively high concentration of droplets, rich mixture ratios low temperatures and high droplet and gas velocities. The main reaction zone was found near the edge of the spray.

The influence of spray characteristics on confined flame behaviour was studied more extensively by Komiyama et al (1977) and Tuttle et al (1976), with air-blast and pressure atomisers. Their studies were restricted to concentration and temperature measurements and no detailed information of the velocity field was provided. The characteristic time of droplet evaporation was found by Komiyama to determine the initial fuel-air mixing rate when it is comparable to the kinetic energy and the characteristic length scale of the spray jet, as for gaseous flames. Tuttle found that related changes in the droplet size and/or evaporation rate influence the local and pollution characteristics of spray flames.

Detailed measurements of droplet velocities, temperature and droplet number density were provided by El Banhawy et al (1979, 1981b) for unconfined and several confined, swirling and non-swirling spray flames. Also, Owen et al (1978) considered the effect of air swirl for confined heavy oil flames produced by pressure atomisers, and showed a general increase in combustion intensity and large increase in flame length with swirl. The confined flame measurements of El Banhawy, which are more relevant to the present work were made in a cylindrical combustion chamber equipped with a rotating cup-atomizer producing a near-monodispersed spray. He concluded that the

evaporation characteristics of the fuel spray, together with turbulent mixing, control the chemical reaction rates and that reduction in swirl leads to a reduced chemical reaction rate within the initial part of the flame and close to the centreline. For low swirl numbers the wall recirculation region becomes important for the flame stabilization. With high swirl the flame length decreased, contrary to the observation of Owen, and the flames were stabilised on the central recirculation zone.

The effects of altering the initial range of droplet sizes through changes in the atomising air flow rate was studied by Attya et al (1981) for two unconfined kerosene spray flames emerging from a pressure atomiser. He concluded that, as expected, smaller initial droplet sizes result in a more rapid temperature rise, and in faster generation of combustion products.

The experimental results obtained to date in confined spray flames, although they have clarified various aspects of spray combustion, they have not exhausted the subject of the interaction of the secondary air and spray characteristics and their effects on the flame behaviour and they cover a limited range of spray flames.

Reviews on the existing approaches to the computation and numerical treatment of the problems of spray-flames have been provided among others by Faeth (1981), Gosman et al (1981), El Banhawy (1979), Jones and Whitelaw (1982) and Jones, Lockwood and Whitelaw (1982). The prediction of local flow properties in spray-flames requires consideration of the details of both the fuel spray and surrounding gases. The modelling of the discontinuous liquid-phase, the coupling between the liquid and gas phases and the modelling of the combustion process which requires consideration of the spray

characteristics, are the main problems that the modeller has to face. With light oils, such as kerosene, droplets will usually vaporize before combustion starts and this simplifies modelling. Additional problems may arise from the modelling of the soot particles, that are very small, so that their burning rate can be treated in the manner of the gas phase fuel component. Thus, soot burnout is probably "turbulence controlled". More important and more complex is the soot formation rate which requires a simplistic model. For the modelling of the liquid-phase, variants of two models are currently employed: The Williams (1965) "statistical spray model" as used by Westbrook (1977) and Cliffe et al (1979), and the "discrete droplet" model used by Crowe et al (1977), Ioannides et al (1980), Abbas et al (1980), El Banhawy et al (1981a).

El Banhawy (1979, 1981a) used the model of Crowe et al (1977), where a spray of droplets is injected in a turbulent gas field, but extented for reacting sprays. Eulerian conservation equations were applied to the gas-phase with the assumption of insignificant influence of local flow discontinuities induced by the presence of the droplets in the gas-phase. Lagrangian equations of droplet-motion and thermal balance equations were applied to a finite number of droplet size ranges representing its distributions within the spray. It was assumed that the evaporating droplets acted as distributed point-injectors of fuel vapour within the flame and the combustion rate of the fuel vapour was treated in a way similar to that used for the prediction of gaseous flames. The interaction between the two phases was accounted for by considering the droplets as sources of mass heat and momentum to the gas-field. This approach according to Ioannides et al (1978) is simple and economic of both computer storage and time. The predicted results of El Banhawy were validated against his experimental data and

both were shown to be in quantitative agreement. It was concluded that only a small number of droplet size ranges (about 5) need to be considered for hollow-cone sprays, with Sauter mean diameter less than 100 μm and that a large number (about 20) is required for solid, polydisperse sprays.

The presently obtained experimental results have been tested against the "discrete particle" model of Ioannides et al (1980) and compared to the results obtained with a continuum model developed by Cliffe et al (1979). Both these models employed the same finite-difference numerical procedure, the same gas conservation equations and the same $k-\varepsilon$ turbulence model. They both apply to two-dimensional steady-state axially symmetrical swirling oil sprays. They differ in that Ioannides' model assumes a velocity difference between the fuel droplets and the gas and calculates droplet trajectories through the gas phase whereas Cliffe's continuum model describes the spray by a probability distribution function which is swept along by the gas velocity producing no velocity difference between the fuel droplets and the gas. There is much argument in the literature, Ioannides (1980), concerning the validity of the continuum assumption under different spray flow conditions and the modelling of the turbulent stress tensor for the liquid or gas phase

To compare the performance of the two models Ioannides suppressed the radiation model and concentration fluctuations in the continuum model. In the discrete model the finite reaction rate was replaced by an infinite rate for comparison purposes only. Both models were used with a 20x20 mesh, and the same boundary conditions except for the initial droplet velocities and locations. The models assumed a Rosin Rammler distribution of input droplet sizes located at 5 mm above the nozzle. The two parameters of this distribution were ob-

tained from droplet size measurements performed at the presently used furnace and with the same atomiser by Negus (1979). The discrepancies were attributed to both experimental uncertainties regarding the initial conditions at the spray, such as droplet size distributions and true droplet velocities and simplifications in the modelling procedures. Overall, it was concluded that exact definition of the conditions at the atomiser influences drastically the performance of the combustion and spray models.

The discrepancies between experimental and predicted results reported by Ioannides et al (1980) and El Banhawy (1981a) in spray flames made obvious the need for the prediction of the flow corresponding to the presently used spray-flame but under isothermal conditions in order to remove uncertainties associated with the combustion model. For this the TEACH-code as described by Gosman et al (1976) was used and the results are discussed in section 4.3.2.

4.2 Experimental and computational program

4.2.1 Flow configurations and burner arrangement

The burner configurations used for isothermal and combustion measurements are described in this section. The layout of the experimental arrangement and the details of the furnace are shown in figures 4.2.1 and 4.2.2 together with relevant dimensions and coordinate system.

For the measurements in isothermal air flows, the furnace steel enclosure was substituted by a 300 mm diameter perspex enclosure see figure 4.2.2, and compressed air was supplied through pressure regulators to the 56 mm

diameter annulus of the burner. The two isothermal flows examined correspond to annulus swirl numbers of 0.0 and 0.70 and a constant mass flow rate of 26.2×10^{-3} kg/s, as shown in table 4.2.1. Swirl was generated by 12 swirl vanes at 45° as shown in figure 4.2.3, which also includes the basic geometrical arrangement of the burner. The volumetric flow rates were measured with rotameters and adjusted to match the flow conditions of Khalil (1976). The annulus Reynolds Number was 2.89×10^{4} for all the measurements in the isothermal annular configurations. The flows were seeded with titanium dioxide particles from a fluidised bed at a rate corresponding to a volumetric concentration of approximately 5×10^{-12} and was of the same order for all the flows presently examined.

The laser Doppler anemometer and signal-processing arrangement used for the isothermal experiments was identical to that used for the combustion experiments and is described in section 4.2.3.

The burner and atomiser arrangement used for the spray-flame experiments is shown diegrammatically in figure 4.2.4 and with the exception of the air-blast atomiser, stabilising disc and quarl geometry is identical to that used for the isothermal annular flow experiments.

For the combustion flow, liquid kerosene was supplied under pressure to a 0.5 mm fuel nozzle through three tangential ports. The fuel, partly atomised, discharged vertically. Atomisation of the fuel was completed with the aid of secondary atomisation air which, highly pressurised, passed through a twelve slot air-shroud, shown in figure 4.2.5, located on the tip of the fuel nozzle and impinged on the fuel jet at 45 degrees. The atomiser was provided by industry and was initially de-

FLOW ENVIRON-MENT	RUN NO.	GEOMETRY	SWIRL NO.	COMBUSTION AIR	ATOMISING AIR		FUEL		AIR FUEL RATIO	SAUTER MEAN DIAMETER	HEAT RELEASE	EXCESS AIR
				FLOW RATE (kg/s)	FLOW RATE (kg/s)	PRESSURE (bar)	FLOW RATE (kg/s)	PRESSURE (bar)		(μm)	(kW/h)	(%)
ISOTHERMAL	-	-ANNULAR -NO CENTRAL JET	0.0	26.2×10^{-3}	-	-	-	-	-	-	-	-
	--	-ANNULAR -NO CENTRAL JET	0.70	26.2×10^{-3}	-	-	-	-	-	-	-	-
	I	-QUARL -STABILISER DISC -CENTRAL JET	0.77	18.05×10^{-3}	0.332×10^{-3}	3.03	-	-	-	-	-	-
COMBUSTION	I	"	0.77	18.05×10^{-3}	0.332×10^{-3}	3.03	1.08×10^{-3}	.204	19.1	150	50	39
	II	"	0.77	18.05×10^{-3}	0.332×10^{-3}	3.03	1440×10^{-3}	.299	14.7	210	61	20
	III	"	0.77	18.05×10^{-3}	0.258×10^{-3}	2.07	1.08×10^{-3}	.204	19.0	170	50	39

γ_{ker} = 21 dynes/cm (surface tension)
ρ_{ker} = 0.89 x 10^3 kg/m^3
ρ_{air} = 1.14 kg/m^3

AIR-FUEL RATIO: Calcutated at inlet on volumetric basis.
Sauter Mean Diameter calculated from;

$$SMD = \frac{2,840}{V} + 446\,\frac{\nu^{0.45}}{MR^{1.5}}$$ (provided by Eisenklam, 1961)

Table 4.2.1: Furnace operating conditions

signed to operate at higher fuel mass flow rates than those required for this small-scale furnace. The design had to be modified and evaluated as are described in section 4.2.4.

The atomiser was surrounded by a 50 mm stabiliser disc and the whole assembly was attached to a 27 mm diameter pipe which, in turn, was kept concentric with the 56 mm diameter annulus of figure 4.2.3 by three 120° spaced, 2 mm thick supports as shown in figures 4.2.3 and 4.2.4. The 56 mm outer pipe ended with a 20 degree quarl with an exit diameter of 90 mm. Swirl was generated, as for the isothermal flows, by the twelve swirl vanes angled at 45 degrees.

Compressed air was supplied to the annulus and atomiser through two separate pressure regulators and the mass flow rates of combustion and atomisation air were measured with rotameters and adjusted to provide 39% excess air above the stoichiometric requirement, to ensure complete combustion. A pump and pressure regulators were used to pressurise the fuel which was subsequently released through the fuel nozzle. The fuel mass flow rate was calculated by discharging fuel into a volumetric tank over 6 minutes at a constant pressure and then measuring the mass of fuel discharged.

The arrangement was operated with the three sets of conditions shown in table 4.2.1. It can be seen that the mass flow rate of secondary-atomisation air was negligible compared to the combustion air through the burner annulus.

The burner arrangement was attached coaxially at the bottom of a 300 mm diameter and 900 mm long, double skinned, water jacketed steel enclosure, divided into five independently water cooled sections. It was kept concentric by a water-cooled double skinned plate, see figure 4.2.1. At 900 mm from this bottom plate, an end plate provided a furnace exit of 90 mm diameter. The bottom and end plates could be moved vertically inside the enclosure with the constant separation of 900 mm. An extractor fan installed above the end plate was used to remove the exhaust gases. Each furnace section and the bottom plate were cooled independently with the aid of centrifugal pumps and the flow rate was controlled and monitored by rotameters.

At one of the furnace sections, four 100 mm wide and 6 mm thick diametrically opposing quartz windows were fitted and allowed the transmission of the laser beams for the velocity measurements. For the temperature measurements one of the quartz windows was substituted by a steel plate with a centrally fitted steel-pipe to allow the traversing and support of the suction pyrometer. The windows did not disturb, at least visually, the flow patterns. The furnace was attached to a traversing mechanism which allowed measurements in the two horizontal directions. For the vertical coordinate, the bottom and end plates were moved with respect to the furnace windows. This permitted measurement only over a distance of 400 mm.

For the combustion experiments only the combustion air was seeded with TiO_2 particles from a fluidised bed in the same manner as for the isothermal flows.

4.2.2 Velocity measurements and assessment of their accuracy

Velocity measurements were obtained with a laser Doppler anemometer comprising an argon-ion laser (Rofin Model 68) operating at 488 nm and approximately 200 mW, a rotating diffraction grating to divide the incident light beam and to provide frequency shifts between the +1 and -1 beams of up to $\pm$ 2.7 MHz, focussing lenses, a light collection arrangement and a photomultiplier (EMI 9655). The resulting signal was band-pass filtered and supplied to the filterbank signal processor as this has been described in chapter 2. The voltage analogue output from the filterbank was used to provide mean and rms values of the signal frequency: in parallel, the amplitude of each filter was read and transferred to paper tape for subsequent analysis. Statistical analysis of the histogram yielded the mean and rms frequencies. Skewness and flatness factors were readily obtained for each of the measuring points. The optical parameters for both the isothermal and combustion systems are tabulated on table 4.2.2.

The laser power is higher than that used for the water flow of chapter III, because of the relation of the scattered number of photons to the residence time of scattering particles in the measuring volume. This implies that higher velocities call for increased power. The choice of laser power, in conjunction with appropriate band-pass filtering, was critical for the combustion experiments where the separation of the pedestal from the Doppler signal amplitude was necessary for measurements close or outside the fuel spray. In the spray region, the dense large droplets and carbon particulates hindered the measurement by absorption and multiple scattering or prevented the measurement of the true gas velocity by scattering from small particles. Close to the

Table 4.2.2: Optical parameters for furnace-type flows

	Isothermal flows	Spray-flame
Laser (Argon Ion)	$\lambda = 0.488 \times 10^{-9}$ m	$\lambda = 0.488 \times 10^{-9}$ m
Focal length of Focusing Lens	f = 500 mm	f = 400 mm
Radial Diffraction Grating	$0 \leq f_s \leq \pm$ 2.7 MHz	$0 \leq f_s \leq \pm$ 2.7 MHz
Long Term Stability	0.3% rms	0.3% rms
Short Term Stability	0.5% rms	0.5% rms
Fringe Volume Dimensions		
Width (at $1/e^2$ intensity)	Δy = 0.259 mm	Δy = 0.293 mm
Length (at $1/e^2$ intensity)	Δx = 6.415 mm	Δx = 4.83 mm
Measured beam-intersection half angle	$\theta/2 = 2.31°$	$\theta/2 = 3.47°$
Number of fringes	∿70	∿100
Frequency Response Constant (with 2 MHz frequency shift)	165.5 KHz/ms^{-1}	248.3 KHz/ms^{-1}
Fringe Spacing	6.0439 µm	4.028 µm
Photomultiplier		
Pinhole Diameter	0.4 mm	0.4 mm
High Voltage Supply	∿8000 V	∿5000 V
Displacement due to:		
flat perspex walls	1.64 mm	—
curved perspex surface at wall (max. displacement)	0.829 mm	—
Incident beam diameter:	1.5 mm	1.5 mm
Magnification	1.5	1.5
Measured Length, cv.	Δx = 5.334 mm	—
Spectral broadening	2.3%	1.5%

geometrical centre line, where turbulence intensities were high, reliable measurements were not possible due to the interference of the broad velocity spectrum with the pedestal frequency.

In these cases band-pass filtering failed to remove the pedestal frequency. An extra difficulty originated from the increase in the photomultiplier dark current, i.e electrons emitted from the cathode for reasons other than incident photons, and associated with the high temperatures in the spray flame. The effect was apparent on the obtained velocity probability distributions and demonstrated itself as a constant frequency. It was removed from the Doppler spectrum when the paper-tape output of the filterbank was processed

Table 4.2.3 summarises the errors in the velocity measurements. Non-turbulent Doppler broadening has already been considered in chapters II and III. The errors due to the sample size and associated with the digital and analog use of the filterbank have been analysed in chapter II. Here, only those error sources that are pertinent to combusting flows are considered.

As known, the volumetric flux rate of the fluid through the measuring volume varies with the instantaneous density of scattering particles and can be important when variations in instantaneous velocity and density become correlated, McLaughlin and Tiederman (1973). An analysis by Asalor and Whitelaw (1975) gives the error as a function of the pressure- or temperature-fluctuation intensity, assuming unity correlation factors with velocity. This can be interpreted as a bias towards the (unburnt) reactant conditions, especially since only the combustion air was seeded. The level of pressure fluctuations is small (proportional to Mach number squared) and even during violent combustion-induced oscillations

Table 4.2.3: Errors estimates for isothermal and combusting flows in furnace

SOURCE	TYPICAL MAGNITUDE OF ERROR	
	$\bar{U}$	$\sqrt{\bar{u}^2}$
Non-turbulent Doppler broadening	Similar to values in table 3.2.3	
Influence of sample size on confidence interval (10^4 to 10^5 samples for 95% confidence int.)	< 0.6%	<1% (% of local values)
Associated with the filterbank	3%	~6%
Scattering-particle concentration bias	$\lesssim -0.05\ \bar{U}_{max}$	negligible
Scattering-particle concentration-gradient broadening	Negligible except in regions of large temperature gradients	
Due to refractive index variation	$\pm$ 0.8 mm/sec	$\simeq$0.1%
Due to the flame oscillation	negligible	$\pm$ 3%

this will only be of the order of 5 per cent, Clare et al (1976) and the errors incurred are small. Figure 4.2.12 shows the variation of the particle concentration across the furnace-radius, for both combustion and isothermal conditions. For the latter case, the high particle concentration above the quarl confirms the above statement. For the combustion case the highest values occur in the region of the spray where high temperature and therefore density gradients exist. The figure suggests that maximum errors in velocities are to be expected around the spray edge.

Broadening arises because of gradients of velocity and particle concentration across the measuring volume and Baker (1974), cited by Asalor and Whitelaw (1975) has found that gradients of 25 per cent mm^{-1} do not introduce large errors and, with the possible exception of the small regions of large radial temperature gradient, the effect is very small.

Refractive index variations stemming from the temperature variations in the furnace can also cause errors. The refractive index, n, of a gas can be linked to the gas density, ρ, by the Lorenz-Lorentz law,

$$\frac{(n^2 - 1)}{\rho(n^2 + 2)} = \text{constant} \qquad (4.1)$$

For air at 273K, n = 1.0003, and under constant pressure equation (4.1) reduces to:

$$\frac{(n - 1)}{\rho} = \text{constant}$$

This enables equation (4.1) to be written

$$(n - 1)\frac{1}{T} \quad \text{or} \quad (n_T - 1) = (n_o - 1)\frac{T_o}{T}$$

the suffix "o" denoting the reference state at which n is known.

The refractive index, n_T, can then be related to a gas temperature $T[^\circ C]$ by

$$n_T = 1 + 0.0003 \frac{273}{273 + T[^\circ C]} \qquad (4.2)$$

The effect of a temperature change of 1.000°C on the absolute value of the refractive index is therefore less than 0.1%, i.e a maximum velocity resolution of $\pm$ .8 mm sec^{-1}.

Refraction occured as the cylindrical enclosure was tranversed horizontally, due to the curvature of the plexiglass enclosure used in the non-reacting flow measurements and its finite thickness (5 mm). It resulted in off-axis deviation of the transmitted beam in the plane of the collection lens and was calculated from the geometry of the optical arrangement to be less than 0.15 mm; the results were, therefore, adjusted by a small position correction. In reacting flows, the windows were optically flat, 5 mm thick and no variation in the beam angle with the furnace position was expected.

The reproducibility of the flow should also be considered when determining the accuracy of the measurements. Limits to the reproducibility are set by the tolerance to which the volume flow rates of reactants could be maintained and the complexity of the chemical reaction. The laboratory supply of compressed air could fluctuate up to $\pm$ 1.5% and the supply of liquid kerosene, obtained from 10 liter barrels, could fluctuate upto $\pm$ 3% depending on the level of kerosene in the barrel and the disposition of carbon particulates on the fuel nozzle. Slow projection of high-speed movies (200 frames per second) obtained in the region close to the burner suggested that, although the fuel-spray characteristics remained unchanged over long operation periods, the flame

shape appeared to change in a repetitive and patterned manner not observable with naked-eye. From the projection of the film it was observed that the heavier droplets could not follow the mainstream flow. They fell outside the flame, got burnt producing a yellow flame and simil-taneously swirled and were carried along with the combus-tion air. This procedure, which was repeated every 1/40 seconds, gave the impression that the flame was oscillating with a 40 Hz frequency. Apparently, this process occured because, as the carbon particles were swept across the burner exit, they influenced the atomisation procedure. Nevertheless, this behaviour of the flame is not believed to have any effect on the of the mean velocity measurements, but could introduce an error of the order of $\pm$ 3% in the measurement of the local rms values due to the 40 Hz fluctuations.

Concluding, in the downstream region, more than 150 mm from the exit plane of the burner, the main source of uncertainty in mean frequency values was the filterbank which limited the measurement precision. In this region, the accuracy of measurement of mean velocities was of the order of $\pm$ 3% and of rms quantities, except at values less than 5%, was around $\pm$ 10% of the measured values.

In the upstream region, and in the combustion case, the presence of fuel droplets presented special dif-ficulties. The probability-density functions of figure 4.2.11 show two maxima and, particularly at the location 40 mm from the centre line, the tw- are of similar magni-tude. In all cases, the lower peak corresponds to the titanium-dioxide particles and to the gas-phase velocity and the higher peak to the kerosene droplets and their velocity. Further downstream, only one peak was detected and further upstream the radial distance over which two peaks were detected decreased significantly. The mean and rms frequencies, in regions where the gas and droplets

had different velocities, were subject to greater uncertainties than those quoted in the previous paragraph. In addition, the existence of larger droplets outside the measuring volume tended to reduce the signal-to-noise ratio with consequent reduction in precision.

Measurements of droplet size were obtained by high speed photography and from the forward-diffraction light from a helium-neon laser and are reported by Negus (1979). The Sauter mean diameter was found to increase from 170 μm at 15 mm to 220 μm at 45 mm downstream of the burner this increase stems from the preferential evaporation and combustion of the smaller droplets at the two measuring stations.

4.2.3 Temperature and heat flux measurements and error estimates

Temperature measurements were obtained in the spray-flame and on the furnace walls. The construction of the furnace jacket as described in section 4.2.2, allowed the measurement of the heat flux for the same flame. The methods of temperature measurement and an assessment of the accuracy are presented below.

a) Temperature measurements in the furnace were obtained with a micro-suction pyrometer consisting of a measuring probe, a filter unit, a manometer, suction pump and a temperature indicator which was used in conjunction with a time domain analyser displaying measured emf's in millivolts. The probe was constructed of a 5 mm outside, 3.5 mm inside diameter twin-bore alumina sheath. Each lead of a 300 μm diameter, Platinum-Platinum Rhodium 13% thermocouple was inserted into one of the two bores of the alumina tube After experimentation to evaluate its influence on the measured temperature the thermocouple

junction was placed 2.5 mm inside the alumina tube. Hot gases were sucked over the thermocouple junction at a rate of 80 ml/s.

The pyrometer is shown in figure 4.2.6 and was constructed by British Gas, Solihul, and calibrated in a constant temperature gas fired oven. The true gas temperature in the oven was measured with an optical pyrometer. The calibration curve, shown in figure 4.2.7, indicated that below 1000° C there was no need for temperature correction. Between 1000° C and 1600° C, namely the temperature range in the spray flame, the calibration indicated that measured temperatures would be underestimated by 50° to 120° C, and the appropriate correction was applied to the measurements.

The performance of the suction pyrometer depends mainly on the following five factors:

- Geometry and material of pyrometer
- Number of shields
- Position of the thermocouple bead inside the sheath
- Suction velocity
- Flow conditions

With the available pyrometers the first two could not be modified. The effect of varying the position of the bead was studied in a constant temperature environment of 1400° C and with the highest possible suction velocity of 145 m/s. It was found that varying its position from 0 mm (the tip) to 4 mm inside the sheath the recorded temperature varied by less than 20° C. The maximum temperature 1420° C, was recorded when the bead was at 2.5 mm from the tip of the sheath, and that is where it was finally placed. The measured temperatures dropped considerably when the position of the bead was greater

than 4 mm, from the exit plane, due to conduction heat loss from the cooler part of the sheath and due to reduced heat transfer between the gases and the hot junction. Also near the sheath tip the radiation error increased and resulted in lower temperatures.

When measurements were first attempted in the upstream region of the spray-flame and at small radii from the centre-line where high concentrations of unburnt liquid droplets existed, there was a tendency for the measured temperature to increase with distance from the tip of the sheath. However, the increase was small, less than 20° C, and was probably due to several factors including droplet impingement on the thermocouple, increase in sheath temperature as a result of the surrounding gas temperature distribution and combustion of kerosene inside the sheath. In this region of the flame, the tendency for probe blockage required that it be cleaned at frequent intervals.

There is a minimum required suction velocity for the thermocouple junction to attain the correct temperature and this increases with gas temperature. To calibrate the pyrometer for the effect of suction rate it was placed in a constant high temperature environment and the suction rate was progressively increased. As shown in figure 4.2.8 the minimum suction rate necessary to achieve temperatures independent of suction rate was 10 ft^3/hr (78.7 ml/s). With this suction rate, a furnace temperature of 1400° C and ambient temperature of 20° C, the suction velocity at the junction was calculated to be about 145 m/s using

$$U\ (m/s) = \frac{\dot{m}'}{A} = \frac{\text{Volumetric flow rate at juction}}{\text{Cross sectional area of suction tube}} \quad (4.3)$$

where $$\dot{m}' = \dot{m} \times \frac{T_{max}}{T_{amb}}$$

and $\dot{m}$ = volumetric flow rate recorded at manometer (in ml/sec)

T_{max} = Max. temperature measured (° C)

T_{amb} = ambient temperature (° C)

Throughout the experiments a steady suction pressure was maintained but the flow rate could have varied as a consequence of blockage of the alumina tube from particles of fuel or soot, or from significant local changes in the convective heat transfer. The error was kept small by using the highest possible suction flow rate, which also accounted for arbitrary changes in the convective heat transfer. To avoid blockage of the suction tube by disposition of soot and fuel droplets the suction pyrometer was frequently removed from the furnace and compressed air blown through the alumina tube. The calibration curve of figure 4.2.8 was reproducible within $\pm$ 20° C at 1400° C and the suction rate used for all measurements was within 25° C of the possible asymptotic value. The response time of the pyrometer (i.e. time required to achieve temperature equilibrium) was found to be about 55 seconds for the first reading and about 45 seconds for subsequent readings, in the region between 700° C to 1400° C. It varied with the temperature level (was much shorter at temperatures below 700° C) and flow conditions. Namely, at regions of steep temperature gradients (i.e. at the spray edge, or at the edge of the central and wall recirculation regions) the response time was found to be much longer.

Visual observation indicated that the suction probe did not interfere significantly with the flow field, and it is assumed not to affect the combustion characteristics and the stability of the flame. However, when the pyrometer was inserted into the fuel spray region it acted as a bluff-body stabiliser and caused significant distortion of the flow field and the spray characteris-

tics. Additionally, the suction probe could get blocked by the fuel droplets. Because of these two reasons no measurements could be obtained in this region.

The efficiency of the pyrometer can be calculated at any point of the furnace, using

$$\text{efficiency} = \frac{T_{(\text{max suction velocity})} - T_{(\text{without suction})}}{T_{(\text{true gas temp.})} - T_{(\text{without suction})}} \qquad (4.4)$$

For the highest recorded temperature (T = 1390° C) the temperature without suction was measured to be 1170° C and the true gas temperature (obtained from the calibration curve) was 1490° C. Thus, the efficiency can be calculated to be 0.67. Similarly, the efficiency at a measured temperature of 1090° C (temperature without suction being 948° C) is 0.98.

Thus, except in regions of the flame where liquid kerosene was present, the precision of temperature values was within approximately +20° C to -45° C. Where liquid droplets existed, measured values could be low by slightly greater amounts but the major problem was blockage and the frequent need to clean the instrument.

b) Wall temperatures were measured with Chromel-Alumel thermocouples embedded in the furnace walls and were simultaneously recorded by a Honeywell temperature recorder. The respective postion of the thermocouples is shown in figure 4.2.9. Each thermocouple entered the furnace wall vertically and it was then bent over to lie in a groove cut into the furnace inner wall, as shown in figure 4.2.10. To ensure good thermal contact each thermocouple was brazed into position. Every section of the furnace was centrally fitted with three thermocouples. The average value of the three readings was taken as the

average furnace wall temperature. At the maximum wall temperature of 140° C the difference between the individual temperature recordings of each thermocouple in the same furnace section was about 20° C. This scattering in the recorded temperatures can be attributed to differences in the construction, mounting and location of the thermocouples.

c) The heat transferred to the different sections of the furnace wall and to the upstream-end plate was determined by recording the inlet and outlet cooling water temperatures at each furnace section, with standard Cr-Al thermocouples (see figure 4.2.9). The average heat-flux at each section was calculated taking into acount the temperature drop across the furnace section, the relative position of the burner and the water flow rate (which was continuously monitored and kept constant at 8.5 l/min) and using the equation

$$\frac{Q_t}{A_H} = \dot{m}_w \, c_p \, (T_o - T_i) \qquad (4.5)$$

where
Q_t = average heat flux
A_H = average heated area of the section
$\dot{m}_w$ = mass flow rate of cooling water
c_p = specific heat of cooling water at (To + Ti)/2 in (J/kg · K)
T_o = outlet cooling water temperature
T_i = inlet cooling water temperature

This method does not distinguish between the radiative and convective heat transfer.

The total wall heat flux can be broken down, approximately into its radiative and convective components as:

$$\frac{Q_t}{A_H} = \sigma (\varepsilon_f T_f^4 - a_{g,w} T_w^4) + h (T_f - T_w) \qquad (4.6)$$

where σ = Planck's constant

ε_f = the effective emissivity of the gas at temperature T_f,

$a_{g,w}$ = the effective absorptivity at T_f for radiation emitted from a surface at temperature T_w (T_f and T_w are the flame and wall temperatures respectively)

h = the local convective heat transfer coefficient.

The solution of this equation requires that the local gas temperature and emissivity be obtained. The furnace construction did not allow this quantities to be measured and an average-method was used. In general, this method could involve large analytical errors because of the averaging over long distances and when big variations in the flame temprature and emissivity are involved.

The heat lost in the exhaust was calculated with the aid of a single temperature measurement on the centre line of the exit plane, and the overall process was subject to some inaccuracy. For the first flame condition of table 4.2.1, the heat transferred to the side wall was determined to be 41.5 kW and the exhaust loss around 6.5 kW. The heat transfer to the burner plate was measured to be more than 2 kW but is uncertain due to the location of the thermocouples. It is estimated that the heat flux to the furnace wall is precise to better than $\pm$ 5%.

4.2.4 Experimental program

Initially, extensive tests were performed to establish the measurement accuracy of the filterbank signal

processor, and are described in section 2.4 of chapter II. They indicated that with the analogue output facility of the filterbank used in conjunction with a time domain analyser, the measurement accuracy of the instrumentation was $\pm$3% and $\pm$6% of the local mean and rms values of velocity. This was judged adequate and used for the isothermal flow measurements. For the combustion case, the filterbank was used to obtain velocity probability distribution as explained in section 2.4, because of the anticipated presence of fuel droplets and the expected bi-modal distributions. The accuracy for the velocity measurements has already been discussed in subsection 4.2.2 and the error estimates have been tabulated in table 4.2.3.

As a first approach to the investigation of the effects that influence the flame characteristics, experiments were performed in two isothermal annular flows of different degree of swirl with the central air-jet blocked. Subsequently, with the same annular geometry of the furnace, the central jet was modified to incorporate the fuel atomiser. The atomiser was initially designed to operate at fuel mass flow rates (above 3×10^{-3} kg/s) incompatible with the furnace size. To reduce the resulting flame dimensions and to adjust the initial droplet size to fit the furnace size requirements i.e. heat release, combustion-air supply and flame dimensions, the fuel mass flow rate through the fuel nozzle had to be reduced without altering significantly the atomisation procedure. Two approaches were tried:

a) An "overspill" attached to the bottom face of the initial fuel nozzle, shown in figure 4.2.4 was expected to reduce the fuel mass flow rate without alteration of the required atomising air pressure.

b) A "cap" with the smaller nozzle diameter that could sit between the original fuel nozzle and the air-shroud, was expected to produce the same result. Three different "caps" are shown in figure 4.2.5.

Extensive tests were performed under different combustion air and fuel mass flow rates with the flames kept unconfined in order to establish the best possible solution to the problem. Photographs of the flame using different size of fuel caps were taken and are shown in figures 4.2.13a and 4.2.13b. It can be seen that the "overspill" solution produced large, heavy droplets which took longer to evaporate and several did not follow the spray trajectory, and burned outside the flame as isolated droplets. The 0.75 mm diameter fuel nozzle cap produced a rather long and thin flame not compatible with the furnace dimension. Finally the 0.5 mm fuel nozzle cap produced a rather short, high intensity flame, appropriate for the furnace. From the photographs it can be seen that reducing the fuel nozzle diameter (i.e. reducing the initial mean diameter of droplets) resulted in a shorter, wider flame and more intense combustion. The colour of the flame changed from dark red to bright yellow as the fuel nozzle diameter was reduced from 1.2 mm to 0.5 mm, implying higher temperatures.

Table 4.2.5 indicates the effect of combustion air, fuel, and atomising air on the size of the flame. Also visual results with different fuel nozzle sizes are tabulated in table 4.2.4. These studies were necessary to enable the optimisation of flame size and heat release in the furnace.

As a next stage, the burner was inserted into the furnace and with the knowledge gathered from the unconfined flame behaviour three sets of operating conditions were chosen and are shown in table 4.2.1. Table 4.2.6 shows the size of the flames and maximum temperatures with the three sets of operating conditions. Extensive measurements were obtained with the operating conditions of RUN I both for combusting and isothermal conditions.

Table 4.2.4: Fuel spray characteristics

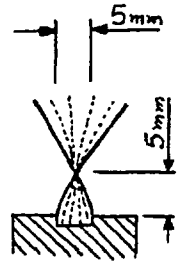
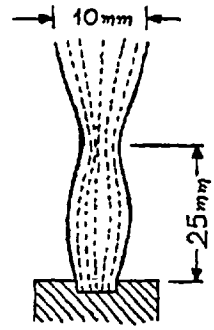
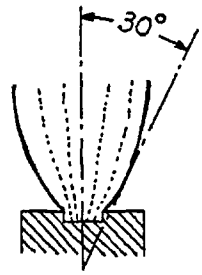
Fuel Nozzle Diameter (mm)	ΔP_{fuel} (p.s.i.)	spray characteristics	$P_{a,a}$ (p.s.i.)	COMMENTS
0.5 mm	5		44	As the fuel mass flow rate is increased the lower part of the spray becomes longer and wider whereas the upper part becomes thinner
	7.5		44	Increasing the fuel pressure above 7.5 psi causes the fuel spray to open up and become as for the 0.75 mm fuel nozzle.
0.75 mm	5		44	The spray angle increases as the fuel mass flow rate is increased.

Table 4.2.5: Effect of combustion air and atomising air on the size of unconfined and confined spray flames

UNCONFINED FLAMES

Increasing: ↓	Consequence
Mass flow rate of fuel	- Increases the length of the flame - Increases the width of the flame significantly. Note: Above p_f = 12 psi (with $\dot{m}_{c,a}$ = 750 lit/min) the flame started burning inside the quarl. To restore stabilisation the combustion air flow rate had to be reduced.
Mass flow rate of combustion air	- Decreases the length of the flame - No significant effect on the width. Note: At $\dot{m}_{c,a}$ = 1128.0 lit/min and p_f = 7.5 psi the flame length was approximately 150 mm. Further increase in combustion air resulted in the flame extinction.
Mass flow rate of atomisation air	- Decreases both the flame length and width with a brighter and whiter flame.
Fuel nozzle diameter	See table 4.2.4

Table 4.2.6: Confined flame characteristics

RUN NO (see table 4.2.1)	$\dot{m}_{c,a}$ (kg/s)	$\dot{m}_f$ (kg/s)	$\dot{m}_{a,a}$ (kg/s)	Flame Length (mm)	Flame Width	$T_{wall\ max}$ (° C)	$T_{\mathfrak{L}\ max}$ (° C)
I	18.05×10^{-3}	1.08×10^{-3}	0.332×10^{-3}	300	280	125	1450
II	18.05×10^{-3}	1.40×10^{-3}	0.332×10^{-3}	380	280	145	1300
III	18.05×10^{-3}	1.08×10^{-3}	0.258×10^{-3}	250	280	127	1270

4.2.5 Finite difference equations and the TEACH computer code

The following section briefly describes the calculation method, beginning with the equations to be solved, their boundary conditions and the procedure for the numerical integration of the equations on a finite difference grid. The equations are elliptic in form and were solved by the numerical procedure described by Gosman and Ideriah (1976), the TEACH computer program and previously used, for example, by Hutchinson et al (1976, 1977) and Gosman et al (1979). In addition to equations for the conservation of mass and momentum, equations for the turbulence kinetic energy and dissipation rate were solved as suggested by Launder and Spalding (1974). This two-equation model has previously been appraised in detail, by Pope and Whitelaw (1976), for separated flows and shown to be far from perfect: on the other hand, as has been reviewed in section 3.1.2, more complex models were shown to have similar defects.

The equations for steady, uniform density flow and the corresponding turbulence model have the following general form in Cartesian co-ordinates

$$\frac{\partial \bar{U}_j}{\partial x_j} = 0 \qquad \text{(Mass conservation)} \qquad (4.7)$$

$$\frac{\partial}{\partial x_j}(\bar{U}_i\bar{U}_j+\overline{u_iu_j})+\frac{1}{\rho}\frac{\partial p}{\partial x_i} = 0 \qquad \text{(Momentum conservation)} \qquad (4.8)$$

$$\frac{\partial}{\partial x_j}(\bar{U}_j K) - \frac{1}{\rho}\frac{\partial}{\partial x_j}\left(\frac{\mu_{eff}}{\sigma_k}\frac{\partial K}{\partial x_j}\right) - \frac{G}{\rho} + \varepsilon = 0$$

$$\frac{\partial}{\partial x_j}(\bar{U}_j \varepsilon) - \frac{1}{\rho}\frac{\partial}{\partial x_j}\left(\frac{\mu_{eff}}{\sigma_\varepsilon}\frac{\partial \varepsilon}{\partial x_j}\right) - \frac{\varepsilon}{\rho K}(C_1 \cdot G - C_2\varepsilon) = 0 \qquad (4.9)$$

$$\text{with} \quad \mu_{eff} = \frac{C_\mu \rho K^2}{\varepsilon}, \quad G = -\overline{u_iu_j}\cdot\frac{\partial \bar{U}_i}{\partial x_j}, \quad K = \frac{\overline{u_iu_i}}{2}$$

$$\text{and} \quad -\rho\overline{u_iu_j} = \mu_{eff}\left(\frac{\partial \bar{U}_i}{\partial x_j}+\frac{\partial \bar{U}_j}{\partial x_i}\right) - \frac{2}{3}\rho K \delta_{ij}$$

The above equations (4.7) to (4.9) were written for high Reynolds numbers and hence in absence of molecular diffusion. They were solved in the common form

$$\frac{\partial}{\partial x}(\bar{U}\Phi) + \frac{1}{r}\frac{\partial}{\partial y}(r\bar{V}\Phi) - \frac{1}{\rho}\frac{\partial}{\partial x}\left(\frac{\mu_{eff}}{\sigma_\Phi}\frac{\partial\Phi}{\partial x}\right) - \\ - \frac{1}{\rho r}\frac{\partial}{\partial y}\left(r\frac{\mu_{eff}}{\sigma_\Phi}\frac{\partial\Phi}{\partial y}\right) - S_\Phi = 0 \qquad (4.10)$$

and with the turbulence-model "constants", in accord with those of Pope and Whitelaw (1976),

i.e. $C_\mu = 0.09$, $\sigma_k = 1.0$, $\sigma_\varepsilon = 1.22$, $C_1 = 1.44$, $C_2 = 1.92$
and $\sigma_\Phi = 1$ in the momentum equation

Partly to economise computer-time requirements logarithmic wall functions were used to link the near-wall grid lines to the wall boundaries. Thus,

$$\tau_w = \frac{U_p}{y_p}\frac{\mu\kappa y_p^+}{\ln E_1 y_p^+} \quad , \text{ where } y_p^+ = C_\mu^{1/4} K_p^{1/2} y_p/\nu \qquad (4.11)$$

$$\varepsilon_p = C_\mu^{3/4} K_p^{3/2}/\kappa y_p$$

where the subscript, p, refers to the near-wall node. The wall-function "constants" included in the above equations had the values $\kappa = 0.419$ and $E_1 = 9.8$

4.2.6 Computational program: Boundary and initial conditions

Typical finite-difference grids used in relation to the furnace geometry are shown in figure 4.2.14 and their importance is discussed in detail later in this section. The axisymmetric nature of the geometry and boundary con-

ditions required consideration of only half of the model geometry for the calculation domain and it should be noted that the grid lines were concentrated mainly in the upstream region and close to the geometrical centre-line.

The boundary conditions for the calculation were as follows:

(i) Symmetry was assumed about the centre-line, i.e.

$$\frac{\partial \bar{U}}{\partial y} = \frac{\partial K}{\partial y} = \frac{\partial \varepsilon}{\partial y} = 0$$

(ii) zero gradient ($\partial\Phi/\partial x = 0$) for variables at the outlet apart from the furnace outlet.

(iii) At x = 0 mm, the inlet boundary conditions for the combustion-air annular velocities were assigned values interpolated from the measured experimental profiles. The interpolated profiles at x = 0 used for the calculation procedure are shown in figure 4.2.15. The axial velocity profile was obtained by interpolation of the experimental results at x = 10 mm and a 23% reduction of the resulting profile to balance the mass flow rate. The radial velocity profile was obtained from the axial velocity profile by multiplication of each value by (tan 20°), which was the angle of the quarl. The swirl profile was obtained by direct interpolation of the experimental profile, at x = 2 mm. To avoid instabilities in the convergence of the solution the values for the swirl profile were introduced gradually over the first 60 iterations using a linear function. Every iteration, 70% of the previous swirl value was added to the new one; the procedure was repeated until the input swirl values were satisfied.

The second boundary condition at x = 0 referred to the atomising air. The geometry of the burner (i e. 12 jets impinging on the centre-line at 45°) could not be exactly simulated by the two-dimensional axisymmetric calculation domain. Several attempts were made to simulate the atomising air. Firstly it was introduced through the centre-line with a $\pm$ 45° angle. The results failed to describe the flow. A second attempt was to introduce the atomising air through an annular gap, at y = 0.005 m from the centre-line and corresponding to the third grid node. It is possible to calculate a "cell-area" to satisfy the mass flow rate and initial velocity of the atomising air. Such a cell is of minimal dimensions and consequently will create instabilities in the momentum balance and convergence of the program. It was thus decided to keep a cell of reasonable dimensions and correct the density to match the atomising air mass flow rate and velocity initial values. This density was used only for the grid node where the atomising air was introduced.

The results obtained using different inlet velocities for the atomising-air are presented in section 4.3.2. A reconstruction of the atomising-air and fuel spray, obtained from the photographs of figure 4.3.28 is shown in figure 4.2.16. The graph allows the calculation of the fuel spray angle before and after it bounces on the centre-line. It can be seen that the angle changes from 45° to 21.5°. This had to be accounted for in the reconstruction of the spray characteristics by attributing to the atomising air a negative radial velocity corresponding to ($\bar{U}_{a,a}$ x tan45°).

(iv) The inlet turbulence kinetic energy was deduced from the measured axial and circumferential normal stresses. The boundary condition was specified as $\kappa = 1/2 \left(\overline{u^2} + 2\,\overline{w^2} \right)$ from the measured and extrapolated values of $\sqrt{\overline{u^2}}$ and $\sqrt{\overline{w^2}}$ at x = 10 mm and x = 2 mm respectively and can be expected to be a good approximation. The value for the energy dissipation was found from $\varepsilon = \kappa^{3/2}/l$, where as a length scale, l, was considered the width of the furnace annular gap.

(v) The boundary condition at the furnace outlet was set by considering the profile at the second before last grid line and adjusting it to satisfy the momentum and mass balance taking into account the dimensions of the furnace-outlet. The mass and momentum continuity was checked at the end of the iteration procedure.

(vi) A constant temperature (308 K) and density (1.14 kg/m^3) was assumed throughout the calculation procedure.

(vii) Wall functions were used as boundary conditions for the grid nodes adjacent to the furnace walls and exit and to the stabiliser disc surface, as described in the previous section. For this empirical law to apply the near wall grid spacing was such that $30 \lesssim y_p^+ \lesssim 300$.

The equations for the velocities, pressure, turbulent kinetic energy and energy dissipation rate were solved in their finite-difference form, using a "staggered" grid, the "hybrid" numerical scheme, an implicit iterative procedure and the "SIMPLE" solution algorithm, Spalding (1972). The iterative cycle of the solution procedure was terminated by a convergence criterion based upon the

ratio of the magnitude of the overall continuity error and the total mass flow rate. The solution was considered to be converged when this ratio has been less than 0.5%.

The influence of the number and location of grid nodes was determined by performing calculations with different grid arrangements. The extent of this investigation was limited by the cost and availability of computer time but encompassed a range from 400 (20 x 20) to 900 (30 x 30) grid nodes. The location at which the dependence of the solution on grid distribution proved most sensitive was between 25 mm and 40 mm from the burner. Axial profiles for two different atomising air velocities are shown in figures 4.2.17 and 4.2.18 and for a range of grid arrangements. It can be seen that refining the grid nodes from 400 to 900 influenced the predicted velocities by less than 10%. Additionally, investigations with a 22 x 22 grid showed important discrepancies when compared to the measured profiles, as can also be seen from the results presented in figures 4.2.17 and 4.2.18; for example the magnitude and shape of wall and central recirculation zone could be altered by 50% by doubling the atomising air velocity. Hence, since it was necessary to improve the modelling of the atomising-air flow, the accuracy of the results obtained with the 25 x 25 grid was accepted, considering that refining the grid to 30 x 30 did not improve the overall discrepancies between the measured and computed profiles and increased the computational cost by ten times.

The number of iterations required for convergence, at each level of grid fineness, was found to increase exponentially i.e. grids of 20 x 20, 25 x 25 and 30 x 30 nodes required 560, 1272 and 1900 iterations respectively. The central processor time per iteration increased from 0.53 secs (20 x 20 grid), to 0.81 secs (25 x 25 grid) and 1.2 secs (30 x 30 grid). The stability of the

calculation also became progressively lower at each successive level and the under-relaxation parameters, factors limiting the maximum change each variable is allowed per iteration (Gosman et al, 1976), had to be decreased. Figures 4.2.19 to 4.2.22 show the improvement on the stability of convergence from 600 to 450 iterations, using the 25 x 25 grid, for two different sets of under-relaxation parameters. In all the graphs the first peak, marked I, corresponds to the final introduction to swirl. The effect of under-relaxing the pressure-correction equation, corresponding to the second set of under-relaxation parameters, is shown clearly in figure 4.3.17 presenting the percentage error in the w-momentum equation versus number of iterations. To summarise, grid refinement was found not to help the accuracy of the predicted results considerably. This was expected, because of the difficulty in the modelling of the upstream geometry. The solution time and cost was improved significantly by adjusting the under-relaxation parameters. The extent to which numerical diffusion may have influenced the accuracy of the results was not extensively examined because of the difficulties in modelling the atomising air. It was anticipated that the predicted results could only be improved by improving the modelling of atomising air and that of the magnitude of the main stream swirl. The results obtained in studying these two effects are presented in section 4.3.2.

4.3 Results

4.3.1 Isothermal annular jet flows in a plexiglass enclosure

Measurements of the three velocity components are presented for two flows of the same geometrical configuration but with swirl numbers equal to zero and 0.70. The value of the swirl number was calculated by integrating the inlet axial and swirl mean velocity profiles, of figures 4.3.8 and 4.3.10a respectively and using

$$S_\Phi = \frac{G_\Phi}{G_x R} = \frac{\int_0^{R_1} (W_r) \rho U 2\pi r \cdot dr}{2\pi R_1 \int_0^{R_1} \rho U^2 r \cdot dr} \qquad (4.12)$$

where G_Φ: is the axial flux of the tangential momentum

G_x: is the value of axial thrust of the axial momentum

R_1: the annulus radius from the geometrical centre-line

Khalil (1976) using the same swirl vanes and with the same furnace geometry reported a swirl number value equal to 0.52. His calculation was based on profiles far downstream of the burner exit and this may be the reason for the difference in the two values.

Figures 4.3.1, 4.3.2 and 4.3.3 present mean and rms values of axial velocities without swirl and at axial distances from the burner equal to 50mm, 100mm and 400mm respectively. The results are normalised with the maximum axial velocity of 16.5 m/s and are compared with the results of Khalil. The measurements indicated agreement of better than $\pm$ 2% in the mean and about $\pm$ 7% in the rms velocities, which is within the accuracy of the filter-bank. Symmetry of axial velocities was checked on two orthogonal diameters at z = 100 mm and z = 400 mm, and is confirmed by figures 4.3.2 and 4.3.3 respectively. The

maximum deviation between any set of four radii at the same value of z was less than 5% and the flow was considered acceptable for further investigation.

Figures 4.3.4, 4.3.5 and 4.3.6 present measurements of the inlet axial and radial velocities and at four downstream axial locations. It can be seen from figure 4.3.5 that there is a preferential entry of the flow through the annulus which gives rise to asymmetries of the order of 5% in the mean values. This asymmetry is associated with the design of the burner which incorporated a 90° bend to redirect the flow at 400 mm below the burner exit, see figure 4.2.3. The introduction of swirl eliminated this asymmetry as can be seen from the inlet axial, radial and tangential velocity profiles abtained with S_w equal to 0.70 and shown in figures 4.3.8, 4.3.9 and 4.3.10a and 4.310b respectively, for the same axial stations.

The profiles of figures 4.3.1, 4.3.2 and 4.3.3. show the gradual spreading of the swirling flow towards the enclosure walls and for the three orthogonal velocity components. In general, the measurements confirm the trends found by other investigators, for example Ribeiro (1976), Habib et al (1980). The presence of swirl creates a central recirculation zone and the length of the corner (or wall) recirculation region decreases. Normal stresses are more than doubled with values no less than $0.2\ \bar{U}_{max}$. Axial normal stresses have their minimum values on the centreline and radial and circumferential normal stresses retain the equal and higher value. The latter is not true for the flow with swirl with which nearly isotropic flow exists in the zone close to the centreline. The double-peak in the normal stress profiles measured without swirl and associated with the regions of steep velocity gradients disappeared with swirl. With swirl, the width, rate of entrainment and rate of decay

of the annular flow are increased. Pressure fields are induced to balance the centrifugal forces and the decay of swirl caused by shear and mixing with surrounding fluid sets up adverse axial pressure gradients which are demonstrated by high values of shear and high turbulence intensity values at the edge of the recirculation zone.

4.3.2 Isothermal swirling flow with quarl in a model furnace

The geometry of the burner used for the experiments of section 4.3.1 was modified to incorporate a quarl-opening, and a stabiliser disc, and the central jet of the annular flow was substituted for a twin-fluid air-blast atomiser, as described in section 4.2.1. The aero-dynamic characteristics were established with isothermal measurements and the experimental results were used as initial values for the calculations of the flow, pre-sented in the second part of this section. The geometry and flow parameters were exactly the same as RUN I of the combustion experiments, as shown on table 4.2.1, and are described in section 4.3.3.

a) Experimental results

Contours of the mean axial and swirl velocities are presented in figures 4.3.18 and 4.3.19 respectively. The results are presented in figures 4.3.14a to 4.3.17b in the form of radial scans of the axial and swirl velocity components. Explanations on the measured components are given in the figure captions. A few profiles of the radial velocity component were also obtained in the up-stream region. They extended upto 35 mm radially from the furnace centreline where the steel enclosure and the size of the furnace windows prohibitited further measurements and they confirmed the symmetry of the flow in this region. From the isotachs of figures 4.3.18 and 4.3.19, plotted in dimensional form, the flow can be divided into five different zones:

i) A core zone which extends around the central atomising-jet and above the stabiliser disc. High axial-forward velocities were measured due to the atomiser air-jet which was injected, as mentioned in section 4.2.1 from twelve slots at 45° to the centreline. The 12 obliquely impinging jets did not meet at exactly the same point at 5 mm above the burner, as can be seen from the flame photograph of figure 4.3.28, at all times as would be expected in a turbulent flow. Occasionally, due to dirt deposition on one of the slots, or due to the T_iO_2 particles seeding the flow, one of the slots would become wholly or partly blocked and a small swirl, opposite to the main combustion air swirl flow would result. The atomising-jet diffused rapidly both in the axial and radial directions. The recirculation zone created due to the stabiliser disc and mainstream swirl, necessarily entrained fluid from this central atomising jet stream. As a result, it detached from the centreline and, due to the action of the main-stream swirl, extended radially beyond the stabiliser disc towards the furnace walls and attained a "Kidney"-shape as can be seen from the axial mean velocity isotachs of figure 4.3.18. The effect of this central atomising jet disappeared at an axial distance of about 250 mm, where the central recirculation zone reached the centreline.

ii) A central recirculation zone which extended to about 500 mm in the axial and to about 90 mm in the radial directions. The length of recirculation corresponds to about ten disc diameters, and is four times more than the length measured behind a single disc of 50% blockage (Taylor, 1981). Comparison with the co-axial flow with swirl of the previous section indicates that the geometrical modifications resulted into a recirculation zone of double the length and triple the width. Therefore, the size and position of the recirculation zone and its associated turbulence field, could be in-

fluenced by the atomising-jet, swirl magnitude and the presence of the stabiliser disc.

The positive momentum of the central jet opposes and overcomes the negative momentum of the recirculation zone. Above the stabiliser disc the presence of the atomising jet increased the turbulence intensities by five times as can be seen from the upstream profiles obtained with and without the atomising jet in figure 4.3.14b. Both figures 4.3.14a and 4.3.14b demonstrate that the development of the flow is not influenced in the radial direction beyond the stabiliser disc from the presence of the atomiser-jet. The same is not true for the swirl component of figure 4.3.15, where it can be seen that the spreading of the flow towards the furnace-wall is delayed by the atomising-jet. The swirl component, see figure 4.3.17a, retains its peak value of about 6.5 m/s above the quarl upto z = 80 mm and at r = 35 mm. Downstream of this it decays rapidly and the high tangential momentum of the main-stream air from the quarl forces the recirculation zone to entrain fluid and expand in the radial direction.

Finally, the presence of the atomising-jet coupled with the swirling motion of the mean-stream flow can cause vortex breakdown instability as suggested by Syred and cited by Lilley (1977). The initial manifestation usually comprises a nearly symmetric swelling of the vortex core, enclosing a recirculation bubble of fluid. This could partly explain the inability of the two-dimensional computational approach to perform well in this geometry of the furnace, as will be discussed later in this section, but cannot be quantitively confirmed.

iii) A free-shear layer zone which extends to elevations of about 500 mm from the burner exit, figure 4.3.18. This is a zone of intense turbulence mixing

between the main-stream zone and recirculation zone, as can be seen from figures 4.3.14b, 4.3.16b and 4.3.17b. As the shape of the normal stress profiles suggests, this shear layer is very thin in the high fluid-shear region near the edge of the disc and becomes thicker downstream and closer to the centreline as the relative velocity between the recirculating fluid and main-stream fluid is decreased.

iv) The main-stream flow zone is defined as the zone of positive axial velocities and is surrounded by the shear layer zone. Its shape is dictated by the degree of swirl and quarl geometry. It extends radially up to the furnace wall, see figure 4.3.18, where the flow is redirected and forced to propagate along the furnace-wall. As a consequence, the swirl component decays very rapidly after z = 110 mm, where the flow reaches the wall, figure 4.3.17a. Turbulence intensities (figure 4.3.20b) also, decay significantly after z = 110 mm.

v) Finally, there is a near-wall recirculation zone, formed behind the backward-facing annular step. It extends up to z = 100 mm, where the main-stream flow attaches to the furnace wall. Its size, again influenced by the quarl geometry, stabiliser disc and degree of swirl is slightly smaller than the same wall-recirculation zone of the co-axial flow with the same degree of swirl (figure 4.3.11).

b) Computational results

The atomising-air emerged as twelve individual jets angled 45° from the grooves of the air-shroud (see figures 4.2.5 and 4.2.16) and interacted at a height of 5 mm above the shroud to produce a cone of fast moving air with a 22° spread-angle These details could not be represented with a finite number of grid nodes and particularly with the 25 x 25 grid used here. Consequently, the

density of the inlet air was assumed to match the experimental value of the atomising air mass flow rate with an annular ring of dimensions convenient to the numerical grid (see section 4.2.6). The change in the atomising air jet angle, from 45° to 22° before and after impingement respectively, could not be represented and the effect of the atomising air on the size and shape of the central and wall recirculation zones was determined by assuming different values of axial and radial atomising air velocities as shown in figure 4.3.20. In general the length of the central recirculation zone was underpredicted. Initially the atomising air was given an axial velocity of 15.3 m/s and a radial velocity of - 15.3 m/s, towards the centreline. With these initial values the length of the lower boundary of the recirculation zone was underpredicted by about 60%. The atomising air initial velocities were then doubled and the predicted axial and circumferential profiles at various axial distances from the inlet are presented in figures 4.3.21 and 4.3.22 respectively, for the two sets of initial atomising air velocities. It can be seen that with $\bar{U}_{a,a}$ = 15.3 m/s and $\bar{V}_{a,a}$ = -15.3 m/s at z = 75 mm the effects of the atomising air have already disappeared. With $\bar{U}_{a,a}$ = 30.6 m/s and $\bar{V}_{a,a}$ = -30.6 m/s the central recirculation zone was always detached from the centreline, see figure 4.3.20. The agreement with the experiments was better for the circumferential velocities in the far downstream region as can be seen in figures 4.3.21 and 4.3.22 at an elevation of about z = 300 mm. At z = 10 mm predicted axial velocities are in good agreement with experiments except in the vicinity of the symmetry axis. At the same location, the circumferential velocities are already substantially underpredicted (figure 4.3.22, z = 10 mm) which is a consequence of the simplifying assumptions in the initial conditions of the atomising air.

An attempt to introduce a swirling motion in the

atomising air jet did not have any significant effect on the length of both the central and wall recirculation zones (see figure 4.3.20, curve $\overline{U}_{a,a}$ = 30.6 m/s $\overline{V}_{a,a}$ = 17.3 m/s, $\overline{W}_{a,a}$ = 20 m/s), but from all sets of initial conditions tested this was the one that gave the best overall agreement with the experiments. Nevertheless, the length of the central recirculation zone was underpredicted by about 35%.

Underprediction of the circumferential velocities can be seen even in regions far from the symmetry axis where the atomising air influence is not likely to be large. This suggested that an enhancement of the combustion air swirling motion would improve the agreement between calculations and experiments. As a result, the combustion air swirl was increased by 87.5% and figure 4.3.23 shows that the resulting length of the central recirculation zone has increased and became comparable to that of the experiment Figures 4.3.24 and 4 3.25 show profiles of axial and circumferential velocities at different elevations and confirm a qualitative improvement. The chosen increase in swirl was excessive and a better assumption can be made.

The uncertainties in specifying the initial conditions and the simplifications made in order to model this aspect of the flow undoubtedly limit the precision of calculated values. The previous results by Khalil (1976) and El Banhawy (1979), in simpler furnace geometries and employing similar two-dimensional computational procedures, showed better agreement between experiments and predictions. It is probable that with complex fuelling devices of the present type, the value of computational methods will lie in their ability to predict the consequences of major changes in flow initial conditions rather than in precise calculations of flow properties for a given geometry.

4.3.3 Kerosene-fuelled spray flame in a model furnace

The velocity results in the spray flame relate mainly to RUN I of table 4.2.1. but temperature measurements are reported for the three operating conditions and are shown in figures 4.3.29 and 4.3.30. All the centreline temperature distributions (figure 4.3.30) have a similar shape and show an initial region, where burning does not take place and temperatures are comparable to that of the surrounding swirling air. The gradual temperature rise with downstream distance is mainly due to the convection of hot gases from the surrounding reaction zone to the central zone by means of recirculation. This heat is used for droplet vaporisation and at about 40 to 60 mm, depending on the initial conditions, the centreline temperatures rise steeply with combustion and continue to do so until about 100 mm to 130 mm, where combustion is nearly completed. The increase in fuel flow rate (RUN II) results in a reduced centreline maximum temperature and in a tendency for the temperature to remain high to a further downstream location. The greater wall temperature of the lower air-fuel ratio (RUN II) suggests that this flame has higher temperatures away from the centreline. The reduction in atomising air pressure (RUN III) results in larger droplets and it can again be seen that the wall temperatures are higher in the initial region and lower than the flame with the same air-fuel ratio in the downstream region. The centreline temperatures are lower up to 300 mm, due to the slightly wider cone angle of the spray and the larger droplets.

The maximum centreline temperature was associated with high luminosity. Near the burner exit, blue flames were surrounding the initial dense spray region (where no combustion occurred) and behaved like gaseous diffusion flames.

The radial profiles of temperature, corresponding to an air-fuel ratio of 19.1 (RUN I) and the smaller droplets, are shown on figure 4.3.29. The temperature maximum at each downstream station is located off the centreline and corresponds to the inside edge of the spray. The measurements extend to 200 mm from the burner and, at that station, the temperature has fallen from the maximum centreline value which was 1380° C at 150 mm. The minima on the centreline have disappeared by around 150 mm where, as will be shown, the region of central recirculation ends. The second temperature maximum occurs at radial locations around 125 mm from the centreline and is also associated with the wall region of recirculation, as is shown by the velocity results. The measurements have been obtained mainly in one radial plane but extended 50 mm across the centreline to demonstrate the extent of asymmetry; as can be seen the asymmetry in mean temperatures is negligible in the upstream region and becomes significant only in the 150 and 200 mm profiles where it is still small.

The temperature mesurements were based on emf readings after the pyrometer had been located for more than 45 secs at the measurement station. The pyrometer response time varied with temperature from less than 30 s at 700° C to more than 60 s in regions of steep temperature gradient. In the vicinity of the spray, blockage occured if the pyrometer was left in position for more than approximately 75 s and between all measurements the pyrometer was removed, blown with compressed air, and relocated. The existence of blockage was obvious in that the emf was observed to decrease: nevertheless, the measurement accuracy in the immediate vicinity of the spray cannot be guaranteed to fall within the +20, -45° C limits suggested in section 4.2.3.

The axial and swirl velocity and temperature results

of figures 4.3.28 and 4.3.29 respectively have been interpolated to yield the contours of figures 4.3.32, 4.3.33. and 4.3.34 which allow the flame characteristics to be more readily understood. For example, the trajectory of the spray, the regions of recirculation and the regions of maximum temperature can readily be observed. Using the flow description presented in section 4.3.2 for the equivalent isothermal flow the following regions can be recognised:

A cool-core region near the burner where local temperatures are low because combustion has not started yet, large fuel droplets are present and fuel persists downstream of the burner exit. The oxygen present in this region is mainly due to the atomizing air, since the flame surrounding the spray acts as an effective barrier to oxygen entrainment. Temperatures are not high enough to allow reaction, but are sufficient to enhance the vaporization rate. Moving towards the spray boundaries, temperatures start increasing, until they reach a local maximum value at the edge of the reaction zone. With combustion taking place at the spray boundaries heat is transported to the cooler core by entrainment causing droplet vaporization. The vapour within the spray thus passes the flammability limits and combustion starts. This is demonstrated by the rapid increase of the mean temperature in this central core region (from about 600° C at z = 25 mm, to 1200° C at 50 mm). The maximum temperature in this region does not occur until about 100 mm (figure 4.3.29) where profiles become flatter, due to the mixing denoting that at this stage the flame front has reached the centreline, that vaporization of liquid droplets is complete and that the combustion of fuel and intermediates is partially completed. In the main reaction zone, temperatures exhibit local maximum values and move radially outwards, denoting the fast mixing and spreading of the jet and they reach a maximum value of 1400° C at about 60 mm.

Further in the radial direction temperatures drop to local minimum values in the region of the main combustion-air stream, which becomes gradually heated by the hot products of the main reaction zone and the wall recirculation zone as the elevation from the burner is increased.

Temperatures start rising again in the wall recirculation zone due to the reversed flow of hot products. It can be seen that the wall recirculation zone extends up to 120 mm from the burner exit, and maximum temperatures recorded were about 850° C, denoting that the wall recirculation zone remains relatively cold, compared to the main reaction zone

Further downstream in the axial direction (see figure 4.3.29) the temperature profiles become flatter and as reaction reaches completion the profiles become representative of a confined hot gaseous jet (at z = 150 mm). The subsequent decrease in temperature along the axis is due to dilution by entrainment.

Mean and rms velocity results are shown in figure 4.3.26 and 4.3.27 respectively in profile form. A representative sample of the measurements is included and shows, for both the axial and swirl components, high values in the region up to 50 mm corresponding to the secondary, atomising air. These maxima decay rapidly and a substantial central region of recirculating flow is indicated between the origin and beyond 150 mm. The recirculation tends to move radially outwards from around 100 mm and does not disappear until a downstream distance of more than 300 mm. The corner recirculation is also obvious and extends to a downstream distance of between 100 and 150 mm. Close to the burner, the presence of droplets presented special measuring difficulties and as shown in figure 4.2.11, the probability density functions

show two maxima, with the kerosene-droplets having the higher velocity values.

The mean velocity measurements were used to determine the magnitude of the swirl number defined as before in section 4.3.1. The results at 40 mm downstream yielded a value of 0.41. The isothermal-flow results, presented in section 4.3.2 and with the fuel jet and atomising air on, yielded a value of 0.70 based on the results at 2 mm downstream and 0.39 based on results at 10 mm. Thus, with the present inability to measure in the immediate vicinity of the spray sheet, an accurate figure for the swirl number cannot be obtained but it is clearly greater than 0.41 and less than 0.7. For calculation purposes, and as will be discussed, the profiles at 40 mm downstream must be used to check any assumed initial values.

The measured values of the rms of the velocity fluctuations are shown in figure 4.3.27. In general, they are approximately 50% higher than in the corresponding isothermal flow although, of course, direct comparisons cannot be made. It is notable, and to be expected, that the rms values have maxima for both velocity components in the vicinity of the edge of the spray and that by 300 mm downstream, where the spray no longer has identifiable droplets, the rms values for both components and the axial intensity are near uniform. The rms values near to the edge of the spray corresponded to around 3.0 m/s and beyond 300 mm to less than 0.5 m/s; the corresponding mean axial velocities were approximately 8 m/s and 1 m/s.

The wall heat-flux distribution, corresponding to the above profiles is shown on figure 4.3.31. It has been obtained from the five water-cooled sections of the furnace wall and by measuring with the end plates 900 mm apart, but at different locations with respect to the

cooled sections. The total heat transfer to the wall was 41.5 kW compared to a possible thermal load, obtained from the mass flow of kerosene and its calorific value of 50 kW. The maximum heat flux occurs at approximately 500 mm from the burner and corresponds to a region just downstream of that where the flame was observed to approach the wall. The temperature profiles do not extend beyond 200 mm but the extrapolations of the isotherms of figure 4.3.24 show that the higher temperature will not reach the wall until beyond 300 mm downstream.

High speed colour movies were taken to examine further the structure of the flame. No individual droplet combustion was observed. Fuel-rich mixtures were observed in the recirculation zone, implying that large quantities of fuel vapour that evaporate close to the burner were swept back into the recirculation zone. Near the burner blue flames were surrounding the initial dense spray region behaving like a gaseous diffusion flame.

The time-averaged number of droplets passing through the laser Doppler anemometer control volume was also measured in the present case using an electronic counter connected to the appropriate output of the amplifier. A few results obtained in the spray-region are presented in figure 4.2.12. It can be seen that the maximum concentration of particles was measured at the region of maximum temperatures, i.e. the edge of the spray. In this region of the high temperature gradients velocity measurements are biased in favour of the kerosene-particle velocity due to velocity bias. However, although the amplifier gain was kept constant, the measured values are influenced by possible variation in signal amplitude due to particle size and velocity.

4.4 DISCUSSION AND CONCLUDING REMARKS

4.4.1 Summary

Three isothermal flows with different degrees of swirl and burner geometry and one combusting liquid-fuel flow have been examined. The following paragraphs summarise the more important findings of the experimental investigation.

The mean velocity results in non reacting swirling flows indicate that the size of the central recirculation region increases with swirl while the length of the wall recirculation decreases with swirl. Visual observation and temperature measurements in the spray flame indicate that the introduction of swirl stabilises the flame and shortens it. Flame spread is wider at high swirl numbers. The use of quarl burner created a central recirculation zone downstream the burner throat which helps in stabilising the flame.

Comparison of the mean velocity results in the isothermal and combusting flow indicate that the size of the central recirculation zone decreases with combustion. The presence of the atomising air results in a deformed recirculation bubble, both for the isothermal and combusting case. The length of the wall recirculation region increases with combustion, and the local mean and rms velocities are higher than the corresponding isothermal velocities. In general the mean and fluctuating velocities in the reacting case were 50% higher than in the isothermal flow partly due to heat release and partly due to the effects of droplet-collisions, break-up, and difference in injection velocity for different droplets, and probably combustion generated turbulence.

In the isothermal flow the length of the central recirculation zone extends beyond eight disc diameters whereas in the spray-flame it extends upto 6.5 disc diameters. In the spray-flame there is a faster drop of axial velocities due to the radial movement of the flow towards the reaction zone Increases in temperatures precede the velocity increases by an amount proportional to the velocity magnitude Temperatures indicate that chemical reaction concentrates at the spray boundaries in the initial flame region but further downstream proceeds towards the flame centreline. Maximum temperatures were recorded within the flame recirculation region, close to the centreline. Temperatures within the spray region were the minimum recorded and influenced by fuel impingement and catalytic effects. An increase in the fuel flow rate results in a spray with a wider spreading angle and bigger mean-droplet size. The effect is due to the increase in the fuel angular momentum and also due to the decreased momentum interaction between atomising air and fuel droplets. The increase in the mean diameter of the droplet-sizes decreases the evaporation rate with the consequent effect of increased probability of combustion occurence away from the fuel nozzle with comparatively lower axial velocities.With an air-to-fuel ratio close to stoichiometric the presence of smaller droplets at near nozzle locations with their lower inertial drag ratio and higher velocities resulted in higher velocity values, with more intense combustion and a shorter flame.

The main difference between the isothermal and spray-flame flowfield occurs in the behaviour of the swirl velocity. The swirl component for the spray flame exhibits double peaks in the upstream region. The peak nearest to the centreline appears as swirl generated by the atomising air. In fact, this is the result of shear action between the tangential (angular) momentum of the combustion air and the high value of axial momentum of

the atomising air. The ratio of the two momenta is proportional to the magnitude of the apparently generated swirl component of the atomising air. At the spray boundaries, where combustion has already started, temperatures are higher with consequent density variations and mass flow rate changes. To restore equilibrium, fluid has to be entrained and the obvious choice is the combustion air mass flow through transport of tangential momentum towards the spray and geometrical centreline. Because of the relative difficulty to redirect the axial momentum of the atomising air in the direction of the swirl, most of the angular momentum of the combustion air is moved towards the centreline. Downstream of the end of the recirculation zone, where temperatures drop there is no more need for momentum transfer. Hence the apparent increase in the magnitude of swirl measured in the combustion case.

This process of momentum transfer and the related action of buoyancy forces was further demonstrated by calculation of the ratio of Grashof to Reynolds number at various axial and radial locations inside the furnace. Low values of Grashof number, indicating the domination of viscous and shear forces, were measured in the upstream region close to the centreline and up to a radial distance of 50 mm. This is consistent with the measured magnitudes of swirl and the explanation given in the previous paragraph. At about 100 mm from the burner, corresponding to a region of intense combustion drastic changes occur and the effect of viscous forces decreases with downstream distance.

Near the furnace wall and in the upstream region buoyancy forces are more dominant than the viscous ones. Downstream their effect moves towards the centreline, and viscous forces become important near the wall.

To conclude, velocity, temperature and heat-transfer characteristics of the kerosene-spray flame have been determined with instrumentation which is appropriate but subject to finite imprecision. In the region away from the spray the precision of measurement is similar to that achieved previously in gas flames and, as a result, allows the characteristics of the flame to be identified and, if required, compared with the results of calculations. In the limited region very close to the spray, the measurements were subject to greater uncertainty and could not be obtained in the immediate vicinity of the spray sheet. In particular, the velocity measurements were influenced by seeding particles and the droplets and the pyrometer could yield low values due to blockage effects. Thus, all but a small region of the furnace flow has been satisfactorily characterised.

4.4.2 Implications of the results for calculation procedures

The experimental and predicted results in the furnace geometry with an air-blast atomiser proved the sensitivity of the flow to initial and boundary conditions.

As a consequence of the experimental difficulties it should be appreciated that, with spray flames of this type, the initial values used in any calculation method cannot be accurately determined and introduce, as a result, a degree of flexibility into any calculated results. In particular, the spray trajectory and initial droplet size cannot be specified with the accuracy required to allow the degree of precision achieved in comparison with gas-flame results. The initial values must, as a result, be estimated and their influence checked with measurements, say at 40 mm, before detailed comparisons can usefully be made at further downstream loca-

tions. With checks of this type, calculation methods can be appraised, improved and used to demonstrate the influence of the various initial and boundary conditions.

In general, the ability of the two-dimensional calculation method to accurately predict all flow variables when compared to experimental data, has been shown to be limited for both two and three-dimenional, turbulent, recirculating flows, e.g. Vasilic-Melling (1977) and Durst and Rastogi (1980). The two main areas of criticism have centred upon the turbulence model and the finite-difference scheme used in the calculation procedure. Related to the turbulence model is also the inability to predict successfully the swirl motion The consistent underprediction of recirculation lengths and peak turbulence kinetic energy levels has been attributed to the k-ε turbulence model and, in particular its inability to account for extra rates of strain imposed by curvature of the streamlines, and to physically represent the interaction between the flow and wall boundaries.

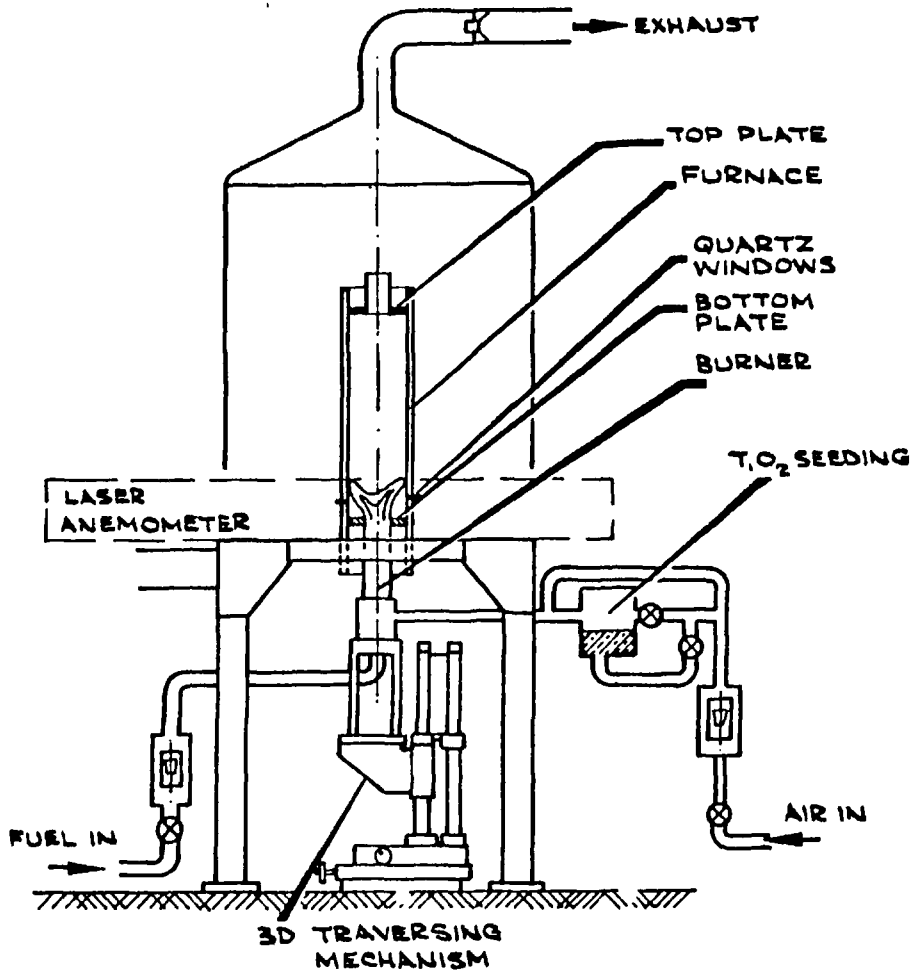


Figure 4.2.1 : General layout of furnace arrangement.

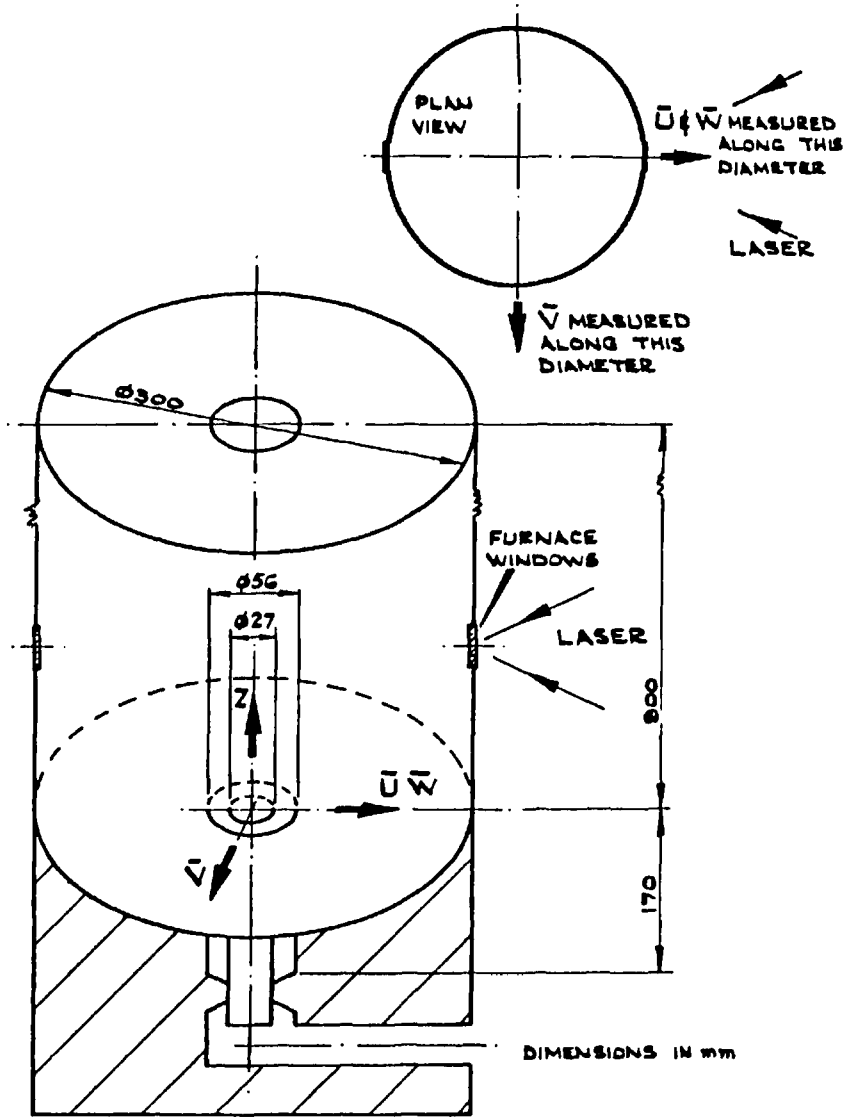


Figure 4.2.2 : Cylindrical enclosure and coordinate system.

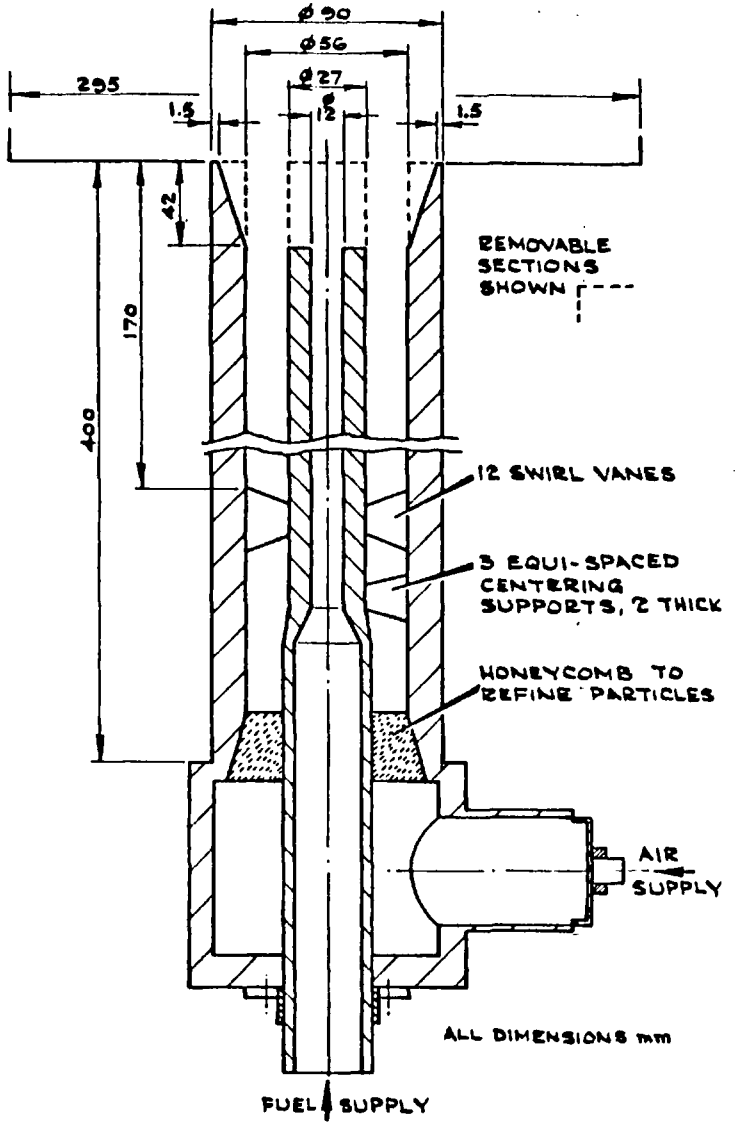


Figure 4.2.3 : Burner basic-geometrical configuration.

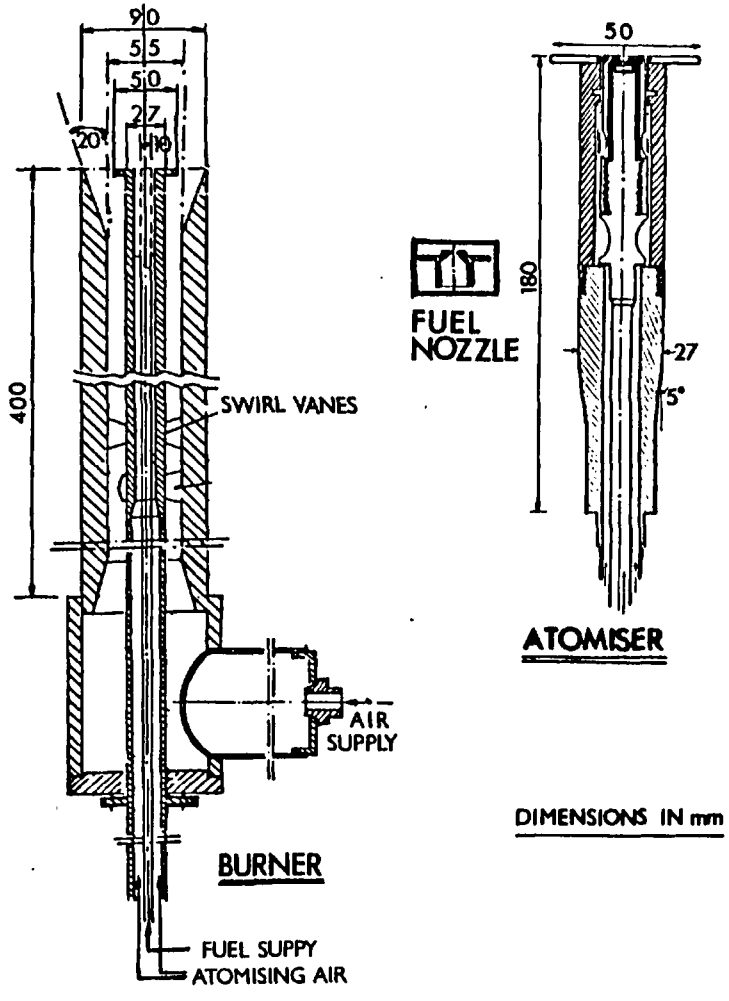
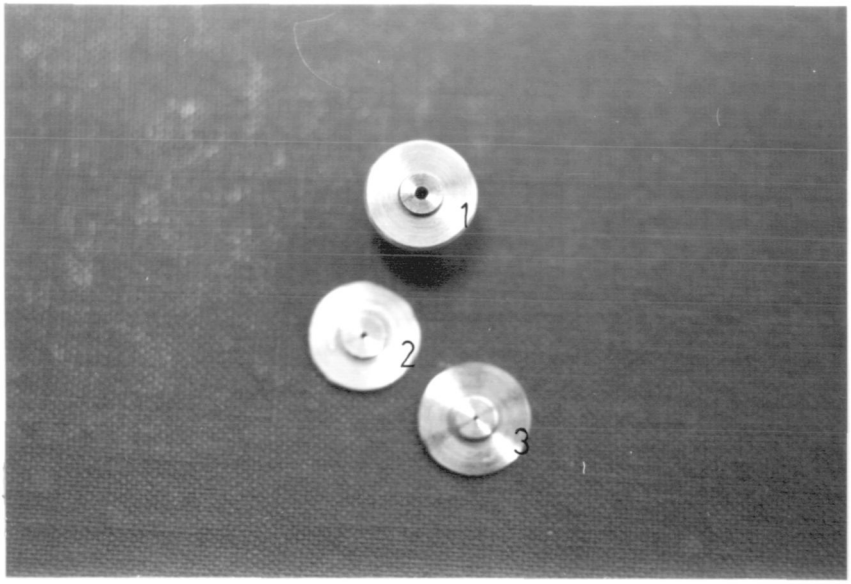
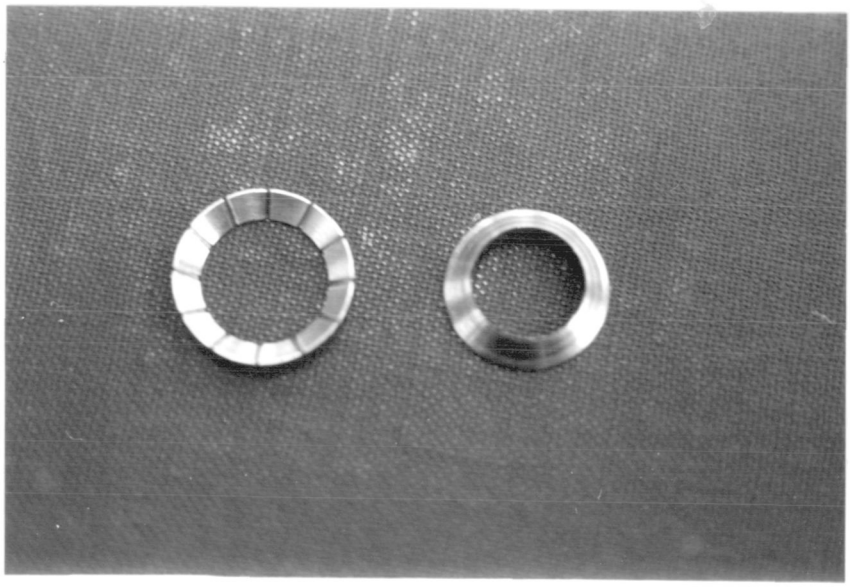


Figure 4.2.4 : Burner and atomiser arrangements for spray-flame experiments.



Nozzle diameter (mm)
1 → 1.2
2 → 0.75
3 → 0.5

Fuel-"cap" nozzles



Air-shroud

Figure 4.2.5 : Details of the air-blast atomiser.

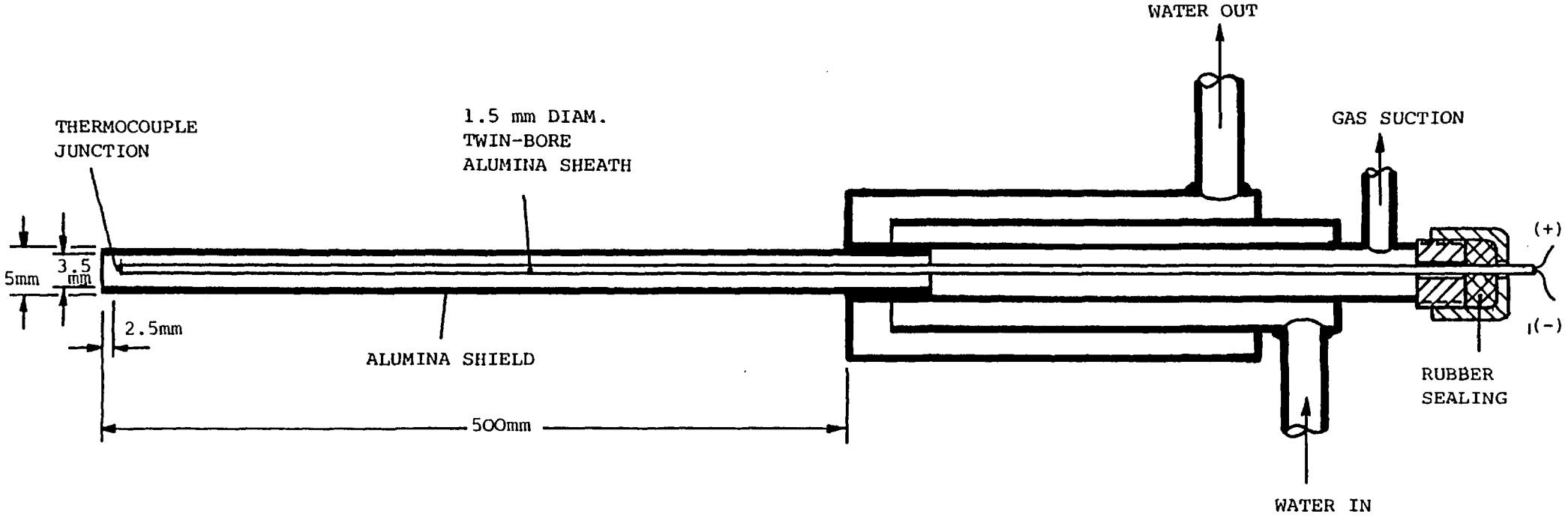


Figure 4.2.6 : The suction pyrometer.

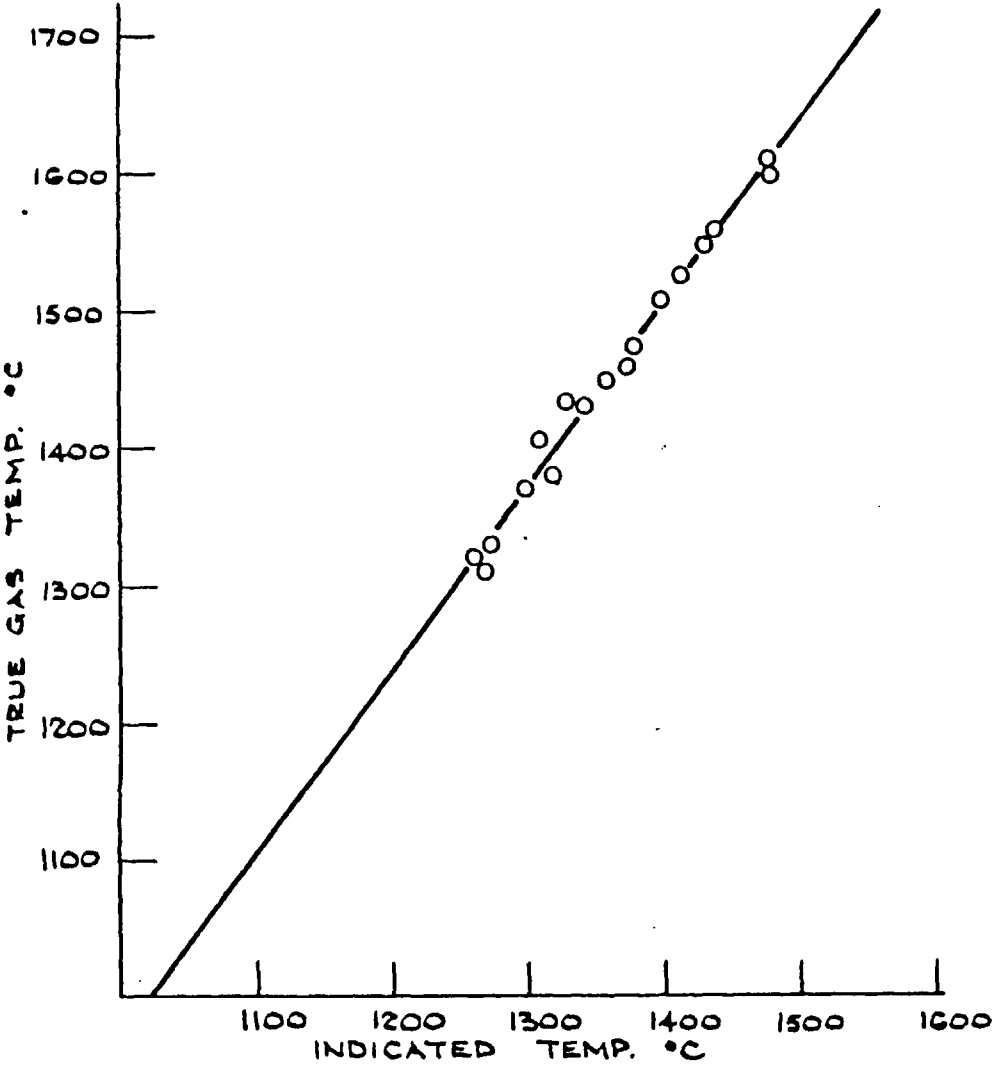


Figure 4.2.7 : Calibration curve for uncooled micro-suction pyrometer.

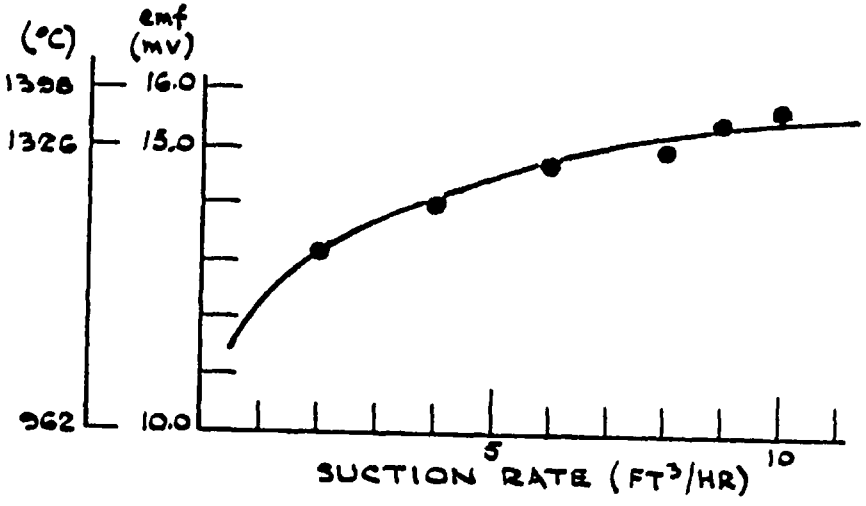
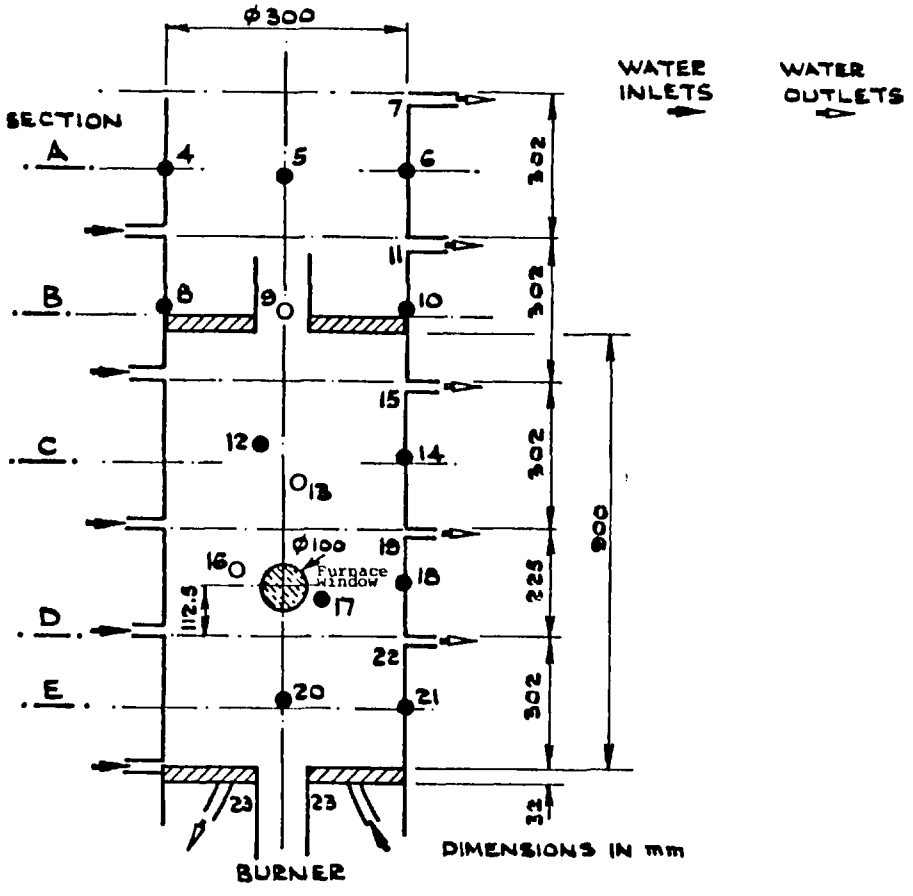


Figure 4.2.8 : Effect of suction rate.



● THERMO COUPLES ON LASER SIDE.

O THERMO COUPLES ON OTHER SIDE OF FURNACE.

THERMO COUPLES NOT SHOWN:-
Nos. 1&2. WATER INLET, LOCATED AT PUMP MANIFOLD.
No. 3. EXHAUST GAS, LOCATED ON TOP-PLATE OF FURNACE.
No. 24. ZERO TEMPERATURE.

Figure 4.2.9 : Thermocouple locations on furnace walls.

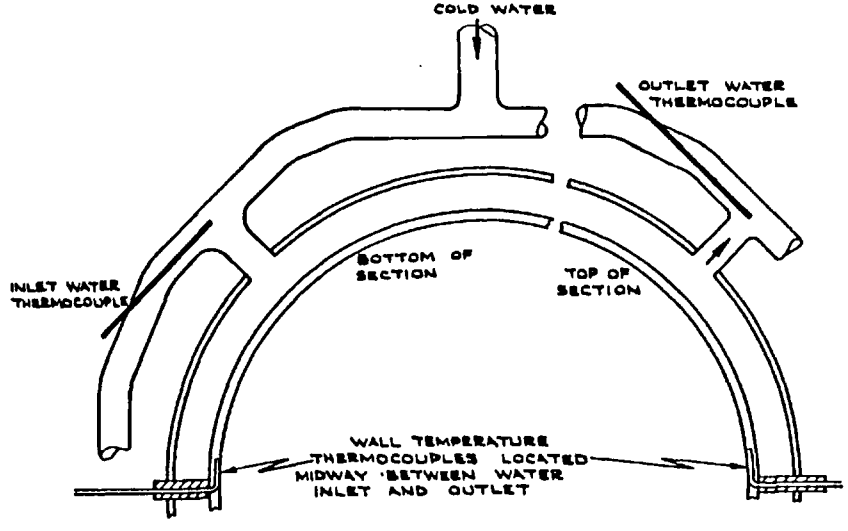


Figure 4.2.10 : Location of thermocouples on the furnace walls.

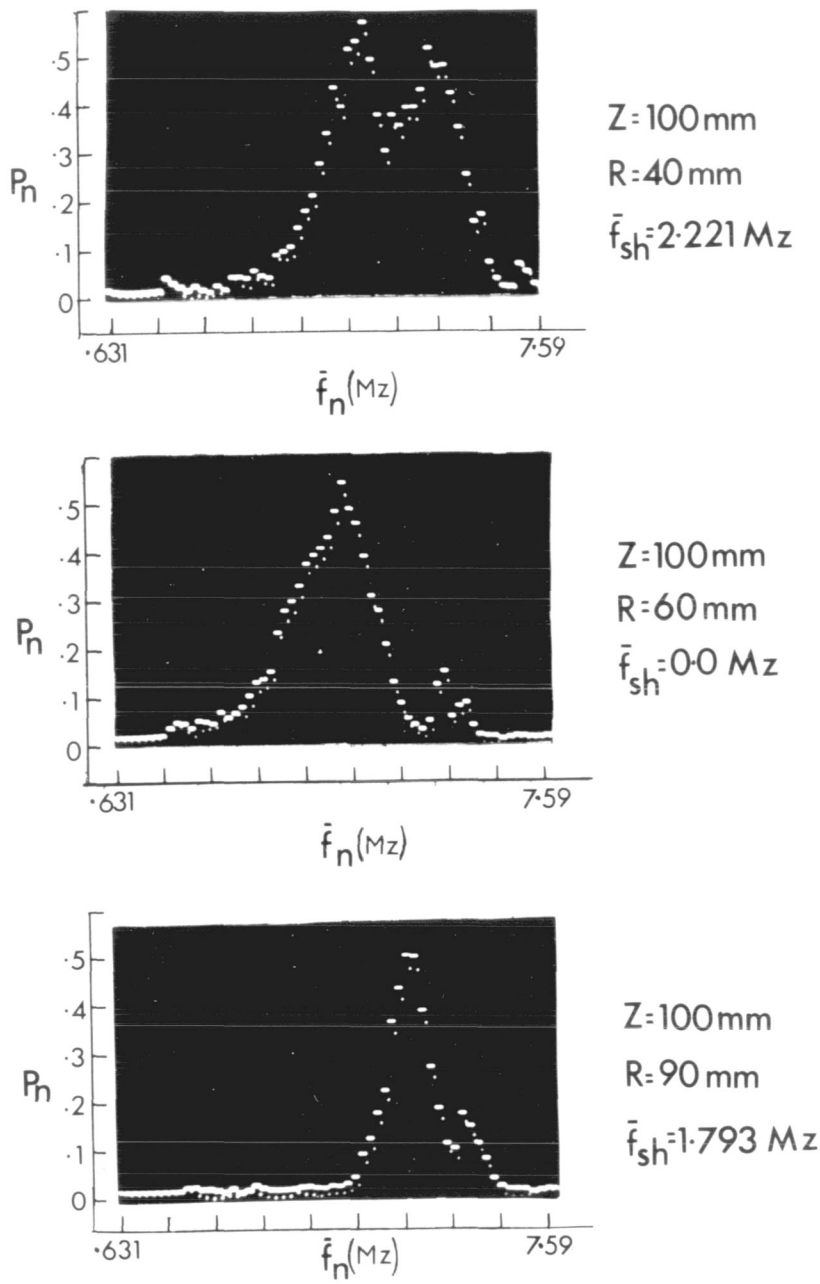


Figure 4.2.11 : Velocity p.d.f.'s in the spray flame .

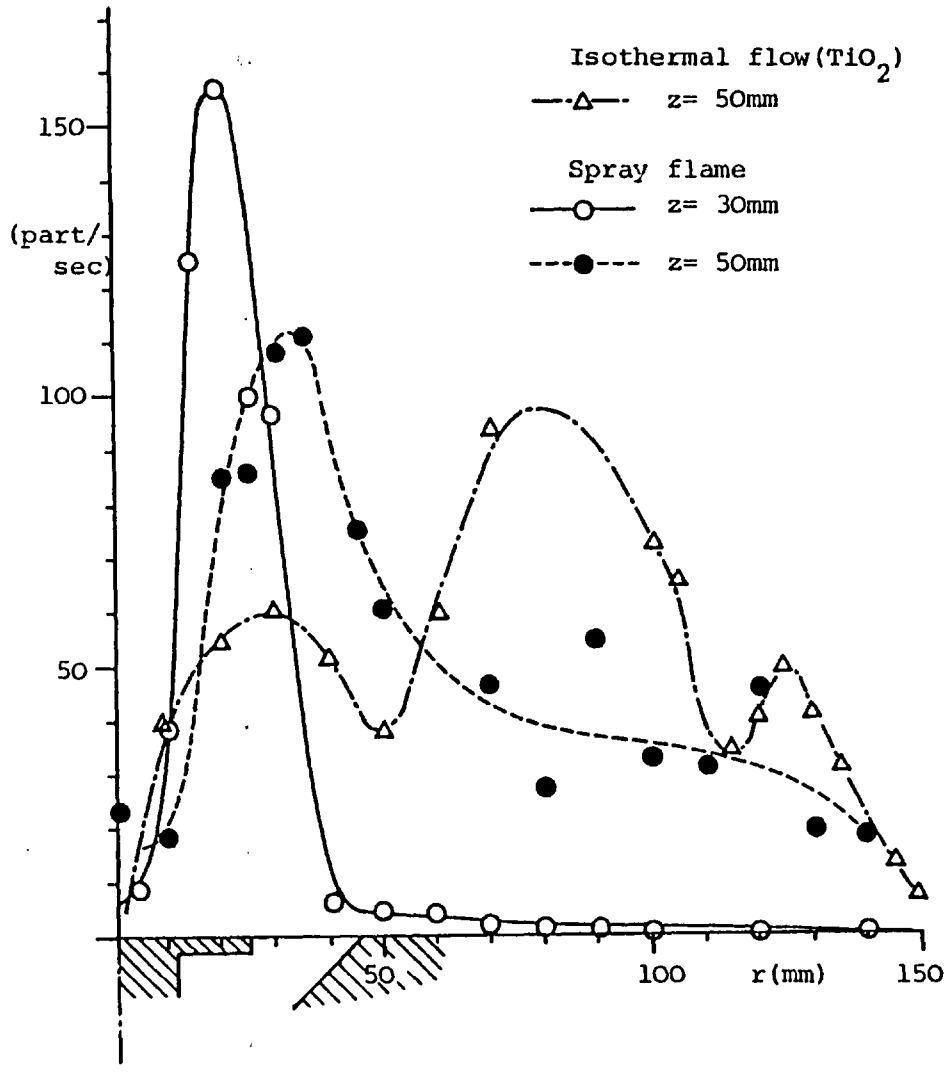
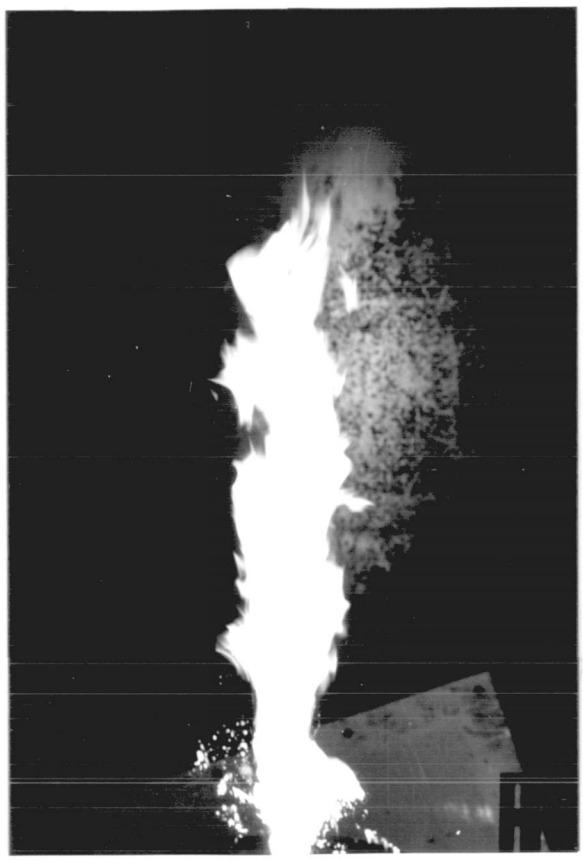


Figure 4.2.12 : Particle concentration around spray region.



Fuel nozzle diam.: 0.5mm

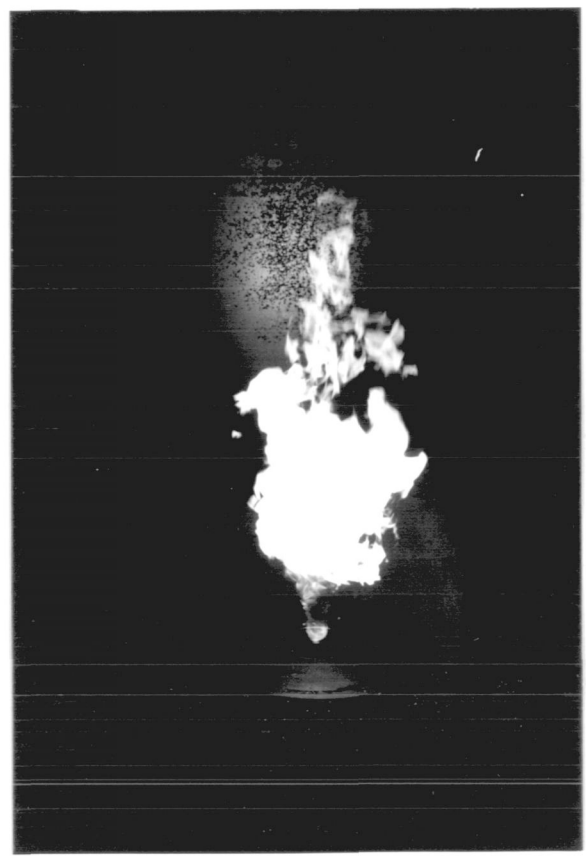
Δp_{fuel} = 5psi

$p_{a,a}$ =20psi

No combustion Air

Length of flame : 670 mm

Width of flame : 120 mm



Fuel nozzle diam.: 0.5mm

Δp_{fuel} = 5psi

$p_{a,a}$ =20psi

$p_{c,a}$ = 2psi

Length of flame : 450 mm

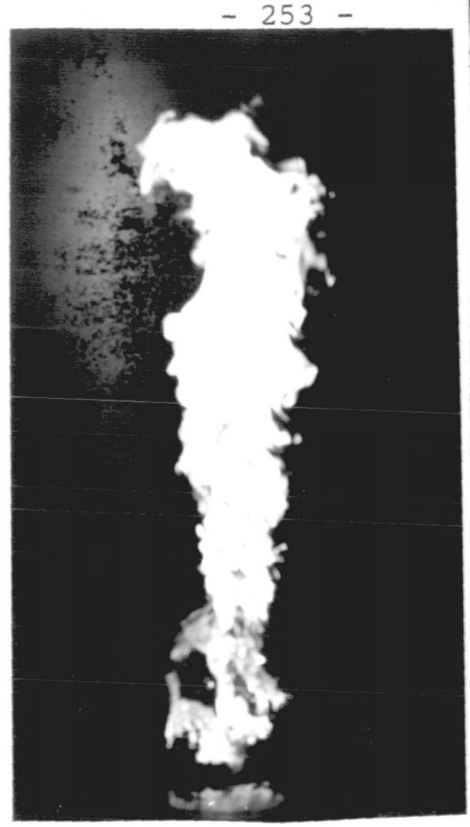
Width of flame : 220 mm

Figure 4.2.13a : Effect of fuel nozzle diameter and combustion air on flame characteristics.

Fuel nozzle diameter : 0.75mm

Δp_{fuel} = 5psi

$p_{a,a}$ =20psi



No combustion Air
Length of flame : 750 mm
Width of flame : 120 mm



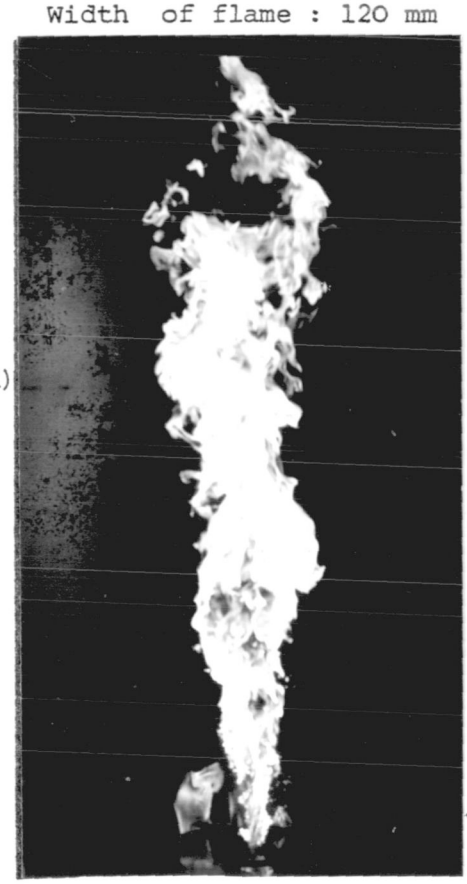
$p_{c,a}$ = 2psi
Length of flame :600 mm
Width of flame :200 mm

Fuel nozzle diameter : 1.2mm

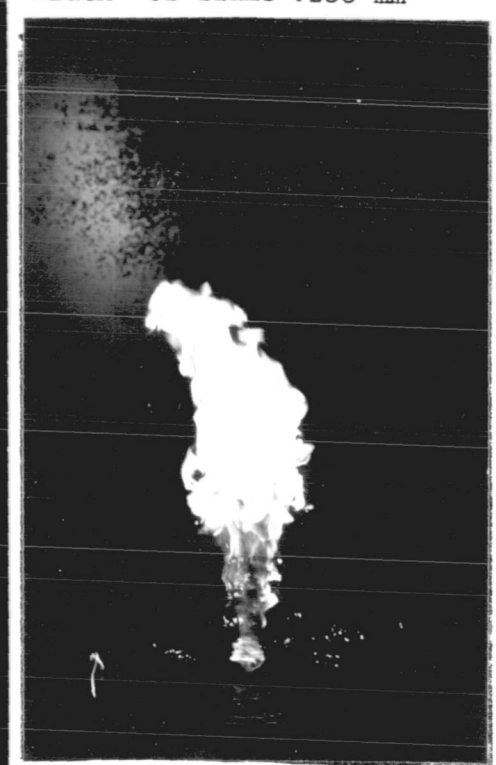
(Overspill Attached)

Δp_{fuel} = 5psi

$p_{a,a}$ =20psi

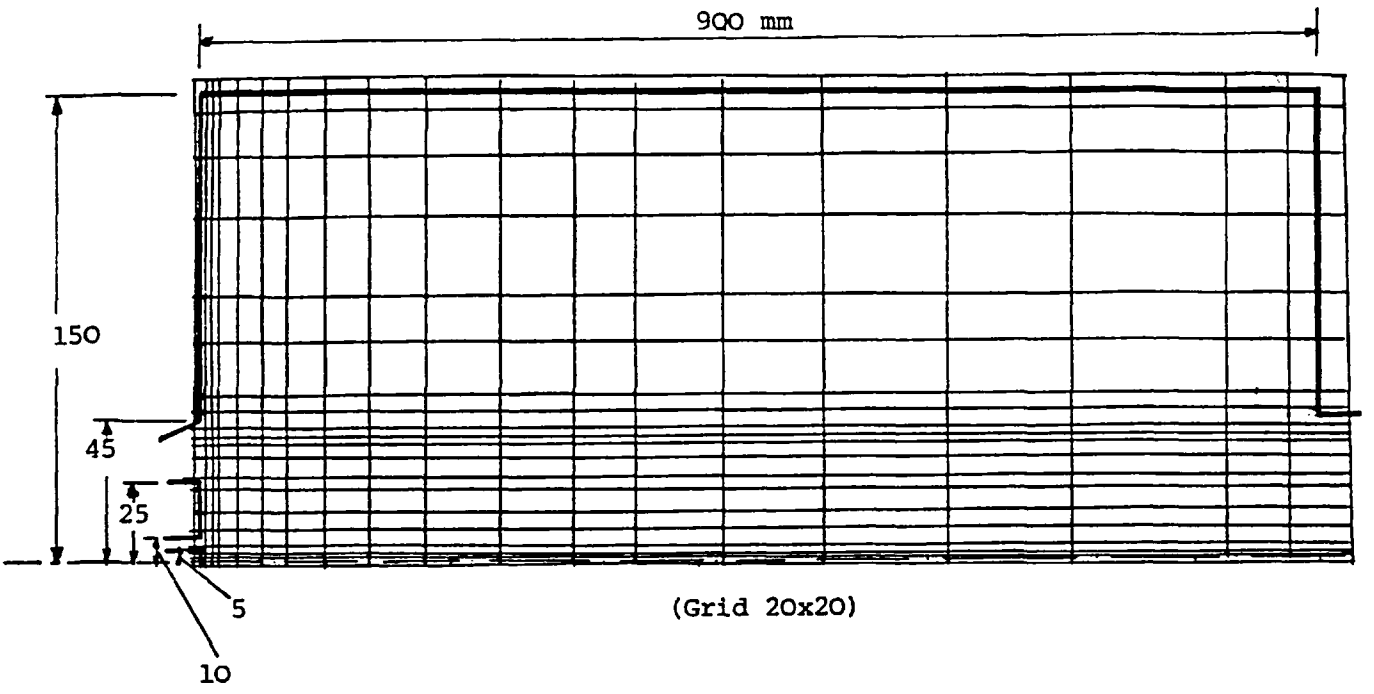


No Combustion Air
Length of flame :1000 mm
Width of flame : 100 mm



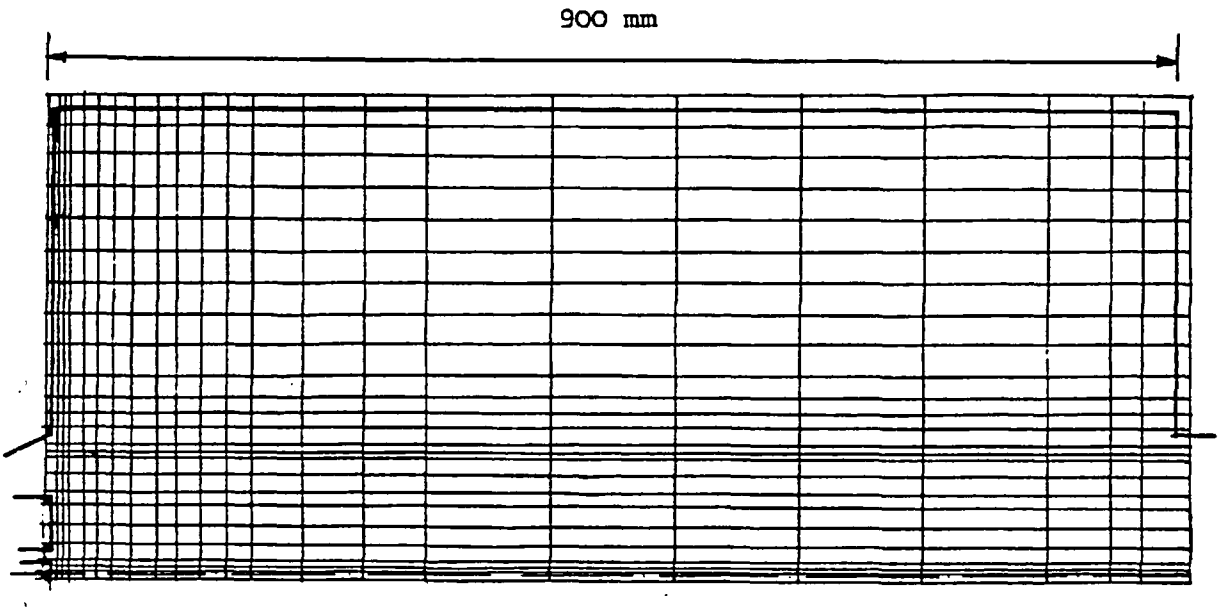
$p_{c,a}$ = 2psi
Length of flame :720 mm
Width of flame :170 mm

Figure 4.2.13b : Effect of fuel nozzle diameter and combustion air on flame characteristics.



(Grid 20x20)

Dimensions in mm



(Grid 25x25)

Figure 4.2.14 : Finite difference grid.

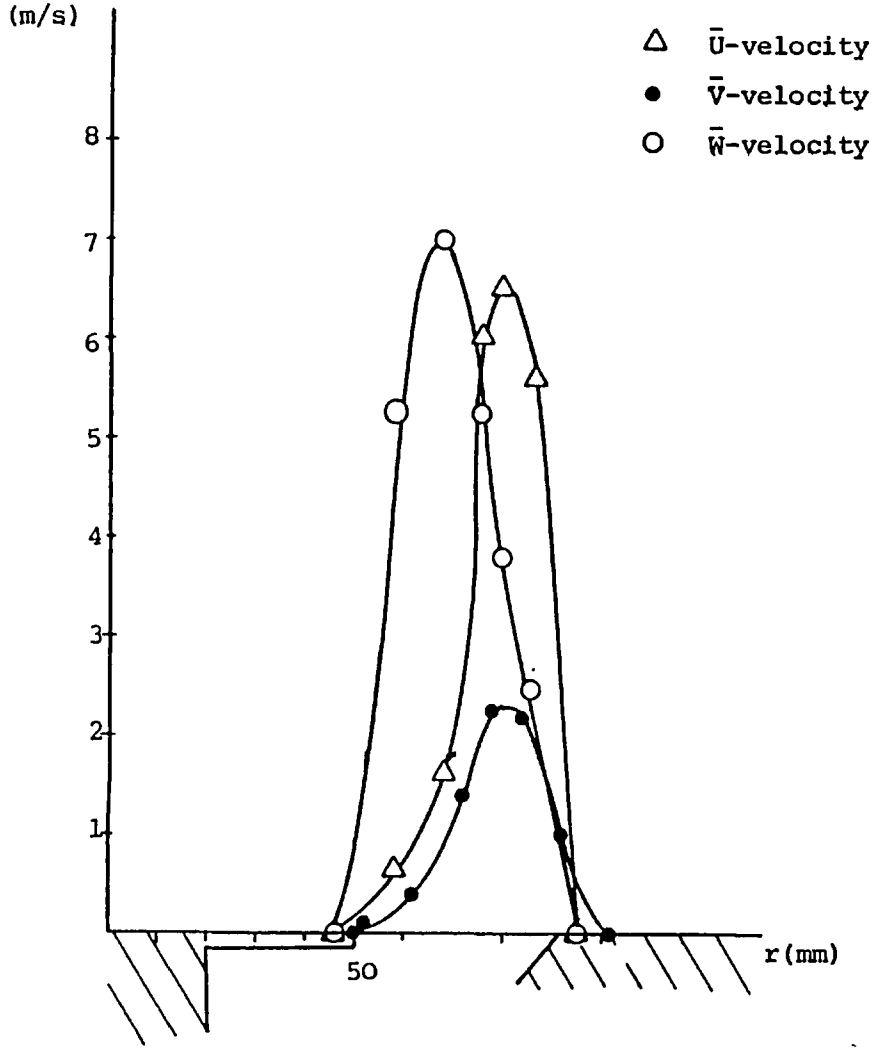


Figure 4.2.15 : Initial profiles used in the calculation procedure.

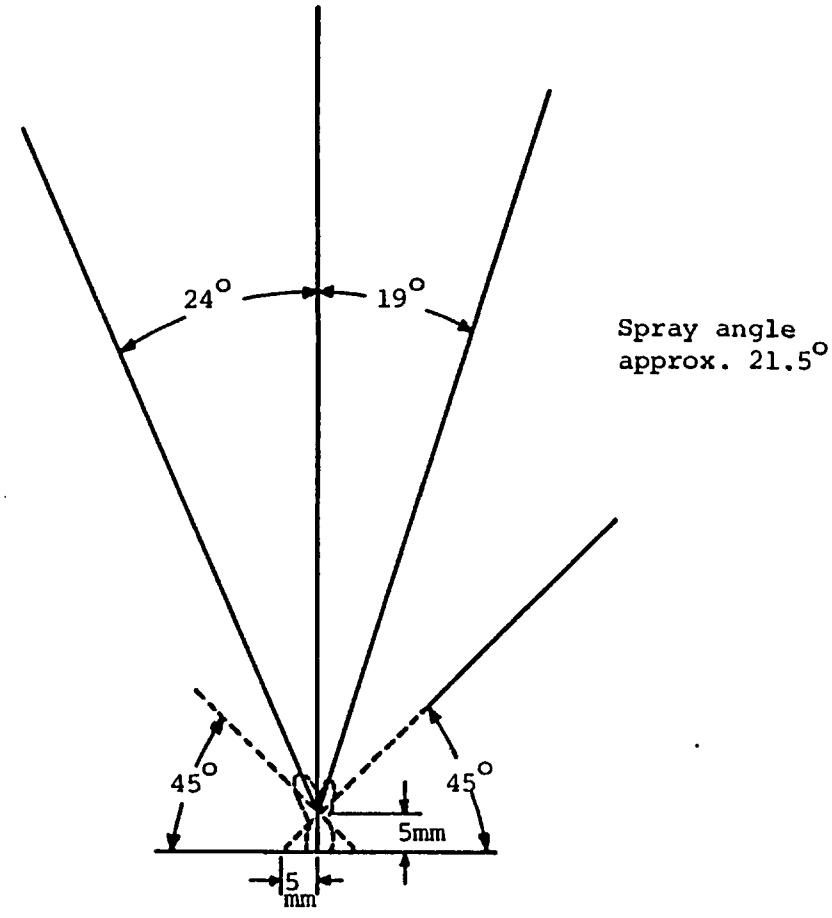


Figure 4.2.16 : Graphical reconstruction of the fuel spray and atomising air for calculation purposes.

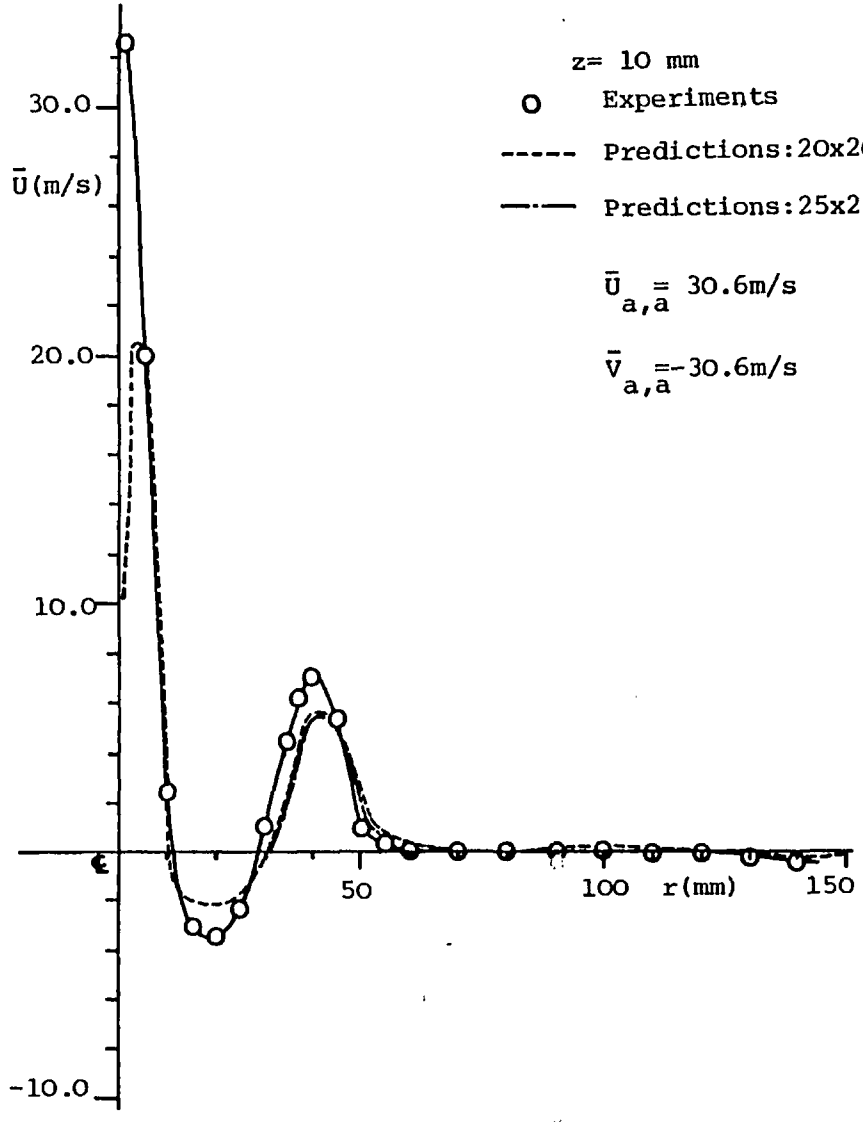


Figure 4.2.17 : Predicted axial velocities for two atomising-air velocities.

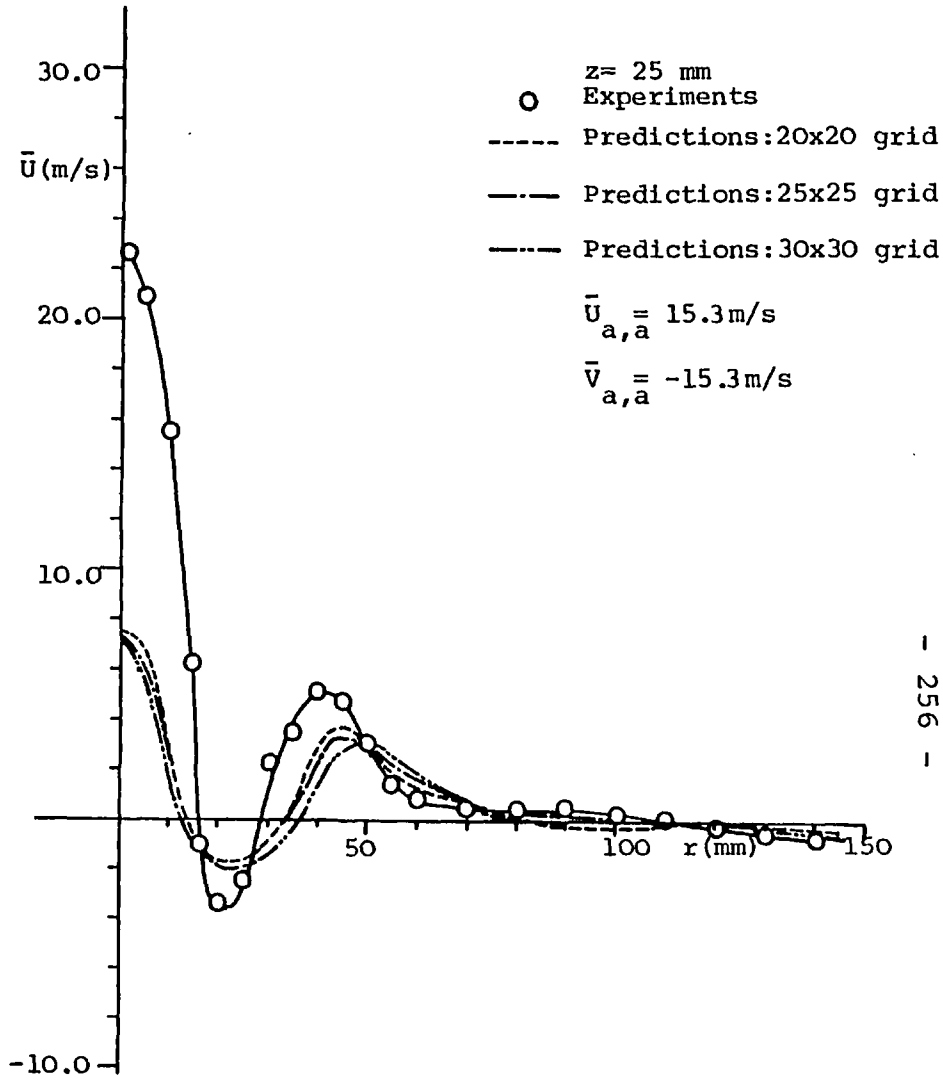


Figure 4.2.18 : Predicted axial velocities for different grid distributions.

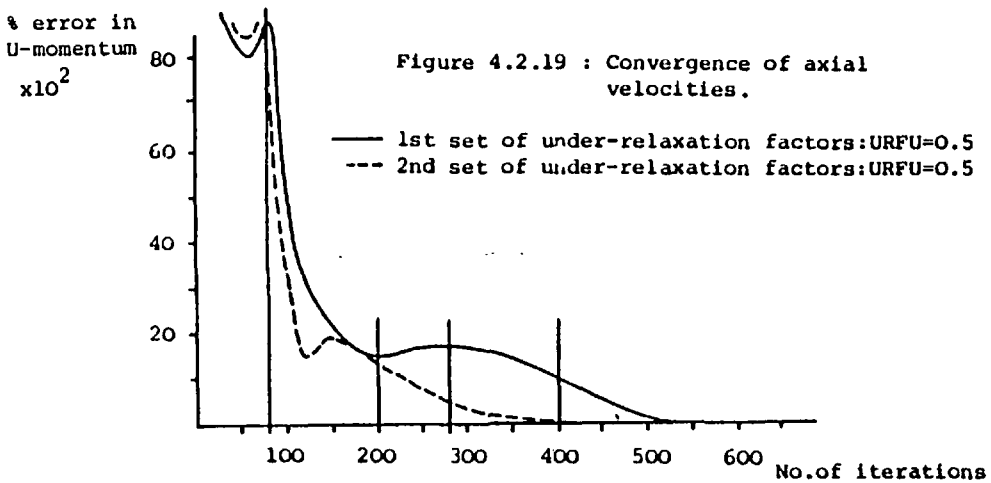


Figure 4.2.19 : Convergence of axial velocities.

—— 1st set of under-relaxation factors:URFU=0.5
--- 2nd set of under-relaxation factors:URFU=0.5

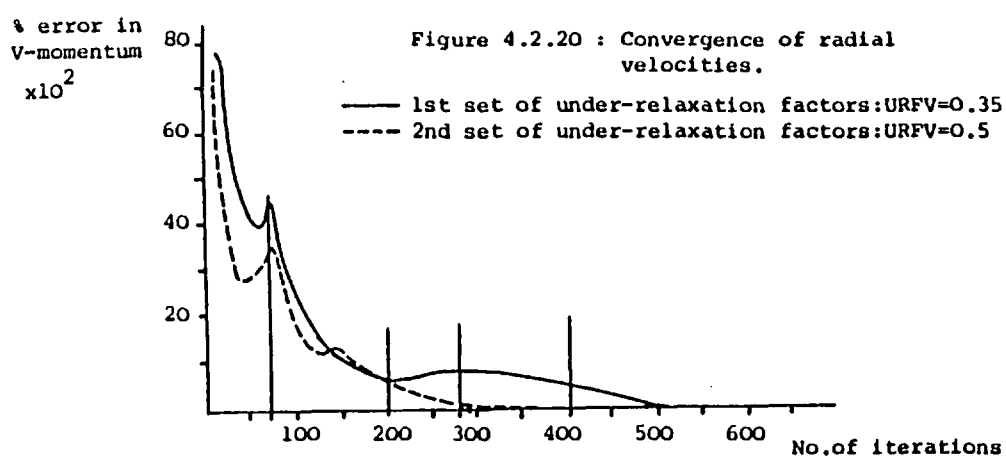


Figure 4.2.20 : Convergence of radial velocities.

—— 1st set of under-relaxation factors:URFV=0.35
---- 2nd set of under-relaxation factors:URFV=0.5

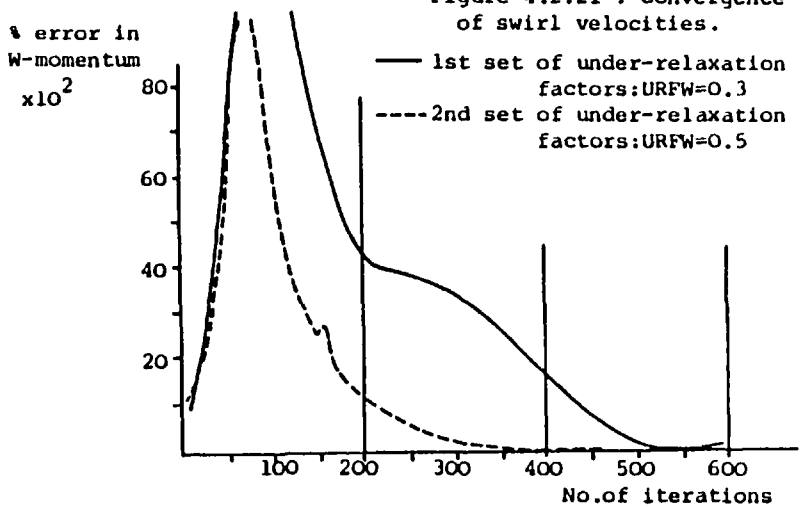


Figure 4.2.21 : Convergence of swirl velocities.

—— 1st set of under-relaxation factors:URFW=0.3
----2nd set of under-relaxation factors:URFW=0.5

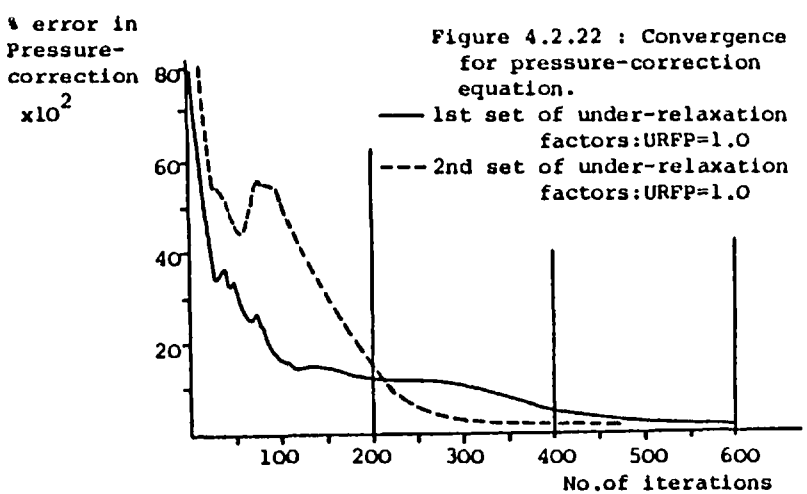


Figure 4.2.22 : Convergence for pressure-correction equation.

—— 1st set of under-relaxation factors:URFP=1.0
---2nd set of under-relaxation factors:URFP=1.0

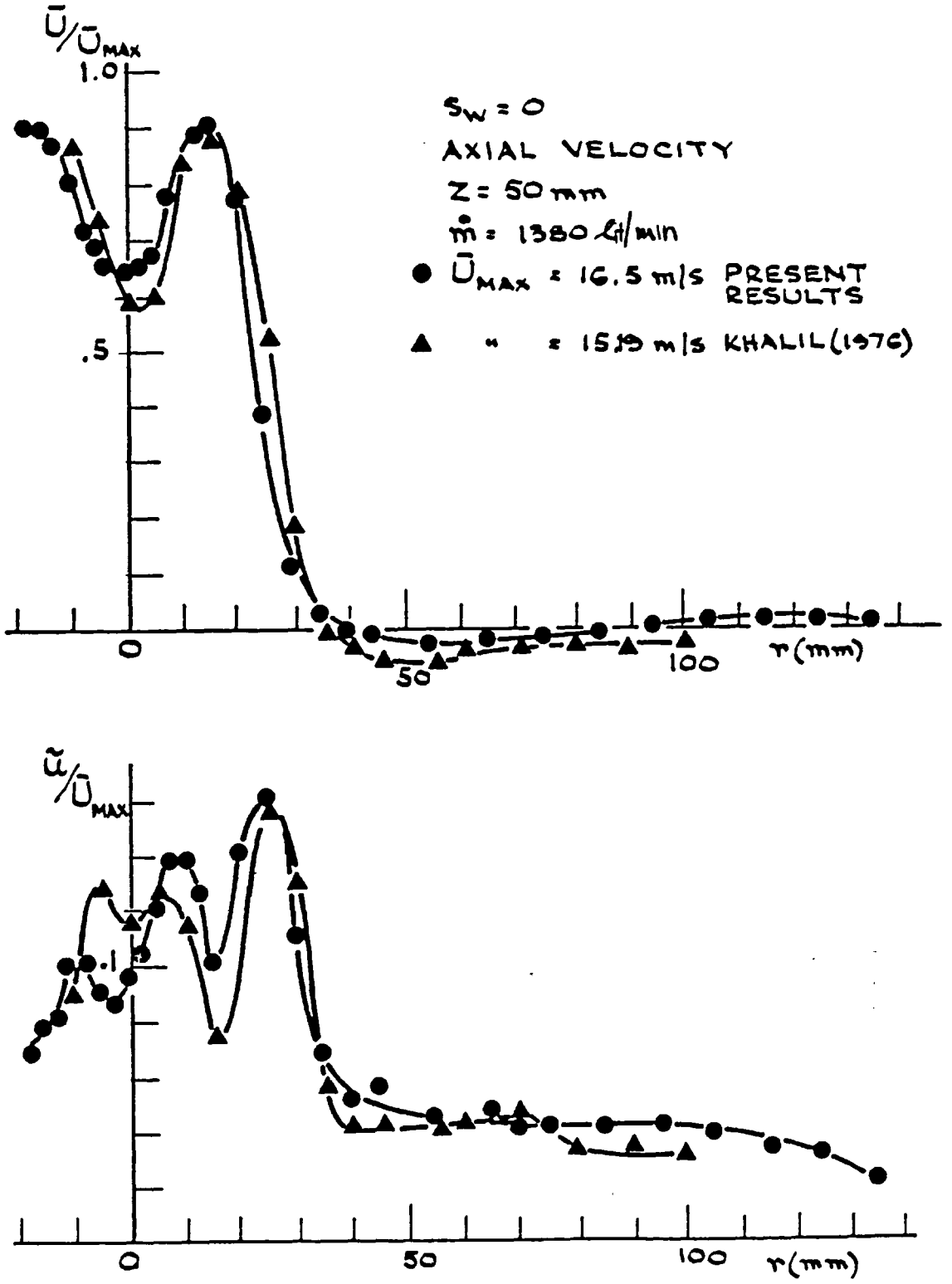


Figure 4.3.1 : Reproducibility of axial velocities for S_w=0.0

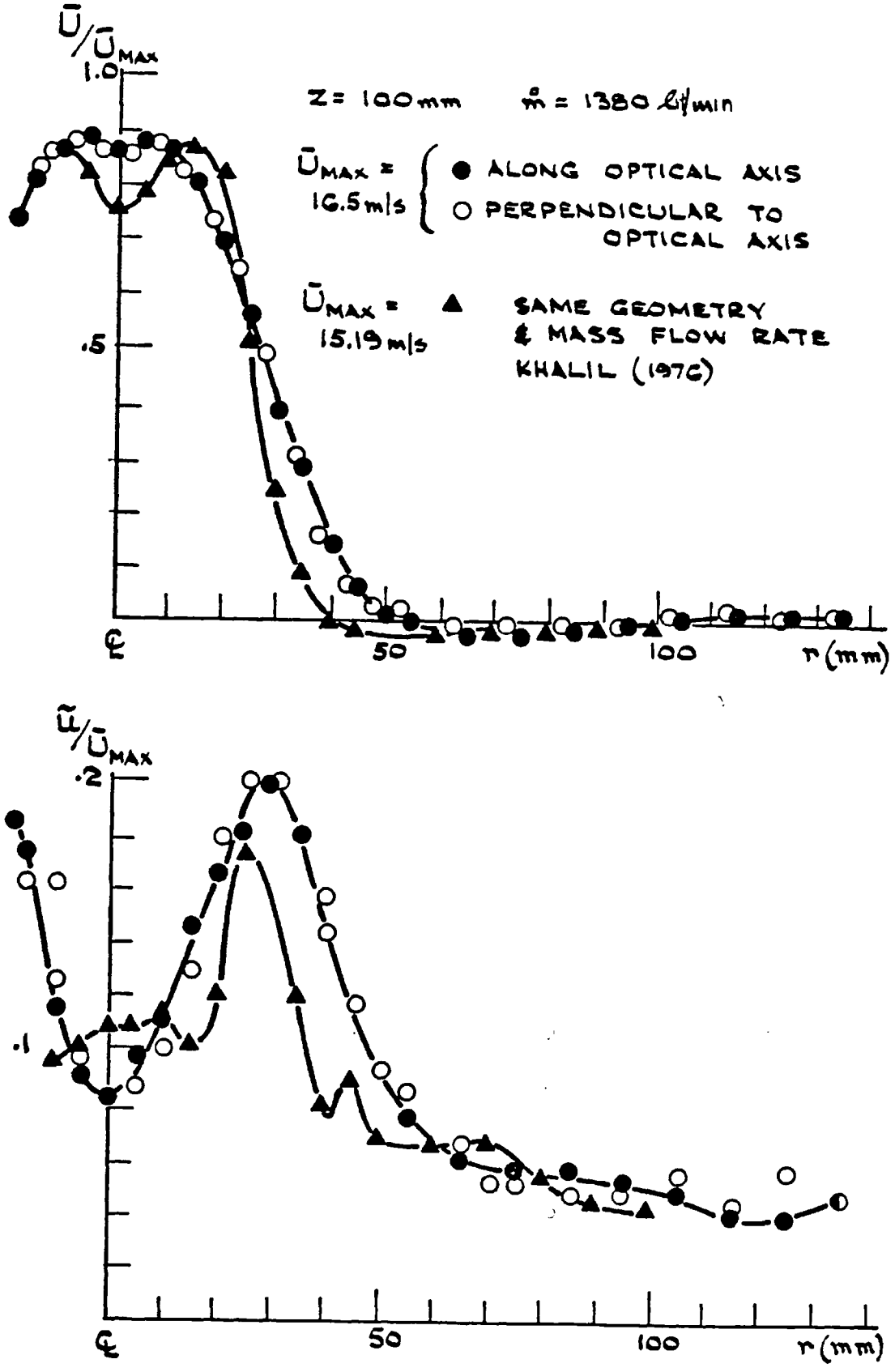


Figure 4.3.2 : Symmetry of axial velocities for S_w=0.0

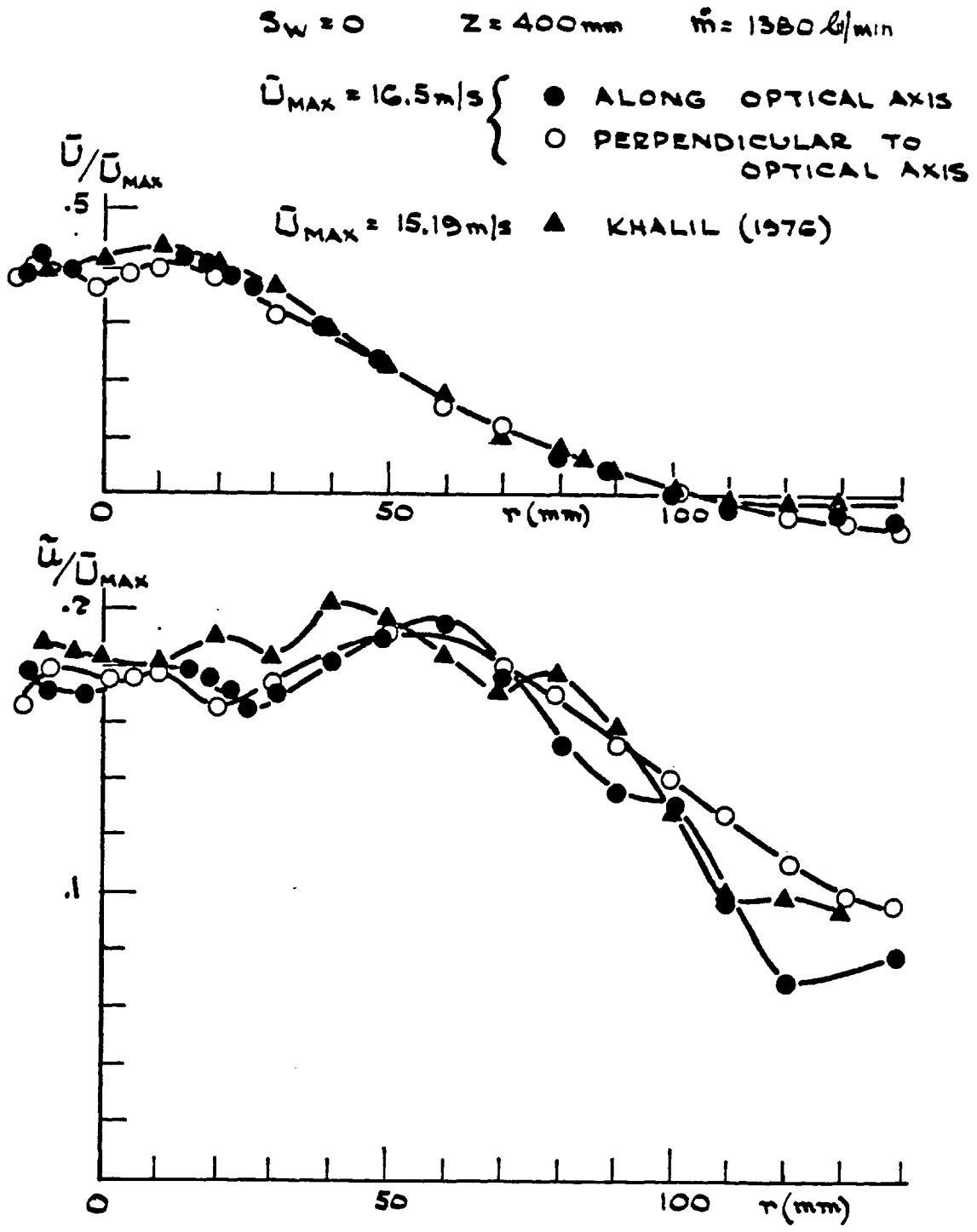


Figure 4.3.3 : Symmetry of axial velocity for S_w=0.0

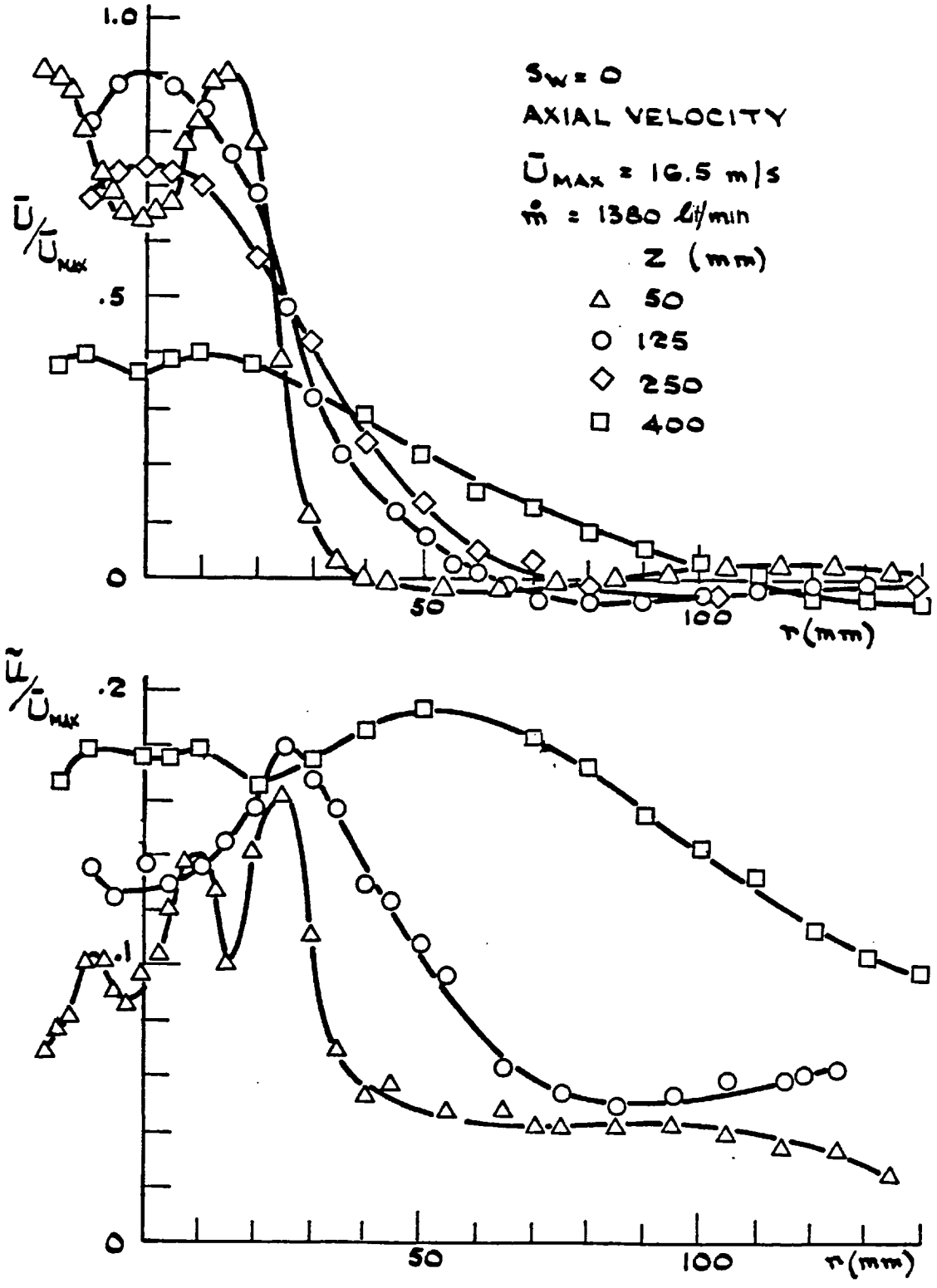


Figure 4.3.4 : Axial velocity profiles for S_w=0.0

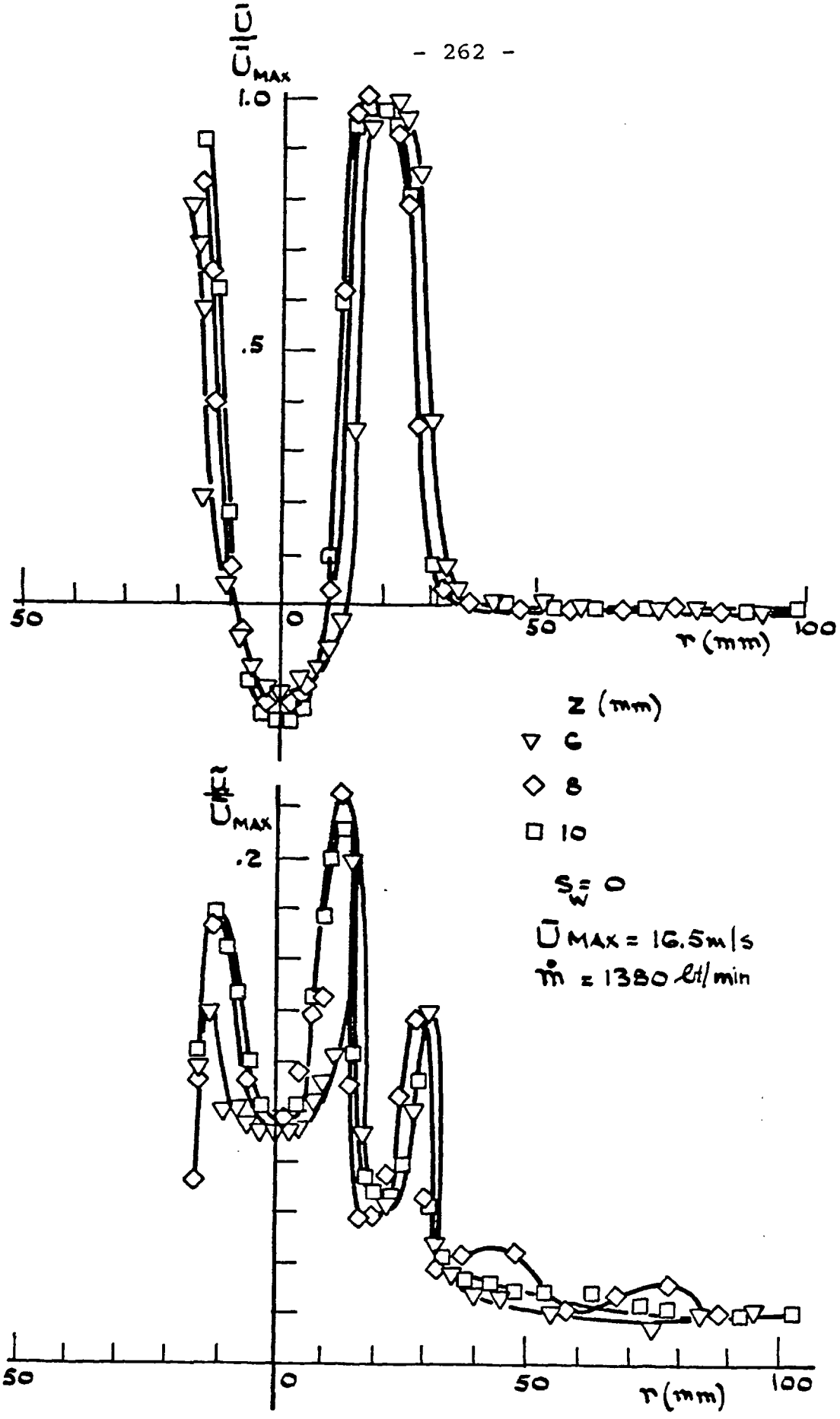


Figure 4.3.5 : Inlet axial velocities for S_w=0.0

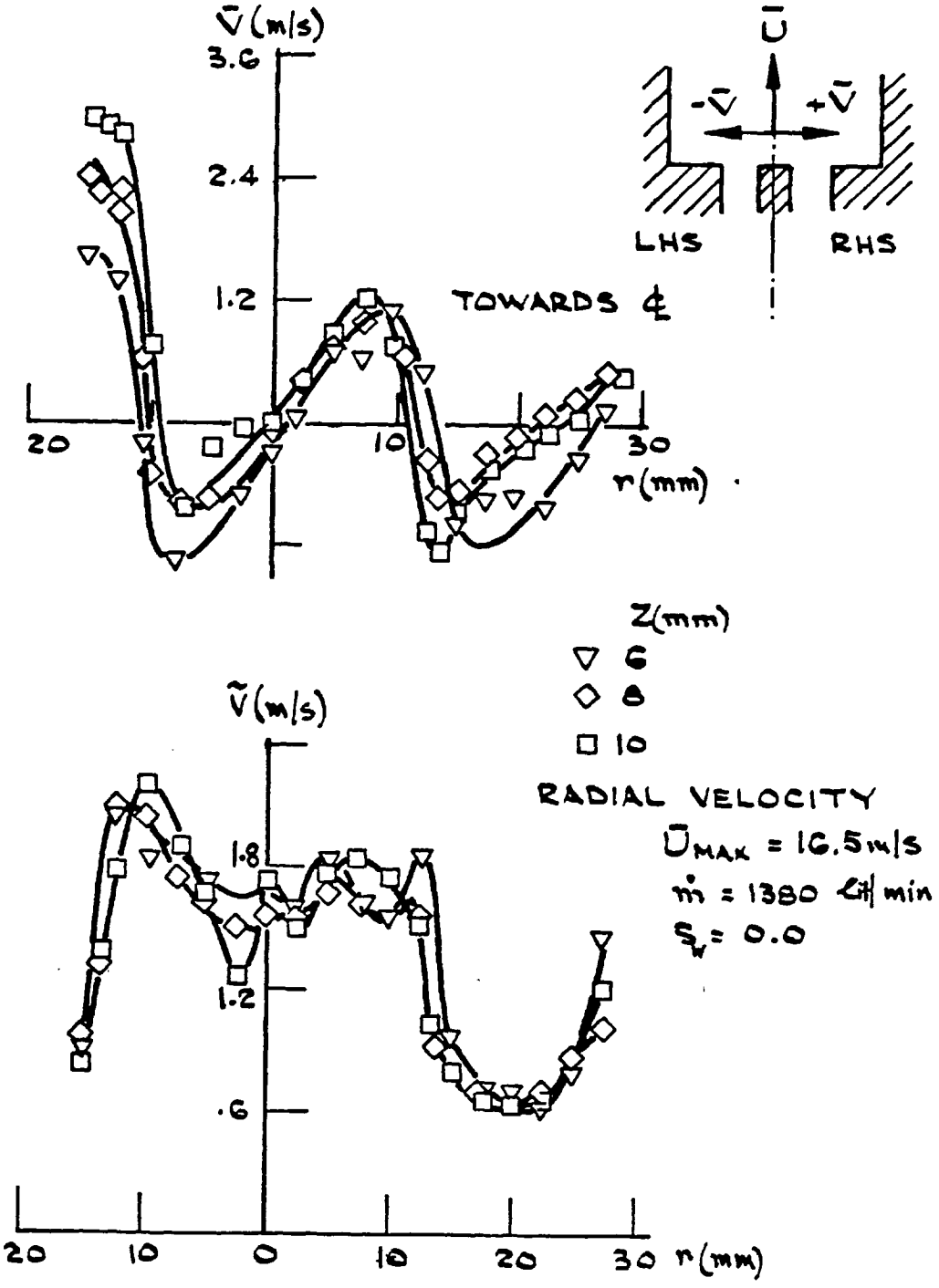


Figure 4.3.6 : Inlet radial velocities for S_w=0.0

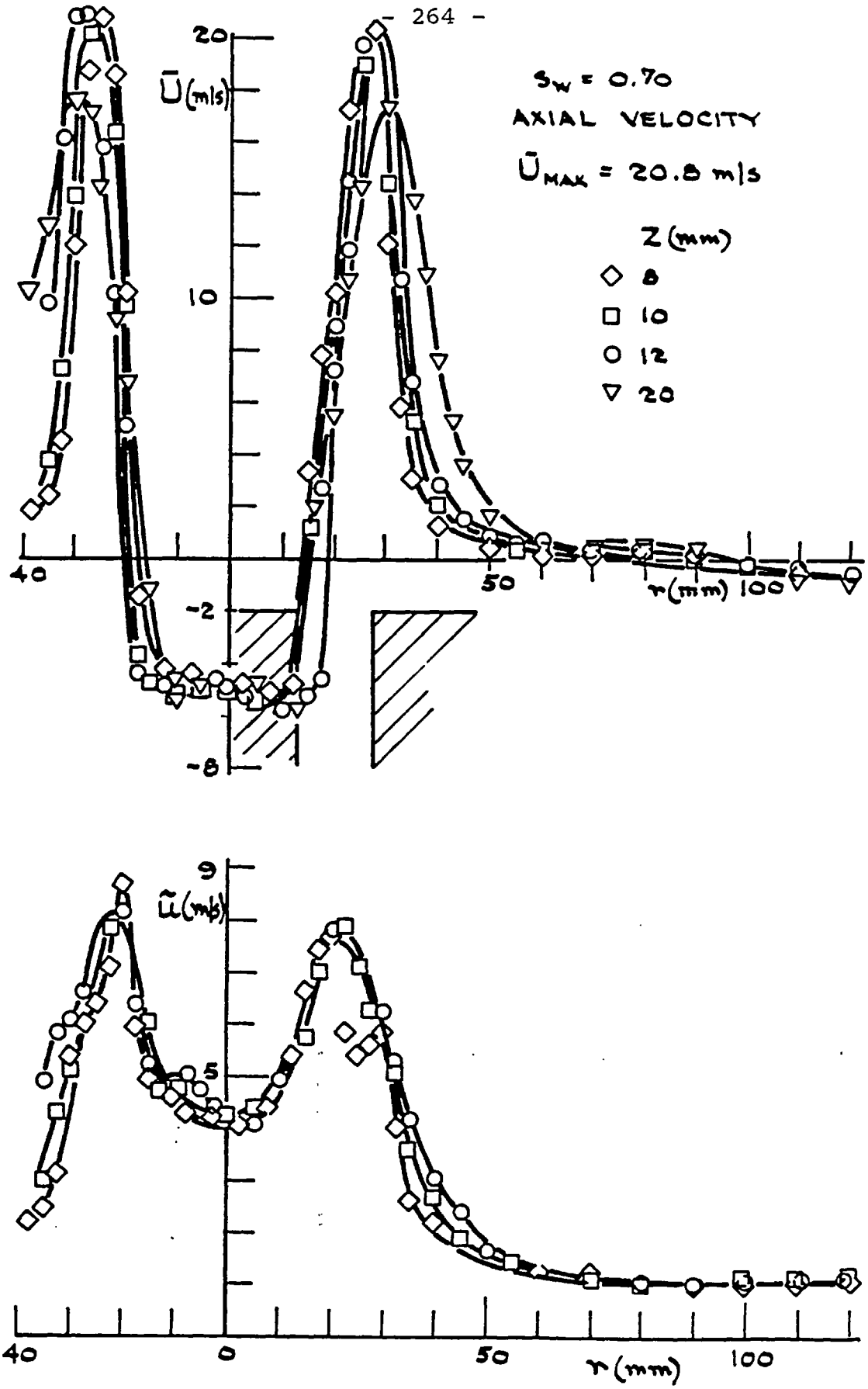


Figure 4.3.8 : Inlet axial velocities for S_w=0.70

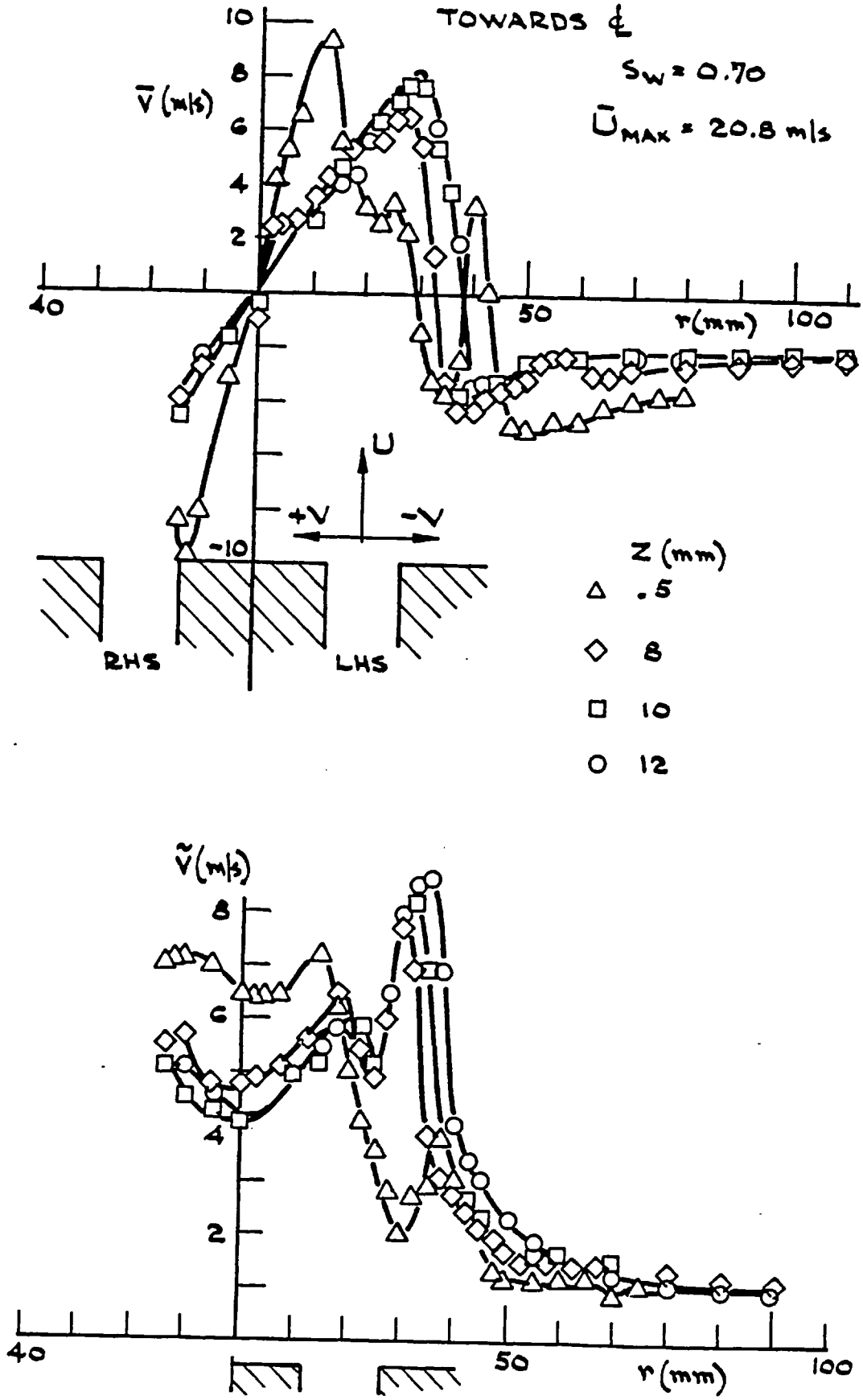


Figure 4.3.9 : Inlet radial velocities for S_w=0.70

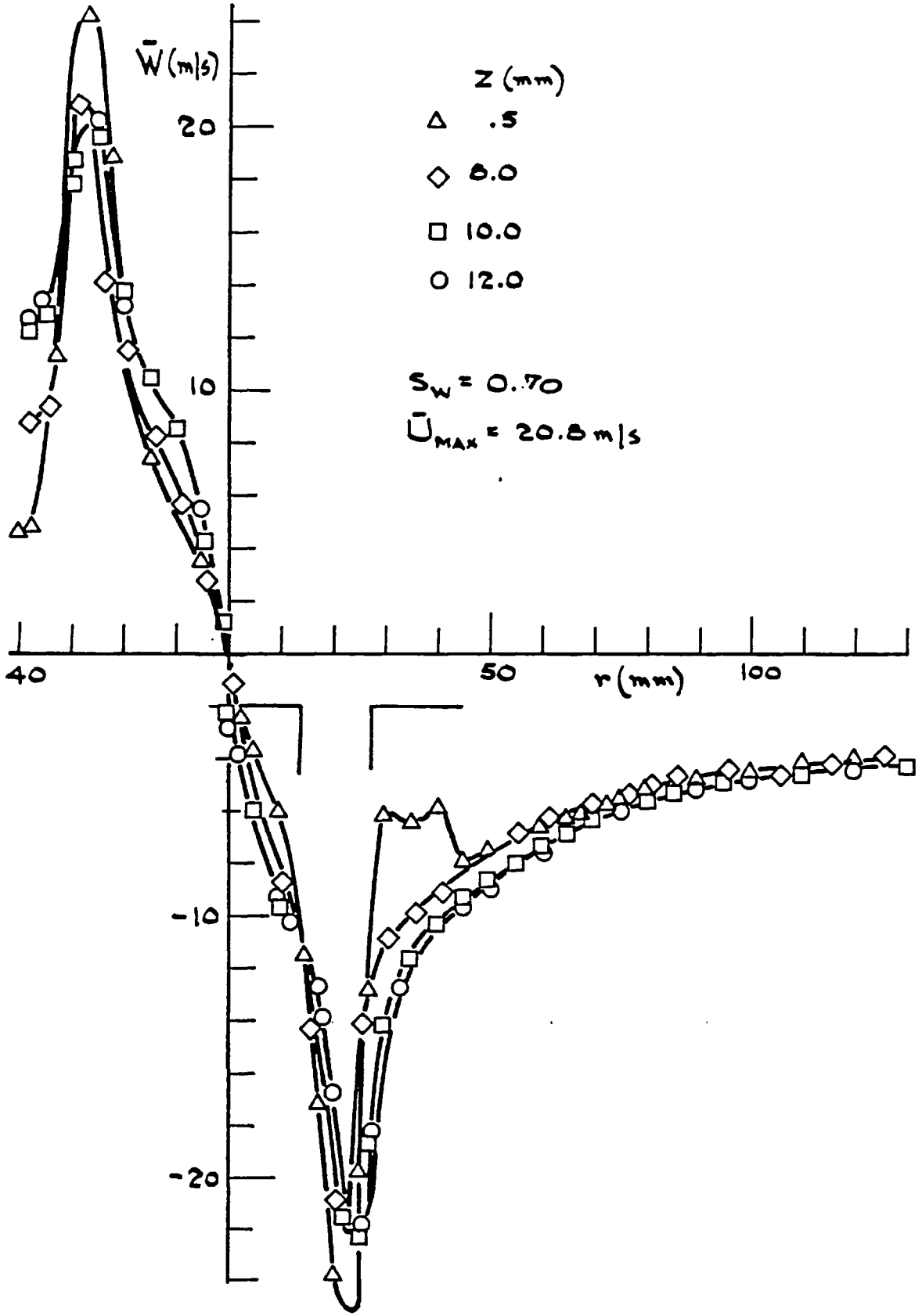


Figure 4.3.10a : Inlet mean circumferential velocities for S_w=0.70

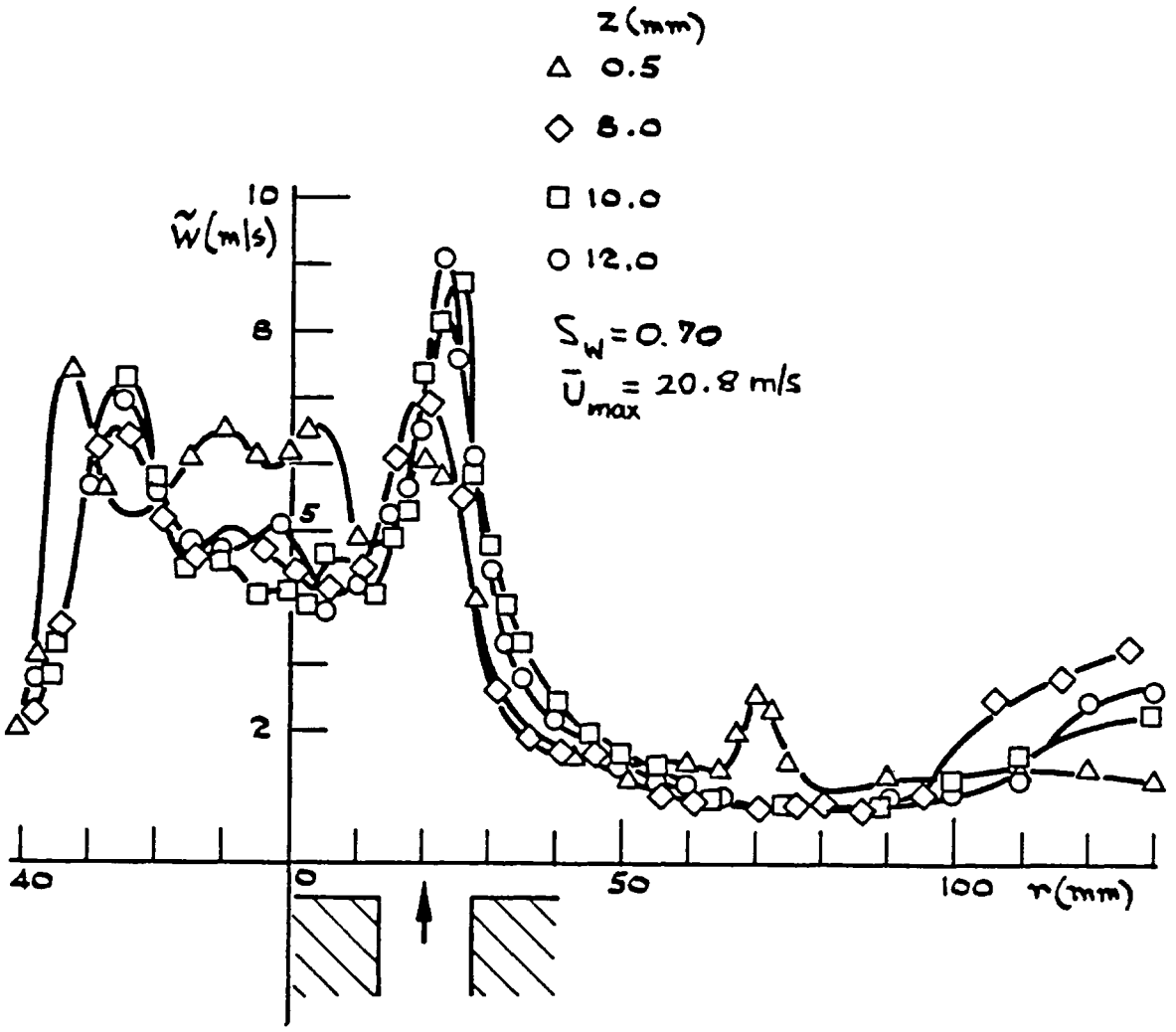


Figure 4.3.10b :Inlet fluctuating circumferential velocities for S_w=0.70

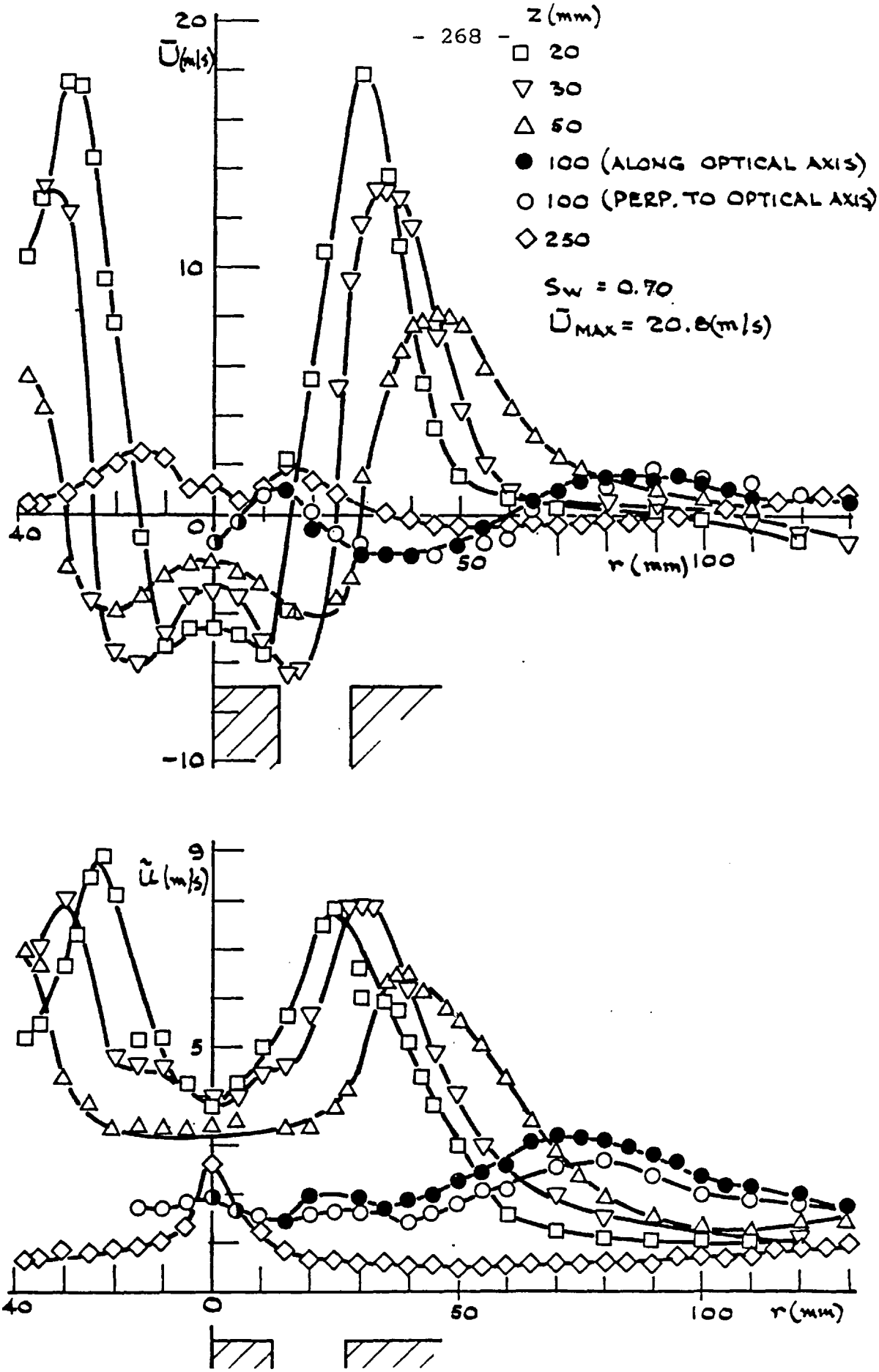


Figure 4.3.11 : Axial velocity profiles for S_w=0.70

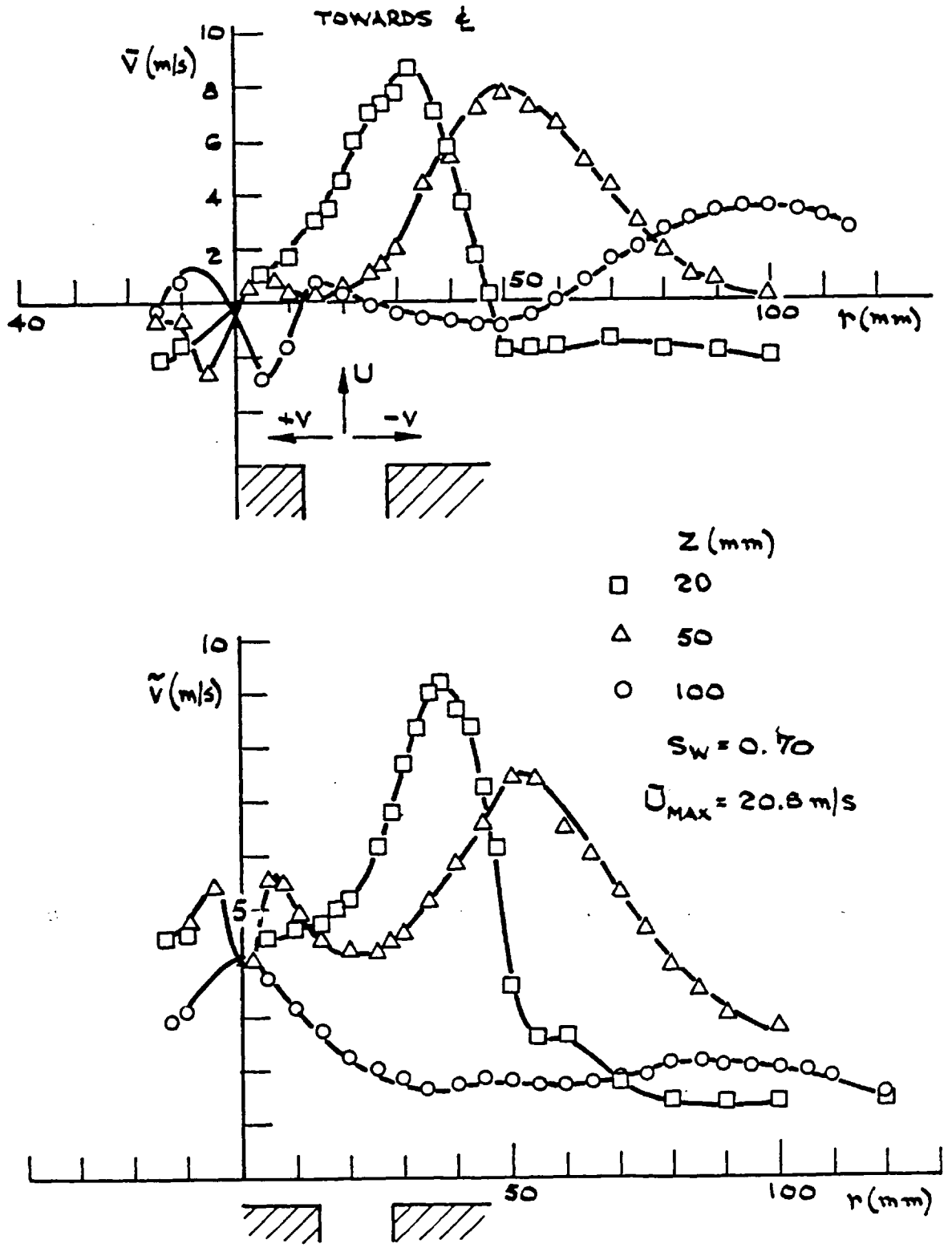


Figure 4.3.12. : Radial velocity profiles for S_w=0.70

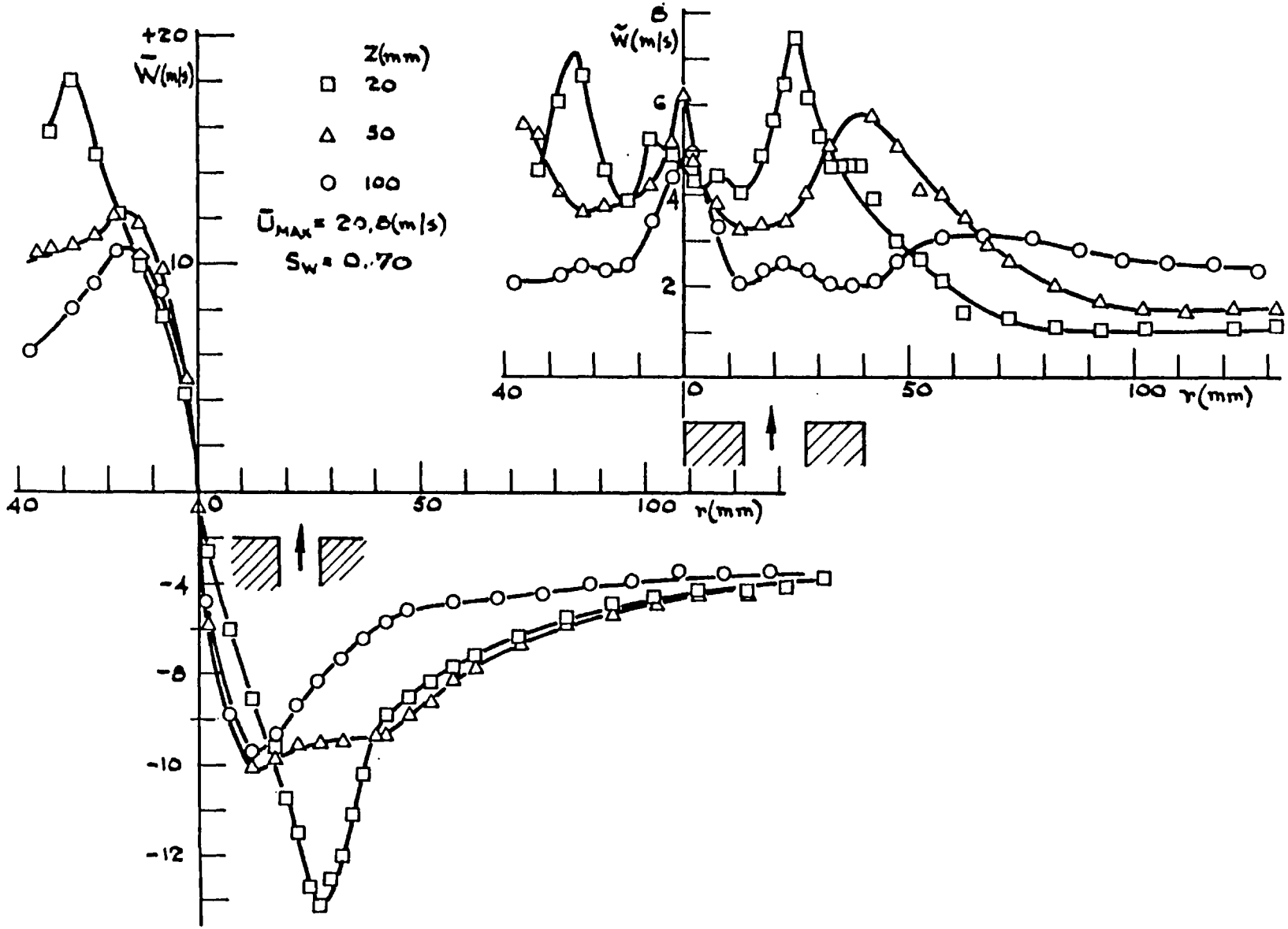


Figure 4.3.13 : Circuferential velocity profiles for S_w = 0.70

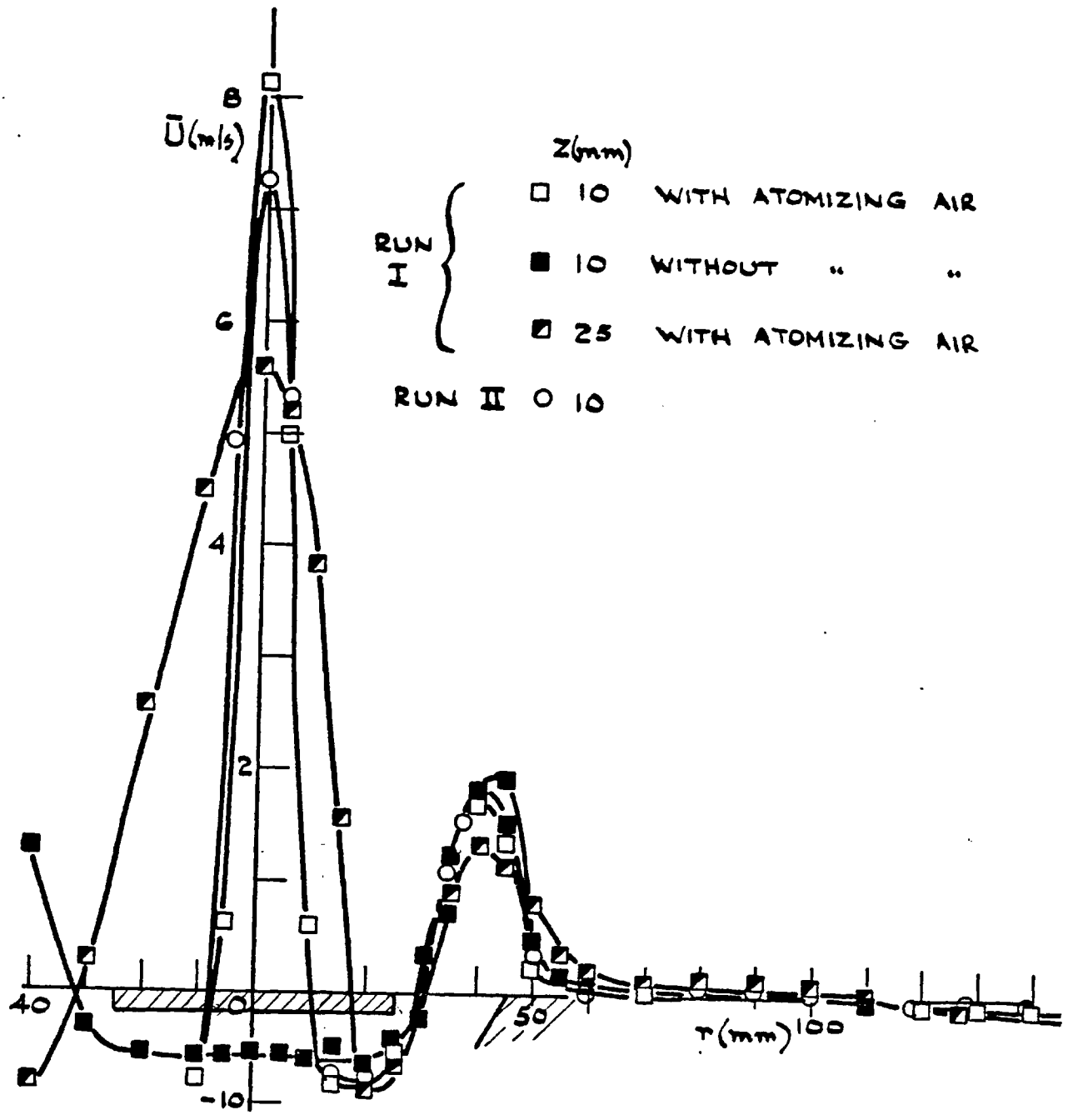


Figure 4.3.14a : Inlet axial mean velocities for isothermal flow with swirl and quarl.

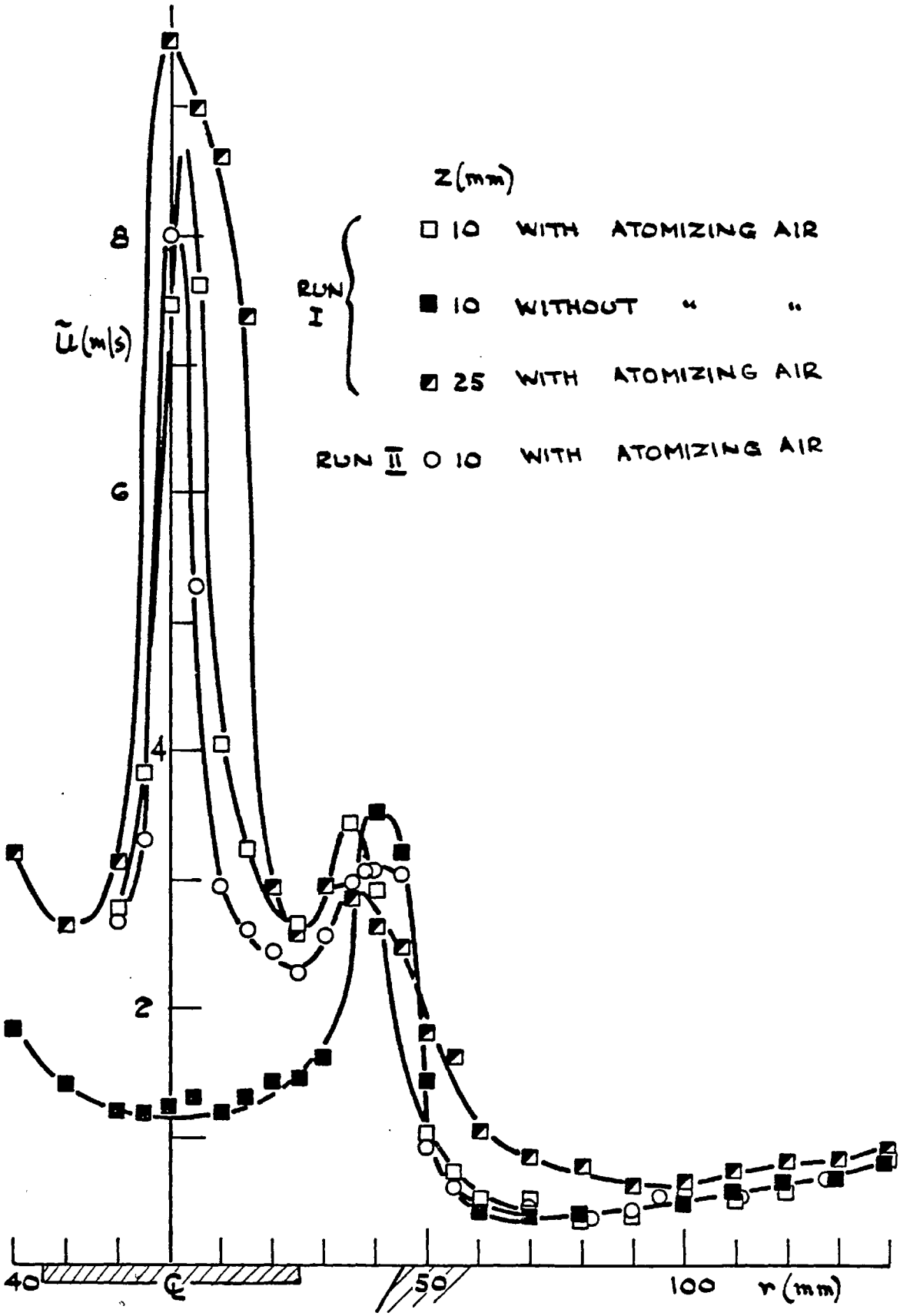


Figure 4.3.14b :Inlet axial normal stresses for isothermal flow with swirl and quarl.

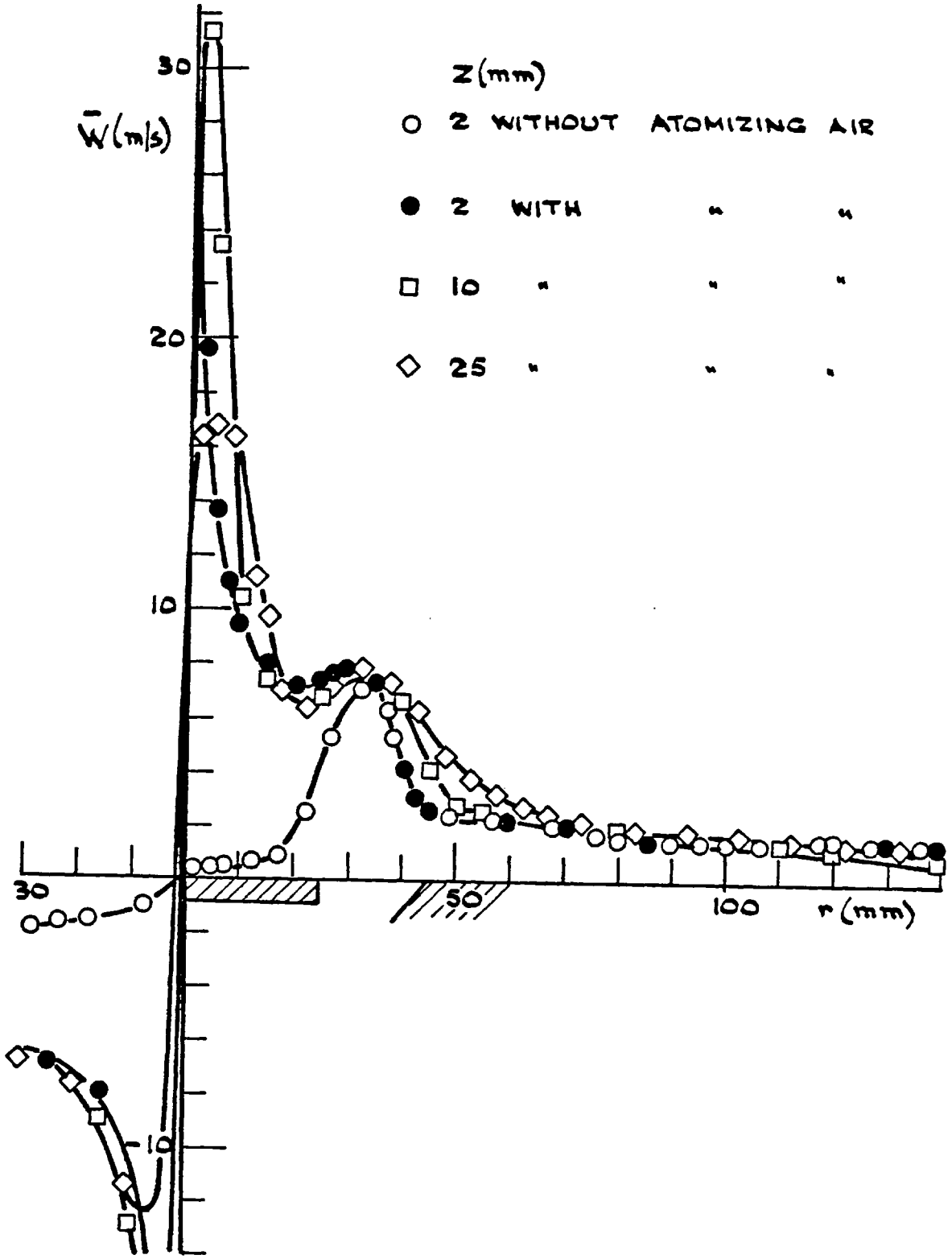


Figure 4.3.15 : Inlet mean tangential velocities for isothermal flow with swirl and quarl.

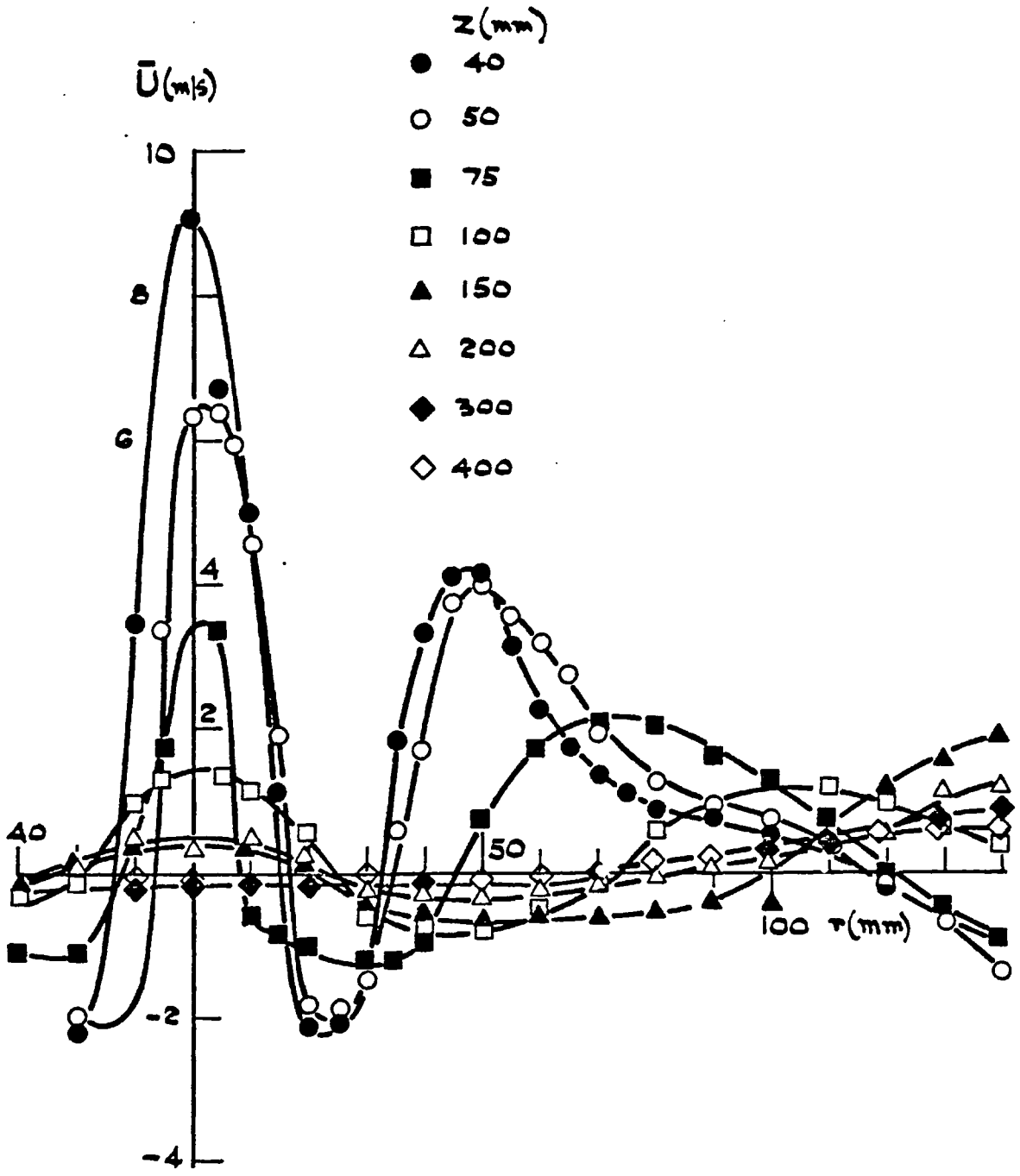


Figure 4.3.16a :Axial mean velocities for isothermal flow with swirl and quarl.

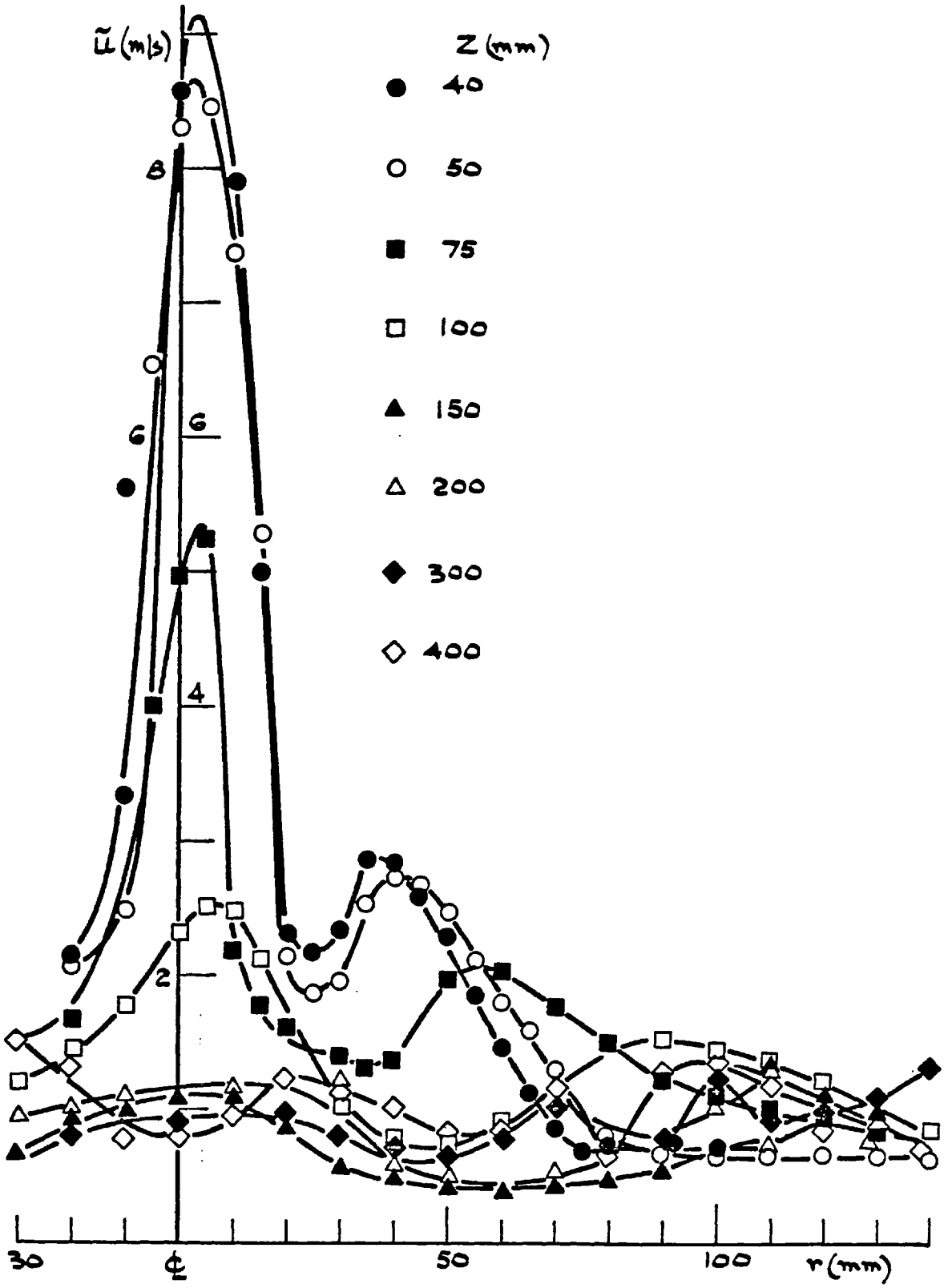


Figure 4.3.16b :Axial normal stresses for isothermal flow with swirl and quarl.

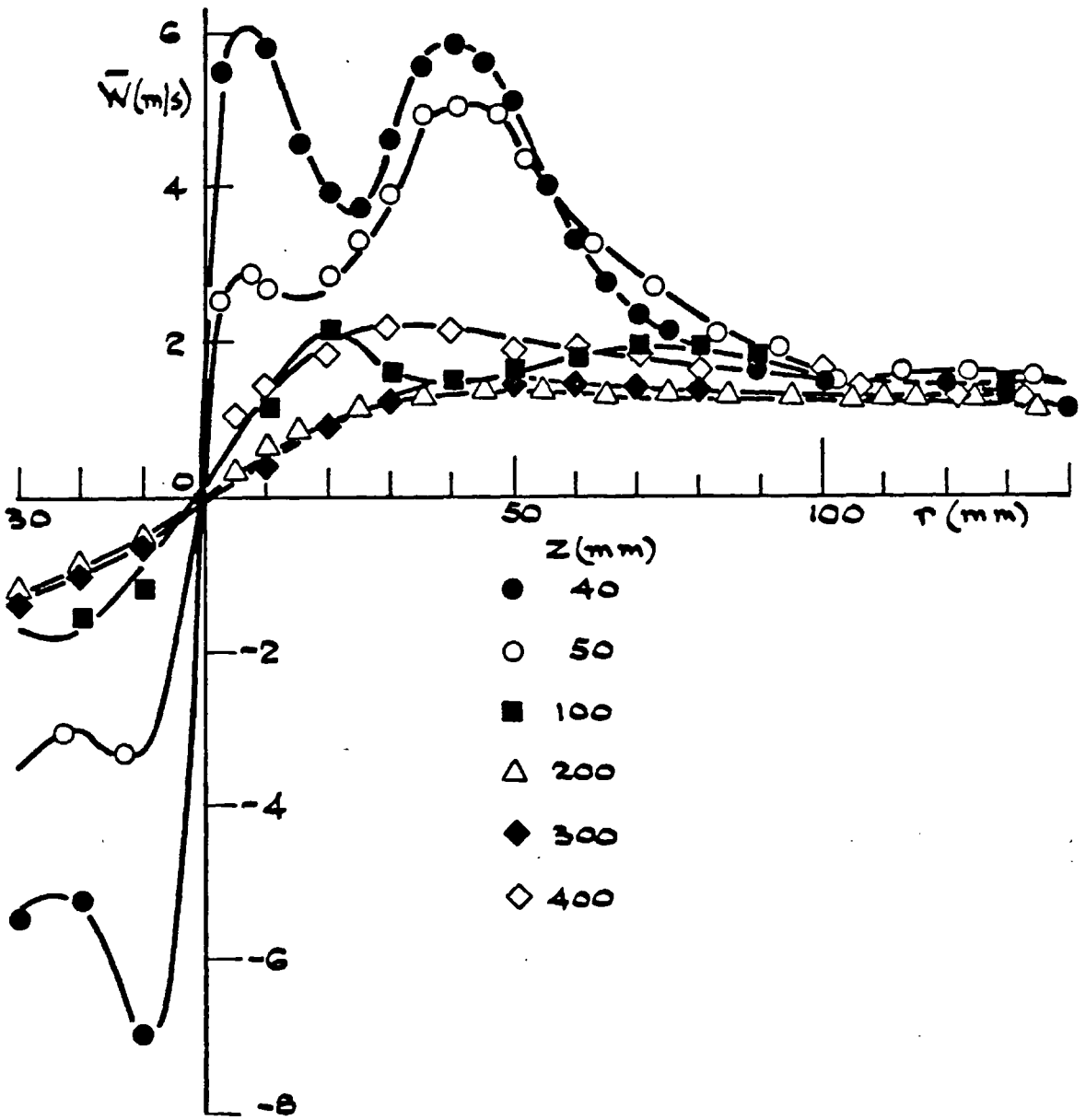


Figure 4.3.17a : Radial profiles of mean tangential velocities for isothermal flow with swirl and quarl.

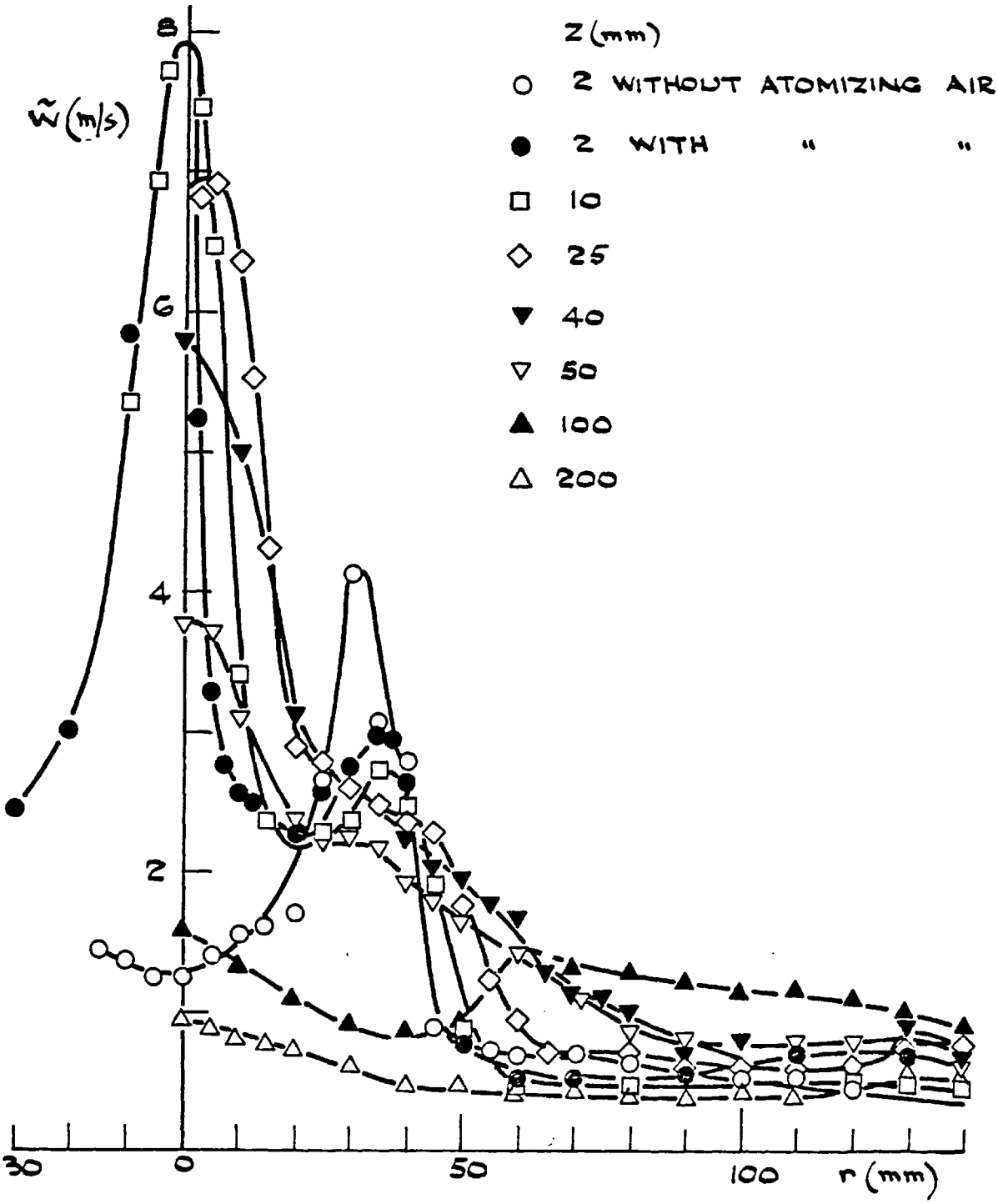


Figure 4.3.17b : Radial profiles of tangential normal stresses for isothermal flow with swirl and quarl.

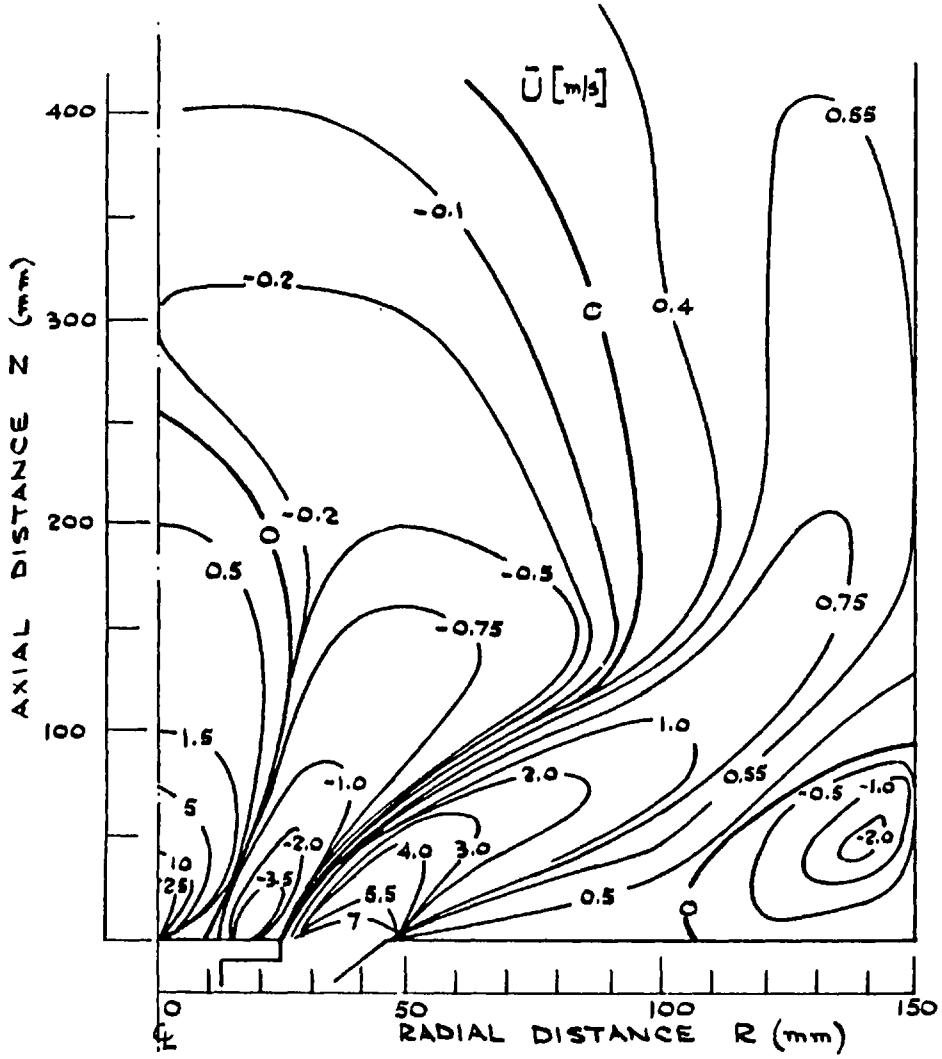


Figure 4.3.18 : Contours of constant axial mean velocity.

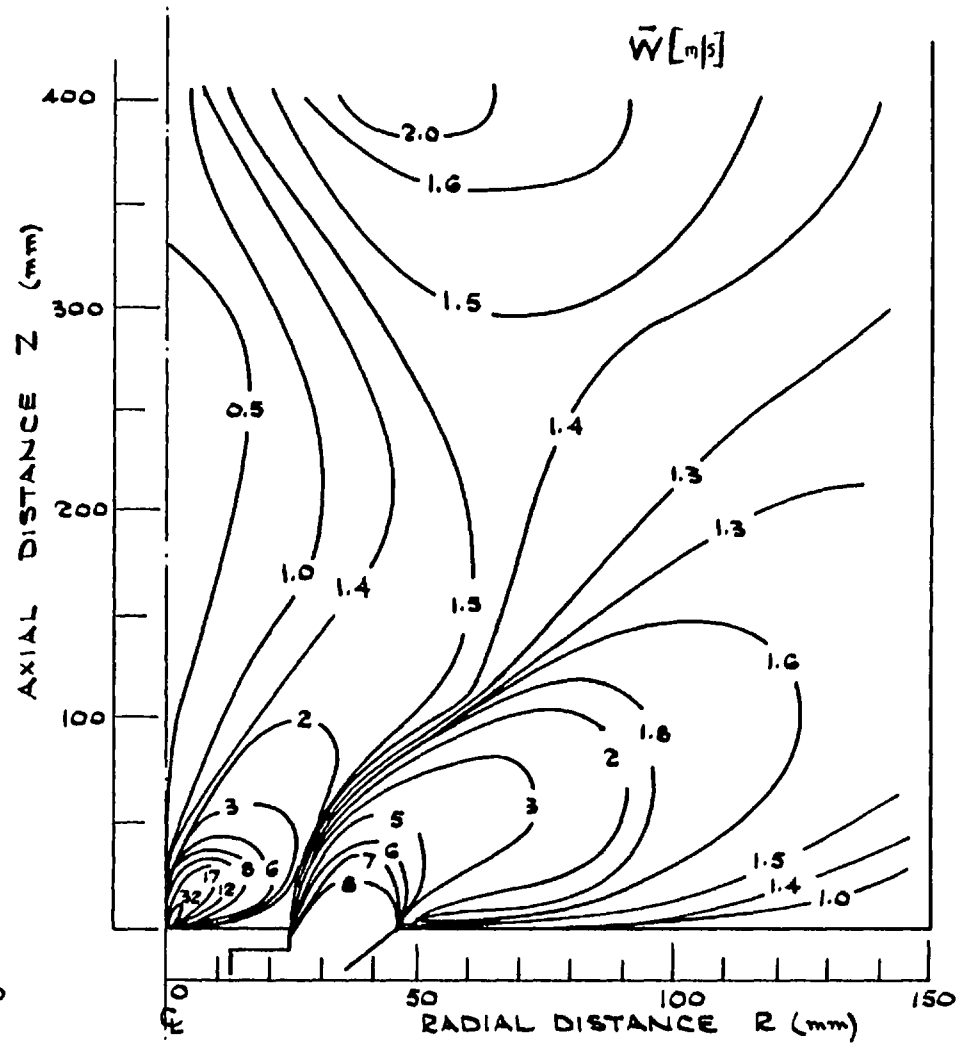


Figure 4.3.19 : Isotachs of tangential mean velocity.

Isothermal flow with swirl and quarl.

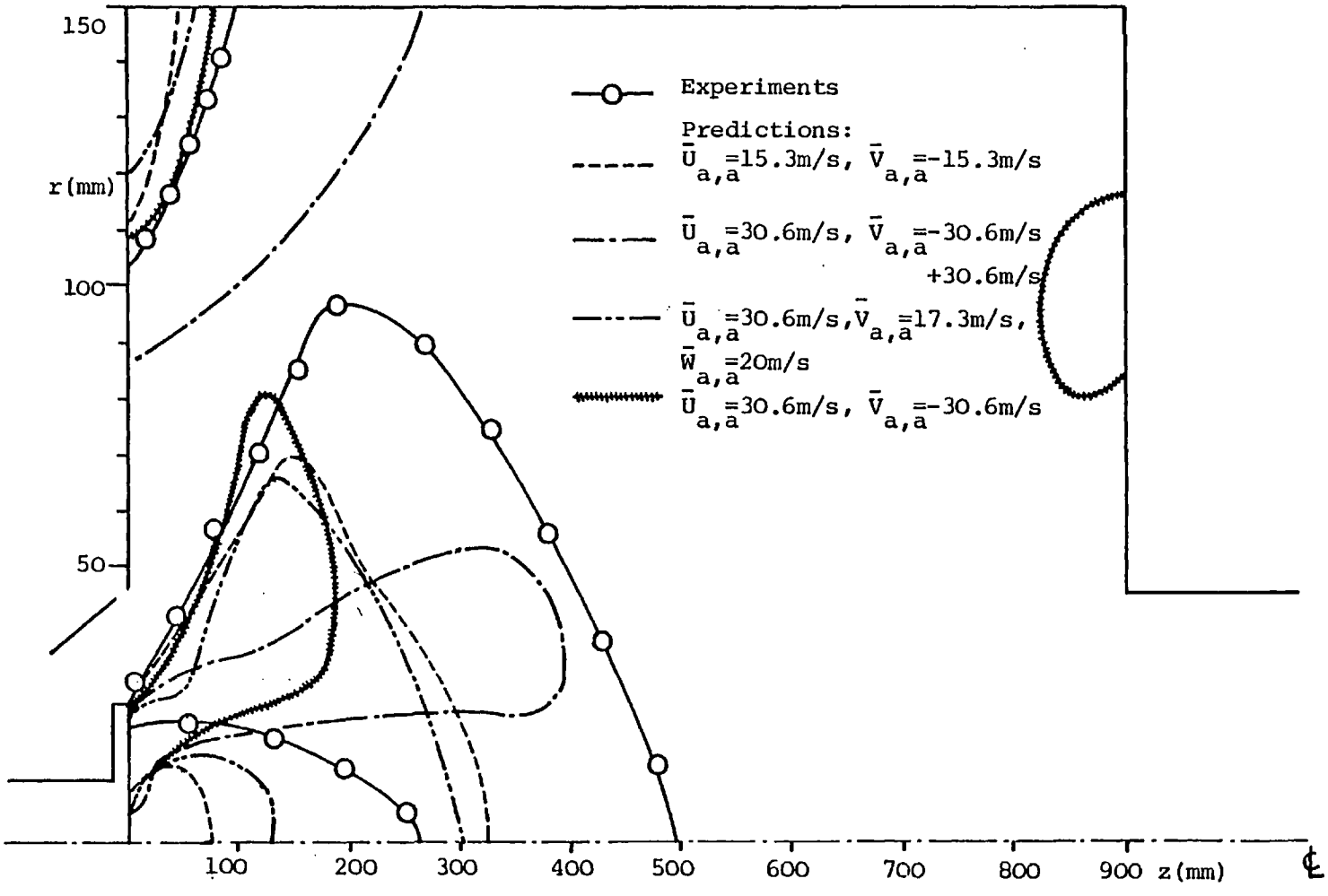


Figure 4.3.20 : Effect of atomising air on the length of recirculation : Comparison between experiments and calculations.

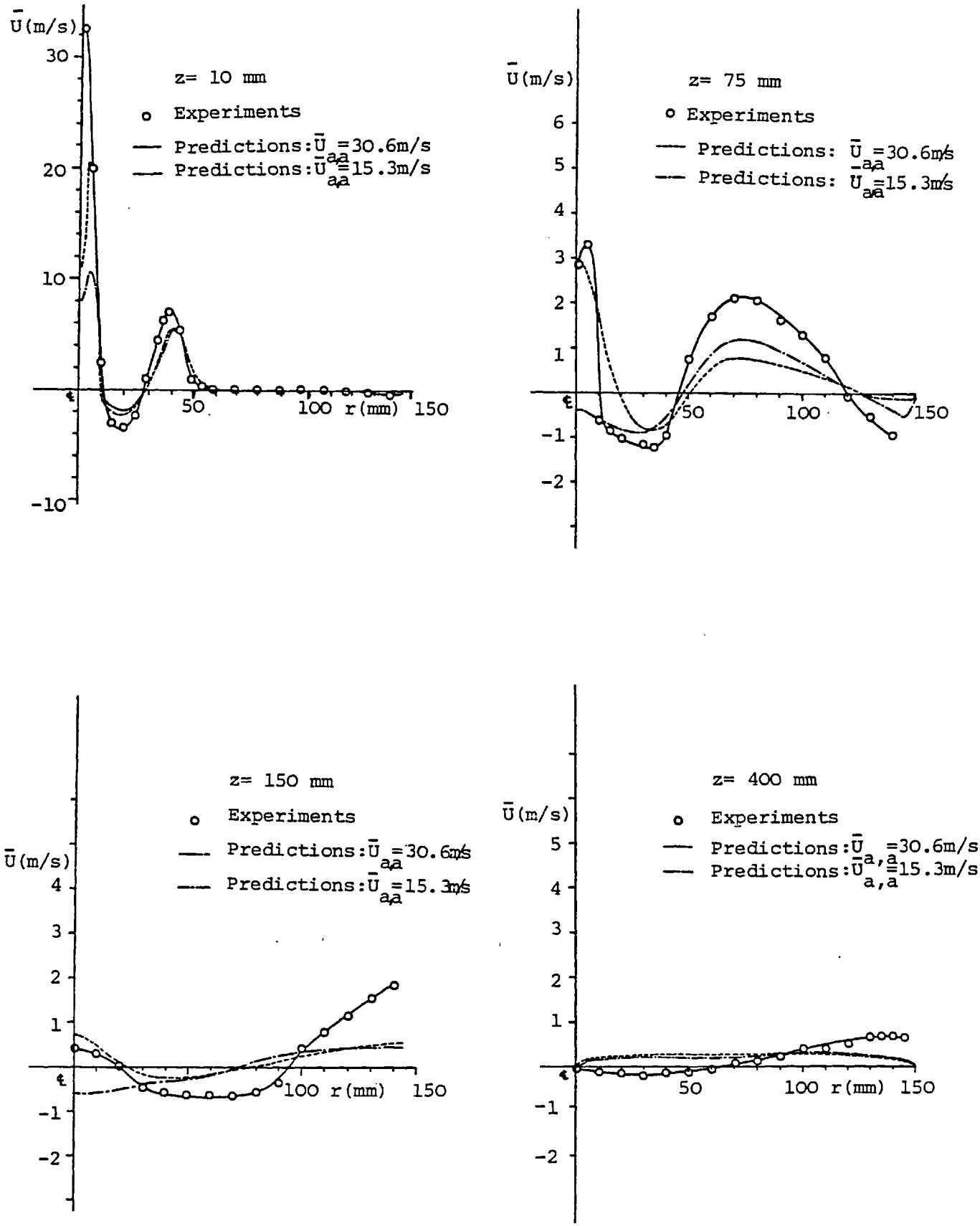


Figure 4.3.21 : Axial velocities: Comparison between experiments and calculations.

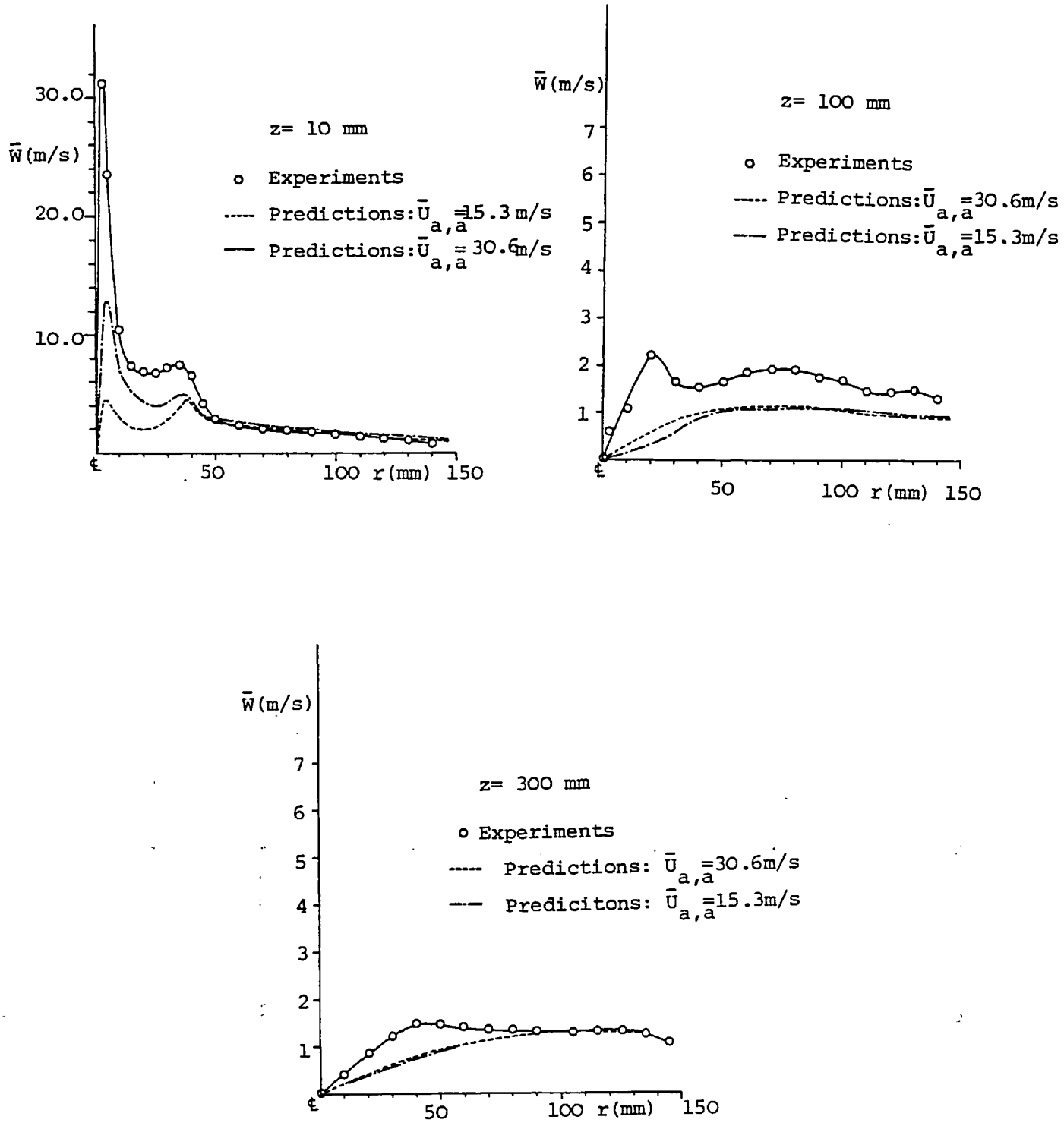


Figure 4.3.22 : Circumferential velocities : Effect of atomising air : Comparison between experiments and calculations.

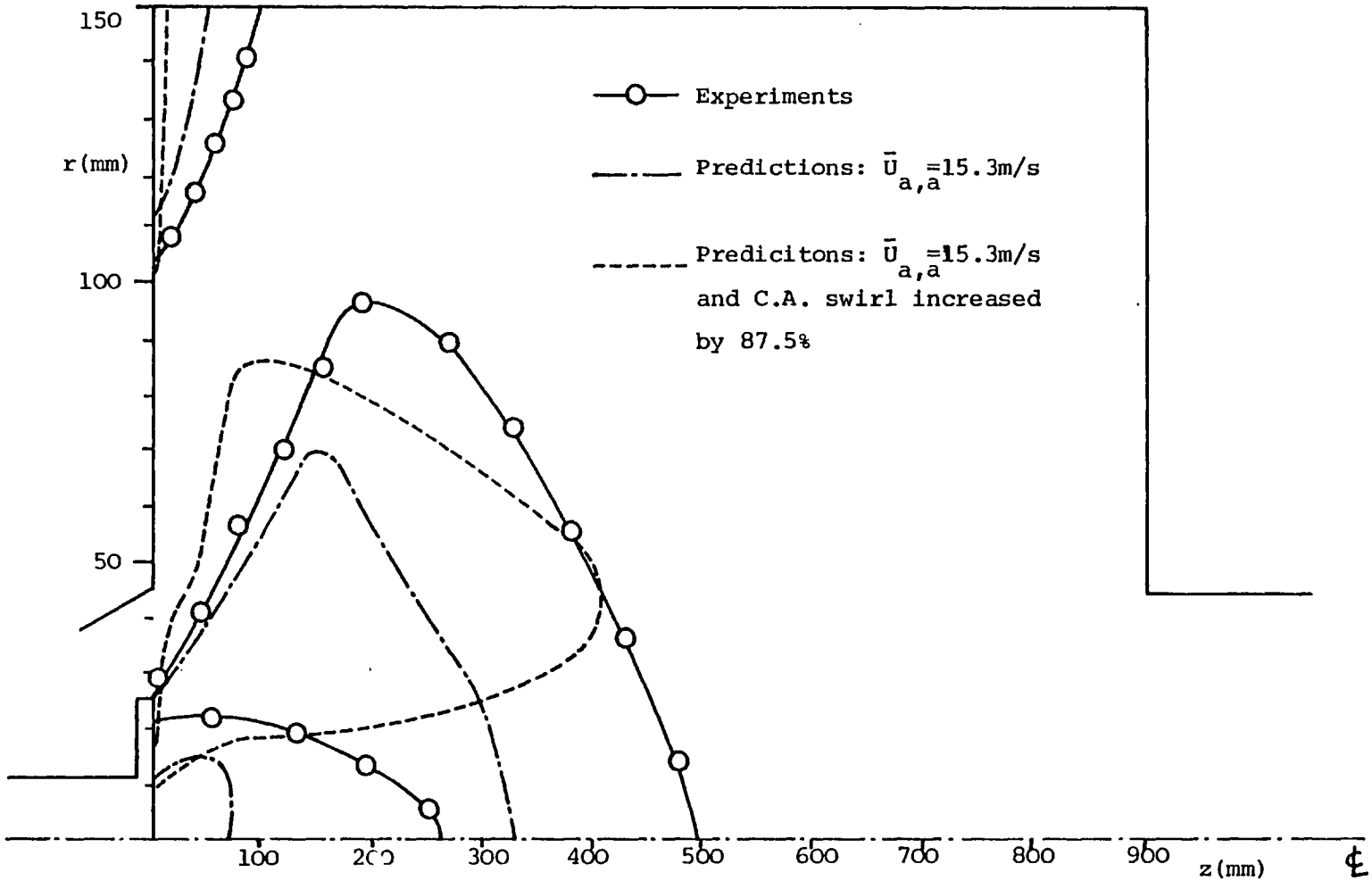


Figure 4.3.23 : Effect of combustion-air on the shape of the recirculation zone : Comparison between experiments and calculations.

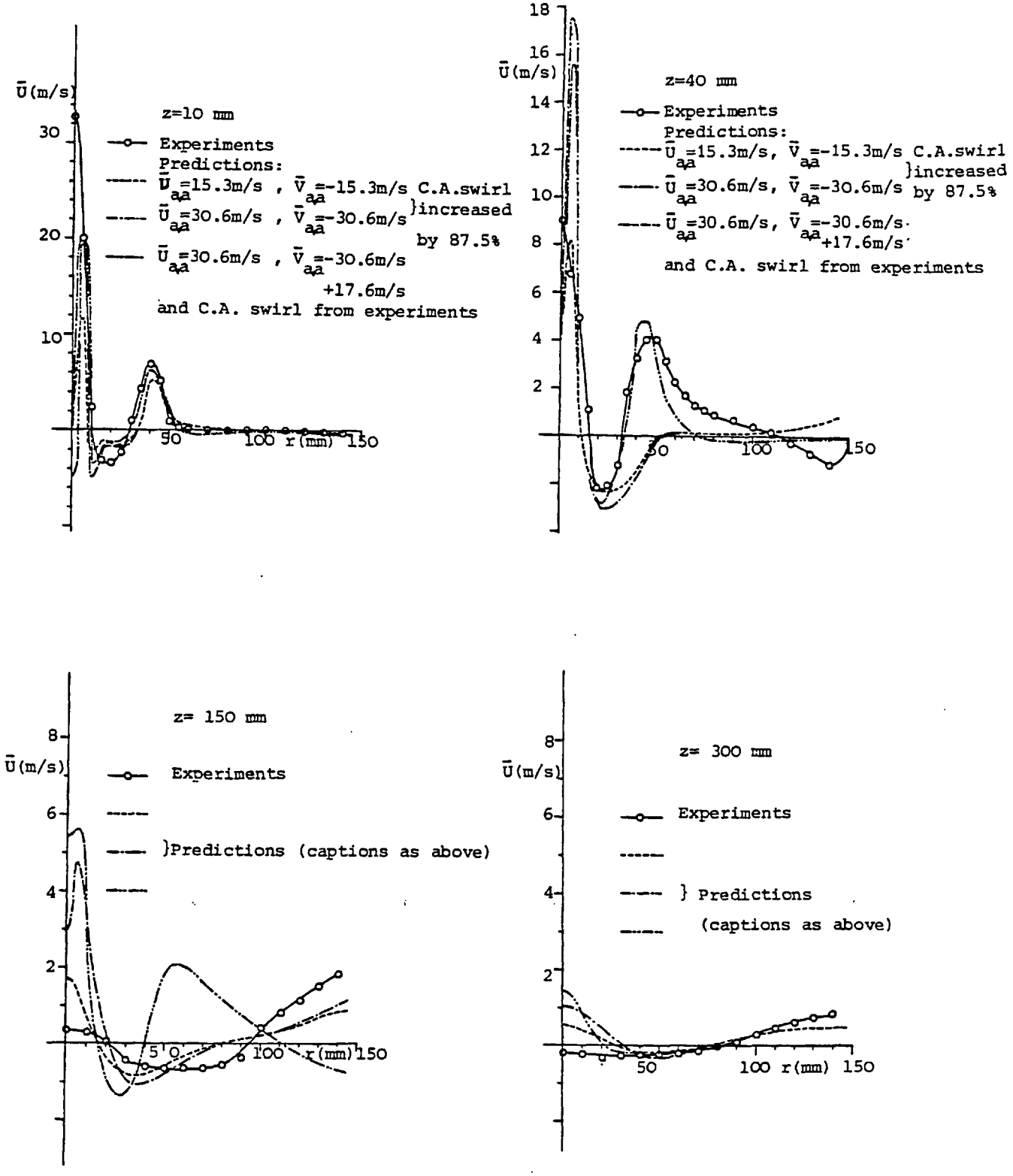


Figure 4.3.24 : Effect of combustion air swirl number on axial velocities: Comparison between experiments and calculations.

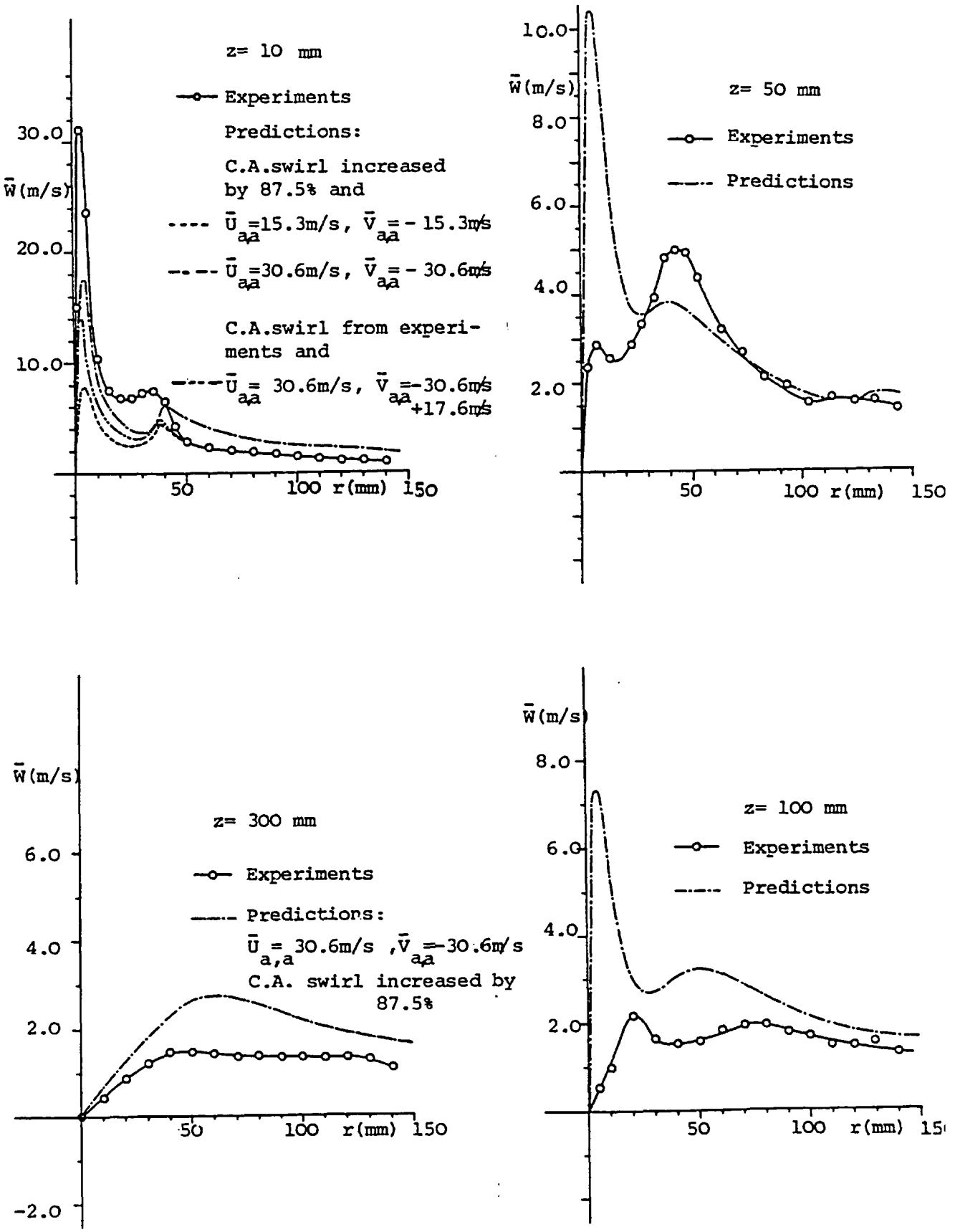


Figure 4.3.25 : Effect of combustion air swirl number on tangential velocities: Comparison between experiments and calculations.

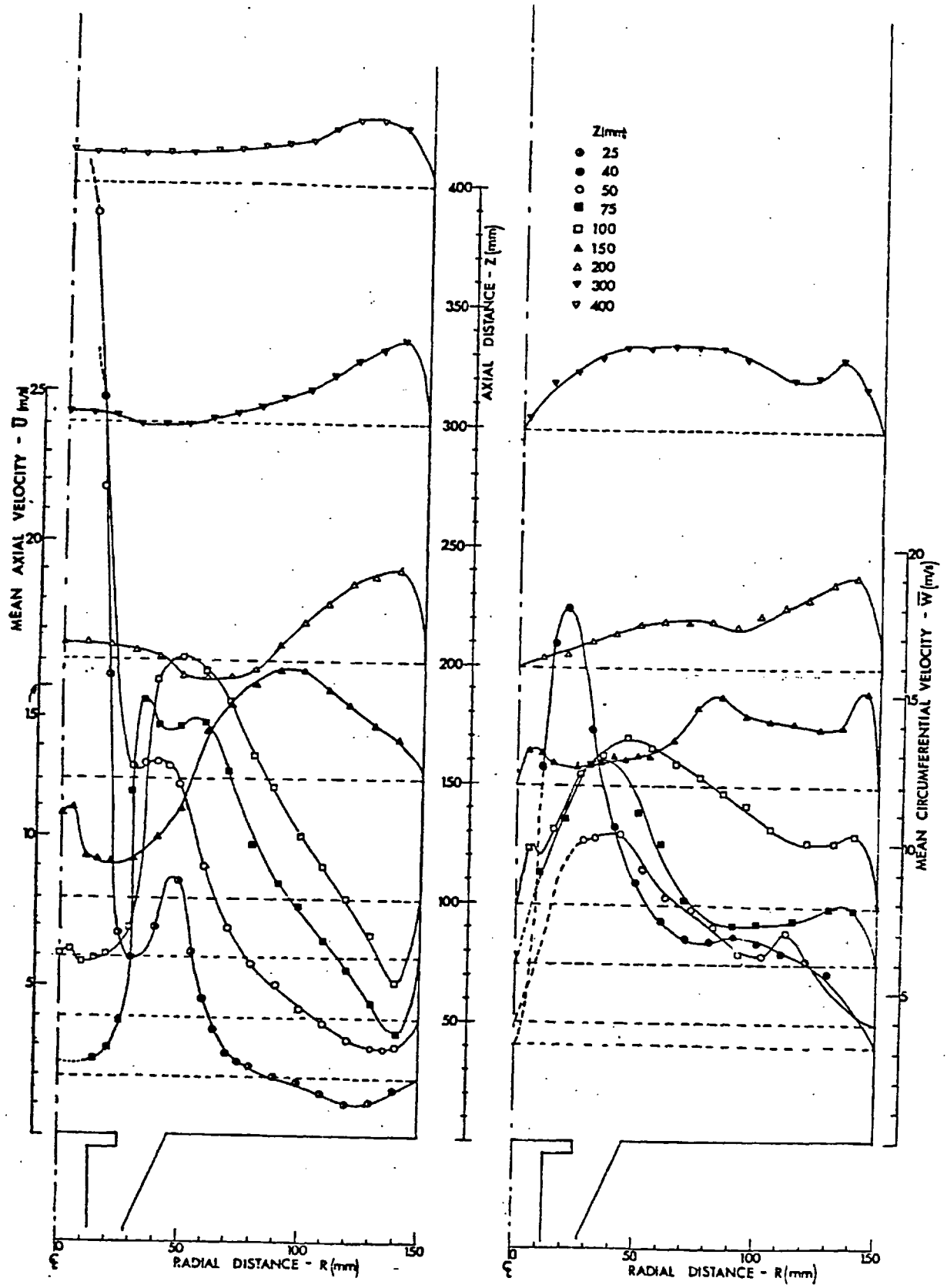


Figure 4.3.26 : Radial profiles of mean axial and circumferential velocity.

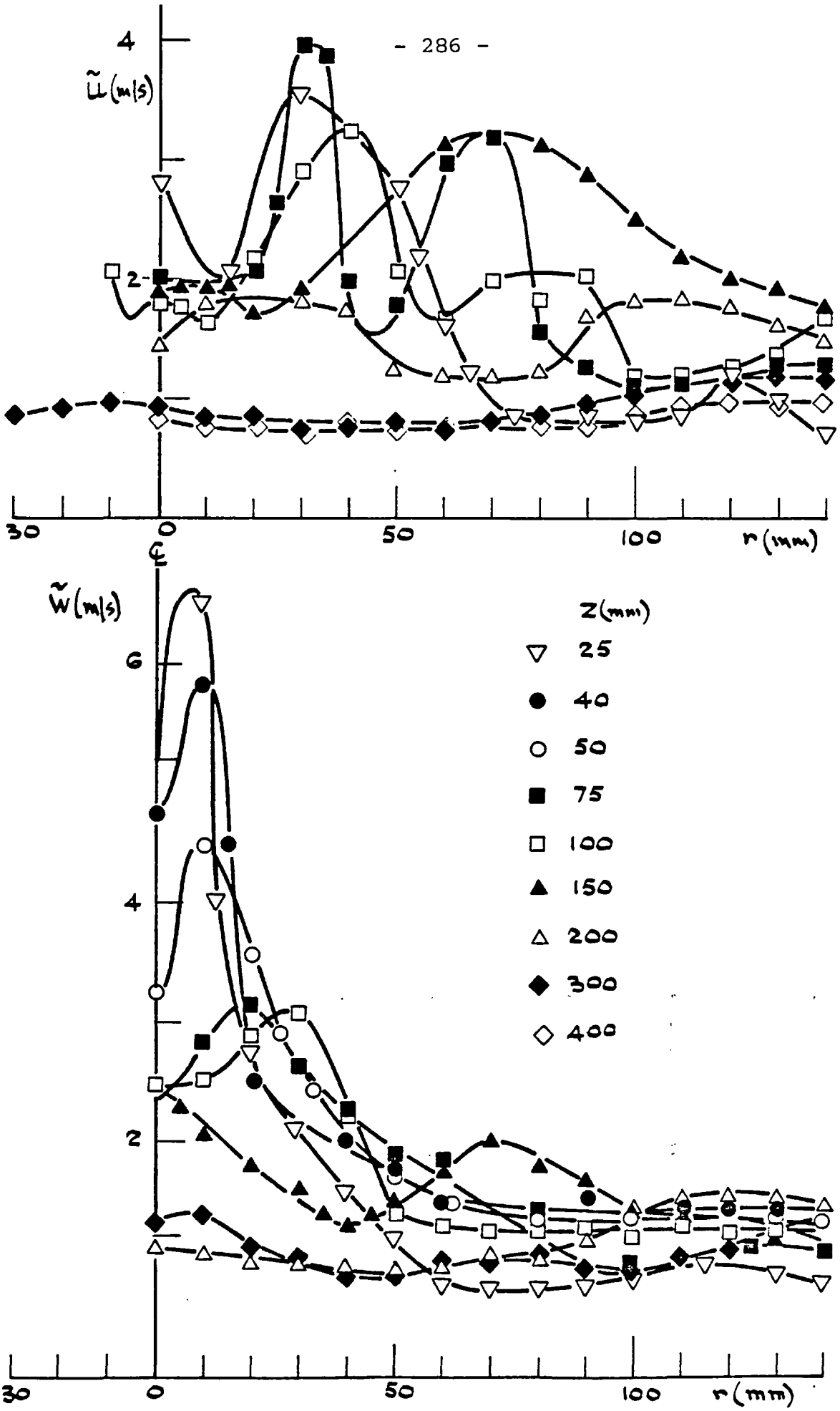


Figure 4.3.27 : Radial profiles of axial and circumferential normal stresses.

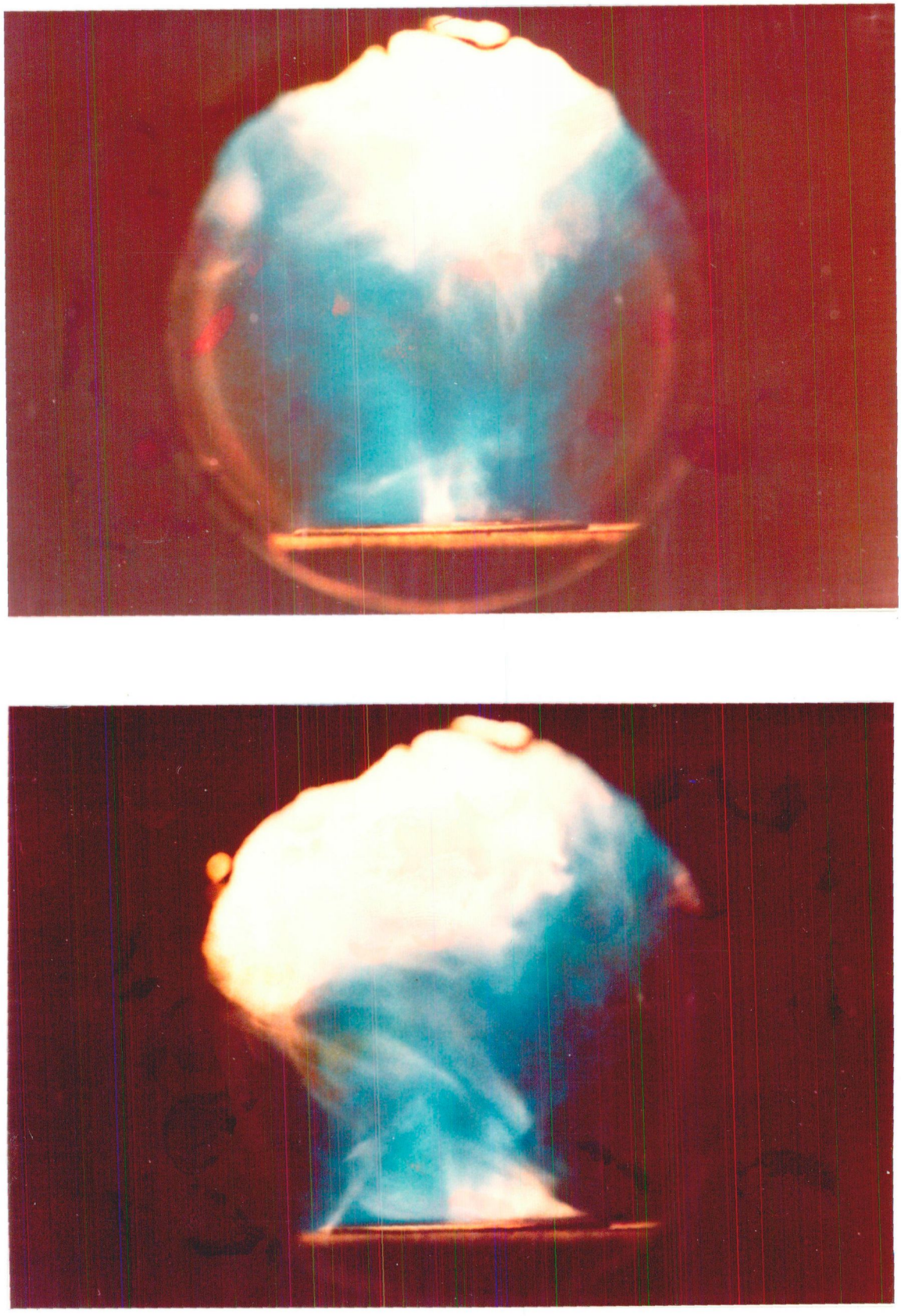


Figure 4.3.28 : Liquid-spray flame.

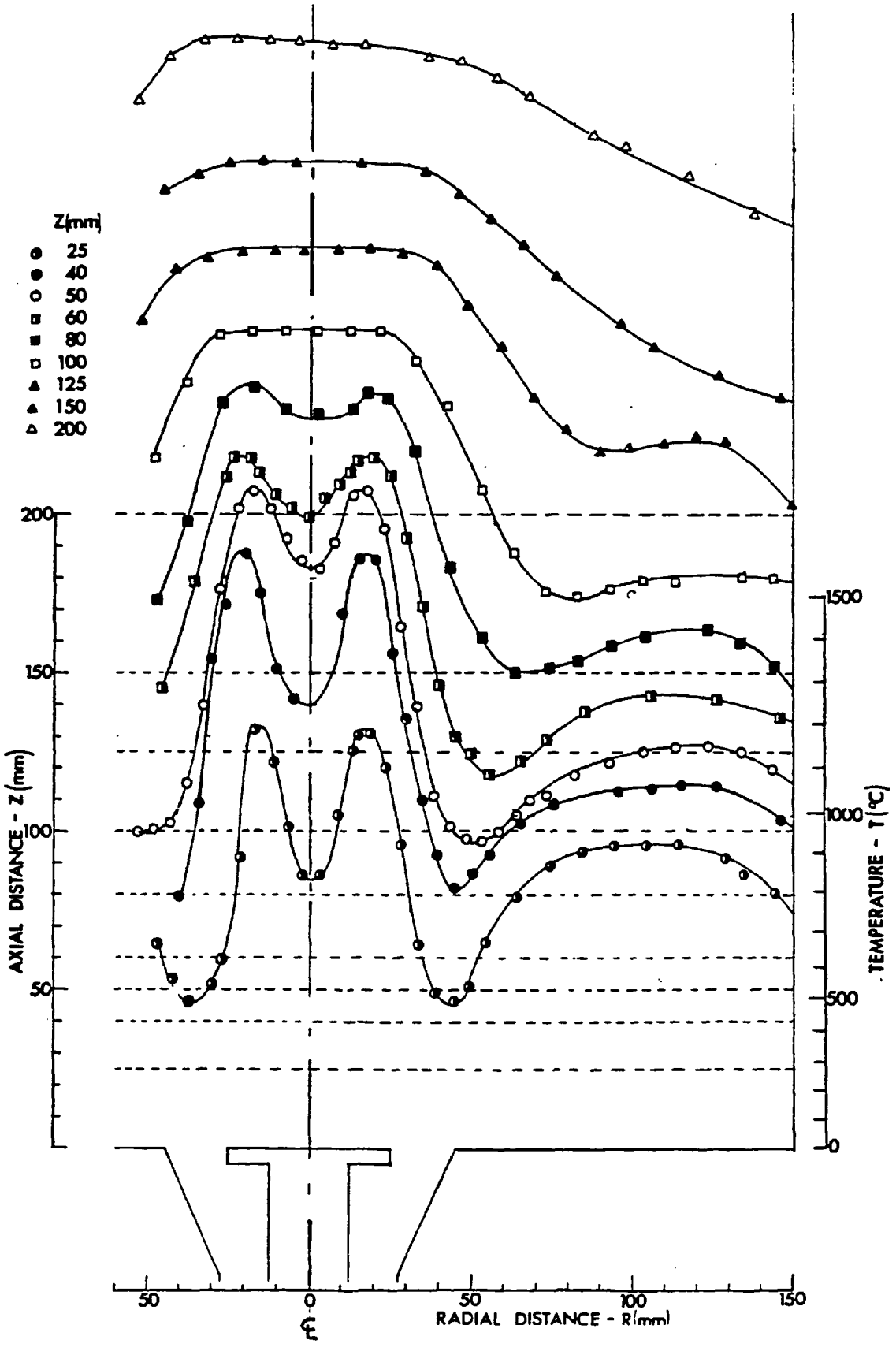


Figure 4.3.29 : Radial profiles of mean temperature.

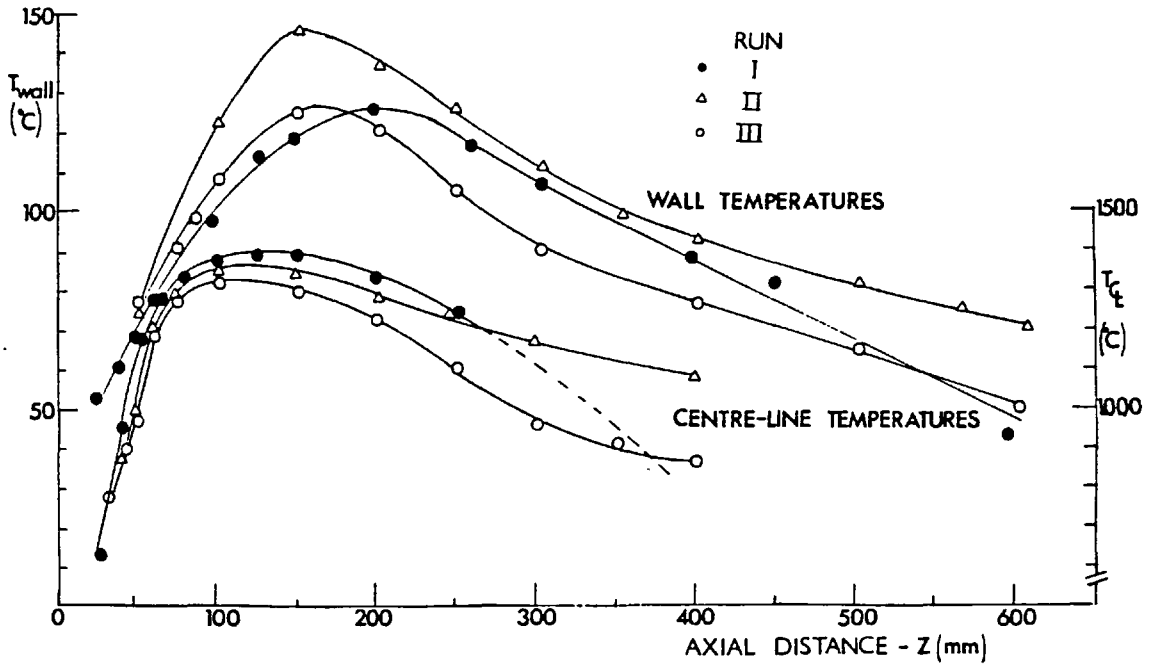


Figure 4.3.30 : Wall and centreline temperature distributions.

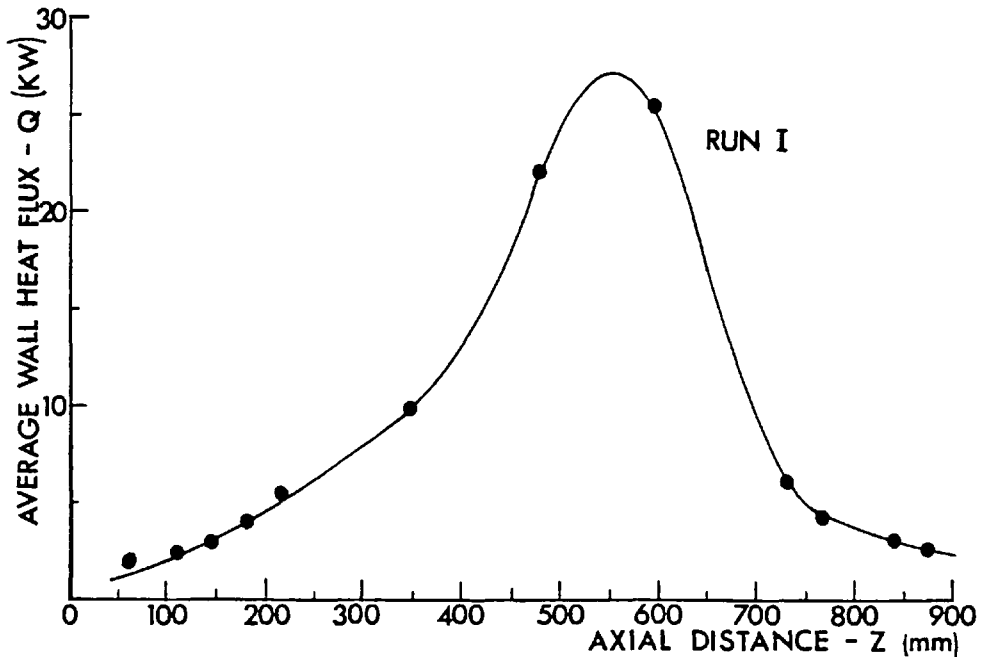


Figure 4.3.31 : Wall heat flux distribution.

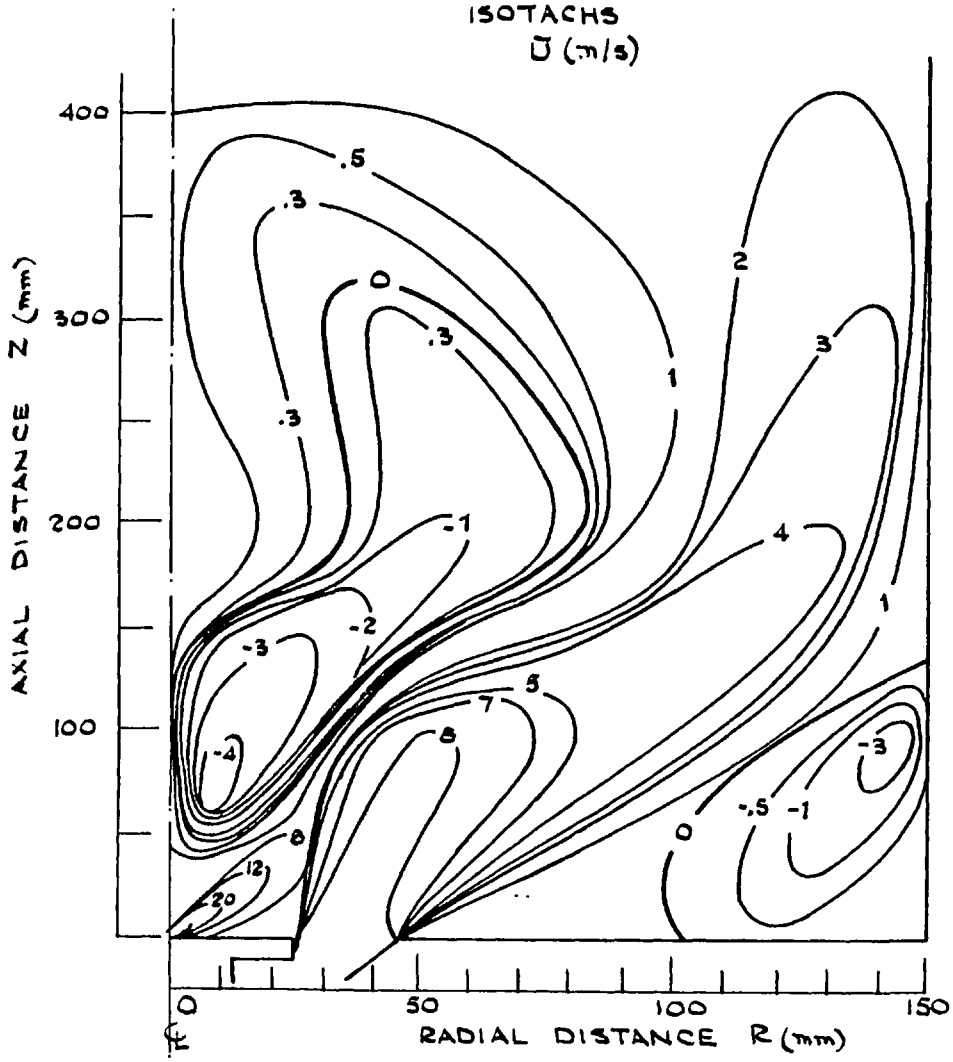


Figure 4.3.32 : Isotachs of axial velocities.

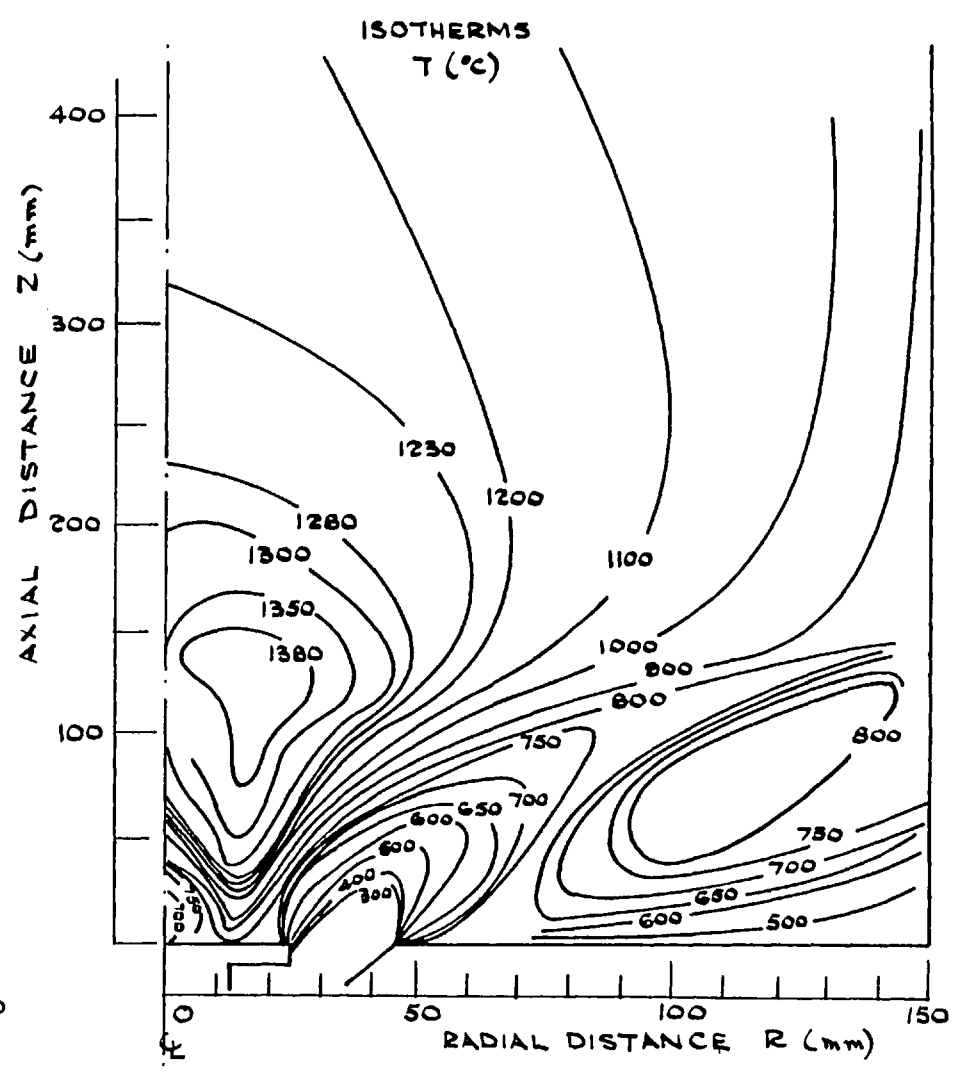


Figure 4.3.34 : Isotherms.

Combusting flow.

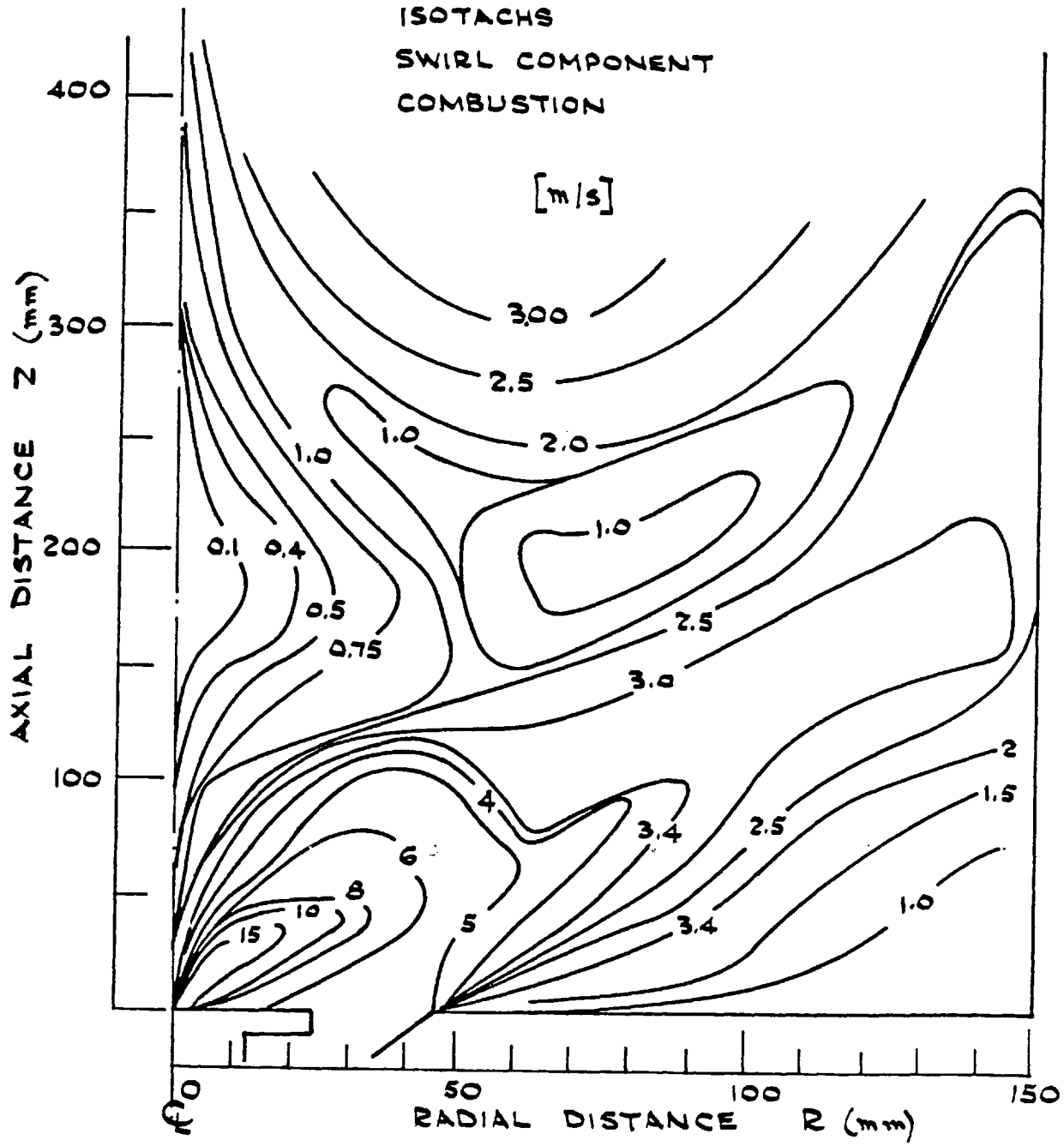


Figure 4.3.33 : Isotachs of tangential mean velocities.

CHAPTER V
CLOSURE TO THE THESIS

5.1 Summary of findings

The main findings of the present study are summarised below under the categories of electronic signal processing systems, heat exchanger flows and furnace-type flows. Detailed information of the achievements and conclusions is included at the end of each chapter and is not repeated here. Section 5.2 proposes further experiments to support the investigations of heat exchanger and furnaces, and suggests improvements to the signal processing instrumentation.

5.1.1 Signal processing systems

The two instruments used to obtain the velocity measurements of this thesis, a frequency counter and a filterbank processor, were chosen because of their special features and matched the flow and signal quality requirements. The counter with its fast re-cycle time, its ability to capture a wide range of turbulence intensities, its simplicity of use and accuracy was shown to be appropriate for highly turbulent water flows, unsteady flows and variable particle density flows. The filterbank worked well with a low signal-to noise-ratio and was appropriate for the measurements in the spray-flame and the furnace geometries. The frequency information was further manipulated, either via an APPLE-microprocessor interfaced to the frequency counter or via the paper-tape output of the filterbank which could be supplied to any mainframe computer. Thus, up to fourth order moments of the spectra could be obtained.

Each of the instruments was extensively evaluated with simple experiments in a free-jet and artificially generated Doppler bursts and accuracy limitations in mean and rms velocities were established. The effects of velocity and amplitude bias were ascertained with the frequency counter and appropriate software. An incorrect setting of the threshold level and an inappropriate sampling method can readily affect the mean and rms local values by upto 5% and 10% respectively for turbulence intensities upto 25%. The frequency resolution of the frequency counter controlled by the microprocessor was of the order of 0.196 and of the filterbank 2.5%. These limitations are related to the way the instruments are constructed and in real flows, the measurement accuracy depends on number of fringes, signal quality, turbulence intensity and the number of samples collected. Typical error bands for, say, a 20% turbulence intensity and 10^4 samples, are 1.5% and 2.5% for mean and rms values measured with the counter and 3% and 6% respectively for the filterbank.

5.1.2 Heat exchanger flows

Measured values of the three orthogonal mean velocity components and their corresponding fluctuations with well defined boundary and inlet conditions were reported for the flow in a model heat exchanger. The flow was controlled largely by pressure gradients and wall pressure distributions were obtained to demonstrate their influence. Decreasing the baffle spacing increased the proportion of back flow and the recirculation zone behind each baffle extended to the following one. Also, by reducing the baffle spacing, the dependence of the recirculation lengths on the initial turbulence intensity and Reynolds number was removed, and the overall pressure drop was drastically increased. These flow characteris-

tics indicated that disc and doughnut baffle arrangements can be efficiently used in liquid-to-liquid shell and tube heat exchangers where the plant performance is sensitive to pressure drop and where the tube-liquid heat transfer coefficient depends primarily on the heat-transfer coefficient of the shell-side.

The development of calculation methods for complex turbulent flows has been reviewed and is based on conclusions reached for flows past bluff-bodies and wall-reattaching flows. It should be recalled that previous calculations using the "k-ε" model of turbulence, have shown comparatively large discrepancies with experiments in quantities such as the length of recirculation zone and the rate of spread of the wake downstream a baffle Even with the existing discrepancies, the level of accuracy achieved is sufficient for many practical situations, especially when the cost and time requirements of "cut-and-try" methods are considered.

5.1.3 Furnace-type flows

In the small scale furnace, measurements of the mean temperature and wall heat flux were obtained in addition to the aerodynamic quantities. Two confined isothermal flows with different degrees of swirl and a spray flame, burning a mixture of kerosene and 39% excess air generated by a twin-fluid air-blast atomiser, were examined. The flame was stabilised by a disc encircling the atomiser and by the quarl geometry of the furnace. The combustion results were compared with corresponding isothermal flow measurements of the velocity characteristics and showed,for example, that the Reynolds stresses in the spray flame were approximately 50% higher than those of the corresponding isothermal case with maxima for the axial and swirl velocities in the vicinity of the edge of

the spray. Maximum temperatures of 1380 degrees Celsius were achieved on the centreline between 100 mm and 130 mm from the burner exit and an increase in fuel rate reduced the centreline maximum temperature, which remained high to further downstram locations and increased the temperatures away from the centreline. Reduction in the atomising air pressure resulted in lower temperatures up to 300 mm due to the wider cone angle. The total heat transfer to the wall was measured to be 41.5 kW with maximum heat flux at approximately 500 mm from the burner, where the flame approached the wall.

Calculated results were obtained for the isothermal flow corresponding to the spray flame with a finite difference technique and the k-ε model of turbulence. The geometry and flow characteristics of the atomising air were shown to influence the predicted flow pattern. Central and corner recirculation regions were underestimated by about 35% and their size was controlled by the spreading rate of the atomising air and the swirl angle of the main air stream.

The agreement between measured and calculated axial velocities was found to depend upon the accuracy of specification of the initial conditions in the atomiser region. In particular, the resolution of steep pressure gradients adjacent to the fuel atomiser. Truncation errors were not extensively investigated but are expected to be significant in regions of high gradients. In general, the main discrepancies between experimental and computed results are associated with the uncertainties in the initial and boundary conditions and particularly to the large influence of the small-diameter central jet.

5.2 Recommendations for future work

Improvement in the accuracy of velocity measurements can be achieved by on line correction of bias effects in laser velocimetry. Apriori removal of bias requires the automatic control and adjustment of the particle arrival rate and the setting of the threshold level. The former should be continuously counter-checked against the instrument's sampling time and the local turbulent time scale, and adjusted to be smaller than the two. Similarly, the threshold level should be instantaneously compared to the maximum signal amplitude and then maintained at a fixed percentage of it. Alternatively, the on line elimination of the velocity bias can be achieved by weighting the local velocity values with the corresponding time between two successive samples.

The temperature measurements of chapter IV have shown that they could be underestimated by up to 120° C, depending on the local temperature mean and fluctuating values. Improved understanding of the measuring accuracy of mean temperatures can, and should, be achieved by the use of digitally compensated, very small bead thermocouples.

Related to the heat exchanger flows suggestions can be made for further experiments involving geometrical variations in the model, such as the increase in baffle size, the interchange of baffle order and the inclusion in the model of the leakage flow between the doughnuts and shell. Also, important is the study of the effects of the insertion of tube rows, which will render refractive index matching an essential feature of the experimental set up.

Refractive index matching, i.e. the use of a liquid with a refractive index close to that of perspex, will

allow measurements of both second- and third-order correlations and with the latter it becomes possible to construct approximations for the balance of turbulent kinetic energy and shear stresses. It should be noted that since the refractive index of a fluid is temperature sensitive, temperature control of the test section is necessary.

Insertion of the tube bundle will allow the quantification of the "resistance" of the tubes and correlate it to the pressure drop across the model. Further investigations in the heat exchanger should be undertaken to quantify the variation of heat transfer coefficient and its relation to the geometrical variations proposed above. Knowledge of the heat transfer characteristics at the wall and also between the tube-bundle and shell-side flow can be used to improve the thermal efficiency of heat exchangers of this type.

In relation to the spray flame work, the results of chapter IV suggested that there is still need for further experiments to cover a wider range of operating conditions and describe the characteristics of both polydispersed and monodispersed sprays. Further understanding of the various processes controlling spray combustion and validation against related models is required. The influence of the combustion air swirl should be further examined with high values of swirl. Regarding the spray operation conditions future experiments should include polydisperse sprays of larger mean droplet diameters,with different levels of air preheating, heavier fuels and pressurised combustor operation. These are conditions more typical of practical combustors and future work in spray-flames should be directed towards this.

The computed results in the furnace geometry implied that initial conditions need to be better specified to

allow accurate predictions of the aerodynamic characteristics of the flows. Thus, as it has been suggested in section 4.4.2, it is desirable to relate the geometry and flow conditions at the atomiser to the flow properties at locations as close as possible to the exit plane.

Combustion models for spray-flames, see section 4.1.2, generally neglect the formation of intermediate chemical species, such as CO, and the influence of chemical kinetics on the reaction rate. Simplistic models are used for the prediction of pollutant species, such as NO and CO, and the soot formation rate, see for example Jones and Whitelaw (1982). Further experimental data for both the major and intermediate chemical species concentrations and soot formation are necessary to assist the development of combustion models.

For the prediction of complex geometry flows, such as the flows in heat exchangers and spray flames in furnaces, the computational methods described in chapter III and IV show promise although there are shortcomings, such as the accurate specifications of initial and boundary conditions. The immediate application of any calculation technique to complex geometries, either isothermal flows or not, is limited by the assumption of simply shaped boundaries as well as by inaccuracies introduced by the turbulence and numerical models. Further work is therefore required to increase the adaptability of the computational approaches, e.g. with body fitted coordinates or irregurarly shaped boundaries and in the field of phase-interactions. In addition, extensions to three-dimensional flows are likely to require improvements of numerical accuracy and economy.

REFERENCES CITED

ABBAS A.S., KOUSSA, S.S. and LOCKWOOD, F.C. (1980)
The Prediction of the Particle Laden Gas Flows.
Fluids Section Report FS/80/1, Dept. of Mech. Eng., Imperial College London.

ARCOUMANIS C., BICEN, A.F. and WHITELAW, J.H. (1981)
Flow in a Simulated Gun Barrel Configuratiom (Part II).
Fluids Section Report FS/81/27, Dept. of Mech. Eng., Imperial College, London.

ARMALY, B.F., DURST, F., PEREIRA, J.C.F. and SCHÖNUNG, B. (1983)
Experimental and Theoretical Investigation of Backward-Facing Step Flow.
J. Fluid Mech., 127, 473.

ARMALY, B.F., DURST, F. and SCHÖNUNG, B. (1980)
Measurements and Predictions of Flow Downstream of a Two-Dimensional Single Backward Facing Step.
Report SFB 80/ET/172, Sonderforschungsbereich 80, University of Karlsruhe.

ASALOR, J.O. and WHITELAW, J.H. (1975)
The Influence of Combustion Induced Particle Concentration Variations in Laser-Doppler Anemometry.
Proceedings LDA-Symposium Copenhagen, PO Box 70, DK-2740 Skovlunde, Denmark.

ATTYA, A.M. and WHITELAW, J.H. (1981)
Velocity, Temperature and Species Concentration in Unconfined Kerosene Spray Flames.
ASME, Paper 81-WA/HT-47.

BAKER, R.J. (1974)
Use of a Filter Bank Signal Processor for Laser-Anemometry.
Chemical Eng. Division, AERE, Harwell, Report No. AERE R7652.

BAKER, R.J. and WIGLEY, G. (1975)
Design, Evaluation and Application of a Filter Bank Signal Processor.
Proceedings LDA-Symposium Copenhagen, PO Box 70, DK-2740 Skovlunde, Denmark.

BERNER C., DURST, F. and McELIGOT, D.M. (1983)
Flow around Baffles.
Report in Preparation, Submitted for presentation at the ASME Winter Annual Meeting, Boston, Mass. 13-18 Nov. 1983.

BOYER, R.C. and PASE, G.K. (1980)
The Energy-Saving NESTS Concept.
Heat Transfer Engineering, 2, 1.

BRADBURY, L J.S. (1976)
Measurements with a pulsed-wire and hot-wire anemometer in the highly turbulent wake of a normal flat plate.
J. Fluid Mech., 77, 3.

BRADSHAW, P., CEBECI, T. and WHITELAW, J.H. (1981)
Engineering Calculation Methods for Turbulent Flow.
Academic Press Inc. (London) Ltd.

BRADSHAW, P. and WONG, F.Y.F. (1972)
The Reattachment and Relaxation of a Turbulent Shear Layer.
J. Fluid Mech., 52, 113.

BREDERODE de V. and BRADSHAW, P. (1972)
Three-Dimensional Flow in Nominally Two-Dimensional Separation Bubbles: Flow behind a Rearward Facing Step.
Aero Report 72-19, Dept. of Aeronautical Eng., Imperial College, London.

B.S. 3274 (1960)
Specification for Tubular Heat Exchangers for General Purposes.
British Standards Institution, London, 1967.

BUCHHAVE, P. (1975)
Biasing Errors in Individual Particle Measurements with the LDA-Counter Signal Processor.
Proceedings LDA-Symposium, Copenhagen, PO Box 70, DK-2740 Skovlunde, Denmark.

BUCHHAVE, P. (1978)
Transducer Techniques.
Proceedings of the Dynamic Flow Conference 1978, Inst. de Mec. Stat. de la Turbulence, Marseille.

BUCHHAVE, P., GEORGE, W.K. and LUMLEY, J.L. (1979)
The Measurement of Turbulence with the Laser-Doppler Anemometer.
Annual Review of Fluid Mechanics, 11, 443.

BUTTERWORTH, D. (1978)
Introduction to Heat Transfer.
Oxford University Press.

CALVERT, J.R. (1967)
Experiments on the Low-Speed Flow Past Cones.
J. Fluid Mech., 27, 2.

CARMODY, T. (1964)
Establishment of the Wake behind a Disc.
Trans. ASME, J. of Basic Eng., Dec. 1964, 869.

CARVER,M.B., CARLUCCI, L.N. and INCH, W.W.R (1981)
Thermal Hydraulics in Recirculation Steam Generators.
THIRST Code User's Manual, AECL report 7254, Chalk River Nuclear Laboratories.

CASTRO, I.P. (1978) in
Numerical Methods in Laminar and Turbulent Flows (Eds Taylor C. et. al). Pentech, London, 329.

CASTRO, I.P. (1979)
Numerical Difficulties in the Calculation of Complex Turbulent Flows.
Turbulent Shear Flows I. (Eds. Durst, F. et al), Springer-Verlag, Berlin.

CASTRO, I.P. CLIFFE, K.A. and NORGETT, M.J. (1981)
Numerical Prediction of the Laminar Flow over a Normal Flat Plate.
Theoretical Physics Division AERE, Harwell, Report No. TP. 870.

CASTRO, I.P. and ROBINS, A.G. (1977)
The Flow around a Surface-Mounted Cube in Uniform and Turbulent Streams.
J. Fluid Mech. 79, 2.

CHENOWORTH, J.M. (1982)
Design of Shell-and-tube Heat Exchangers to avoid Flow Induced Vibration.
Heat Transfer 1982, Proc. of the 7th Int. Heat Trans. Conference, Munich, FRG, 6 , 173.

CHEUN, B.S., TOY, N. and MOSS, W.D. (1981)
The Effect of Upstream Boundary Layer Thickness upon Flow past a Backward-Facing Step.
7th Biennial Symposium on Turbulence, University of Missouri-Rolla, paper 7-1.

CHIGIER, N.A. (1976)
The Atomization and Burning of Liquid Fuel Sprays.
Prog. Energy Comb. Sci 2, 97.

CHIGIER, N.A. and YULE, A.J. (1977)
Vaporization of Droplets in High Temperature Gas Streams.
Physical Chemistry and Hydrodynamics Levich Birthday Conference, Oxford, July 1977.

CHIU, H.H. and LIU, T.M. (1977)
Group Combustion of Liquid Droplets.
Comb. Sci and Tech., 17, 127.

CLARE, H., DURAO, D.F.G., MELLING, A. and WHITELAW, J.H. (1976)
Investigation of a V-gutter Stabilized Flame by Laser Anemometry and Schlieren Photography.
Applications of Non-Intrusive Instrumentation in Fluid Flow Research AGARD-CP-193, Paper No. 26.

CLIFFE, K.A., LEVER, D.A. and WINTERS, K.H. (1979)
A Finite Difference Calculation of Spray Combustion in Turbulent Swirling Flow.
HTFS Research Symposium, AERE, Harwell, RS 266, also AERE, Harwell Report R9507.

CRABB, D., DURAO, D.F.G. and WHITELAW. J.H. (1978)
Velocity Characteristics in the Vicinity of a two-Dimensional Rib.
Fluids Section Report FS/78/74, Dept. of Mech. Eng. Imperial College, London.

CROWE, C.T. SHARMA, M.P. and STOCK, D.E. (1977)
The Particle-Source-in-Cell (PSI-CELL) Model for Gas-droplet Flows.
Dept. of Mech. Eng., Washington state University, Washington.

DAVIES, T.W. and BEER, J.M. (1971)
Flow in the Wake of Bluff-Body Flame Stabilizers.
13th Symp. (International) on Combustion, The Combustion Institute, Pittsburgh, Pa.

DIMOTAKIS, P. (1976)
Single Scattering Particle Laser Doppler Measurements of Turbulence.
Applications of Non-intrusive Instrumentation in Fluid Flow Research.
AGARD-CP-193, Paper No. 10.

DRAIN, L. (1980)
The Laser-Doppler Technique.
John Wiley and Sons.

DURAO, D.F.G., FOUNTI, M. and WHITELAW, J.H. (1979)
Velocity Characteristics of Three-Dimensional Disc-Stabilised Diffusion Flames.
Letters in Heat and Mass Transfer, 6, 1979.

DURAO, D.F.G. and WHITELAW, J.H. (1974)
Performance Characteristics of two Frequency-Tracking Demodulators and a Counting System: Measurements in an air-jet.
Heat Transfer Section Report HTS/74/12, Dept. of Mech. Eng., Imperial College, London.

DURAO, D.F.G. and WHITELAW, J.H. (1975)
The Influence of Sampling Procedures on the Velocity Bias in Turbulent Flows.
Proceedings LDA-Symposium, Copenhagen, PO Box 70, DK-2740 Skovlunde, Denmark.

DURAO, D.F.G. and WHITELAW, J.H (1978)
Velocity Characteristics of the Flow in the Near Wake of a Disc.
J. Fluid Mech., 85, 2.

DURAO, D.F.G. and WHITELAW, J.H. (1979)
Relationship between Velocity and Signal Quality in Laser Doppler Anemometry.
J. Phys. E.: Sci. Instrum., 12, 47.

DURAO; D.F.G., LAKER, J. and WHITELAW, J.H. (1980a)
Bias Effects in Laser Doppler Anemometry.
J. Phys. E.: Sci. Instrum., 13, 442.

DURAO, D.F.G. and WHITELAW, J.H. (1980b)
Bias in LDA due to Velocity Amplitude Correlation.
Proceedings of Symposium on Long Range and Short Range, Optical Velocity Measurements, Saint-Louis, Paper XXV.

DURRANI, T.S, and GREATED, C.A. (1976)
Laser Systems in Flow Measurements.
Plenum Press.

DURRANI, T.S. and GREATED, C.A. (1973)
Statistical Analysis and Computer Simulation of Laser Doppler Velocimeter System.
IEEE. Trans. on Instrum. and Measurement. IM-22, 23.

DURST, F., MELLING, A. and WHITELAW, J.H. (1976, 1981)
Principles and Practice of Laser-Doppler Anemometry
Academic Press, New York, 2nd Edition.

DURST, F. and WHITELAW, J.H. (1971)
Integrated Optical Units for Laser Anemometry
J. Phys, E.: Sci. Instrum., 4, 804.

DURST, F. and RASTOGI, A.K. (1980)
Turbulent Flow over Two-Dimensional Fences.
Turbulent Shear Flows 2 (Eds. Bradbury J.S. et al).
Springer-Verlag, Berlin.

DURST, F. and WHITELAW, J.H. (1973)
Light Source and Geometrical Requirements for the Optimization of Optical Anemometry Signals.
Opto-Electronics, 5, 137.

DURST, F. and ZARE, M. (1974)
Removal of Pedestals and Directional Ambiguity of Optical Anemometer Signals.
Appl. Optics, 13, 2562.

EATON, J.K. (1982)
Incompressible Separated Flows-Internal Flows-Backward Facing Steps.
1980-81 AFOSR-HTTM-STANFORD, Conference on Complex Turbulent Flows (Eds Kline, S.J. et.al.) II, 886.

EATON, J.K. and JOHNSTON, J.P. (1981)
A Review on Subsonic Turbulent Flow Reattachment
AIAA Journal, 19, 1093

EATON, J.K. and JOHNSTON, J.P. (1980)
Turbulent Flow Reattachment: An Experimental Study of the Flow and Structure behind a Backward-Facing Step.
Report MD-39, Thermosciences Division, Dept. of Mech. Eng., Stanford University.

EDWARDS, R.V. (1981)
A New Look at Particle Statistics in Laser-Anemometer Measurements.
J. Fluid Mech. 105, 317.

EDWARDS, R.V., ANGUS, J.C. and DUNNING, J.W. (1973)
Spectral Analysis of the Signal from the Laser Doppler Velocimeter; Turbulent Flows.
J. Appl. Physics, 44, 1694.

EDWARDS, R.V., ANGUS, J.C., FRENCH, M.J. and DUNNING, J.W. (1971)
Spectral Analysis of the Signal from a Laser-Doppler Flowmeter Time-Independent System.
J. Appl. Physics, 42, 837.

EISENKLAM, P. (1961)
Atomisation of Liquid Fuel for Combustion
J. of Inst. of Fuel, 130

ERDMANN, J.C. and TROPEA, C. (1981)
Turbulence Induced Statistical Bias in Laser-Anemometry.
Turbulence in Liquids, Rolla-Missouri, paper 20.1

ETHERIDGE, D.W. and KEMP, P.H. (1978)
Measurements of Turbulent Flow Downstream of a Rearward-Facing Step.
J. Fluid Mech., 86, 3.

EL BANHAWY, Y.H. (1979)
Open and Confined Spray Flames.
Ph.D Thesis, University of London.

EL BANHAWY, Y.H. and WHITELAW, J.H (1981a)
Assessment of an Approach to the Calculation of the Flow Properties of Spray Flames.
Combustor Modelling AGARD-CP-275, Paper No.12.

EL BANHAWY, Y.H. and WHITELAW, J.H. (1981b)
Experimental Study of the Interaction Between a Fuel Spray and Surrounding Combustion Air.
Combustion and Flame, 42, 253.

FAETH, G.M. (1977)
Current Status of Droplet and Liquid Combustion.
Prog. Energy Comb. 3, 191.

FAETH, G.M. (1981)
Evaporation and combustion of sprays
Report of the Dept. of Mech. Eng., Penn. State Univ.
(Submitted to Prog. in Energy Comb. Sci.)

FOUNTI, M. and WHITELAW, J.H. (1981)
Shell-Side Flow in a Model Disc-and-Doughnut Heat Exchangers.
Fluids Section Report FS/81/37. Dept. of Mech. Eng., Imperial College, London.

FOUNTI, M. (1977)
Bluff-body Stabilised Flows.
M.Sc. Thesis, Dept. of Mech. Eng., Imperial College, Univ. of London.

FRAAS, A.P. and ÖZISIK, M.N. (1965)
Heat Exchanger Design.
J. Wiley and Sons Inc., N. York.

FREEMAN, A.R. (1975)
Laser Anemometer Measurements in the Recirculation Region Downstream of a Sudden Pipe Expansion.
Proceedings LDA-Symposium Copenhagen, PO Box 70, DK-2740 Skovlunde, Denmark.

GEORGE, W.K. (1978)
Processing of Random Signals (with Appendices by P.D. Beuter and J.L. Lumley).
Proceedings of the Dynamic Flow Conference, I.M.S.T., Marseille, 757.

GEORGE, W.K. and LUMLEY, J.L. (1973)
The Laser-Doppler Velocimeter and its Application to the Measurement of Turbulence.
J. Fluid Mech, 60, 321.

GINOUX, J.J. (1969)
On some Properties of Reattaching Laminar and Transitional High Speed Flows
Von Karman Institut for Fluid Dynamics, VKI TN 53.

GOLDSTEIN, R.J. and KREID, D.K. (1967)
Measurement of Laminar Flow Development in a Square Duct using a Laser-Doppler Flowmeter.
Trans. of ASME: J. of Appl. Mech., 34, 813.

GOSMAN, A.D., IOANNIDES, E., LEVER, D.A. and CLIFFE, K.A. (1980)
A Comparison of "Continuum" and "Discrete Droplet" Finite-Difference Models used in the Calculation of Spray Combustion in Swirling, Turbulent Flows.
HTFS Research Symposium, AERE, Hawell, RS 308. also AERE, Horwell, Rep. No. Tp. 865.

GOSMAN,A.D. and IOANNIDES, E. (1981)
Aspects of Computer Simulation of Liquid-Fuelled Combustors.
AIAA 19th Aerospace Sciences Meeting, Missouri, Paper No. 81-0323.

GOSMAN, A.D. and IDERIAH, F.J.K. (1976)
TEACH-T: A General Computer Program for two-dimensional, Turbulent, Recirculating Flows.
Dept. of Mech. Eng., Imperial College, London.

GOSMAN, A.D., KHALIL, E.E. and WHITELAW, J.H. (1979)
The Calculation of two-dimensional Turbulent Recirculation Flows.
In Turbulent Shear Flows I, (Eds Durst, F et al), Springer-Verlag, Berlin

GREATED, C. and DURRANI, T.S.(1971)
Signal Analysis for Laser Velocimeter Measurements,
J. Phys. E: Sci. Instrum. 4, 24.

GREEN, A.S.(1981)
Isothermal Models of Combustion Chamber Flows,
Ph.D. Thesis, University of London.

GÜNTER, A.Y., SENNSTROM, H.R. and KOPP. S. (1947)
A Study of Flow Patterns in Baffled Heat Exchangers,
ASME Paper 47-A-103.

HABIB, M.A. and WHITELAW, J.H. (1980)
Velocity Characteristics of a Confined Coaxial Jet With and Without Swirl.
Trans. of ASME, J. of Fluids Eng. 102, 47.

HOESEL, E. and RODI, W. (1977)
New Biasing Elimination Methods for Laser-Doppler Velocimeter Counter Processing.
Rev. Sci. Instrum. 48, 910.

HANJALIC, K. and LAUNDER, B.E. (1972)
A Reynolds Stress Model of Turbulence and its Application to thin Shear Flows
J. Fluid Mech., 52, 4.

HUTCHINSON, P., KHALIL, E.E., WHITELAW, J.H. and WIGLEY, G. (1976)
The Calculation of Furnace Flow Properties and their Experimental Verification.
J. Heat Transfer, C98, 276.

HUTCHINSON, P., KHALIL, E.E. and WHITELAW, J.H. (1977)
The Measurement and Calculation of Furnace-Flow Properties
AIAA, J. of Energy, 1, 212.

HUMPHRIES W. and VINCENT, J.H. (1976)
Experiments to Investigate Transport Processes in the Near Wakes of Disks in Turbulent Air Flow.
J. Fluid Mech, 75, 4.

IOANNIDES, E. and GOSMAN, A.D. (1978)
A Survey of the Literature Relating to Oil-Spray Combustion,
HTFS Research Symposium, AERE, Harwell, RS 254.

IOANNIDES, E. and GOSMAN, A D. (1980)
Combustion of Oil Sprays,
HTFS Research Symposium, AERE, Harwell, RS 310.

IRWIN, H.P.A.H. and ARNOT SMITH, P. (1975)
Prediction of the Effect of Streamline Curvature on Turbulence.
The Physics of Fluids, 18, 6.

JONES, W.P. and WHITELAW, J.H. (1982)
Calculation Methods for Reacting Turbulent Flows: A Review.
Combustion and Flame, 48, 1.

JONES, W.P., LOCKWOOD, F.C. and WHITELAW, J.H. (1982)
Modelling of Combustion Chambers and Furnaces
Notes for a Lecture Course, Dept. of Chemical and Mech. Eng., Imperial College, London.

JOHNSON, D.A., MODARESS, D. and OWEN, F.K. (1981)
An Experimental Verification of Laser Velocimeter Sampling Bias and its Elimination in Highly Turbulent Shear Flows.
3rd Symp on Turb. Shear Flows. Univ. of California, Davis.

KHALIL, E.E. (1976)
Flow and Combustion in Axisymmetric Furnaces
Ph.D. Thesis, Univ. of London.

KHALIL, E.E. and WHITELAW, J.H. (1977)
Aerodynamic and Thermodynamic Characteristics of Kerosene-Spray Flames.
16th Symp. (International) on Combustion.
The Combustion Institute, 559.

KIM, J., KLINE, S.J. and JOHNSTON, J.P. (1978)
Investigation of Separation and Reattachment of a Turbulent Shear Layer: Flow Over a Backward-Facing Step.
Thermoscienes Div., Dept. of Mechanical Eng., Stanford Univ. Rept MD-37 also Trans. of ASME. J. Fluids Eng. 102, 302.

KOMIYAMA, K., FLAGAN, R.C. and HEYWOOD, J.B. (1977)
The Influence of Droplet Evaporation on Fuel-air Mixing Rate in a Burner.
16th Symp (International) on Combustion. The Combustion Institute. 549.

LAUNDER, B.E. and SPALDING, D.B. (1974)
The Numerical Computation of Turbulent Flows.
Computer Methods in Applied Mechanics and Engineering, 3, 269.

LAUNDER, B.E. PRIDDIN, C.H., and SHARMA, B. I. (1977)
The Calculation of Turbulent Boundary Layers on Spinning and Curved Surfaces.
Trans. of ASME, J. Fluids Eng., 99, 231.

LAUNDER, B.E., REECE, G.J. and RODI, W. (1975)
Progress in the Development of a Reynolds Stress Turbulence Closure.
J. Fluid Mech., 68, 3.

LAUNDER, B.E. LESCHZINER, M.A. and SINDIR, M. (1982)
Coparison of Computation with Experiment,
Summary Report 1980-81, AFOSR-HTTM-Stanford Conference on Complex Turbulent Flows (Eds. Kline S.J. et al) III, 1390.

LAW, C.K. (1976)
Unsteady Droplet Combustion with Droplet Heating.
Combustion and Flame, 26, 17.

LEONARD, B.P. (1979)
A Stable and Accurate Convective Modelling Procedure Based on Quadratic Upstream Interpolation.
Comp. Meths. Appl. Mech. Engrg. 12, 59.

LESCHZINER, M.A. and RODI, W. (1981)
Calculation of Annular and Twin Parallel Jets Using Various Discretization Schemes and Turbulence-Model Variations.
Trans. ASME, J. of Fluids Eng. 103, 352.

LEONARD, B.P. LESCHZINER, M.A. and McGUIRK, J. (1978)
Third Order Finite-Difference Method for Steady two-dimensional Convection.
Proc. 1st Internat. Conference on Numer. Methods in Laminar and Turbulent Flows (Eds Taylor C. et al).
Pentech. London.

LIBBY, P.A. and BRAY, K.N.C. (1980)
Counter-Gradient Diffusion in Premixed Turbulent Flames.
AIAA 18th Aerospace Sciences Meeting, Pasadena, Calif.
Paper No. 80-0013.

LILLEY, D.G. (1977)
Swirl Flows in Combustion: A Review
AIAA 9th Fluid and Plasma Dynamics Conference, San Diego, Calif., Paper No. 76-405.

LILLINGTON, J. N. (1981)
A Vector Upstream Differencing Scheme for Problems in Fluid Flow Involving Significant Source Terms in Steady-State Linear Systems.
International J. for Numerical Methods in Fluids, 1, 3.

MARTIN, W.W., ELPHICK, I.G. and COLLISH, S. (1982)
Flow Distribution Measurement in a Model of a Heat-Exchanger.
Engineering Applications of Laser Velocimetry, Winter Annual Meeting of ASME, Phoenix, Ariz., 23.

MATARAJAN, R. and GHOSH, A.K. (1975)
Velocity Histories of Vaporizing Fuel Drops Moving through Standard Gas.
Fuel, 54, 153.

MELLING, A. (1973)
The Influence of Velocity Gradient Broadening on Mean and Rms Velocities Measured by Laser Anemometry.
Fluids Section Report HTS/73/33, Dept of Mech Eng., Imperial College, London.

MELLING, A. (1975)
Investigation of Flow in Non-Circular Ducts and other Configurations by Laser Doppler Anemometry,
Ph.D. Thesis, Univ. of London.

MELLING, A. and WHITELAW, J. H. (1973)
Seeding of Gas Flows for Laser Anemometry.
DISA Information, 15, 5.

MELLOR, A.M. (1973)
Simplified Physical Model of Spray Combustion in a Gas Turbine Engine.
Combustion Science and Technology, 8, 101.

MILLIZER, J., NICOLL, W.B and ALPAY, S.A. (1977)
Some Observations on the Numerical Calculation of the Recirculation Region of Twin Parallel Symmetric Jet Flow,
Turbulent Shear Flows I (Eds. Durst, F. et al), Springer-Verlag, Berlin.

MOREL, T. and BOHN, M. (1980)
Flow Over Two Circular Discs in Tandem,
Trans. ASME, J. of Fluids Eng. 102, 104.

MOSS, W.D., BAKER, S. and BRADBURY, L.S.J. (1979)
Measurements of Mean Velocity and Reynolds Stesses in Some Regions of Recirculating Flows.
Turbulent Shear Flows I (Eds Durst F. et al) Springer-Verlag, Berlin.

McLAUGHLIN, D.K. and TIEDERMAN, W.G. (1973)
Biasing Correction for Individual Realization of Laser Anemometer Measurements in Turbulent Flows.
Physics of Fluids, 16, 12, 2082.

NATIONAL ENGINEERING LABORATORY (1975)
Advances in Thermal and Mechanical Design of Shell-and-Tube Heat Exchangers.
NEL Rep. No. 590, Dept. of Industry, U.K.

NEGUS, C.R. (1979)
Experimental Studies in Fuel Sprays,
HTFS Research Symposium, AERE Hawell, RS264.

OKAMOTO, S. (1981)
Turbulent Shear Flows behind two-Dimensional Obstacles Placed on Plane Boundany.
2nd Biennial Symp. on Turbulence, Univ. of Missouri-Rolla, Paper No 3-1.

ONUMA Y. and OGASAWARA, M. (1975)
Studies on the Structure of a Spray Combustion Flame.
15th Symp. (International) on Combustion. The Combustion Institute, 453

ONUMA, Y., OGASAWARA, M. and INQUE, T. (1977)
Further Experiments on the Structure of a Spray Combustion Flame.
16th Symp. (International) on Combustion. The Combustion Institute, 561.

OWEN, F.K. SPADACCINI, L.J., KENNEDY, J.B. and BOWMAN,C.T. (1978)
Effects of inlet air swirl and fuel volatility on the structure of confined Spray Flames.
17th Symp. (Int) on Combustion, The Combustion Institute, 467.

PALEN, J.W. and TABOREK, J. (1969)
Solution of Shell Side Flow Pressure Drop and Heat Transfer by Stream Analysis Method.
CEP Symp. Ser. 65, 92, 53.

PATANKAR, S.V. (1980)
Numerical Heat Transfer and Fluid Flow.
Hemisphere Publishing Corp., Washington.

PATANKAR, S.V. and SPALDING, D.B. (1974)
A Calculation Procedure for the Transient and Steady-State Behaviour of Shell-and-Tube Heat Exchangers.,
Cited in Heat Exchangers Design and Theory Sourcebook.
(Eds Afgan N.N. et al) Scripta Book Company, Washington.

POPE, S.B. and WHITELAW, J.H. (1976)
The Calculation of Near-Wake Flows.
J. Fluid Mech. 73, 1.

PLETCHER, R.H. and KWON, O.K. (1982)
Prediction of Some Complex Turbulent Flows Using the Boundany Layer Equations and Viscous-Inviscid Interaction.
Summary Report, 1980-81 AFOSR-HTTM-Stanford Conference on Complex Turbulent Flows. (Eds Kline, S J et al) III, 1479.

RAITHBY, G.D (1976)
Skew Upwind Differencing Schemes for Problems Involving Fluid Flow.
Comp. Methods in Appl. Mech and Eng. 9, 153.

RESTIVO, A. and WHITELAW, J.H. (1978)
Turbulence Characteristics of the Flow Downstream of a Symmetric Plane Sudden Expansion
Trans. ASME, J. of Fluids Eng., 100, 308.

RIBEIRO, M.M. (1976)
The Turbulence Structure of Free Jet Flows with and without swirl.
Ph.D. Thesis, Univ. of London.

RIBEIRO, M.M. and WHITELAW, J.H (1975)
Statistical Characteristics of a Turbulent Jet
J. Fluid Mech. 70, 1.

ROACHE, P.J. (1976)
Computational Fluid Dynamics
Revised Printing, Hermosa Publishers, Albuquerque, N.M.

RUDINGER, G. (1975)
Effect of Velocity Slip on the Burning Rate of Fuel Particles
Trans. ASME, J. of Fluids Eng., 97, 321.

SAMI, S. and LIU, W.H. (1977)
Confined Shear Layer Approaching a Stagnation Point
Proc. 14th Midwestern Mech. Conf. Developments in Mechanics, 8, 497.

SAMSON, R., BEDEAUX, D., SAXTON, M.J. and DEUTCH, J.M. (1978)
A Simple Model of Fuel Spray Burning, Part I: Random Sprays Part II: Linear Droplet Stream.
Combustion and Flame, 31, 215 (Part I), 223 (Part II).

SCHLICHTING, H. (1955)
Boundany Layer Theory
McGraw-Hill Inc, N. York.

SCHOFIELD, W.H. BARBER, D.S. and LOGAN, E. (1981)
Turbulent Boundary Layer Flow through a Gap in a Wall-Mounted Roughness Element.
Trans. ASME, J. of Fluids Eng. 103, 97.

SMYTH, R. (1979a)
Turbulent Flow Over a Disk Normal to a Wall
Trans. ASME, J. of Fluids Eng. 101, 461.

SMYTH, R. (1979b)
Turbulent Flow Over a Plane Symmetric Sudden Expansion
Trans. ASME, J. of Fluids Eng. 101, 348.

SIMPSON, R.L. (1981)
REVIEW-A Review of Some Phenomena in Turbulent Flow Separation,
Trans. ASME, J. of Fluids Eng. 103, 520.

STYLES, A.C. and CHIGIER, N.A. (1977)
Combustion of Air-Blast Atomized Spray Flames
16th Symposium (International) on Combustion.
The Combustion Institute, 619.

SPALDING, D.B. (1972)
A Novel Finite- Difference Formulation for Differential Expressions Involving both First and Second Derivatives.
Intern. J. of Numerical Methods in Eng. 4, 551.

SPARROW, E.M., BALIGA, B.R. and PATANKAR, S.V. (1977)
Heat Transfer and Fluid Flow Analysis of Interrupted-Wall Channels with Application to Heat Exchangers,
Trans. ASME. J. of Heat Transfer, 1 ,4.

SULLEREY, R.K., GUPTA, A.K. and MOORTHY, C.S. (1975)
Similarity in the Turbulent Near Wake of Bluff Bodies
AIAA Journal, 13, 11.

TABOREK, J. (1979)
Evolution of Heat Exchanger Design Techniques
Heat Transf. Eng. 1, 1, 1.

TAYLOR, A.M.K.P. (1981)
Confined, Isothermal and Combusting Flows behind Axisymmetric Baffles
Ph.D. Thesis, Univ. of London.

TAYLOR, C. and HOOD, P.(1973)
A Numerical Solution of the Navier-Stokes Equations Using the Finite Element Technique.
Computers and Fluids, 1, 73.

TAYLOR, C. and HOOD, P. (1974)
Navier-Stokes Equations Using Mixed Interpolation.
Proc. of the 1st Internat. Conf. on Finite Element Methods in Flow Problems, p, 121.

TINKER, T. (1951)
Shell Side Characteristics of Shell and Tube Heat Exchangers, Parts I, II and III,
Proc. General Discussion Heat Transfer, Inst. of Mech. Eng., London.

TOWNSEND, A.A. (1976)
Structure of Turbulent Shear Flow
2nd Edit, C.U.P.

TROPEA, C. (1982)
Die Turbulente Stufenströmung in Flachkanälen und offenen Gerinnen.
Ph. D. Thesis, Univ. of Karlsruhe

TUTTLE, J.H., SHISLER, R.A. and MELLOR, A.M. (1976)
Investigation of Liquid Fuelled Turbulent Diffusion Flames,
Combustion Science and Technology, 14, 229.

TWARDUS, E.M. and BRZUSTOWSKI, T.A. (1978)
An Experimental Study of Flame Spread and Burning in Arrays of Monosize Hydrocarbon Droplets.
Com. Sci. and Tech., 17, 215.

VAFIDIS, C. (1982)
The Influence of Asymmetic Inlet Flow on the Presssure and Velocity Characteristics of an Isothermal Heat-Exchanger Model,
Fluids Section Report, FS/82/9, Dept. of Mech. Eng., Imperial College, London.

VAN ATTA, C.W. (1975)
Sampling Techniques in Turbulence Measurements.
Annual Review of Fluids Mechanics, 6, 75

VASILIC-MELLING, D.(1977)
Three Dimensional Turbulent Flow Past Rectangular Bluff Bodies.
Ph. D. Thesis, Univ. of London.

WATRASIEWICZ, B.M. and RUDD, M.J. (1976)
Laser-Doppler Measurements,
Butterworths.

WESTBROOK, C.K. (1977)
Three Dimensional Numerical Modeling of liquid Fuel Sprays.
16th Symposium (Intern.) on Combustion, The Combustion Institute, 1517.

WHITELAW, J.H. (1981)
Recirculating Flows, Laser-Doppler Anemometry and Calculation Methods.
Fluids Section Report FS/81/2 also Comptes Rendus du Huitième Congrès Canadien de Mécanique Appliquée, Moncton.

WIGLEY, G. (1974)
The Application of Radial Diffraction Gratings to Laser Anemometry,
Chemical Engineering Division, AERE Harwell Oxfordshire, AERE R-7886.

WILLIAMS, F.A. (1965)
Combustion Theory
Addison-Wesley

WILLIAMS, A. (1973)
Combustion of Droplets of Liquid Fuels: A Review.
Combustion and Flame, 21, 1.

WILLIAMS, A. (1976)
Fundamentals of Oil Combustion
Prog. Energy. Combust. Sci. 2, 167.

WINTERFIELD, G. (1965)
On Processes of Turbulent Exchange Behind Flame Holders.
Tenth Symp. (International) on Combustion,
The Combustion Institute, Pittsburgh.

YANTA, W.J. (1973)
Turbulence Measurements with a Laser-Doppler velocimeter,
Naval Ordnance Laboratory, White Oak, Silver Spring,
Maryland, NOLTR 73-94.

YULE, A., SENG, C., FELTON, P. UNGUT, A. and
CHIGIER, N.A. (1982)
A Study of Vaporizing Fuel Sprays for Laser Techniques.
Combustion and Flame, 44, 71.